3-4 october 2016
St Pierre d'Oléron
France

NUTTS'16

19 TH NUMERICAL TOWING TANK SYMPOSIUM

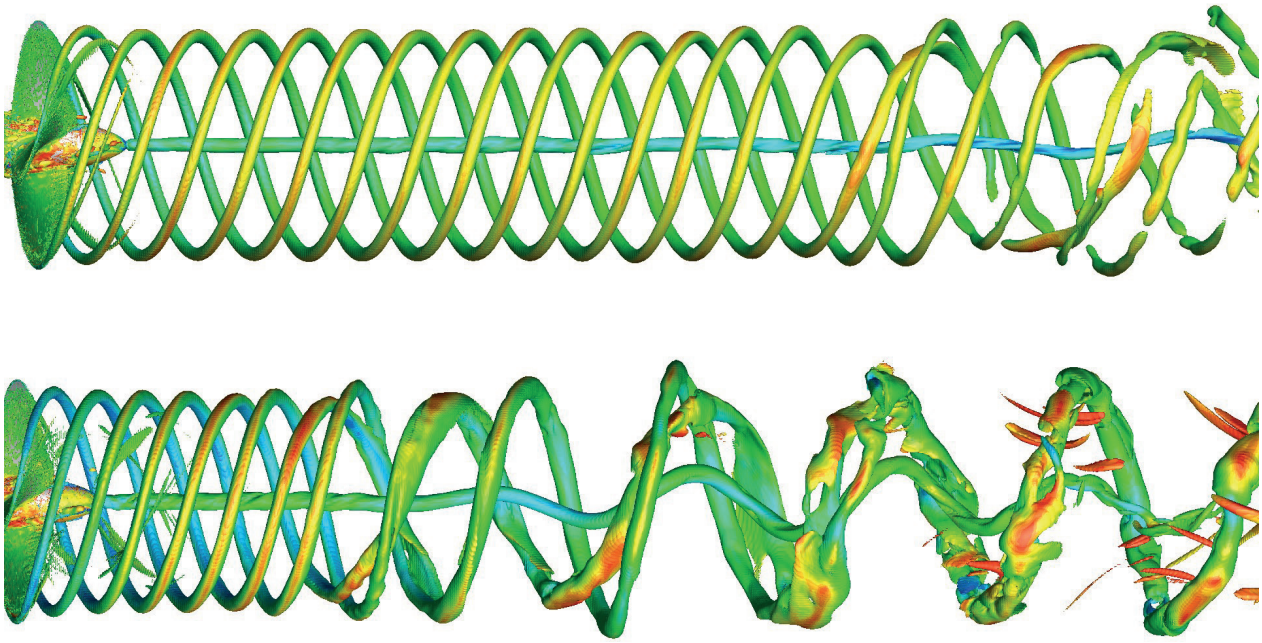

JEROEN WACKERS (ED.)

ECN Centrale Nantes

cnrs

SPONSORED BY

CD-ADAPCO

DCNS RESEARCH

NUMECA

Cover image: DES simulation of INSEAN E779A propeller at J=0.71 and J=0.45
Source: Emmanuel Guilmineau (CNRS / Centrale Nantes)

Contents

Density-based Compressible Solver with Equilibrium Cavitation Model in OpenFOAM

Mohammad Hossein Arabnejad[*], Rickard Bensow[*],Claes Eskilsson[*]
[*]Department of Shipping and Marine Technology, Chalmers University of Technology, Gothenburg, Sweden
mohammad.h.arabnejad@chalmers.se

1 Introduction

Cavitation is responsible for vibration, erosion and performance degradation in many engineering devices. To better understand cavitation and avoid its undesirable effects, cavitating flows have been the subject of many numerical studies. In most of these studies, the simulation is based on a two-phase incompressible Navier-Stokes solver together with a mass-transfer model. Because of their incompressible assumption, these solvers are not able to capture shock waves and high pressure peaks which are essential in the physics of cavitation erosion. Furthermore, the mass-transfer models normally include several empirical parameters. These parameters must be tuned for a particular flow condition and geometry by several numerical experiments.

An alternative approach to two-phase incompressible solvers is to use density-based compressible solvers with equilibrium cavitation models. These cavitation models assume that the two phases are in thermal and mechanical equilibrium and the transition between phases can be modeled by an equation of state for the mixture density. A widely used example of equilibrium cavitation models is the barotropic cavitation model (Venkateswaran et al.,2002). In this model, the densities of the fluids are assumed to depend only on pressure. With the barotropic assumption, the pressure gradient is always aligned with the density gradient, therefore the barotropic term in vorticity transport equation becomes zero. Gopalan and Katz (2000) have shown that the barotropic vorticity generation is important in closure region of sheet cavities. The under-prediction of the barotropic vorticity term can be avoided by using a more complete equilibrium cavitation model introduced by Saurel et al. (2002). In this approach, the full set of equations, including the energy equation, are solved with the suitable temperature dependent equations of state for each phase. This approach has been successfully used for different cavtiating flows by Koop (2008) and Schnerr et al. (2008).

The purpose of this paper is to present an implementation of a density-based compressible solver with equilibrium cavitation (similar to Koop (2008) and Eskilsson and Bensow (2012)) in the open-source finite volume framework OpenFOAM (Jasak et al.,1995). To check the implementation, simulation of a 1D Riemann water problem and a collapsing bubble are considered. Then, the validated solver is used to simulate the cavitating flow over a 2D NACA0015 foil.

2 Governing Equations

In the present study, the compressible Euler equations are used as the governing equations. These equations include continuity, momentum, and energy equations. To close the governing equations, an equation of state (EOS) is required to provide the relations between pressure and temperature with internal energy and density. In two-phase water-vapour flows, three equations of states must be provided for the three possible cases.

Pure Liquid

If the calculated density is higher than the liquid saturation density, the fluid is assumed to be pure liquid. The liquid phase is then described by the modified Tait EOS (Saurel et al., 1999),

$$p(\rho,T) = K_0\left[\left(\frac{\rho}{\rho_{l,sat}(T)}\right)^N - 1\right] + p_{sat}(T). \quad (1)$$

The temperature is obtained by the caloric EOS,

$$T = \frac{e-e_{l0}}{C_{vl}} + T_0. \quad (2)$$

Pure Vapour

When the density drops below the vapour saturation density, the fluid is assumed to be pure vapour. The perfect gas law is used to describe the pure vapour phase,

$$p(\rho,T) = \rho RT. \quad (3)$$

The temperature is obtained by the caloric EOS,

$$T = \frac{e-e_{l0}-L_v(T_0)}{C_{vv}} + T_0. \quad (4)$$

Mixture phase

With the thermodynamic equilibrium assumption, the mixture pressure can be considered equal to saturation pressure,$p = p_{sat}(T)$. The temperature is calculated from the equation of internal energy in the mixture as,

$$T = \frac{\rho(e-e_{l0})-\alpha\rho_{v,sat}L_v(T_0)}{\alpha\rho_{v,sat}C_{vv}+(1-\alpha)\rho_{l,sat}C_{vl}} + T_0, \quad (5)$$

where α is the vapour fraction and can be computed from the mixture density,

$$\alpha = \frac{\rho-\rho_{l,sat}}{\rho_{v,sat}-\rho_{l,sat}}. \quad (6)$$

The parameters in above equations are given in Table 1. The saturated values of pressure, $p_{sat}(T)$, and liquid and vapour density, $\rho_{l,sat}$ and $\rho_{v,sat}$, used in the above equations are obtained from IAPWS-IF97 library(Wagner et al. ,2008).

Table 1: Parameters used in Eq.1-6

N	K_0	C_{vl} $(Jkg^{-1}K^{-1})$	T_0 (K)	e_{l0} (Jkg^{-1})	γ	R $(Jkg^{-1}K^{-1})$	C_{vl} $(Jkg^{-1}K^{-1})$	$L_v(T_0)$ $(Jkg^{-1}K^{-1})$
7.15	3.3×10^8	4180	1.0×10^4	617.0	1.327	461.6	1410.8	2.753×10^6

3 Numerical Methods

The following numerical method has been implemented in OpenFOAM. The numerical flux is evaluated by solving the approximate Riemann problem using HLLC-AUSM low-Mach Riemann solver (Koop,2008). Second order accuracy in space is achieved by the piece-wise linear

reconstruction method with the limiter function of Venkatakrishnan (1995). For time advancing, explicit low storage Runge-Kutta schemes are employed.

4 Results

4.1 Validation

In order to validate the implementation of the compressible solver, numerical simulations of a 1D Riemann problem for water flow and a collapsing bubble are performed.

1D Riemann problem for water flow

In this section, the simulation of 1D Riemann problem for water flow is presented. The purpose of this simulation is to check the capability of the implemented method in capturing shock waves in compressible water flows. The computational domain, shown in Fig. 1, is a tube of length 1m filled with water. A diaphragm at the center of the tube separates two regions with different initial conditions. This diaphragm is removed at the start of simulation.

The solution of this Riemann problem includes a left-running expansion wave, a contact surface, and a right-running shockwave. The numerical solution at different instances is plotted in Fig. 2, which shows that the implemented numerical methods are able to capture expansion and shock waves without overshoot.

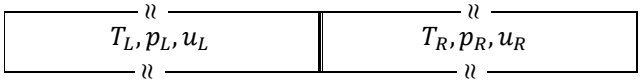

p_L (pa)	u_L (m/s)	T_L (K)	p_R (pa)	u_R (m/s)	T_R (K)
1.0×10^8	0.0	293	$1e \times 10^4$	0.0	293

Fig. 1: Computational domain and initial conditions for 1D Riemann problem for water flow

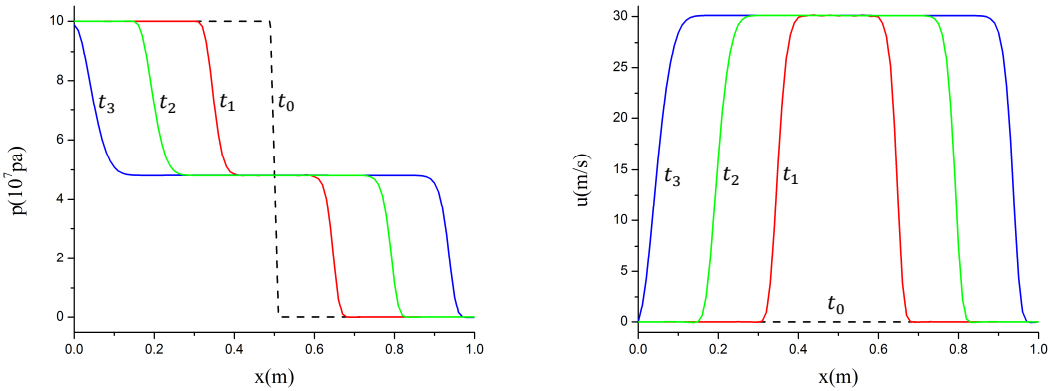

Fig. 2: Solution of Riemann problem for water flow at $t_N = N\Delta t$ (left: pressure, right: velocity, $\Delta t = 9 \times 10^{-5}$).

Collapsing Bubble

In this section, the implementation of a homogeneous cavitation model is validated for the collapse of a single bubble. To minimize the computational cost, an asymmetric wedge mesh with angle of five degrees is created. The mesh is a section of a sphere and has 100 cells in radial direction and 100 cells in circumferential direction. The mesh spacing is very refined near the location of bubble collapse in order to capture the rapid movement of bubble interface. The computational domain and boundary conditions are shown in Fig. 3. As the initial conditions, the pressure inside the bubble is set to $P_v = 2340\ pa$,while the pressure in surrounding liquid is $P_\infty = 1bar$.

To compare numerical results with the solution of the Rayleigh-Plesset equation, this equation is solved using the ODE solver in OpenFOAM. The fluid properties that are used in this solution are the same as those in numerical simulation. Fig. 4 shows the agreement between the result of numerical simulation and the solution of Rayleigh-Plesset equation. This agreement demonstrates the validation of the implemented cavitation model and numerical methods.

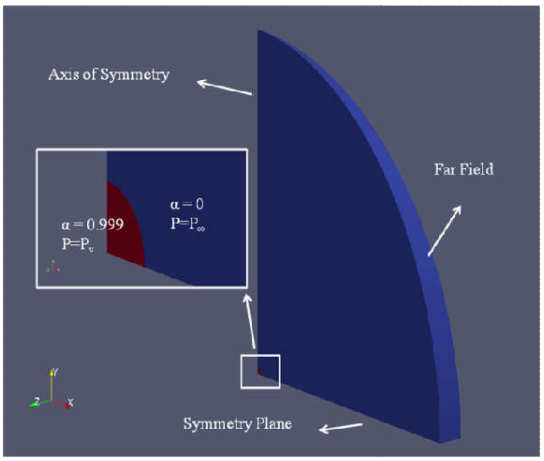

Fig. 3: Computational Domain and BCs for the collapsing bubble case.

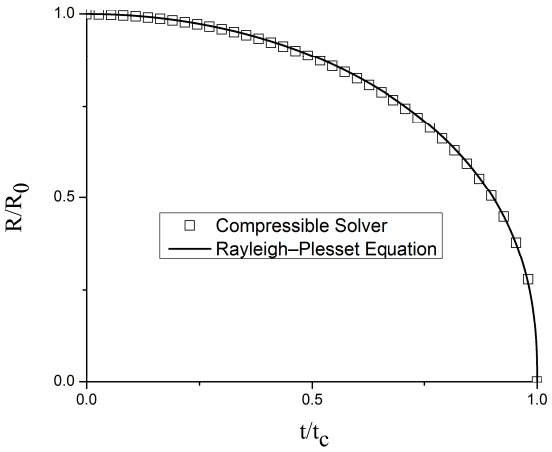

Fig. 4: Comparison of numerical simulation and solution of Rayleigh-Plesset equation for a collapsing bubble.

4.2 Cavitating Flow over 2D NACA0015

The hydrofoil considered in this study, is a 2D NACA0015 foil at an angle of attack of 6^o with chord length c = 0.13m. The computational domain, shown in Fig. 5, is a channel with height 2c and a length of 2c upstream of the hydrofoil leading edge and 3c behind the trailing edge. The inlet velocity is 12 m/s, the temperature 293 k and the density 998.2 kg/m^3. The pressure at the outlet is set to 74.2 kPa which corresponds to the cavitation number equal to one. Slip boundary conditions are applied to the foil and the channel walls, as the Euler flow is computed. A C-type mesh with 38280 cells is used for this simulation.

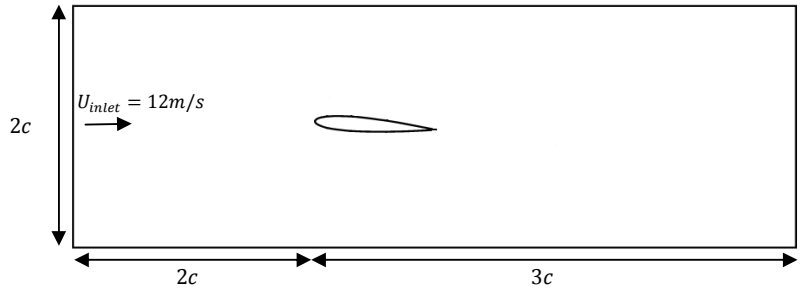

Fig. 5: Computational domain for simulation of cavitating flow over 2D NACA0015.

Koop (2008) has reported that for this case, the growth and shedding of the sheet cavity has an approximately periodic behavior. To show this behavior, the total vapour volume V_{vap} is calculated at every time step. The time history of the total vapor volume V_{vap} during several cycles are presented in Fig. 6. The figure shows a periodic behavior with period of 0.025s and a frequency of 40 Hz.

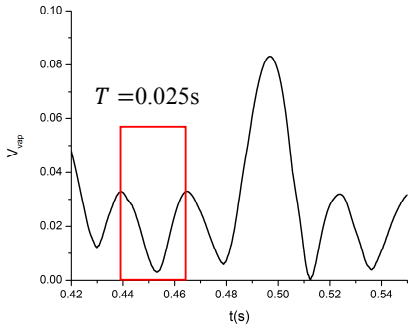

Fig. 6: Time-history of the total vapor volume V_{vap} in simulation of the cavitating flow over 2D NACA0015

In Fig. 7, the distribution of vapour fraction α is presented for a number of equidistant time instances during one cycle. At the start of the cycle, Fig7.(a), a new sheet cavity appears at the leading edge, while the shed cloud cavity from previous cycle is convected downstream. The sheet cavity continues to grow and the shed vapour structure starts collapsing as it is transported into the high pressure region near the trailing edge ,Fig.7(b). The collapse of the shed vapour structure produces a high pressure pulse which is shown in Fig 8(a). As the sheet cavity has reached its maximum length, a re-entrant jet has developed at the closure region of the sheet cavity, Fig.7(c). The re-entrant jet travels upstream along the foil surface and collides with the liquid interface. This collision splits the sheet cavity into several vapour structures with rotational motion, Fig.7(d-e). While the shed vapour structures merge by circular motion and create a cloud cavity, Fig.7(f), the remaining part of sheet cavity collapses leading a pressure pulse shown in Fig 8(b).

5 Conclusion

A density based compressible solver with equilibrium cavitation model has been implemented in OpenFOAM. The implemented solver is tested for three cases. The simulation of 1D Riemann problem for water flow and collapsing bubble are performed to validate the implemented numerical methods and cavitation model. After checking the implementation, the simulation of a cavitiating flow

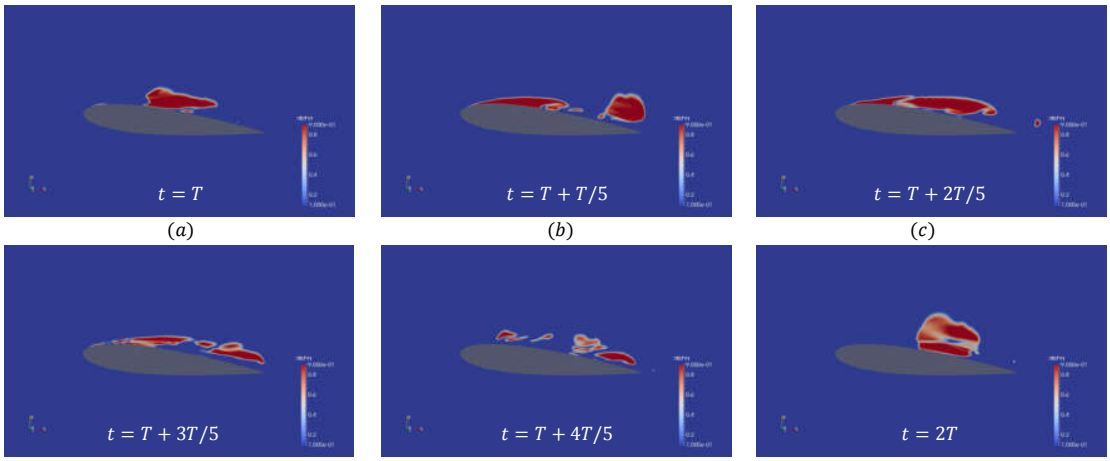

(a) (b) (c) (d) (e) (f)

Fig. 7: Distribution of vapour fraction α during one shedding cycle.

(a) (b)

Fig. 8:Pressure pulses produced by the collapse of (a)the cloud cavity and (b)the sheet cavity.

over a 2D NACA0015 foil is performed. The results show that the cavitating flow has a periodic behavior with the frequency of 40 Hz. The re-entrant jet mechanism is found to be responsible for this periodic behavior. In the future, the solver will be extended to include viscous fluxes. Furthermore, the solver will be used to simulation cavitating flows in 3D and compare with experimental data.

References

C. Eskilsson ,R. Bensow(2011). A compressible model for cavitating flow: comparison between Euler, RANS and LES simulations. 29th Symposium on Naval Hydrodynamics, Gothenburg, Sweden.

S. Gopalan and J. Katz(2000). Flow structure and modeling issues in the closure region of attached cavitation, *Physics of Fluids*, **12**(4), 895–911.

H. Jasak H.G. Weller, G. Tabor and C. Fureby(1998). A tensorial approach to CFD using object oriented techniques. *Computer in Physics*, **12**(6).

A.H. Koop (2008), Numerical Simulation of Unsteady Three Dimensional Sheet Cavitation, PhD thesis, University of Twente.

R. Saurel, and R. Abgrall(1999). A multiphase Godunov method for compressible multifluid and multiphase flow, *Journal of Computational Physics*,**150**, 425–467.

G.H. Schnerr, I.H. Sezal, and S.J. Schmidt (2008) Numerical investigation of three-dimensional cloud cavitation with special emphasis on collapse induced shock dynamics. *Physics of Fluids*, **20**, 40703.

W. Wagner and H. Kretzschmar (2008). *International steam tables: properties of water and steam, based on the industrial formulation IAPWS-IF97*. Springer.

V. Venkatakrishnan(1995). Convergence to Steady-State Solutions of the Euler Equations on Unstructured Grids with Limiters". *Journal of Computational Physics*, **118**,120–130.

S. Venkateswaran, J.W. Lindau, R.F. Kunz, and C.L. Merkle (2002) Computation of multiphase mixture flows with compressibility effects, *Journal of Computational Physics*, **180**, 54–77.

Numerical Analysis of Tip Vortex Flow

Abolfazl Asnaghi, Andreas Feymark, Rickard E Bensow,
Chalmers University of Technology, Gothenburg/Sweden,
{abolfazl.asnaghi,andreas.feymark,rickard.bensow}@chalmers.se

The roll-up and formation of the tip vortex occur on the tip of a lifting wing of finite span. Close to the tip, a pressure differential exists between the upper and lower surfaces which drives the fluid around the tip from the high pressure side on the lower surface to the low pressure side on the upper surface. The fluid becomes highly three-dimensional as it undergoes this motion. The vortex then moves downstream and rolls up more and more of the wing wake until its circulation is nominally equal to that of the wing. This typically extends to a few wing spans downstream of the trailing edge. This proves to be a challenging flow field to study because of the presence of turbulence and the large gradients of pressure and velocity in all three directions especially across the vortex core.

In cavitation research and propeller design, tip vortex characteristics have a direct impact on the tip vortex cavitation inception which itself is important in defining the boundaries of the cavitation free bucket chart of a propeller. Due to the interaction of two phase flow and tip vortex, this phenomenon concerns very small scale dynamics making it very complicated to be studied through experimental or numerical tools. Understanding the physics of these flows therefore is important in finding the tip vortex inception speed in order to prevent or control the occurrence of cavitation on propellers.

Experimental analysis of tip vortex flow around elliptical foils have been performed by many researchers [1-4]. This type of foil has similar tip vortex behaviour as to a propeller making it a suitable benchmark for both numerical and experimental investigations of tip vortex flows.

In the experiments conducted by Arndt et al. [1-3], cavitation inception is studied on a series of elliptical planform hydrofoils, named Arndt elliptical foil. It is observed that the cavitation inception and its growth in the tip region strongly depends on the size and number of nuclei in the free stream and also on the strength of the vortex. Further, in most of the tested conditions the lowest pressure region of the tip vortex appears in a region very close to the tip where the vortex is not completely rolled up. It is also noted that for this type of foil, an excess axial velocity exists in the vortex core which increases with angle of attack; the axial velocity at the vortex core can go up to 2.4 times of the free stream velocity value. It is highlighted that the presence of bubbles in the flow and their trapping into the vortex does not significantly affect the vortex trajectory. The vortex is asymmetric, indicating the velocity measurements made with a single traverse through the vortex can be misleading. It is suggested to use particle image velocimetry (PIV) for further study and analysis. Observation indicates that the cavitation inception occurs both inside and outside the vortex core. Nuclei which cavitate just outside the core quickly spiral into the vortex axis. Moreover, it is noted that in strong water, where the amount of the nuclei is limited, larger bubbles are created when inception occurs. Then considering the inception pressure provides more consistent cavitation data than considering the saturation pressure. In the weak water it is found that the cavitation inception pressure was often greater than the saturation pressure. Moreover, significant level of tension can be tolerated before inception occurs in the strong water.

Following the suggestion by Arndt et al. [1-3] to use PIV method for tip vortex analysis, Pennings et al. [4] conducted Stereoscopic PIV measurements on the Arndt's foil in non-cavitating and cavitating conditions. They employed correlation averaging in PIV images post processing in order to minimize the interrogation area size.

The current paper reports parts of some tip vortex inception research undergoing in the Rolls-Royce University Technology Centre at Chalmers [5,6]. As a first step, numerical analysis of the wetted tip vortex around the Arndt elliptical foil is conducted using OpenFOAM.

The OpenFOAM package, used in this study for numerical simulation, is an open source code written in C++ to model and simulate fluid dynamics and continuum mechanics. It is possible to adopt the code and build new functionalities, libraries, solvers, and utilities. The software is community driven where various communities are working on different fields of applications. This has expedited the progress and development of the software. In OpenFOAM, the spatial discretization is performed using a cell centred collocated finite volume (FV) method for unstructured meshes with arbitrary cell

shapes, and a multi-step scheme is used for the time derivatives. To complete the FV-discretization the face fluxes need to be reconstructed from grid variables at adjacent cells, requiring interpolation of the convective fluxes and difference approximations for the inner derivatives of the diffusive fluxes; see [7-9] for more details on the discretization and the numerical schemes used in OpenFOAM.
The geometry of the Arndt foil is an elliptical planform having the NACA $66_2 - 145$ as cross section, see Figure 1. Having NACA 6 series section introduces a low adverse pressure gradient over the foil and therefore longer laminar boundary layer. The computational domain has the same dimensions and geometry as the cavitation tunnel at TU Delft. In Figure 2, the computational domain and related boundary positions are presented.

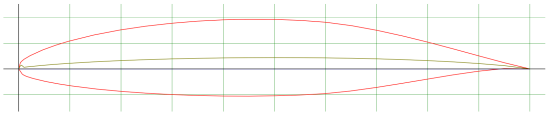

Figure 1. NACA $66_2 - 145$

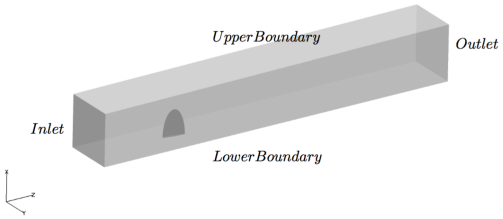

Figure 2. Boundary positions, Arndt foil

In the computational domain, the inlet is placed approximately five chord lengths in front of the foil, and the outlet is placed ten chord lengths behind the foil. The foil is positioned in the middle of the channel width where the distance to each side is equal to 150mm. The chord length of the foil at the root is equal to 125.6mm, and the coordinate system is located at the center of the chord. The trailing edge has been cut off with a thickness of 0.3mm, and the total area of the foil from the 3D CAD model is 0.01465 m^2. It should be noted that the current study is performed for the foil having geometrical angle of attack of 9 degrees. The inlet velocity is set equal to 6.8 m/s which corresponds to the Reynolds number of 8.5e05. The outlet pressure is set fixed equivalent to cavitation number four.
One of the most challenging parts of numerical analysis of tip vortex flows is to provide appropriate mesh resolution at the vortex core region. As one of the main tasks of the research was to find the spatial resolution requirement for numerical analysis of tip vortex flows, applying hexahedral cells at the tip vortex region became advantageous. To address this, StarCCM+ of CD-Adapco is used to generate the mesh.
At the first step, a coarse mesh is employed to simulate the tip vortex in order to find the approximate trajectory vortex path. The trajectory location is then used in StarCCM+ to define refinement zones. Two cylindrical regions are considered around the trajectory path to specify the mesh resolution, having 10 and 60 mm diameter, respectively, corresponding to approximately 10 and 60 times the vortex core diameter. These cylindrical regions extend two chord length downstream of the foil. In Figure 3 and 4, general distribution of the cells in the streamwise and inplane directions are presented.

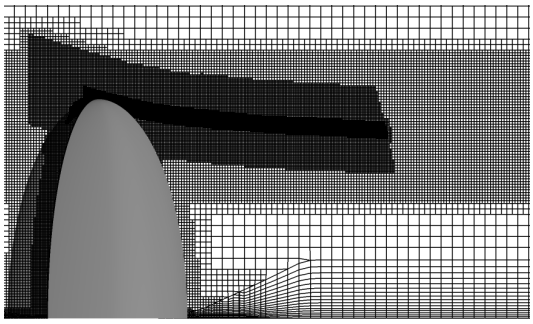

Figure 3. Streamwise mesh distribution

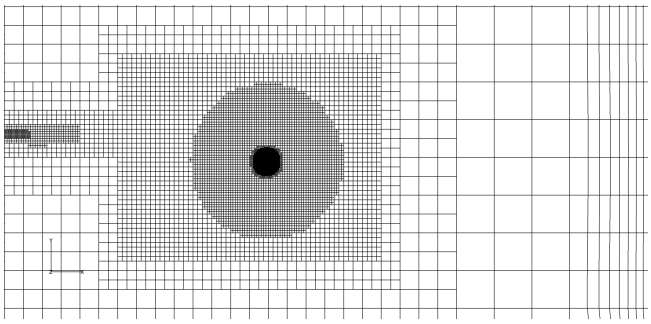

Figure 4. Inplane mesh distribution

Five different resolutions having different inplane and streamwise resolutions are created. The surface resolutions and prismatic layers (y^+=1) of these meshes are the same, and the only difference between them is the resolution of the inner refinement cylinder, Figure 4. In Table 1, the specifications of these

meshes are presented. It is reported that the tip vortex core for the selected operating condition has a diameter equal to 1 mm. Therefore, the sizes and dimensions in Table 1 are selected accordingly.

Table 1. Mesh specifications for mesh independency study

	Name	Total number of Cells (M)	In-plane cell size (mm)	Streamwise cell size (mm)	Number of cells in vortex core
In-Plane resolution	P1S1	8.3	0.125	0.25	8
	P2S1	24.4	0.062	0.25	16
	P3S1	88.3	0.031	0.25	32
Streamwise resolution	P2S1	24.4	0.062	0.25	16
	P2S2	44.3	0.062	0.125	16
	P2S3	84.9	0.062	0.062	16

Due to the computational resources limitation, the simulations are carried out in steady manner. The governing equations of a steady incompressible Newtonian fluid consist of conservation of mass, and momentum. In the filtered manner, these equations can be written as follow,

$$\frac{\partial(\overline{u_k})}{\partial x_k} = 0, \tag{1}$$

$$\frac{\partial(\overline{u_k}\,\overline{u_j})}{\partial x_j} = -\frac{1}{\rho}\frac{\partial \overline{p}}{\partial x_k} + \frac{\partial}{\partial x_j}\left[(\nu + \nu_t)\,\partial u_k/\partial x_j\right]. \tag{2}$$

To model the turbulent viscosity, the simulations are carried out as laminar (i.e. no turbulence model applied) and with kOmegaSST-RANS method [10]. The linear eddy viscosity assumption is insensitive to the flow streamline curvature, thus for highly swirling flows, this can lead to over prediction of turbulent viscosity in the swirling region. In order to compensate for that, various curvature corrections have been proposed [11].
For the kOmegaSST model, the empirical function that multiplies the production term P in both the k and ω equations is,

$$f_{r1} = max[min\{f_{rotation}, 1.25\}, 0], \tag{3}$$

where

$$f_{rotation} = (1 + C_{r1})\frac{2r^*}{1+r^*}[1 - C_{r3}tan^{-1}(C_{r2}\hat{r})] - C_{r1}. \tag{4}$$

All the variables and their derivatives are defined with respect to the reference frame of the calculation, which may be rotating with rotation rate Ω^{rot}. The remaining functions are defined as,

$$r^* = \frac{S}{W}, \tag{5}$$

$$\hat{r} = \frac{2W_{ih}S_{jh}}{WD^3}\left(\frac{DS_{ij}}{Dt} + \left(\varepsilon_{imn}S_{jn} + \varepsilon_{jmn}S_{in}\right)\Omega_m^{rot}\right), \tag{6}$$

$$S_{ij} = \frac{1}{2}\left(\frac{\partial u_i}{\partial x_j} + \frac{\partial u_j}{\partial x_i}\right), \tag{7}$$

$$W_{ij} = \frac{1}{2}\left[\left(\frac{\partial u_i}{\partial x_j} - \frac{\partial u_j}{\partial x_i}\right) + 2\varepsilon_{mji}\Omega_m^{rot}\right], \tag{8}$$

$$S^2 = 2S_{ij}S_{ij}, \tag{9}$$

$$W^2 = 2W_{ij}W_{ij}, \tag{10}$$

$$D^2 = max(S^2, 0.09W^2), \tag{11}$$

$$C_{r1} = 1.0,\ C_{r2} = 2.0,\ C_{r3} = 1.0. \quad (12)$$

The term DS_{ij}/Dt represents the components of the material derivative of the strain rate tensor. The rotation rate, Ω^{rot}, is nonzero only if the reference frame itself is rotating.
In Table 2, lift coefficient predictions using different mesh resolutions are presented. For laminar simulations, these different mesh resolutions show similar accuracy level in prediction of lift force (under predicted around 8 percent). The kωSST and kωSST-CC show over prediction of the lift force but in the same accuracy level. This indicates that the lift is unaffected by the prediction of the tip vortex. One reason for the difference between the laminar and the RANS results can be the effects of laminar-turbulent boundary layer transition. In the RANS simulation, the boundary layer is fully turbulent from the leading edge which contributes to the velocity distribution of the vortex core. To investigate further, one has to also model this case with a laminar-turbulent transitional RANS model.

Table 2. Lift coefficients for different mesh resolutions, laminar simulations

	In-plane refinement			Stream wise refinement			kωSST	kωSST-CC
Case	P1S1	P2S1	P3S1	P2S1	P2S2	P2S3	P2S1	P2S1
Lift Coefficient	0.604	0.605	0.608	0.605	0.605	0.606	0.716	0.714
Experiment	0.66							
Comparative Error %	-8.5	-8.3	-7.8	-8.3	-8.3	-8.2	8.5	8.2

Appearance of accelerated axial velocity at the vortex core decreases pressure below the saturation pressure. Therefore, in order to measure the distance that the vortex can be transported downstream, one can measure the length of the pressure iso-surface of $p=p_{sat}$. Figure 5 and Table 3 represent the iso-surface of pressure for different mesh resolution and also for different turbulence models. RANS simulations fail totally in predicting accelerated axial velocity, and as a result the length of the iso-surface is very short, just 12 mm. It should be also noted that no noticeable difference is observed by employing the curvature correction.

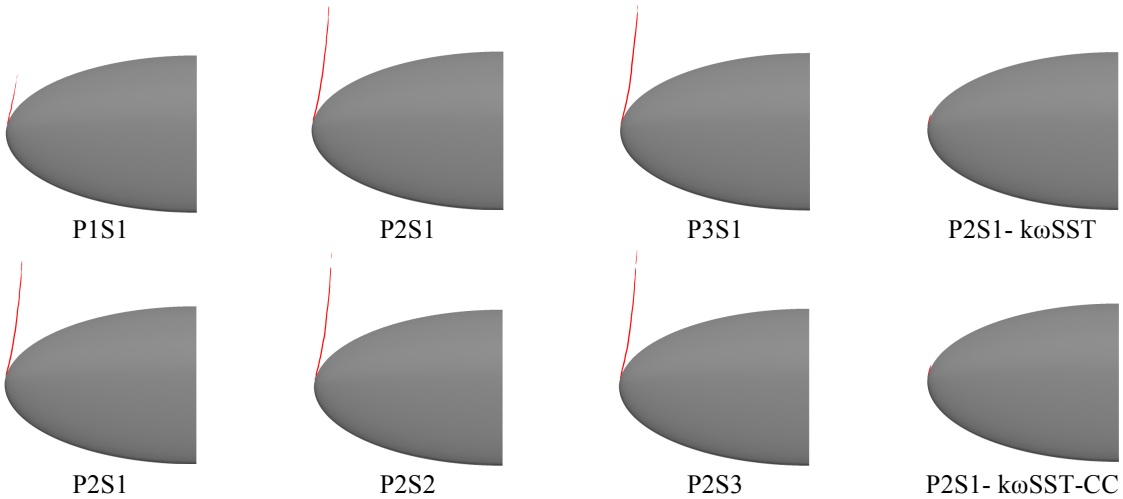

Figure 5. Pressure iso-surfaces ($p=p_{sat}$) for different mesh resolutions

Table 3. Pressure Iso-surface length ($p=p_{sat}$)

	In-plane refinement			Stream wise refinement			kωSST	kωSST-CC
Case	P1S1	P2S1	P3S1	P2S1	P2S2	P2S3	P2S1	P2S1
Length (mm)	43	96	98	96	107	107	12	12

For inplane resolution investigation, results of P2S1 is independent of the mesh resolution. Therefore, the cell size suggestion is 0.1 mm for inplane section which is equivalent to have 16 cells per vortex

core diameter. For streamwise resolution investigation, it is observed that for P2S2 mesh the convergence of results is achieved and results are independent of the resolution. Therefore, suggestion for the cell size in the streamwise direction is 0.2 mm corresponding to $1/8^{th}$ of the core diameter. For the cases that the vortex core diameter is not available, one can use Kolmogorov scale (η). For the current case, Kolmogorov scale was 5e-6 m. Therefore, the suggested sizes would be 20η for inplane resolution and 40η for streamwsie resolution.

Acknowledgements

Financial support of this work has been provided by Rolls-Royce Marine through the University Technology Centre in Computational Hydrodynamics hosted at the Dept. of Shipping and Marine Technology, Chalmers. The simulations were performed on resources at Chalmers Centre for Computational Science and Engineering (C3SE) provided by the Swedish National Infrastructure for Computing (SNIC).

References

[1] Arndt, Roger E.A.; Maines, Brant H. (1994). Viscous effects in tip vortex cavitation and nucleation. Retrieved from the University of Minnesota Digital Conservancy, http://purl.umn.edu/49809

[2] Arndt RA; Keller AP. Water Quality Effects on Cavitation Inception in a Trailing Vortex. ASME. *J. Fluids Eng.* 1992;114(3):430-438. doi:10.1115/1.2910049.

[3] R. E. A. Arndt, V. H. Arakeri and H. Higuchi (1991). Some observations of tip-vortex cavitation. Journal of Fluid Mechanics, 229, pp 269-289 doi:10.1017/S0022112091003026

[4] Pennings, P. C. and Westerweel, J. and van Terwisga, T. J. C., Flow field measurement around vortex cavitation, Experiments in Fluids, Vol 56, No 11, 2015.

[5] B. L. Zhang , J. Lou ; C. W. Kang ; A. Wilson ; J. Lundberg ; U. Svennberg ; Rickard E. Bensow; CFD Modeling of Propeller Tip Vortex over Large Distances; International Journal of Offshore and Polar Engineering (1053-5381). Vol. 24 (2014), 3, p. 181-183.

[6] Rickard E. Bensow, Mats G. Larson, Residual based VMS subgrid modeling for vortex flows, Computer Methods in Applied Mechanics and Engineering, Volume 199, Issues 13–16, 1 February 2010, Pages 802-809, ISSN 0045-7825, http://dx.doi.org/10.1016/j.cma.2009.08.004

[7] H. Jasak H.G. Weller, G. Tabor and C. Fureby, 'A tensorial approach to CFD using object oriented techniques'. Computational physics, 12, 1997.

[8] Hrvoje Jasak. 'Error Analysis and Estimation for the Finite Volume Method with Applications to Fluid Flows' PhD thesis, Department of Mechanical Engineering, Imperial College of Science, Technology and Medicine, 1996.

[9] Rusche Henrik. 'Computational Fluid Dynamics of Dispersed Two-Phase Flows at High Phase Fractions', PhD thesis, Department of Mechanical Engineering, University of London, Technology and Medicine, 2002.

[10] Gotfred S. Berntsen, Morten Kjeldsen, and Roger E. A. Arndt, Numerical modeling of sheet and tip vortex cavitation with fluent 5, CAV2001:sessionB5.006.

[11] Pavel E. Smirnov and Florian R. Menter, Sensitization of the SST Turbulence Model to Rotation and Curvature by Applying the Spalart–Shur Correction Term, Journal of Turbomachinery, OCTOBER 2009, Vol. 131

Validation of CFD for a deterministic breaking wave impact on a semi submersible

Henry Bandringa[*], Joop Helder[†], Tim Bunnik[†]
[*]MARIN Academy, Wageningen, NL (h.bandringa@academy.marin.nl), [†]MARIN, Wageningen, NL

1 Introduction

For structural design, prediction of run-up, green water and impact loads have to be taken into account, to assure the integrity and safety of structures offshore. For predicting these highly non-linear phenomena, most of the offshore industry relies on detailed model testing. In the last couple of years, however, CFD simulations have shown more and more promising results in predicting these events (Iwanowski (2014), Pakozdi (2015), Veldman (2015)). For the offshore industry to have sufficient confidence in the accuracy of CFD simulations in the challenging field of extreme wave impacts, it is essential that a proper verification and validation study of such CFD tools is performed.

In this paper, two CFD simulation tools, i.e. ComFLOW and ReFRESCO will be considered. In Bandringa et al. (2016), these two CFD tools were successfully validated for a regular wave impact on a fixed semi submersible. To increase the complexity of the validation, in the present paper we focus on simulating a deterministic *breaking* wave impact on a fixed semi submersible, for which results will again be validated against experiments carried out by MARIN. Details on the two CFD tools can be found in Bandringa et al. (2016) and the references therein. Considering the topic at hand, the most relevant differences between the two CFD tools can be summarized as follows: ComFLOW explicitly reconstructs the free surface on a structured grid and integrates the free surface explicitly in time, using a variable time step. In ReFRESCO the free surface is implicitly reconstructed on an unstructured grid and implicitly integrated in time with a fixed time step. ComFLOW has the option to run in single-phase mode, whereas ReFRESCO always solves in two-phase mode. ComFLOW was specifically developed to simulate inertia driven free-surface flows (Luppes (2013)). ReFRESCO (Vaz (2009)) was developed to simulate viscous flows with complex geometries (Koop (2011), Kerkvliet (2014)).

2 Model tests

The model experiments for a semi submersible, at a scale of 1:50, were executed by MARIN. A simplified version of a semi submersible configuration (only half of a semi submersible) was placed at the center of the basin, see Fig. 1 for clarification.

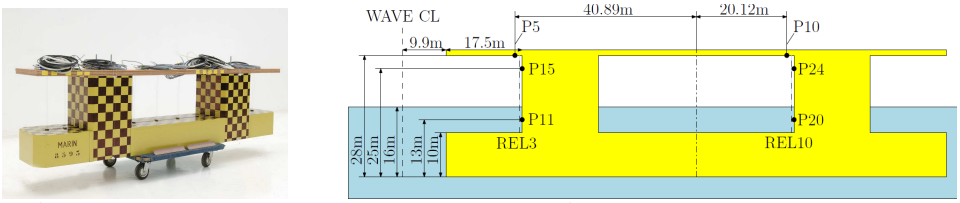

Fig. 1: Left: Model in experiment. Right: Schematic overview of the sensor locations on the semi submersible.

On full scale, the dimensions of the semi submersible are 114.5m long, 17.5m wide and 28.0m high, with a draft of 16.0m. The basin, with solid side walls, is 200m long, 4m wide and 4m deep, which equals 10000m×200m×200m on full scale. To generate the waves in the basin, a flap-type wave generator is used. The water heights were monitored with wave resistance probes at 100Hz (model scale) and pressures were recorded by Piezo-type transducers at 5kHz (model scale). In total 28 Piezo pressure probes and 24 wave probes were incorporated. In Fig. 1, some of these probes are visualized. The wave probes close to the first and second column, i.e. REL3, REL10 are located 0.5m (full scale)

from the column. For the numerical simulations, we selected one extreme wave event (see Fig. 3) from a 3-hour experiment using a Jonswap seastate with significant wave height (H_s) of 8.0m, peak period (T_p) of 11.0s and a gamma value of 3.3.

3 Reconstruction of the selected breaking wave event

To mimic the extreme wave event in the CFD simulation, it is important that the wave kinematics, the time derivate of the wave elevation and the wave crest are reproduced as accurately as possible. To reconstruct the measured basin wave one can mimic the stroke of the wave maker in the numerical simulation. However, in general the distance between the wave maker and the model in the basin is large, giving rise to a large amount of grid cells and issues with numerical wave dissipation and phase differences when the wave is numerically propagated. Therefore, another approach is considered, in which the incoming wave is generated by an iterative wave calibration procedure as proposed by Bunnik and Helder (2015, 2016). As initial inflow boundary condition, the incoming wave is estimated at a location upstream from the target location, using the measured basin wave at the target location and linear dispersion theory. After the incoming wave is propagated through the CFD domain, the numerically reconstructed wave at the target location (i.e. WAVE CL in Fig. 1) is compared to the measured basin wave, and based on the differences the inflow is corrected. This iterative procedure continues until a satisfactory match is obtained between the measured target wave and numerically reconstructed wave. The focus hereby is on matching both the wave crest elevation and its time derivative. For the selected target wave, the above reconstruction was performed in ComFLOW, on a 2D domain. The outcome was interpolated to both a 3D ComFLOW and a 3D ReFRESCO computational domain. The best match for the selected extreme wave event is shown in Fig. 2.

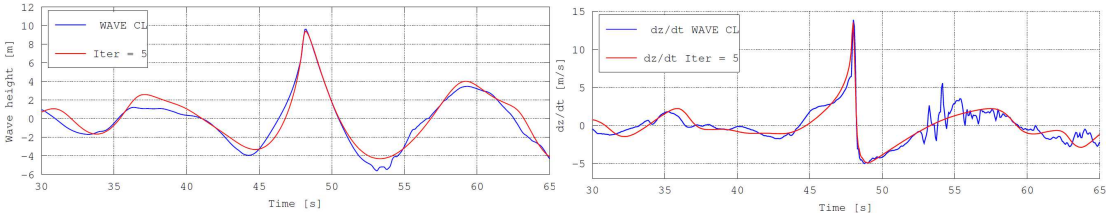

Fig. 2: Comparison between measured WAVE CL (i.e. target wave) and reconstructed numerical wave (Iter = 5), based on the wave elevation (left) and its time derivative (right).

4 Numerical set-up

To reduce computational time, the considered 3D computational domain was taken significantly smaller than the full scale basin. The inlet, where we impose the wave kinematics, is positioned at x=-167m. At the outlet, the wave should leave the domain without reflecting back. In ReFRESCO this is achieved by applying a Sommerfeld boundary condition. In ComFLOW a dispersive absorbing boundary condition (GABC) is imposed which, in contrast to the Sommerfeld boundary condition, has the capability to absorb a range of wave frequencies (Luppes (2013)). The water depth is set to 90m

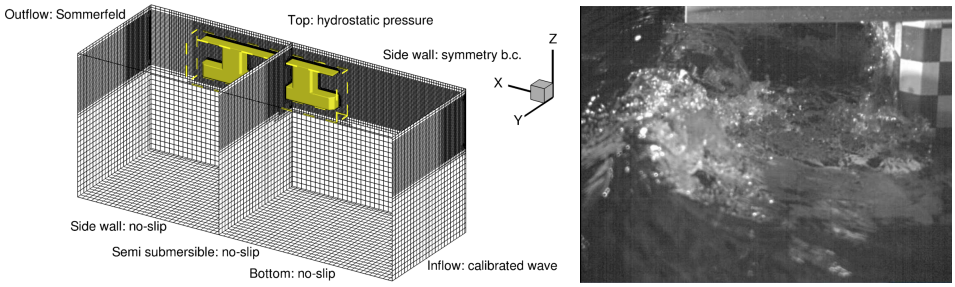

Fig. 3: Left: Illustration of coarse mesh in ReFRESCO. Medium and fine mesh have 1 resp. 2 grid refinement zones around the semi submersible. Right: Snapshot of the selected extreme wave event from the experiment.

(approximately half of the wave length, based on the wave peak period), and the computational domain ends 26m above the free surface. Local grid refinement is employed and no turbulence modelling was used since it is assumed that the physics related to waves impacting the semi submersible are inertia dominated. A no-slip boundary condition is imposed at the semi submersible, at the solid side walls and at the bottom of the domain. As the incoming wave is impacting the semi submersible at zero-angle, at y=0 a symmetry boundary condition is prescribed. Finally, a hydrodynamic pressure is imposed at the top of the domain. The numerical simulations start with a fully developed wave in the domain. In the analysis, the first 6 seconds are omitted as these will contain startup effects (e.g. the build-up of diffraction effects from the semi submersible).

5 Simulation results

To verify the ComFLOW and ReFRESCO results, a grid sensitivity study has been performed. The outcome is then validated against the experimental data. We considered three grids, which are listed in Table 1. The variable time step in ComFLOW is restricted to CFL_{max} = 0.6. To compromise between computational costs and accuracy, the time step in ReFRESCO is taken (approximately) equal to the maximum time step occurring in the ComFLOW simulations. Notice that the amount of cells solved in ComFLOW is considerably smaller than in ReFRESCO, because only the cells containing fluid are considered while ReFRESCO also takes the cells containing air into account.

Table 1 Grid details for 3D simulation, with the grid resolution near the vicinity of the semi submersible is listed.

		#cells (total)	#cells (solved)	*dx* [*m*]	*dy* [*m*]	*dz* [*m*]	*dt* [*s*]
ComFLOW	Fine	3.66M	1.88M	0.25	0.25	0.25	0.001-0.004
	Medium	0.89M	0.47M	0.50	0.50	0.50	0.002-0.008
	Coarse	0.47M	0.27M	1.00	1.00	1.00	0.004-0.032
ReFRESCO	Fine	3.87M	3.87M	0.25	0.25	0.25	0.005
	Medium	1.14M	1.14M	0.50	0.50	0.50	0.010
	Coarse	0.61M	0.61M	0.99	1.04	1.00	0.020

In Fig. 4, the undisturbed wave from the 2D reconstruction and the wave from the 3D simulation including the semi submersible are plotted together against the model test results. Also the corresponding time derivatives are included. For both CFD tools, the results suggest that mainly the trough is affected due to diffraction from the structure, and that the gradient seems to decrease slightly when the incoming wave is disturbed. It is hereby noted that from Fig. 4 on, the numerical results were slightly shifted in time in order to directly compare with the experiments.

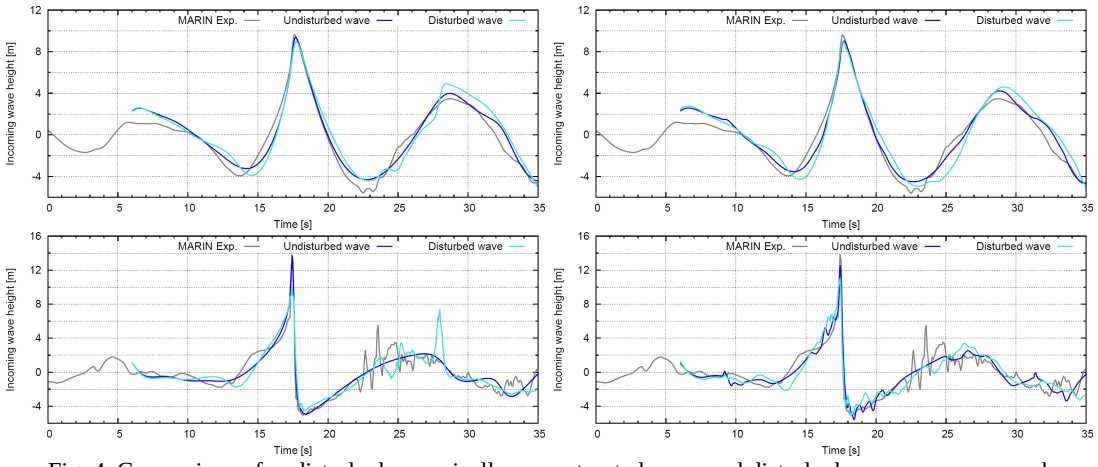

Fig. 4. Comparison of undisturbed numerically reconstructed wave and disturbed wave on coarse mesh, including the corresponding time derivatives. Left: ComFLOW. Right: ReFRESCO.

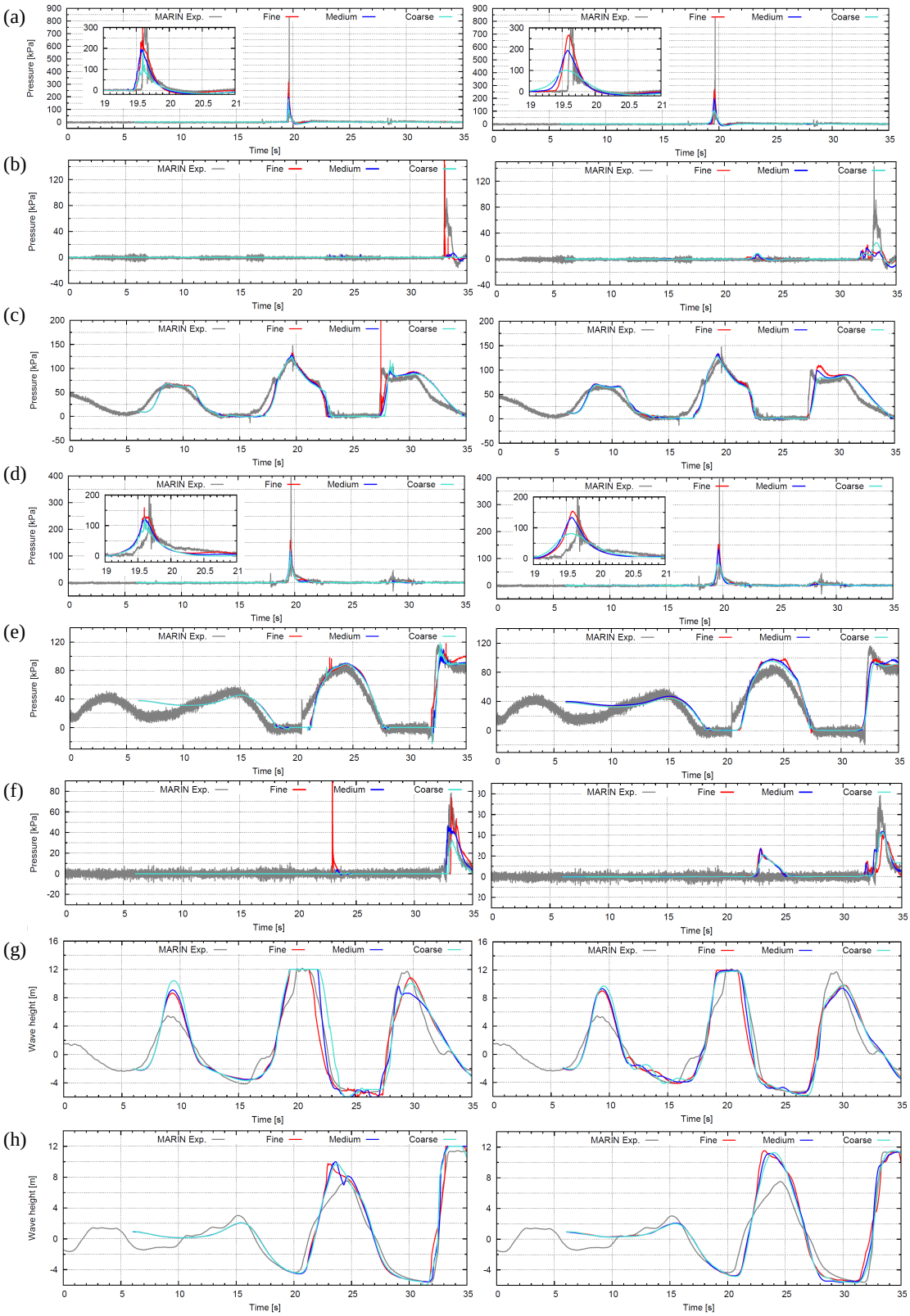

Fig. 5. Simulation results compared to the basin experiments. Left: ComFLOW. Right: ReFRESCO. (a) Deck impact at P5. (b) Deck impact at P10. (c) Horizontal impact at P11. (d) Horizontal impact at P15. (e) Horizontal impact at P20. (f) Horizontal impact at P24. (g) Run-up at REL3. (h) Run-up at REL10.

Results for a selection of the measured probes (see Fig. 1 for their locations) are given in Fig. 5. The top two figures show the vertical pressures underneath the deck at both the front and aft column. At the front column (P5, Fig. 5(a)) the trend of the measured deck impact is predicted well by both CFD tools on the fine mesh. Hereby the pressures obtained with ReFRESCO appear smoother and show more grid dependence than with ComFLOW, possibly due to the implicit free surface reconstruction in ReFRESCO. The maximum measured value of the short duration pressure peak at P5 is not reached by the CFD simulations, indicating the large sensitivity of the pressure peak to small differences between the reconstructed wave and the measured basin wave. At the aft column (P10, Fig. 5(b)), both CFD tools seem to under predict the deck impact, which is again believed to be caused by not exactly representing the propagating breaking wave. The predicted horizontal impact pressures are plotted in Fig. 5(c)-(f). At the front column an accurate correspondence with the experimental data was found. From Fig. 5(c) the rise time of the second impact at the bottom of the column (P11, around T=27.2s) seems to be somewhat large in the CFD. Only the result of the ComFLOW simulation on the fine mesh shows an accurate match in rise time but it also shows a somewhat overestimated pressure and a double-peaked impact. For the horizontal pressure at the top of the front column (P15, Fig. 5(d)) similar observations can be made as for the vertical pressure at the P5 location. The horizontal pressures located at the second column (Fig. 5(e)-(f)) are again accurately predicted by both CFD tools. Both CFD tools however record an additional wave impact at P24 around T=23s, which is not observed in the experiments. Finally, the wave run-up at the first column and second column are predicted quite well, as depicted in Fig. 5(g)-(h). The first wave oscillation in Fig. 5(g) is hereby not considered as it does not include diffraction effects.

In terms of grid dependency, only limited variation was observed when comparing the coarse mesh results to the medium mesh results. The results on the medium mesh seem to be almost fully converged, only a mesh dependency for the very short duration pressure peaks at P5 and P15 is observed, which can be further investigated.

The evolution in time of the breaking wave impacting the semi submersible is visualized in Fig. 6 for both ComFLOW and ReFRESCO. The snapshots show that, on the same grid, somewhat more detail around the free surface is visible in the ComFLOW simulation due to the explicit reconstruction.

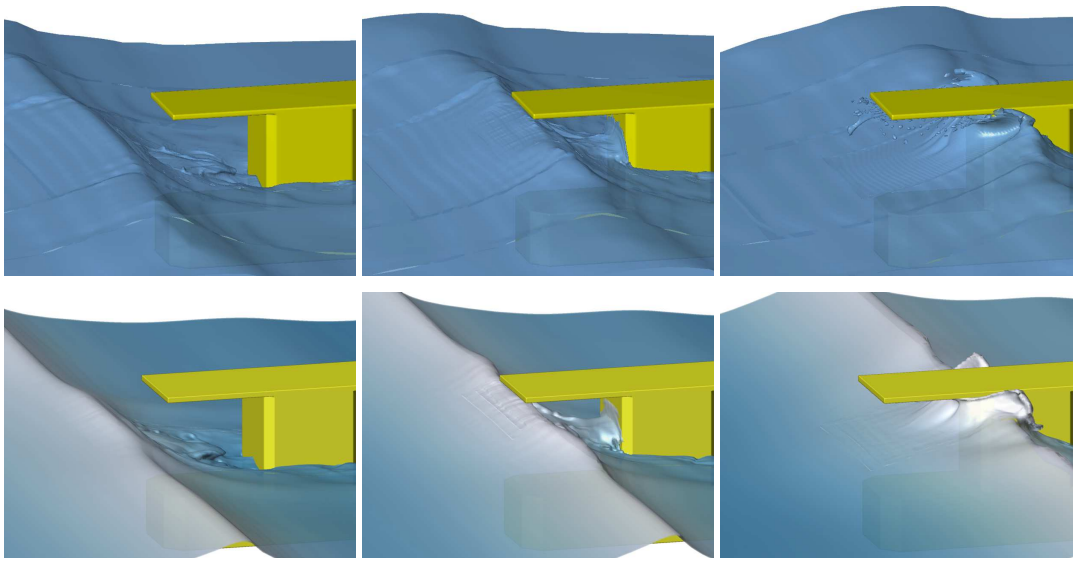

Fig. 6. Evolution of breaking wave impact on fixed semi submersible. Above: ComFLOW. Below: ReFRESCO.

The computational costs for both CFD tools are summarized in Table 2. All the simulations were performed on the MARIN in-house HPC cluster. The last column lists the total amount of CPU time,

and shows the advantage of the structured mesh approach over an unstructured approach for this type (i.e. inertia dominated) of free surface applications.

Table 2 Computational costs for both CFD tools.

		#cells (solved)	#cores	Wall clock [h]	#cores × wall clock [h]
ComFLOW	Fine	1.88M	4	136	545
	Medium	0.47M	4	10	41
	Coarse	0.27M	4	2	9
ReFRESCO	Fine	3.87M	96	68	6566
	Medium	1.14M	48	20	995
	Coarse	0.61M	32	7	227

4 Conclusions and discussions

Based on the results, it seems justified to conclude that the presented CFD methodology is capable of accurately reconstructing an extreme basin wave event, and reproduce measured impact loads and run-up for an extreme breaking wave impacting a fixed structure. As such, the presented results should provide the industry with a greater confidence in applying CFD in the area of extreme wave impacts. It should hereby be stressed that using the present deterministic approach is believed to always lead to differences between the CFD results and experiments, due to the large sensitivity of wave impacts to deviations in the incoming wave characteristics. These differences are to be expected in any deterministic analysis of wave impacts, even when considering repeat tests of the same extreme event in a wave basin. Therefore, future work will involve the incorporation of CFD analysis in a statistical approach towards wave impact predictions. Additionally, on more short term the basin wave reconstruction methodology will be further improved using wave kinematics predictions validated with PIV measurements.

Acknowledgements

This work was performed within the MARIN Academy.

References

Iwanowski, B. et al. (2014) “Wave-in-deck load on a jacket platform, CFD calculations compared with experiments”, OMAE 2014, Paper OMAE2014-23434, San Francisco, CA.

Pakozdi, C. et al. (2015), “Estimation of Wave in Deck Load Using CFD Validated Against Model Test Data”, Proceedings of 25th International Society of Offshore and Polar Engineers (ISOPE). Hawaii, USA.

Veldman, A.E.P. et al. (2015) “Turbulence Modeling for Locally-Refined Free-Surface Flow Simulations in Offshore Applications”, ISOPE-2015. Hawaii, USA.

Bandringa H., Helder J.A., Jaouen F. and Koop A. (2016) Validation of CFD for run-up and wave impact on a semi submersible, International Conference on Violent Flows, Osaka, Japan, March 9-11

Luppes, et al. (2013) “Simulations of Wave Impact and Two-Phase Flow with ComFLOW: Past and Recent” ISOPE-2013. Anchorage, Alaska, USA.

Vaz, G. et al. (2009) “Free-surface viscous flow computations. Validation of URANS code FRESCO”, OMAE 2009, Paper OMAE2009-79398, Honolulu, Hawaii.

Koop, A. et al. (2011) “Viscous-Flow Calculations for Model and Full-Scale Current Loads on Typical Offshore Structures”, MARINE 2011.

Kerkvliet, M. et al. (2014) “Analysis of u-type anti-roll tank using URANS. sensitivity and validation”, OMAE 2014, Paper OMAE2014-23483, San Francisco, CA.

Helder, J.A. and Bunnik, T. (2016) “Deterministic breaking wave simulation for offshore applications”, SNAME 2016, Houston, TX.

Bunnik, T. et al. (2015) “Deterministic simulation of breaking wave impact and flexible response of a fixed offshore wind turbine”, ASME 2015, Paper OMAE2015-41989, St. John’s, Canada.

Advanced Simulations = Better Results. Really?

Volker Bertram[*], Tobias Zorn[*], and Olav Rognebakke[†]
[*]DNV GL, Hamburg/Germany, [†]DNV GL, Høvik/Norway
volker.bertram@dnvgl.com

1. Introduction

We generally all want the best possible solution. But how do we define "good"? What is our measure of merit? The value of any product (or service) can be classified according to:

- Quality – For us, this means typically accuracy (of the full-scale prediction).
- Time – For us, this is the total time from order to report delivery, not just computational time.
- Cost – For us, this is total cost including labor and material cost. Cost for training and maintenance of software should not be forgotten in comparing alternatives.

In practice, we have constraints for all three objectives. "It should be at least X% accurate". "We need an answer within the next Y months." "We have a budget of Z dollars for the project." Modelling thus often starts with determining constraints on time, budget and required accuracy, before meaningful discussions on the best modelling approach can start. The main options for modelling of hydrodynamics problems are model tests, design experience, potential flow simulations and CFD. See Bertram et al. (2015) for a more extensive discussion of these options. Here we focus on:

- Potential-flow computations – The main commercial codes (e.g. WAMIT) are widely used and validated. Inherently, potential-flow codes do not model viscosity and associated effects like viscous damping. They also are not able to model breaking waves. On the other hand, they are fast and are relatively easy to handle.
- CFD, typically RANSE – Codes model viscosity directly in the field equation. The main commercial codes and the open-source alternative OpenFOAM are verified in terms of numerical implementation, and their application is in principle validated for many marine applications. Accuracy depends on many user options and computational power.

Often, hybrid modelling combining various model techniques leads to cost-effective and accurate results. E.g., steady CFD simulations may determine force coefficients on large, hydrodynamically transparent structures (e.g. jack-up legs) and then be used in potential-flow codes for seakeeping analyses. The response time is several orders of magnitude shorter, but the accuracy only slightly worse than using only CFD.

2. Selected Applications

2.1. Numerical Wave Basin

For 3d wave problems, choosing the best modelling approach is not at all straight-forward. Several factors play a role and may influence the final choice:

- 2d or 3d – The real world is 3d, but long-crested waves and very elongated structures may allow 2d modelling in simulations. Wave generation, propagation and attenuation are then much easier.
- Regular or irregular waves – Linear potential-flow codes have no problem in specifying arbitrary spectra of superimposed regular waves. Time-domain potential-flow codes and particularly CFD methods struggle with irregular seas. In principle, it can be done, Fig.1. But attenuation of waves of varying direction and wave lengths poses problems with unwanted

numerical diffusion and required computational power to avoid unwanted reflections at domain boundaries.

- Speed or no speed – Everybody loves zero speed (problems). For significant forward speed, the physics and numerics become more difficult. E.g., 3d potential-flow codes do not model large transom sterns in waves adequately. This favors CFD, unless engineering insight or experience allows semi-empirical corrections for viscous effects. Hydrodynamically transparent or not – For wide displacement bodies, wave forces dominate which is good for potential-flow codes. For slender structures with typical diameters much smaller than the waves, flow separation and vortex shedding dominate the physics. Then full-scale CFD is the obvious choice. (For simple structures, also empirical formulae may work). Structures with blunt bodies and hydrodynamically transparent appendages call for hybrid modelling. For example, the blunt part may be directly modelled in a potential-flow code and the hydrodynamically transparent part can be modelled by external forces which in turn may be based on experience or dedicated CFD. In principle, CFD can model both waves and flow separation, but in practice grid resolution for largely varying scales makes hybrid modelling often both faster and more accurate. We applied such hybrid modelling e.g. for offshore wind power installation vessels using a RANSE code to determine force coefficients (per length) for the jack-up legs and standard radiation-diffraction solver for the subsequent seakeeping analyses, Fig.2.

In conclusion, CFD is a welcome additional to traditional modelling choices, but not always the best choice. For the foreseeable future, we will have “numerical wave basins” based on potential-flow models possibly enhanced by CFD-based corrections for viscous effects.

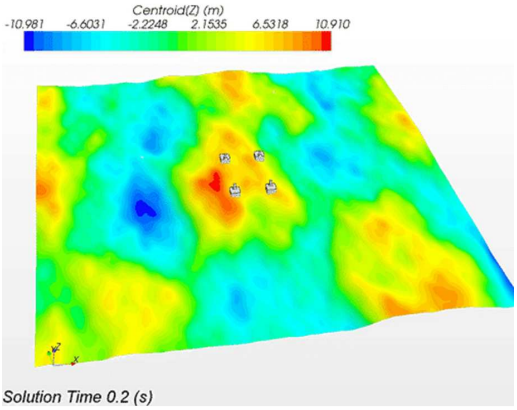

Fig. 1: Offshore platform in natural seaway in RANSE simulation, Kim et al. (2013)

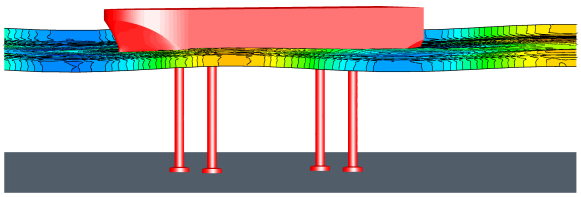
Fig. 2: Offshore installation vessel; hull modelled directly in AQWA, jack-up legs modelled as external forces based on CFD pre-processing

2.2. Second-Order Forces in Waves

Added resistance in seaways for ships with forward speed is difficult to determine, particularly for short waves. Both model tests and numerical simulations show large scatter of predicted added resistance for given wave height. This is discussed in more detail in Söding et al. (2012):

- The added resistance (= average force over time) is small compared to the amplitude of the oscillations of the longitudinal force and the resistance in steady flow. This makes singling out the added resistance numerically sensitive.
- Linear frequency-domain potential methods have difficulties with submerged transom sterns. For short waves, there are also grid resolution problems. Forward-speed problems require proper modelling of the interaction between steady and unsteady flow. Progress in code efficiency and parallel computing power improved our abilities to calculate added resistance in short waves. By 2014, we were able to compute wave lengths as short as $\lambda/L = 0.1$,

Shigunov and Bertram (2014), covering the whole range of practically relevant wave lengths. However, the development is too recent to expect the range of validation we would like to see, including blind tests with high-quality experimental data.

- In RANSE-based seakeeping simulations, the calm-water resistance needs to be computed separately (preferably on the same grid) and subtracted from the average total resistance to obtain the value of the added resistance. Resolution and unphysical numerical damping are challenges. A strategy needs to be set for how to control the vessel; soft springs or an autopilot are required to maintain speed and average position and course, unless first-order horizontal motions are prevented.

In conclusion, potential-flow codes offer finer resolution for affordable time and cost and remain the preferred choice over RANSE simulations for this application.

2.3. Formal Optimization of Offshore Structures

Formal optimization has become state of the art in ship hull design, employing RANSE or at least hybrid models. In principle, formal optimization could also be applied to offshore platforms, e.g. Bertram et al. (2015), Fig.3. In the case shown, the target was a reduction of relative motions in waves. The optimization achieved 4% improvement. In this case, the physics are captured well by potential flow codes. Resources are better invested in exploring more parameter variations than into solving better flow equations. Using a free-surface RANSE code does not lead to significantly better results, just much higher costs.

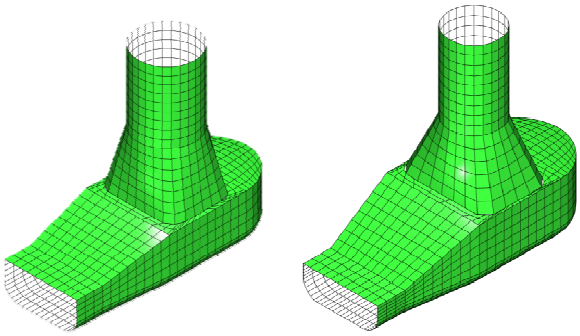

Fig. 3: Optimization of semi-submersible for relative motion / air gap; original (left) and optimized (right)

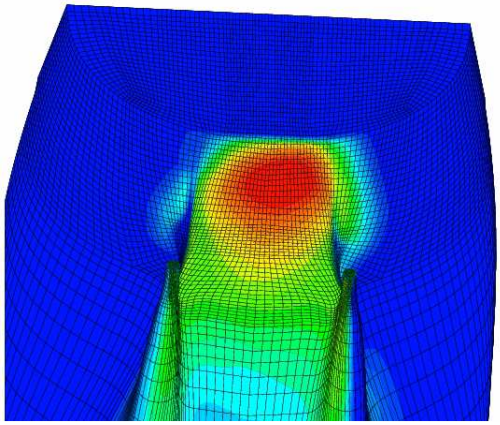

Fig. 4: CFD simulation of stern slamming in twin-screw LNG tanker

2.4. Slamming

Most slamming applications and “validation” studies are shown for a computationally friendly, but unrealistic test case: a 2d wedge with small deadrise, but large enough deadrise to avoid air trapping. But ship slamming is a strongly three-dimensional phenomenon involving highly nonlinear complexities. The complexity of the physics involved has been used as an argument for CFD as the best modelling approach. This is debatable. Slamming involves rapidly changing flows, possibly local super-sonic flows where compressibility plays a role, fine spray formation and other effects that require very fine resolution in time and space if you want to capture them directly in a free-surface RANSE scheme. Adaptive grids and time steps may bring progress in years to come, but at present practical limitations in computational resources and associated grid-dependent errors may explain why there is no clear supremacy for CFD approaches. In choosing the modelling approach, we need to consider the larger picture of why we perform slamming simulations. The highly nonlinear physics of impact load problems mean that large scatter depending on initial conditions is unavoidable. Thus, responses of ships in entering waves (rather than perfectly smooth water as assumed in most simula-

tions and experiments), asymmetries to ship motions and phase shifts in encountering waves will lead to wide spectra of possible responses and maximum loads encountered. For fatigue analyses, such scatter changes expected fatigue life. We may then prefer a multitude of cases with moderate accuracy over more accurate determination which we can afford only for a few selected cases.

3. Conclusions

In conclusion, the most accurate model is not automatically the best model. Modelling is a trade-off between what you have (time, money) and what you want (purpose). Sometimes there is no clear-cut solution; often it is a question of priorities.

References

Bertram, V., Zorn, J.T., Rognebakke, O. (2015). Advanced simulations = Better results. Really?. OMAE, St.John's.

Kim, J., Tan, J.H.C., Magee, A., Wu, G., Paulson, S., Davies, B. (2013). Analysis of ringing response of a gravity based structure in extreme sea states. OMAE, Nantes.

Shigunov, V., Bertram, V. (2014). Prediction of added power in seaway by numerical simulation. 9th Int. Conf. on High-Performance Marine Vessels (HIPER), Athens, pp.102-113.

Söding, H., Shigunov, V., Schellin, T., El Moctar, O. (2012). A Rankine panel method for added resistance of ships in waves. OMAE, Rio de Janeiro.

Experimental and Computational Analysis of the Ship Propeller in Open Water Conditions for Inclined Flow

Judyta Felicjancik[*†], Przemysław Król[*†] and Tomasz Bugalski[*]
[*]Ship Design and Research Centre (CTO), Gdansk, Poland,
[†]Conjoint Doctoral School at the Faculty of Mechanical Engineering,
Gdansk University of Technology, Poland

1 Introduction

The paper presents the results of computational analyses simulating the open water tests of ship propeller in inclined flow. The results of computations are compared with the results of corresponding experimental analyses carried out in the towing tank of Ship Design and Research Centre CTO S.A. The object of the research was the model propeller identified as CP469. The aim of the study was to validate the results of numerical simulations performed at model scale. The computational analyses were carried out at model scale with the use of two computational models: Reynolds-Averaged Navier-Stokes model implemented in Star CCM+ software and lifting surface model, implemented in the in-house code. The numerical simulations and experimental studies were carried out for exactly the same load conditions of the propeller. The work is part of a series of activities aimed at the development of advanced numerical methods supporting the design process of ship propellers with taking into account their actual operating conditions.

2 Content

The benchmark propeller from „NAWIGATOR XXI“ vessel is the object of model test and numerical analysis. Numerical results were compared to the experimental results obtained from the towing tank of Ship Design and Research Centre CTO S.A. The aim of investigations was the validation of undertaken numerical approach. The hydrodynamic characteristics of the propeller were evaluated by means of standard tests conducted in the model towing tank to enable the validation of numerical methods.

In the present experiment, the propeller was tested in inclined flow in pull conditions and at the draft of the shaft corresponding to 1.5 diameter propeller *D*. The analysis was performed for three loading conditions at three inflow angles. The propeller characteristics were evaluated in the following range of advance coefficient *J*: 0.1 – 0.9 for model test and 0.3, 0.5 and 0.7 for numerical analysis. Results of experimental tests and numerical analyses are presented in form of dimensionless coefficients defined as follows:

Thrust coefficient: $$K_T = \frac{T}{\rho n^2 D^4} \quad (1)$$

Torque coefficient: $$K_Q = \frac{Q}{\rho n^2 D^5} \quad (2)$$

Advance coefficient: $$J = \frac{V_A}{nD} \quad (3)$$

Efficiency of the propeller: $$\eta_0 = \frac{J}{2\pi}\frac{K_T}{K_Q} \quad (4)$$

where: T - thrust [N]; Q - torque [Nm]; V_A - flow velocity [m s-1]

The object of analysis is a four-bladed, left-handed propeller identified as CP469 with a design pitch ratio $P_{0.7}/D$ = 0.942. It is a controllable pitch propeller (CPP). The geometry of the propeller is shown in Fig. 1. The scale factor of the propeller is 1:10. The water parameters (density, viscosity)

Editor's note: the typesetting of this paper was adjusted by the editor to make it fit in the 6 page limit.

correspond exactly to the parameters in the towing tank tests. Basic geometric data of the propeller are summarized in Table 1.

Table 1: Geometrical details of investigated propeller

	Symbol	*Unite*	*Full scale*	*Model scale*
Propeller name	—	—		CP469
Type of propeller	—	—	CPP	
Diameter	D	m	2.26	0.226
Pitch ratio at r/R=0.7	$P_{0.7}/D$	—	0.942	
Expanded area ratio	A_E/A_0	—	0.673	
Hub ratio	d_h/D	—	0.302	
Number of blades	Z	—	4	
Hand	—	—	left-handed	
Scale factor	λ	—	1	10

Fig. 1: Four-bladed propeller CP469 - experimental model

3 Numerical analyses

3.1. RANS - CFD computations

The CFD simulations were carried out with the use of commercial StarCCM+ solver. The reason for using RANS approach is to keep effective time of calculations. The code solves continuity equations in integral form on a polyhedral mesh by means of the finite volume technique. The k-ω turbulence model was used, which has an advantage over the k-ε model due to its improved performance for boundary layers under adverse pressure gradients. The Steady Reference Frame model was used to model the movement of the propeller by rotating whole computational mesh around propeller axis.

Numerical simulations were carried out according to recommendations given by the software producer. The features of the simulation were as follows:

- solver: Star CCM+ package;
- equations discretized with the use of finite volume method (FVM);
- turbulence model: two-equation SST k-omega;
- mesh size was optimized taking into account different aspects (y+ distribution, mesh size adjusted for the proper edges modelling);
- uniform inflow conditions.

As a result of discretization, over 4.5 million finite volumes were applied. Domain was discretized by polyhedral nonstructural grid with the use of prism layer in near-wall region. Discretized model is depicted in Fig. 2.

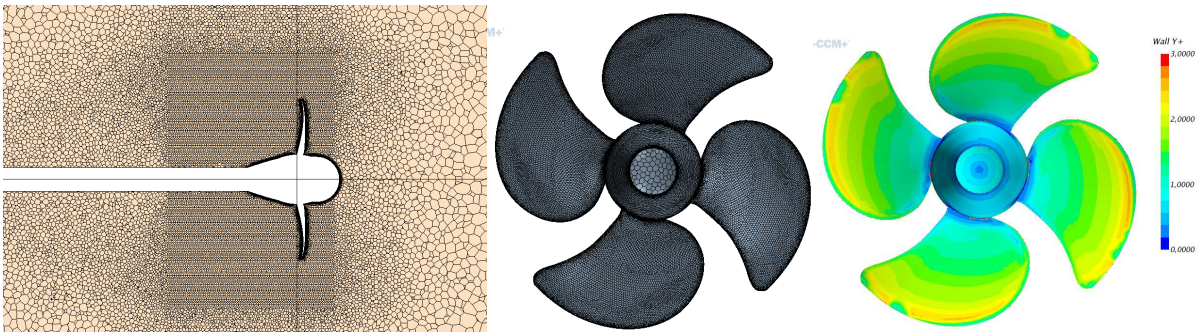

Fig. 2: a) mesh distribution around propeller, b) mesh distribution on the propeller, c) y+ distribution on the propeller

3.2. Lifting Surface (LS) computations

Lifting Surface (LS) is one of most classical models of propeller performance. It replaces propellers blade with system of hydrodynamic singularities. The system consists of:

— bound vortices, located on nominal helical surface, corresponding to the blade
— trailing vortices, supplying bound vortices to satisfy continuity of circulation theorem
— sources modelling effects of finite blades thickness

Kinematic boundary condition is satisfied on the nominal helical surface and then pressure difference between the pressure side and the suction side is calculated. Surface integration of pressure difference over the blade leads to values of thrust and torque.

The most neuralgic part of lifting surface propeller calculations is the geometry of free trailing vortices. During the calculations their geometry was established in an iterative way. Initial assumption for their geometry was regular helical surface with pitch value of:

$$H = \pi D \frac{r}{R} \tan\left(0.8\varphi + 0.2\beta\right)$$

Local flow velocities were calculated for chosen free vortex segments and than interpolated for remaining ones. Free vortex segments were not convected, but rather re-oriented, to align the local flow. Unfortunately the iteration loop came out to be instable for non-zero inclination angles, where initially assumed free vortex geometry was used.

Mentioned model is quite simple, when compared with RANSE viscous flow computations, but it gives reasonable results in short time. Thus, due to its efficiency and reasonable accuracy, lifting surface method is suitable for design purposes where multiple repeated analyses are required in relatively short time.

4 Open water test results

4.1 Load conditions

Three load conditions were considered, characterized by different advance coefficient and flow angle. For each advance coefficient three angles θ were considered: 0˚, 9˚ and 15˚. Table 2 contains the details of investigated conditions. The same conditions as in an experiment were applied in numerical analyses.

Table 2: Main data for experiment and numerical analysis

Parameter	*Unit*	*Value*
Water density ρ	$kg\ m^{-3}$	998.60
Kinematic viscosity υ	$m^2\ s^{-1}$	1.071E-6
Dynamic viscosity μ	*Pa·s*	1.070E-3
Revolution rate *n*	s^{-1}	16.00

4.2 Results

The results of experimental results (*EFD*) and numerical analyses are shown in Tables (Tab.3-5) and on the graphs (Fig. 3-5). Results from computation of Computational Fluid Dynamics are signed as *CFD* and results from Lifting Surface computations are signed as *LS*. The differences between results are also shown.

For open water test at 0˚ (Tab. 3 and Fig. 3) underestimation can be observed for both numerical approach. The difference between values of efficiency η_0 of the propeller from numerical analyses and experimental results is larger for higher advanced coefficients. The differences between thrust K_T and torque $10K_Q$ coefficient for both numerical approach and experimental results are much lower. Generally, results obtained from both numerical approach are close to experimental results.

Table 3: Results of open water test for different advance coefficient at inflow angle θ=0˚

			Results [-]			**Difference [%]**	
		Parameter	*EFD*	*CFD*	*LS*	*(CFD-EFD)/ EFD*100*	*(LS-EFD)/ EFD*100*
	J=0.3	K_T	0.3275	0.3157	0.3048	-3.63	-6.94
		$10K_Q$	0.4489	0.4550	0.4331	-1.36	-3.52
		η_0	0.3484	0.3312	0.3360	-4.92	-3.54
	J = 0.5	K_T	0.2209	0.2086	0.2236	-5.57	1.24
		$10K_Q$	0.3328	0.3366	0.3494	1.16	4.99
		η_0	0.5281	0.4930	0.5093	-6.65	-3.57
	J = 0.7	K_T	0.1122	0.1040	0.1177	-7.33	4.92
		$10K_Q$	0.2121	0.2206	0.2360	4.00	11.26
		η_0	0.5892	0.5250	0.5556	-10.90	-5.70

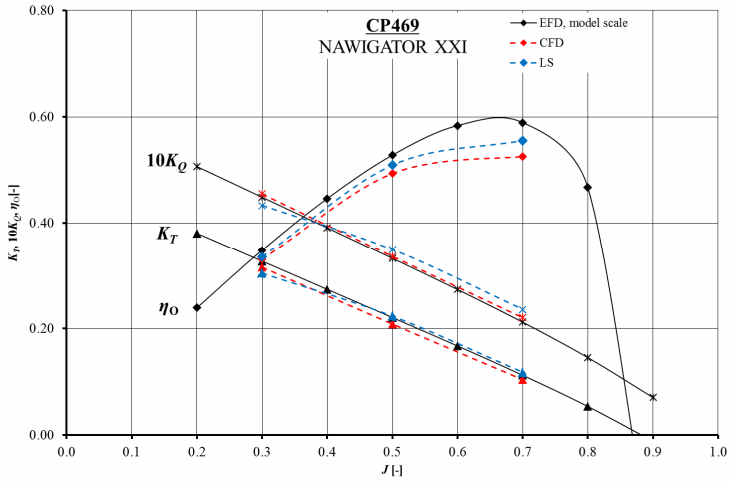

Fig. 3: Comparison of experimental results and numerical analyses for open water test

For inclined flow at 9˚ (Tab. 4 and Fig. 4) underestimation can be observed for Lifting Surface (*LS*) approach for all coefficients. The differences between thrust K_T and torque $10K_Q$ coefficients for this approach and experimental results are highest for lowest load. In CFD analyses can be observed lower differences between CFD results and experimental results. Results for both numerical approach are most similar to experimental results at highest load.

Table 4: Results of OWT for different advanced coefficient at inflow angle θ=9˚

			Results [-]			Difference [%]	
		Parameter	*EFD*	*CFD*	*LS*	*(CFD-EFD)/ EFD*100*	*(LS-EFD)/ EFD*100*
	J = 0.3	K_T	0.3318	0.3277	0.2624	-1.24	-20.92
		$10K_Q$	0.4525	0.4687	0.3739	3.60	-17.37
		η_0	0.3502	0.3294	0.3351	-5.91	-4.30
	J = 0.5	K_T	0.2275	0.2333	0.1928	2.58	-15.24
		$10K_Q$	0.3394	0.3646	0.2972	7.42	-12.43
		η_0	0.5333	0.5026	0.5162	-5.76	-3.21
	J = 0.7	K_T	0.1203	0.1406	0.1331	16.95	10.67
		$10K_Q$	0.2214	0.2624	0.2298	18.51	3.78
		η_0	0.6051	0.5894	0.6453	-2.60	6.64

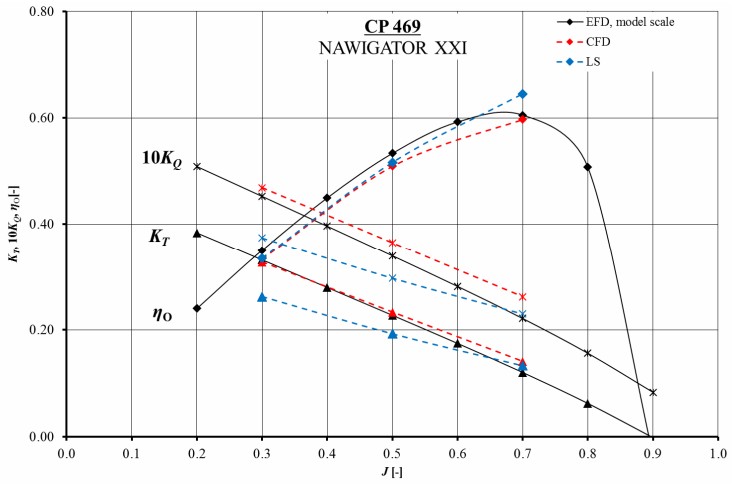

Fig. 4: Comparison of experimental results and numerical analyses for inclined flow at 9˚

For inclined flow at 15˚ (Tab. 5 and Fig. 5) underestimation for all coefficients of Lifting Surface approach can be observed. The most underestimation exist for thrust K_T and torque $10K_Q$ coefficients at highest load. In CFD analyses significant overestimation of thrust K_T and torque $10K_Q$ coefficients can be observed. Generally, in this case, results from Lifting Surface approach are closer to experimental results.

5 Conclusion

Calculations results shows good agreement with experiment for zero inclination angle. With rising inclination angle calculated propeller loading tends to deviate strongly from experimental one. What is surprising calculated propeller efficiency curve seems to be very resistant to loading calculations errors. Upon that we conclude that the main problem is proper modelling flow separation phenomena and free vortices geometry - in lifting surface calculations. Further investigations of modelling viscous effects could be useful to establish that.

Table 5: Results of OWT for different advanced coefficient at inflow angle θ=15˚

			Results [-]			Difference [%]	
		Parameter	*EFD*	*CFD*	*LS*	*(CFD-EFD)/ EFD*100*	*(LS-EFD)/ EFD*100*
	J = 0.3	K_T	0.3367	0.3662	0.2622	8.77	-22.12
		$10K_Q$	0.4584	0.5149	0.3846	12.33	-16.09
		η_0	0.3507	0.3351	0.3255	-4.43	-7.18
	J = 0.5	K_T	0.2354	0.2949	0.1970	25.28	-16.32
		$10K_Q$	0.3483	0.4379	0.3123	25.72	-10.34
		η_0	0.5379	0.5290	0.5020	-1.65	-6.67
	J = 0.7	K_T	0.1322	0.2225	0.1406	68.38	6.39
		$10K_Q$	0.2345	0.3596	0.2617	53.37	11.61
		η_0	0.6279	0.6804	0.5985	8.36	-4.68

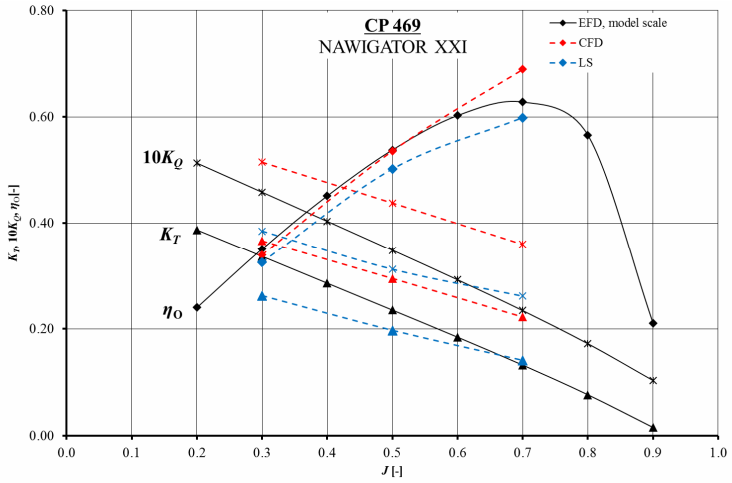

Fig. 5: Comparison of experimental results and numerical analyses for inclined flow at 15˚

Acknowledgements

This research was carried out within the framework of European Project INRETRO.

Literature

J. Carlton (2007). *Marine Propellers and Propulsion*, Elsevier.

J. Felicjancik (2015). Propeller investigations by means of numerical simulation. Proceedings of the 4th International Conference on Advanced Model Measurement Technology for the Maritime Industry AMT 2015, Istanbul, Turkey.

J.H. Ferziger and M. Perić (2002). *Computational Methods for Fluid Dynamics*. 3rd edition, Springer.

H. Jarzyna, T. Koronowicz and J. Szantyr (1996). *Design of Marine Propellers*. Wrocław, Poland.

S. Kowalczyk and J. Felicjancik (2016). Numerical and experimental propeller noise investigations. *Ocean Engineering*, **120**, 108–115.

K. Koyama (1993). Comparative calculations of propellers by surface panel method. Workshop organized by 20th ITTC Propulsor Comitee.

H. Schlichting (2011). *Boundary layer theory*.

Ship Design and Research Center S.A. (2016). Report no RH-2016/B-19489-19495. Gdańsk, Poland.

Ship Design and Research Center S.A. (2016). Report no RH-2016/B-19504-19505. Gdańsk, Poland

J. Szantyr (1984). *Metoda deformowalnej powierzchni nośnej do wyznaczania niestacjonarnej kawitacji na skrzydle śruby i jej hydrodynamicznych skutków*. Gdańsk, Poland (in polish).

H.K. Versteeg and W. Malalasekera (2007). *An Introduction to Computational Fluid Dynamics The Finite Volume Method*. 2nd edition, Harlow, England.

Star CCM+ UserGuide.

Wave Diffraction CFD Nonlinear Time–Spectral Simulations in foam–extend

Inno Gatin, Gregor Cvijetić, Vuko Vukčević and Hrvoje Jasak
University of Zagreb, Zagreb/Croatia, {inno.gatin, gregor.cvijetic, vuko.vukcevic, hrvoje.jasak}@fsb.hr

1 Introduction

Harmonic Balance (HB) method is applied to the problems of surface gravity waves in the `Naval Hydro` pack in foam–extend, which enables time–spectral simulations of wave diffraction. HB transforms a transient problem into a set of coupled steady state equations by assuming a temporally periodic flow. The method is extensively used in the field of turbomachinery [Cvijetić et al., 2016], however no application in field of naval hydrodynamics has been published to our knowledge.

In CFD wave related problems are often simulated in time domain, which requires significant number of periods to be simulated in order to reach periodic steady state. HB assumes the flow variables to be temporally periodic, expanding them into finite Fourier series, resulting in $2N + 1$ coupled steady–state equations, where N is the arbitrary number of resolved harmonics in the Fourier series. Depending on the flow characteristics, the number of harmonics, i.e. spectral resolution, can be adjusted to capture relevant higher order phenomena. For a large number of problems in naval hydrodynamics, solving $2N + 1$ steady–state problems is less computationally demanding than running a full transient simulation. The present HB two–phase method is especially adequate for regular wave problems without violent free surface effects with non–zero mean velocity.

The two–phase HB method is implemented by combining the existing single–phase model for turbomachinery application [Cvijetić et al., 2016] and the existing two–phase flow framework comprising SWENSE (Spectral Wave Explicit Navier–Stokes) solution decomposition [Vukčević et al., 2016a], Ghost Fluid Method (GFM) [Huang et al., 2007] accounting for the pressure and density jump conditions at the interface, and implicitly redistanced Level Set (LS) interface capturing method [Sun and Beckermann, 2007].

In this paper the mathematical model of the time–spectral two–phase HB method is briefly described, followed by the governing equations in the HB form. A detailed mathematical model of the HB method can be found in [Cvijetić et al., 2016]. Next an outline of the numerical framework is given, and finally a working example is shown for regular wave diffraction of a DTMB hull model.

2 Harmonic Balance method

In HB the solution of flow variables is assumed to be periodic in time and expanded in finite Fourier series:

$$\phi(t) = \Phi_0 + \sum_{i=1}^{N} \Phi_{S_i} \sin(i\omega t) + \Phi_{C_i} \cos(i\omega t), \tag{1}$$

where ϕ stands for a general flow variable in time–domain, while Φ denotes its spectral counterpart. ω is the base frequency of the harmonic oscillation, while indices S_i and C_i denote the sine and cosine Fourier coefficients, respectively. A general transport equation for ϕ can be written in abbreviated form as:

$$\frac{\partial \phi}{\partial t} + \mathcal{R} = 0, \tag{2}$$

where $\mathcal{R}$ represents convection, diffusion and source/sink terms, which are also periodic in time, and hence expanded into Fourier series as well. HB is based on equating the corresponding harmonics after inserting the Fourier series of ϕ and $\mathcal{R}$ in Eq. (2), which results in a system of equations that has the following form in the matrix notation:

$$\omega \underline{\underline{A}}\, \underline{\Phi} + \underline{R} = \underline{0}, \tag{3}$$

where $\underline{\underline{A}}$ is the coefficient square matrix with dimensions $2N + 1$, while $\underline{\Phi}$ and $\underline{R}$ represent vectors of Fourier coefficients of ϕ and $\mathcal{R}$, respectively. In the matrix form the Fourier expansion Eq. (1) of ϕ can be

written as $\underline{\phi} = \underline{\underline{E}}^{-1}\underline{\Phi}$, where $\underline{\underline{E}}$ represents a discrete Fourier transformation operator. By applying inverse Fourier transform Eq. (3) the time–spectral form of the equations is obtained, which is used in this work:

$$\omega \underline{\underline{E}}^{-1}\, \underline{\underline{A}}\, \underline{\underline{E}}\, \underline{\phi} + \underline{\mathcal{R}} = \underline{0}. \tag{4}$$

Eq. (4) represents a set of $2N + 1$ coupled steady–state equations in discrete tie–domain. The HB method effectively replaces the time derivative term with by the harmonic coupling source term:

$$\underline{S\,(\phi)} = \omega \underline{\underline{E}}^{-1}\, \underline{\underline{A}}\, \underline{\underline{E}}, \tag{5}$$

which written in the expanded form reads:

$$S_{\,j}\,(\phi) = -\frac{2\omega}{2N+1}\left(\sum_{i=1}^{2N} P_{i-j}\phi_{t_i}\right)\ , j = 1 \ldots 2N+1\,, \tag{6}$$

where P denotes inter–equation coupling matrix defined as:

$$P_i = \sum_{k=1}^{N} k \sin(ik\omega\Delta t)\,, \text{ for } i = 1 \ldots 2N\,, \tag{7}$$

with $\Delta t = T/(2N + 1)$, where T presents the base period of oscillation.

3 Numerical model

HB method is applied to the existing two–phase incompressible numerical model in the `Naval Hydro` pack [Vukčević and Jasak, 2015a, Vukčević and Jasak, 2015b, Gatin et al., 2015, Vukčević et al., 2016b].

SWENSE decomposition is used to decompose the flow field into the incident and perturbed component, where the incident is known from an external potential flow model such as analytical wave solution or nonlinear potential flow solution, while the perturbed component represents the difference between the forced incident component and the full CFD solution. The reader is referred to [Vukčević et al., 2016a] for more details.

In order to prevent wave reflection perturbed component is gradually damped to zero towards the far–field boundaries using implicit relaxation zones.

The kinematic free surface boundary condition and normal stress balance at the free surface are modelled using the GFM [Huang et al., 2007], which implicitly imposes the jump conditions in the cells adjacent to the interface via interface–corrected interpolation schemes.

LS method derived from the Phase Field equation [Sun and Beckermann, 2007] with implicit redistancing is used for interface capturing.

In the present work the coupling between equations is performed implicitly in a block linear system. Implicit coupling enables stable simulations with small or zero mean velocities with respect to the magnitude of oscillation variable ϕ, which cannot be achieved by explicit coupling [Hall et al., 2013]. This is specially important for the application in naval hydrodynamics where the ship velocity can be of the same order of magnitude of the orbital wave velocity in the case of low Froude numbers. The above described HB method is applied on the momentum equation and the LS transport equation, while the pressure equation has no temporal derivative, hence no special treatment is needed.

4 DTMB regular wave diffraction

In this section a HB simulation of regular head wave diffraction for a DTMB hull is presented. Results and computational times are compared to a transient simulation. Hull model with scale 49.59 is used, with length $L_{PP} = 3.05$ m, draught $T = 1.7$ m, and velocity of 1.53 m/s for $F_r = 0.28$. Realistic wave parameters are chosen with wave height $H = 0.036$ m, wave length $\lambda = 4.57$ m and period $T = 1.09$ s. Mesh with 521 000 cells is used in both HB and transient simulations with only half of the domain being simulated. In the HB simulations two harmonics are used, while 20 encounter wave periods are used in

the transient simulation with 200 time steps per encounter period, resulting in $dt = 0.005$ s.

Hydrodynamic forces acting on the hull in the longitudinal and vertical direction, denoted with F_x and F_z respectively, are compared for zeroth and first order of harmonic oscillation, which are obtained using a discrete Fourier transform of the HB steady state equation results, while a moving window Fast Fourier Transform (FFT) is performed on the time history from the transient simulations, where successive FFT's are performed for each encounter wave period. Forces convergence in the HB simulations is shown on Fig. 1, where F_x and F_z are shown against the number of iterations of the steady state solver. It takes $\approx$ 3000 iterations for the longitudinal forces to converge and 2000 iterations for the vertical. Periodic convergence from the transient simulation is show on Fig. 2, where zeroth and first order of F_x and F_z are shown against the number of simulated periods, showing that 20 periods of simulation time suffices in order to reach convergence for all items.

Fig. 3 shows the perspective view of the free surface in the transient and HB simulation corresponding to $t = T$. Free surface elevation in the HB simulation agrees well with the transient simulation, although minor differences can be observed. The comparison of zeroth and first order harmonic amplitudes of F_x and F_z is shown in Table 1, where the relative difference between the transient and HB solution is expressed as $\epsilon = S_t - S_{hb}/S_t S_t$, with S_t and S_{hb} denoting the transient and HB solution, respectively. The relative difference ranges from -0.11% and -10.2 %, while for most items the difference is below 10 %.

The required CPU time 20 periods of simulated time in the transient simulation is 18.9 hours, while it took 8.6 hours for 3000 iterations in the HB simulation which represents a significant savings in terms of CPU time. Moreover, larger savings could be achieved with coarser mesh and larger number of resolved harmonics, since the convergence rate of implicitly coupled HB equation system improves with the increase of cell size and number of resolved harmonics.

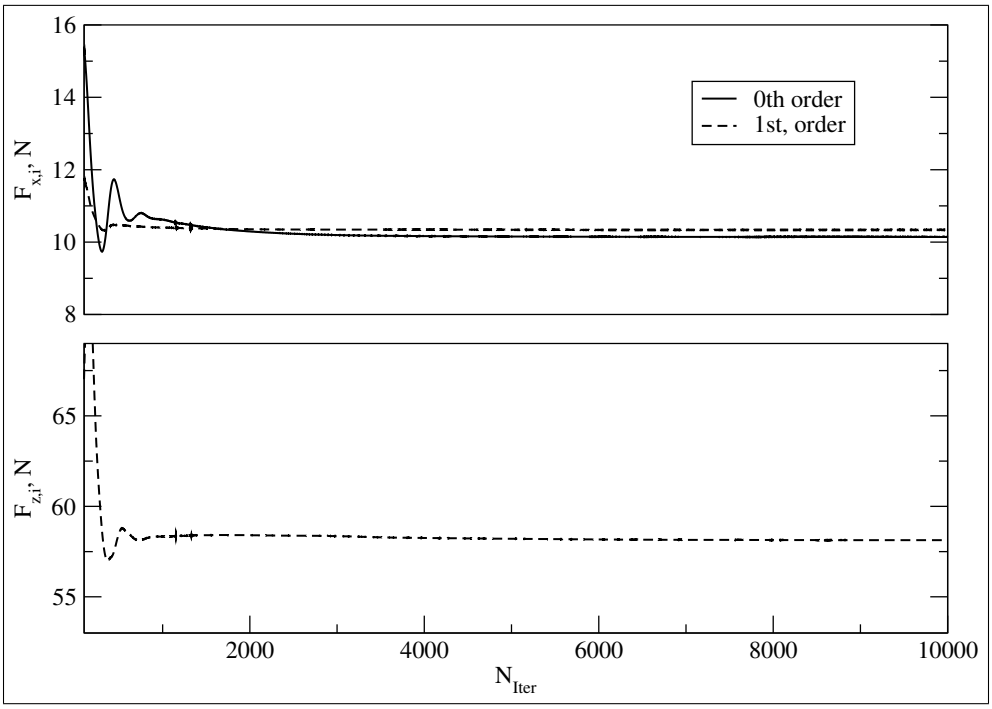

Fig. 1: Convergence of 0th and 1st longitudinal F_x and vertical F_z force harmonic amplitudes in the harmonic balance simulation of DTMB wave diffraction.

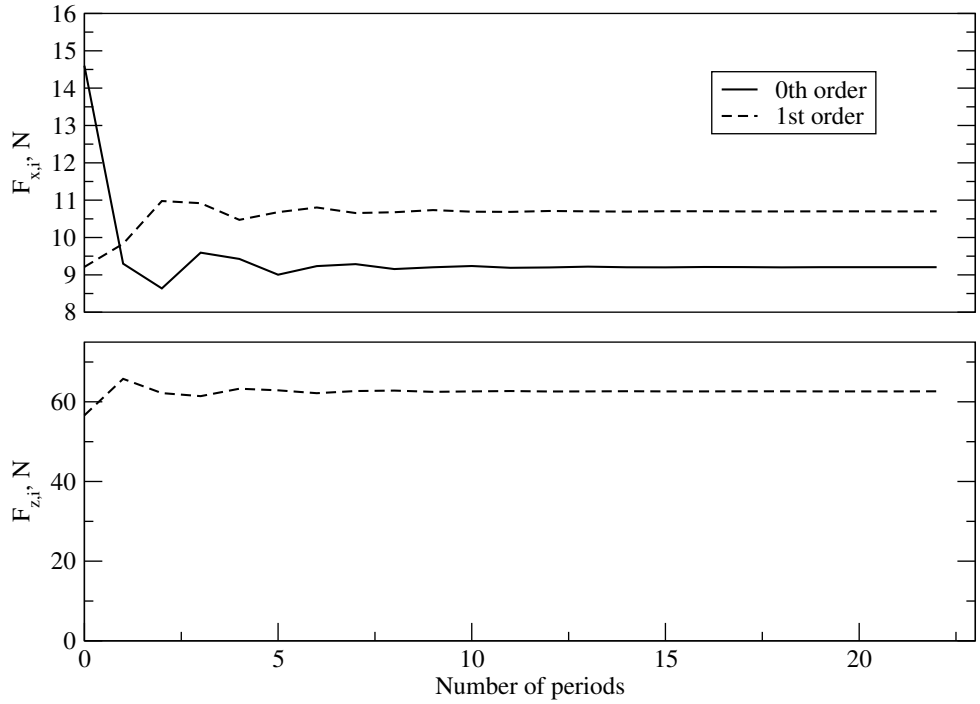

Fig. 2: Convergence of 0th and 1st longitudinal F_x and vertical F_z force harmonic amplitudes in the transient simulation of DTMB wave diffraction.

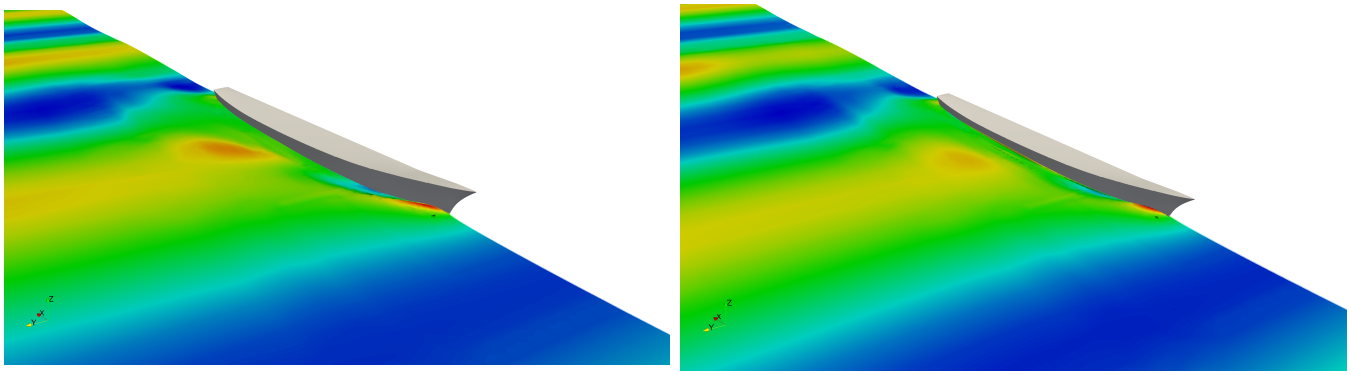

(a) (b)

Fig. 3: Perspective view of the DTMB diffraction simulation at $t = T$: a) transient, b) harmonic balance simulation.

Table 1: Comparison of harmonic amplitudes of horizontal F_x and vertical F_z wave forces on DTMB hull.

Item	Transient	Harmonic balance	ϵ, %
$F_{x,0}$, N	9.20	10.14	-10.2
$F_{x,1}$, N	10.70	10.34	3.36
$F_{z,0}$, N	784.88	785.72	-0.11
$F_{z,1}$, N	62.63	58.14	7.17

5 Conclusion

The two–phase Harmonic Balance method proved to be applicable on naval hydrodynamics problems regarding wave–structure interaction. The advantage of HB is in the steady state formulation of the periodic problem, reducing the required computational effort to reach a periodic steady state solution.

Comparison of HB and transient DTMB head wave diffraction simulations showed that accurate results can be achieved in less than half of the computational time required for the transient simulation. Larger savings could be achieved if coarser mesh and more harmonics are used.

New step is to formulate a spectral rigid body motion model to enable full seakeeping simulations. The stability and rate of convergence of implicitly coupled HB steady state equations increases with coarser mesh, increasing the savings with respect to the transients simulation. This characteristic renders the present method a perfect choice for early design stages.

References

Cvijetić, G., Jasak, H., and Vukčević, V. (2016). Finite volume implementation of the harmonic balance method for periodic non–linear flows. In *54th AIAA Aerospace Sciences Meeting*, page 0070.

Gatin, I., Vukčević, V., and Jasak, H. (2015). Validation and Verification of Steady Resistance KCS Simulations with Dynamic Sinkage and Trim of KCS using Embedded Free Surface Method. In *Tokyo 2015: A workshop on CFD in Ship Hydrodynamics*.

Hall, K. C., Ekici, K., Thomas, J. P., and Dowell, E. H. (2013). Harmonic balance methods applied to computational fluid dynamics problems. *International Journal of Computational Fluid Dynamics*, 27(2):52–67.

Huang, J., Carrica, P. M., and Stern, F. (2007). Coupled ghost fluid/two–phase level set method for curvilinear body–fitted grids. *Int. J. Numer. Meth. Fluids*, 44:867–897.

Sun, Y. and Beckermann, C. (2007). Sharp interface tracking using the phase–field equation. *J. Comput. Phys.*, 220:626–653.

Vukčević, V. and Jasak, H. (2015a). Seakeeping Validation and Verification using Decomposition Model based on Embedded Free Surface Method. In *Tokyo 2015: A workshop on CFD in Ship Hydrodynamics*.

Vukčević, V. and Jasak, H. (2015b). Validation and Verification of Decomposition Model based on Embedded Free Surface Method for Oblique Wave Seakeeping Simulations. In *Tokyo 2015: A workshop on CFD in Ship Hydrodynamics*.

Vukčević, V., Jasak, H., and Malenica, S. (2016a). Decomposition model for naval hydrodynamic applications, Part I: Computational method. *Ocean Engineering*, 121:37–46.

Vukčević, V., Jasak, H., and Malenica, S. (2016b). Decomposition model for naval hydrodynamic applications, Part II: Verification and validation. *Ocean Engineering*, 121:76–88.

A multi-scale Eulerian-Lagrangian model for simulation of cavitating flows

Ebrahim Ghahramani and Rickard E. Bensow
Chalmers University of Technology Gothenburg/Sweden
ebrahim.ghahramani@chalmers.se

1 Introduction

Cavitation is a common phenomenon in industrial hydraulic systems, such as marine propulsion systems and fuel injectors. It is in many cases an undesirable and unavoidable occurrence. Cavitation erosion is believed to be the result of violent collapses of the flowing micro-bubbles within very short time scales, which is often accompanied with issues of noise, vibrations, load variations and loss of efficiency in devices such as propellers and pumps. Created by the sheet cavity breakup, bubbly vapour clouds are transported into regions of higher pressure, where collapse-like condensation results in the formation of liquid jets and pressure shocks. Due to the mentioned significance and complexity of the flow field understanding and controlling cavitation has been a major challenge in engineering in recent decades.

In recent years various experimental and numerical methods have been widely used to analyse this complex phenomenon; high-speed video filming has been considered a relatively suitable tool to study cavitation. However, due to the limitations in measuring detailed instantaneous data, cavitation erosion is yet not fully understood using experimental methods. Computational Fluid Dynamics (CFD) simulation, which in the last decade has gained in popularity due to advances in computational resources and modelling, is an alternative to prototype experiments. Numerical simulations can also supplement experimental measurements to have a more comprehensive understanding of the hydrodynamics of cavitation erosion. For example, in a recent study by Gavaises et al. (2015), direct observation of the flow structures was not possible, however vortex shedding was inferred from relevant simulations in the same conditions.Also, Lu et al. (2013) studied propeller cavitation where CFD supported the experimental observations to explain the differences in performance between designs.

Various numerical methods are being used by different researchers today (selectively Bensow and Bark (2010), Giannadakis et al. (2008), Hsiao et al. (2015), Schnerr et al. (2008) and Yakubov et al. (2015)); most of these methods can be categorized in two general approaches. The first approach is based on the mixture equation of state, assuming the thermodynamic equilibrium. In this approach the vapour volume fraction is directly obtained from the cell-averaged fluid state. However, this approach requires very small timesteps since it considers compressible liquid and vapour phases. Therefore, even if there are suitable models that can adequately estimate the behaviour of cavitation structures, their application in industrial problems (especially the large scale marine industry) is limited, as they require considerably higher computational resources.

The second approach is based on a rate equation for vaporization and condensation. Various numerical models are included in this general classification which may be further categorized in different groups. Both Eulerian and Lagrangian viewpoints can be used to track the vapour structures and their interactions with the liquid phase. One of the widely used Eulerian models is when the flow is treated as a single fluid mixture via the interface capturing Volume of Fluid (VOF) and mass transfer between the phases is defined by explicit source terms. The Eulerian methods perform well in regions with moderate flow changes but in zones of strong, vortical flow they cannot capture cavity transport accurately. One of the main reasons is that, typically, these models utilise the asymptotic form of the well-known Rayleigh-Plesset equation of bubble dynamics (Abdel-Maksud et al., 2010). Another limitations of the Eulerian formulations is that the vapour structures smaller than the grid size, e.g. cavitation nuclei and bubbles, cannot be handled exactly.

The Lagrangian models, on the other hand, enable more detailed formulations for transport, dynamics and acoustics of discrete vapour bubbles. These models, based on a more accurate form of the Rayleigh-Plesset equation, are more accurate for cavitating flows with large values of vorticity and pressure gradients. While the bubble sizes in this viewpoint can be much smaller than the grid size, these models are sometimes quite computationally expensive, and cannot represent large non-spherical vapour structures of the size of computational cells or larger.
Considering the abovementioned capabilities and limitations of the Eulerian and Lagrangian formulations, a solution can be to develop a hybrid multi-scale model that is capable in both resolving the large vapour structures and capture the small-scale bubbles. There are a few studies in the literature that follows this method, primarily Vallier (2013) and Hsiao et al. (2015). In the current study a multi-scale model similar to the work of Vallier (2013) is implemented in OpenFOAM. In this model, the large vapour structures are handled using the Eulerian single fluid mixture method and the small scale spherical bubble are tracked in the Lagrangian framework. Also, a criterion for transition between the Eulerian and Lagrangian vapour structures is defined. The new model is developed in the open source C++ package OpenFOAM by improving the InterPhaseChangeFOAM solver.
In the following sections a more detailed expression of the developed model and a qualitative validation of its performance are presented.

2 Method

As mentioned above, a multi-scale model that uses the strength of both the Lagrangian and Eulerian formulations is developed. In this model, for the continuum liquid phase, the continuity and Navier–Stokes equations are solved and the vapour phase can be treated in either a Eulerian or a Lagrangian framework based on the length scale of the structure. One feature of the VOF method is that it treats structures that are smaller than the grid size as a homogenous mixture, thus sparse vapour clouds or subgrid inhomogeneity in cavitation clouds are not well treated. An extremely high mesh resolution is required to capture the small individual cavitation bubbles. Thus, as a solution, we here combine the Eulerian mixture formulation with a Lagrangian model to account for evolution of individual bubbles aiming for a more realistic estimation of the whole range of cavity sizes. Small bubbles can be identified from the mixture solution at each timestep, and transferred to a Lagrangian framework.

In this section the numerical methods in the Eulerian and Lagrangian formulations and the transition criterion are described.

2.1 Eulerian model

In the Eulerian formulation, the VOF method is used to simulate the vapour transport. This method is suitable for modelling large resolvable vapour structures, such as sheet cavitation. A scalar equation is solved for the transport of the vapour volume fraction quantity,

$$\frac{\partial \alpha_1}{\partial t} + u_i \frac{\partial \alpha_1}{\partial x_i} = \frac{\dot{m}}{\rho}, \qquad (1)$$

where, α_1 is the liquid volume fraction. The right hand side source term represents the rate of vaporisation / condensation of water. Various formulations have been suggested for this source term; in this study the Sauer-Schnerr method is used (Schnerr and Sauer, 2001).

2.2 Lagrangian model

The small-scale cavities are described with a Lagrangian vapour bubble model, i.e. they are tracked individually with the Discrete Bubble Model (DBM). In this approach, the individual bubble dynamics is modelled through the Rayleigh-Plesset equation, in order to consider the collapse and rebound of individual bubbles based on the variations in the surrounding pressure. The Rayleigh-Plesset equation is written as,

$$R(t)\ddot{R}(t) + \frac{3}{2}\dot{R}^2(t) = \frac{p_B(t) - p_l(\infty,t)}{\rho_l} - 4\vartheta_l \frac{\dot{R}(t)}{R(t)} - \frac{2\sigma_{st}}{\rho_l R(t)}, \quad (2)$$

where, R is the instantaneous radius of the bubble , p_l is the surrounding pressure, σ_{st} is the surface tension and p_B is the bubble inside pressure which includes both vapour and dissolved gas pressures. The Lagrangian model has a fourway coupling, i.e., the effects of bubbles on the continuum flow and other bubbles are considered. In this study, the bubbles are decided to interact with each other through collisions. Furthermore, the bubbles may grow (rebound) due to the surrounding pressure variations, and if they become sufficiently large, they are transferred back from the Lagrangian to the Eulerian frame. Also, if a bubble hits a Eularian cavity interface, it will be transferred to the Eulerian.

2.3 Transition Criterion

Transition from the Eulerian to the Lagrangian frame

Cavity structures that are too small to be described using the single fluid mixture approach, are transformed to Lagrangian bubbles. The strategy used to identify this transition is currently similar to the technique used by Vallier (2013). At each time step, the vapour structures are identified with a so-called connected components technique. It consists in associating the adjacent grid cells that have a liquid volume fraction smaller a threshold value (e.g. $\alpha_{th} = 0.9$). The size of the coherent vapour structure is estimated based on the number of cells that they occupy, and small structures are transformed into bubbles. The adjacent cells that fulfil the criterion (i.e., $\alpha_{cell} < \alpha_{th}$) are stored together with the number of the coherent structure (bubbleID) they belong to. A given minimum number of connected cells, denoted by $N_{E\text{-}L}$, is required to represent the smallest vapour structure. Any vapour structure that is described in the Eulerian frame by less than $N_{E\text{-}L}$ cells is a candidate for being transformed to the Lagrangian frame. The position, size and velocity of the new bubbles are extracted from the Eulerian data of the related vapour structure and the liquid volume fraction of the occupied cells is set to 1. The bubbles are small enough to be considered as spherical due to the surface tension and , their diameter is derived from a sphere that has the same volume as the related vapour structure.

Transition from the Lagrangian to the Eulerian frame

A Lagrangian bubble may become very large after coalescence or due to an explosive growth when the surrounding pressure becomes lower than the critical pressure. Bubbles that are too large to be tracked with DBM approach, or large enough to be described through the volume fraction function, should be transformed to the Eulerian framework. The current criterion for this is based on the number of grid cells that the bubble occupies in relation to a threshold value denoted by $N_{L\text{-}E}$. $N_{L\text{-}E}$ should be chosen larger than the $N_{E\text{-}L}$ value so that the bubble is allowed to grow and the model can capture the collapses and rebounds following the growth phase. The bubble may also be transferred to the Eulerian frame if it hit a Eulerian vapour interface. This criterion is measured if the bubble comes close enough to a Eulerian isosurface with $\alpha = 0.5$. When a bubble is transformed to a Eulerian cavity, the cell that hosts the bubble centre and the closest neighbouring cells are filled with vapour. The number of these depends on the bubble volume and also on the available volume in the neighbouring cells that can be converted into vapour.

3 Results

In this section the model performance is validated qualitatively in three simulations.

3.1 Case 1

In this case the collision of two particles in a stationary fluid is simulated. The induced velocity vectors and the particles motions are depicted in Fig. 1. In the left figure, the particles are shown before colliding and in the right figure they are shown afterwards. The induced velocity vectors and

the change in the particles directions after collision are proof of the effect of particles on each other and on the flow field. This case was simulated to test the fourway coupling feature of the solver.

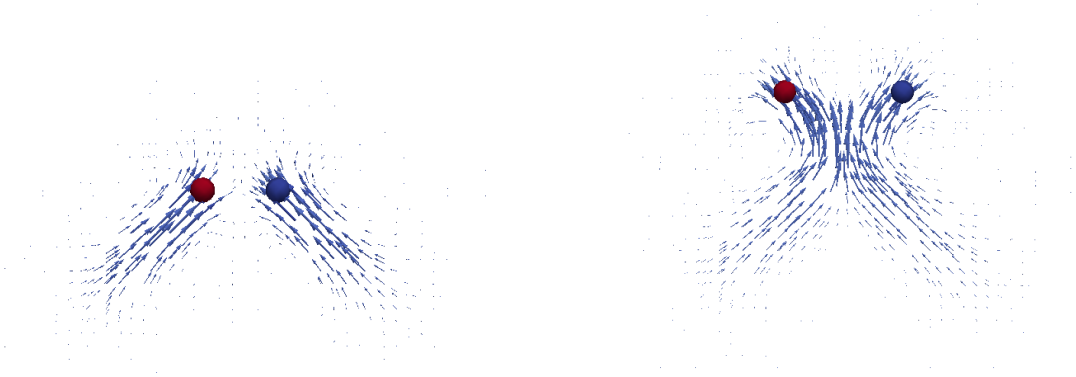

Fig. 1: particle collision in a stationary fluid

3.2 Case 2

In this case a collapsing vapour structure in a 2D channel flow is simulated. The vapour structure is defined by initializing the vapour volume fraction value in the domain and it is subjected to pressure variations along the channel. Some different steps of this simulation are shown in Fig. 2. When the cavity in the first figure becomes small enough, it is transformed into a Lagrangian bubble in the second figure. Due to the dissolved gas content in the bubble and its pressure (which is inversely related to bubble radius) it grows (rebounds) in the third figure. Finally, by further increase in the bubble radius which leads to the reduction of the gas content effect, the bubble collapses again in the last figure. This case was simulated to test the solver capability in capturing the Eulerian-Lagrangian transformation and bubble collapse and rebound.

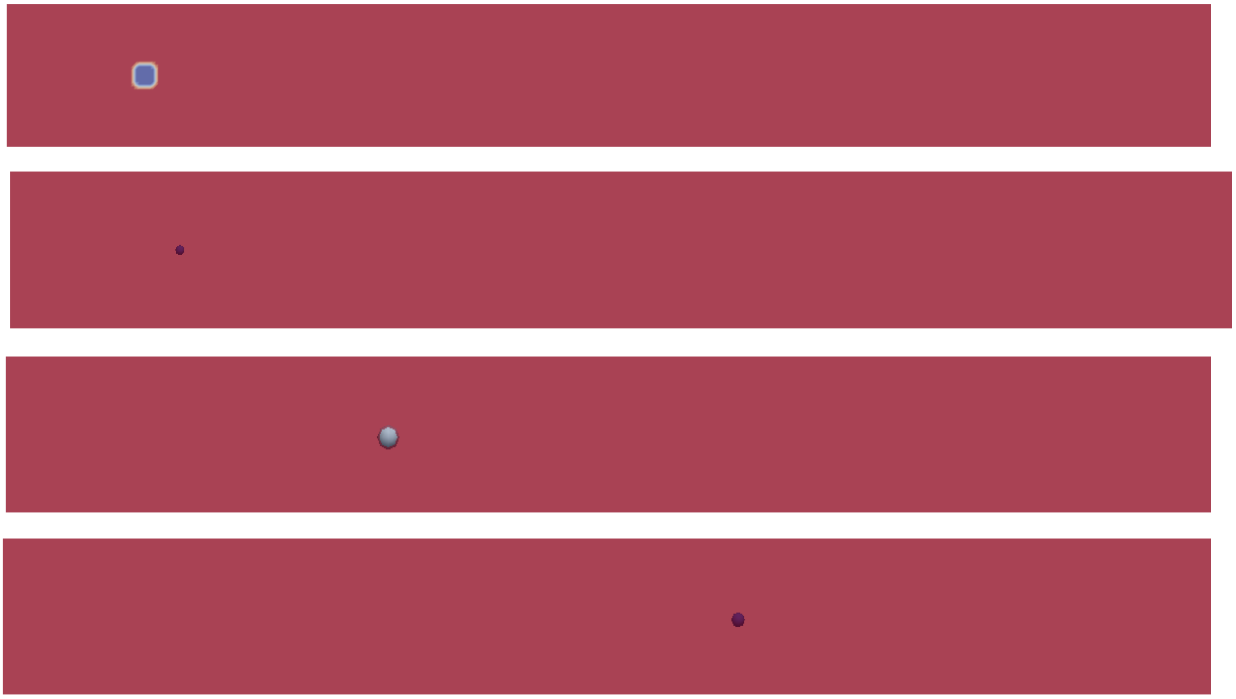

Fig. 2: Cavity collapse and rebound in a 2D channel flow

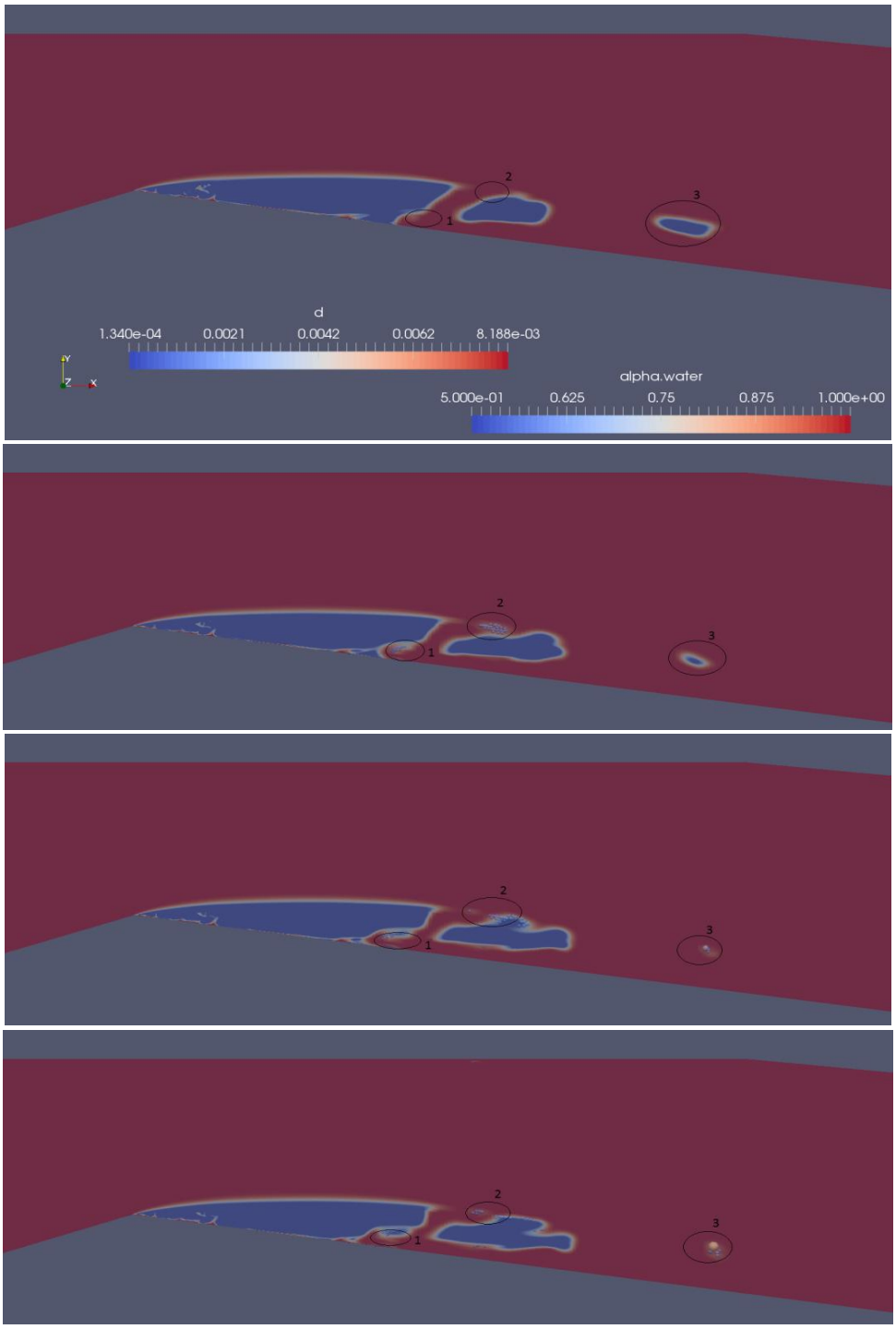

Fig. 3. Cavitating flow in a 2D venturi

3.3 Case 3

In this case a more complicated cavitating flow in a 2D venturi is simulated. Different scenarios can be seen in this simulations, shown in regions 1-3 in Fig. 3. In region 1, some small vapour structures are formed in the re-entrant jet flow which are transformed to small Lagrangian bubbles, and transported upstream. In region 2, the very small cavity structures are transformed to Lagrangian bubbles. Some of these bubbles hit a Eulerian cavity interface in the third figure, and therefore transform back to a Eulerian structure in the fourth figure. Finally, in region 3 a Eulerian cavity is collapsing in the first and second figure. Then, as it becomes small enough, it is transformed to a

Lagrangian bubble in the third figure. Due to the remained vortical flow downstream, some cavities are created which are transformed to more Lagrangian bubbles in the fourth figure. This more complicated simulation clearly show different features of the hybrid solver.

4. Conclusion and future works

In this study, a hybrid solver is described that can resolve an extensive range of scales in cavitating flows. Using this model, bubble growth and collapse due to the variations of the surrounding pressure are captured. The new model has some benefits in erosion prediction as well. In fact the solver can be improved to calculate the radiated acoustic pressure wave due to bubble collapse and rebound which can be used in surface erosion estimation (Eskilsson and Bensow, 2015). Besides that, the residence time of the bubbles gives a less expensive estimation of the regions exposed to successive collapse and rebound.

Although the new model may be used to improve the prediction of cavitating flows, it still needs some basic improvement to give a more reliable estimation. First of all, the Lagrangian library can be improved to include the effect of different forces on bubble trajectory and bubble-wall interaction. Currently, the solver only considers the drag and gravity forces on the bubbles. Also, the bubble-wall interaction is the same as the default settings in the OpenFOAM Lagrangian library which should be improved according to bubble characteristics. Second, bubble-bubble coalescence should be considered in the Lagrangian framework in addition to the currently resolved bubble-bubble collision. Last but not least, there are some more points to be considered like the emitted pressure wave due to the sudden change of the liquid volume fraction in a incompressible flow solver and also to check the continuity criterion during the at the transition times between Eulerian and Lagrangian frames. These last features have not been seen to be considered in the work of Vallier's (2013).

References

M.Abdel-Maksoud, D. Hänel and U. Lantermann (2010) "Modelling and computation of cavitation in vortical flow" . *International Journal of Heat and Fluid Flow*, 31, 1065–1074

R.E. Bensow, G. Bark (2010). "Implicit LES predictions of the cavitating flow on a propeller". *Journal of Fluids Engineering*, 132(4), 041302 .

C. Eskilsson and R.E. Bensow (2015). "Estimation of cavitation erosion intensity using CFD: Numerical comparison of three different methods". *Fourth International Symposium on Marine Propulsors*, 9-16.

M. Gavaises, F. Villa, P. Koukouvinis, M. Marengo and J-P. Franc (2015). "Visualisation and les simulation of cavitation cloud formation and collapse in an axisymmetric geometry". *International Journal of Multiphase Flow*, 68, 14-26.

E. Giannadakis, M. Gavaises, and C. Arcoumanis. (2008). "Modelling of cavitation in diesel injector nozzles". *Journal of Fluid Mechanics*, 616, 153-193.

N.-X. Lu, R.E. Bensow, and G. Bark (2013). "Large Eddy Simulation of Cavitation Developent on Highly Skewed Propellers". *J. Marine Science and Tech*.

C-T Hsiao, J Ma and G. Chahine. (2015). "Simulation of sheet and tip vortex cavitation on a rotating propeller using a multiscale two-phase flow model". *Fourth International Symposium on Marine Propellers*. Austin, Texas, USA.

G. H. Schnerr, I. H. Sezal and S. J. Schmidt (2008). "Numerical investigation of three-dimensional cloud cavitation with special emphasis on collapse induced shock dynamics". *Phisics of Fluids*, 20, 040703.

Vallier, A. (2013). " Simulations of cavitation from the large vapour structures to the small bubble dynamics". *PhD thesis*. Lund University

G. H. Schnerr and J. Sauer (2001). "Physical and Numerical Modeling of Unsteady Cavitation Dynamics". *Proc. 4th International Conference on Multiphase Flow*, New Orleans, U.S.A.

S. Yakubov, T. Maquil and T. Rung (2015). "Experience using pressure-based CFD methods for Euler–Euler simulations of cavitating flows". *Computers & Fluids*, 111, 91–104.

Flow characteristics around marine propellers in self propulsion test condition

Nobuhiro Hasuike[1], Masafumi Okazaki[2]and Akinori Okazaki[3]
Nakashima Propeller Co., Ltd., Okayama/Japan, web page: http://www.nakashima.co.jp/
E-mail: [1]nobuhiro@nakashima.co.jp, [2]m-okazaki@nakashima.co.jp, [3]a-okazaki@nakashima.co.jp

1 Introduction

In propeller design, self propulsion test (SPT) and propeller open water test(POT in short) are performed for evaluation of propulsive performance as practical use. POT result is used for extrapolation to full scale propeller open characteristics (POC) and for the analysis of self-propulsion factors. POC used for self-propulsion analysis is derived from POT at high Reynolds number by consideration of difference of Reynolds number between POT and SPT conditions.

For practical use, typical scale correction of propeller characteristics is based on the simple correction of friction coefficient which is an analogy of flat plate friction, although separation effect to the propulsive efficiency is not considered. This typical procedure often causes irrational eata-r drop problem especially small blade area propellers. As a result, propulsive efficiency of small blade area propellers is not accurately estimated.

To solve this problem, an alternative way is to conduct an additional POT which Reynolds number corresponds to that of SPT[1]. The other high Reynolds POT result is used for full scale propeller characteristics (This procedure is called as '2POT method'). This '2POT method' is widely used at Japanese towing tanks and also recommended by ITTC[2]. As this method is experimental, detail propeller geometry effects are all included. The advantages of '2POT method' are including consideration of not only friction component but also pressure component of propeller characteristics. Laminar flow separation effects to the propulsive efficiency are also taken in account. These features are very important for recently demanded smaller blade area propellers. It is effective when flow characteristics such as separation ranges and friction distributions in POT and SPT conditions are similar.

In generally, propellers in SPT condition are operated in the flow field with higher turbulence intensity by the ship wake field. Streckwall et al.[3] pointed out the importance of consideration of the difference of turbulence intensity in between POT and SPT conditions. Higher turbulence intensity in wake field will cause earlier transition from laminar to turbulence in comparison with POT condition. Therefore, it is necessary to investigate the flow characteristics in POT condition and SPT condition to validate effectiveness of '2POT method'.

Inflow to the propeller in SPT condition is more turbulent than that of POT condition by the ship wake flow,. Lee et al.[4] (2003) investigated wake flow of KVLCC by wind tunnel. Tsuda et al.[5] (1978) investigated the flow pattern of MAU propellers in POT and SPT conditions. In totally, flow character at SPT condition was still mainly laminar flow even though the turbulence intensity in SPT condition was higher than that in POT condition. Flow characteristics at tip region were partially more turbulent than POT condition. MAU propellers have the blade section with maximum thickness at 32% chord position from leading edge, which means MAU propellers are more turbulent than modern NACA section. Regarding the effect of blade section type, the experimental visualization results with modern blade section are little known.

In this research, 27 propeller designs with modern NACA blade sections for 749 chemical tanker were tested and compared with numerical calculation. The blade profiles of these 27 propellers were parametrically changed (ex. pitch, camber, chord, thickness, rake and blade section) and investigated.

2 Flow characteristics in model test condition

Table 1 shows principal particulars of propeller models and test condition. These test series were mainly focused on the small blade area propellers. Oil flow visualization results of suction sides in POT and SPT conditions are shown in Fig.1. Laminar streamlines from leading edge were radially directed by the lower shear stress and centrifugal force. Separation lines radially directed were clearly

observed near the trailing edge. After the clear separation near the trailing edge, flow seemed to be reattached at Rn(K)= 6.0×10^5 in POT condition(Paint was clearly removed). Circumferentially streamlines related to the turbulent region were observed over 90% radius in both POT and SPT conditions. Boundary radii between laminar and turbulent region were almost same in POT condition and SPT condition. Flow characteristics of 27 propellers in the range of Rn(K)=abt. 3.0×10^5 to 6×10^5 were mainly laminar.

In comparison with POT condition, SPT condition showed separation lines near inner radii located upper stream (leading edge) side, which were caused by slower axial velocity and higher attack angle by ship wake. On the other hand, attack angle near the tip was fluctuated in SPT condition. At the top position, axial flow velocity was slower and attack angle was increased. On the other hand, axial flow velocities at side and bottom position were higher and attack angle was decreased. As oil flow patterns were resulted by all of the blade position, paint remained at upstream at top position was removed at less separation conditions which were in side and bottom situation. As a result, separation line near outer radii located downstream side.

From these results, flow characteristics in POT and SPT conditions at Rn(K)=abt. 3.0×10^5 were mainly laminar and frictional component seemed to be almost same in POT and SPT conditions although turbulence intensity between POT and SPT conditions were different. Both POT and SPT conditions include clear flow separation near root part and trailing edge.

In full scale, flow characteristics of small blade area propellers seem to be turbulent and flow separation is hard to occur. This means simple scale correction only by consideration of friction component is insufficient. In the case of small blade area propellers, unexpected eata-r drop problem may occur by simple scale correction, which doesn't take account separation effect. Using additional low Reynolds POT, which Reynolds number corresponds to that of SPT condition, is one of the effective ways to cancel separation effect in SPT condition and derive pure hull, rudder and propeller interaction (eata-r, wake fraction and thrust deduction), because flow separation and friction condition in POT and SPT conditions were similar at Rn(K)=abt. 3.0×10^5. Full scale propeller open efficiency should be extrapolated from the other higher Reynolds POC which includes less separation effect.

3 Numerical model

In this research, transitional flow around propeller was simulated using SOFTWARE CRADLE SC/Tetra V10 software, which was based on a finite volume method with an unstructured grid. 3-equations k-k_L-ω model was selected based on the previous research (Hasuike et al.[6] 2013).

It is important to predict the transition point of a flow around a propeller in operating in low Reynolds number. LKE (Laminar Kinetic Energy) model (Walters & Leylek 2004) was developed to simulate the transitional flow.In the LKE model, the disturbance energy in a pre-transitional region of a boundary layer is represented as Laminar Kinetic Energy (k_L), while the turbulence energy is as *k*. The transport equation of k_L is solved by using two equations of fully turbulent model. SC/Tetra introduces the following k-k_L-ω model (Walters & Cokljat 2008) .

The computational domain is composed of the inner rotational part including the propeller and the outer stationary part. The stationary part and the rotational part are connected discontinuously. Constant velocity and zero pressure are prescribed at the inlet and the outlet boundary respectively. Fig. 2 shows the computational domain for POT condition. The numerical mesh is an unstructured grid, and basic cells are tetrahedral and prismatic cells are applied to near the blade surface for resolving the boundary layer (Fig. 3). The first layer thickness of the prism layer was set to a non-dimensional wall distance for a wall-bounded flow (y^+ in short) =1. Fig. 4 shows the computational domain for SPT condition. The wake flow of model ship of 749 Chemical tanker[7] was simulated. Fig. 5 shows the simulation result of axial and circumferential velocity component of wake distribution at propeller position.

Table 1: Principal particulars of propellers and test condition

MPNO	Dp(m)	Chord0.7(m)	POT condition	SPT condition			
			J	Vm(m/s)	Fn	n(rps)	Rn(Kempf)
Propeller A-1	0.2583	0.0465	0.516	2.490	0.337	13.24	300814
Propeller A-2	0.2583	0.0465	0.502	2.502	0.338	13.45	305320
Propeller A-3	0.2583	0.0465	0.494	2.503	0.338	13.45	305117
Propeller A-4	0.2583	0.0465	0.500	2.499	0.338	13.44	305019
Propeller A-5	0.2583	0.0465	0.499	2.493	0.337	13.34	302775
Propeller A-6	0.2583	0.0465	0.497	2.499	0.338	13.46	305243
Propeller A-7	0.2583	0.0465	0.494	2.499	0.338	13.45	305083
Propeller A-8	0.2583	0.0465	0.500	2.495	0.337	13.44	305018
Propeller A-9	0.2583	0.0465	0.501	2.490	0.336	13.31	302840
Propeller A-10	0.2583	0.0465	0.499	2.500	0.338	13.46	305503
Propeller B-1	0.2583	0.0465	0.518	2.232	0.302	12.05	274651
Propeller B-2	0.2583	0.0465	0.509	2.224	0.301	11.90	270994
Propeller B-3	0.2583	0.0480	0.501	2.224	0.301	11.85	277977
Propeller B-4	0.2583	0.0469	0.509	2.216	0.299	11.73	268974
Propeller B-5	0.2583	0.0465	0.515	2.224	0.301	11.95	272151
Propeller B-6	0.2583	0.0465	0.508	2.224	0.301	11.98	272699
Propeller B-7	0.2583	0.0481	0.514	2.218	0.300	11.91	280306
Propeller B-8	0.2583	0.0480	0.514	2.215	0.299	11.90	279619
Propeller B-9	0.2583	0.0469	0.516	2.212	0.299	11.83	271395
Propeller B-10	0.2583	0.0480	0.510	2.215	0.299	11.84	278044
Propeller B-11	0.2583	0.0469	0.515	2.214	0.299	11.83	271420
Propeller B-12	0.2454	0.0446	0.547	2.219	0.300	11.93	248263
Propeller B-13	0.2712	0.0486	0.496	2.208	0.298	11.76	293067
Propeller B-14	0.2583	0.0469	0.510	2.215	0.299	11.87	272289
Propeller C-1	0.25	0.0661	0.512	2.668	0.361	14.74	461532
	0.25	0.0661	0.570	2.387	0.323	11.71	368846
Propeller C-2	0.25	0.0521	0.513	2.670	0.361	14.49	357530
	0.25	0.0521	0.567	2.388	0.323	11.57	287055
Propeller C-3	0.25	0.0524	0.526	2.005	0.271	10.89	270629
	0.25	0.0524	0.593	1.791	0.242	8.60	215416

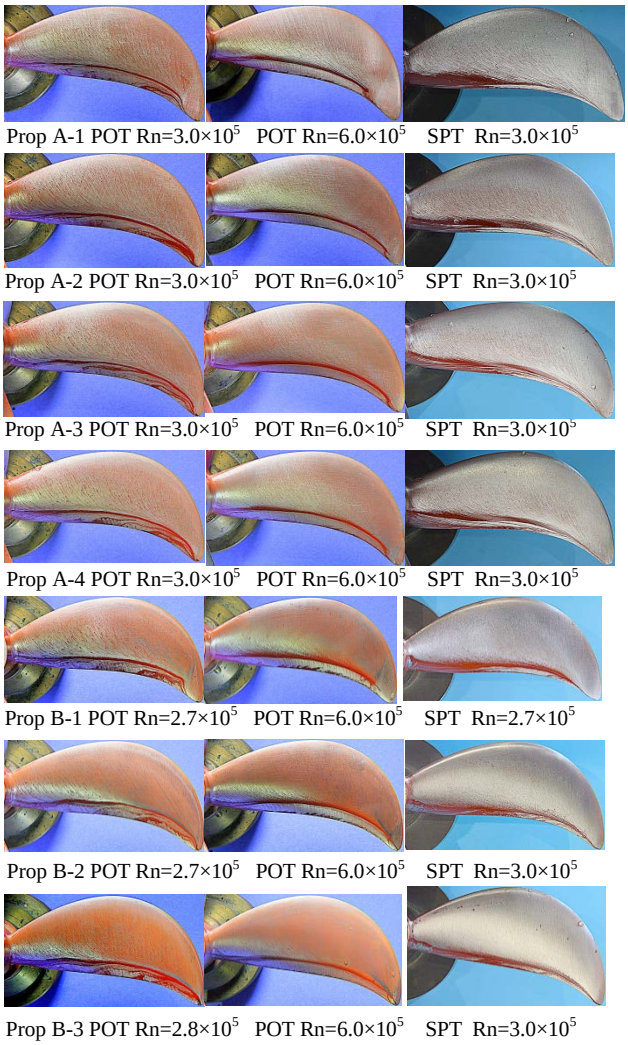

Fig. 1: Oil flow visualization of POT and SPT conditions

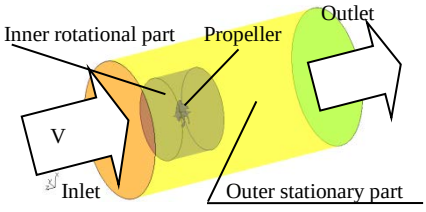

Fig. 2: Computational domain(POT)

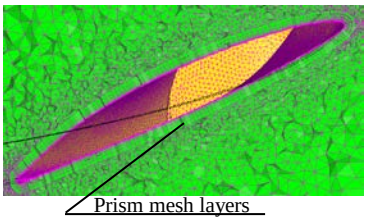

Fig 3: Prism mesh arrangement near blade surface

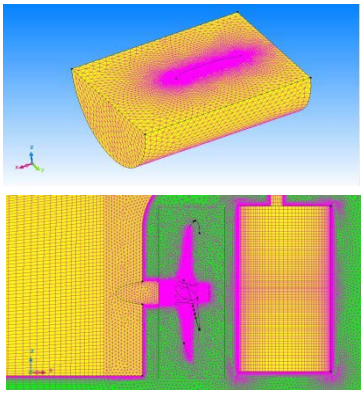
Fig. 4: Numerical grids for self propulsion analysis

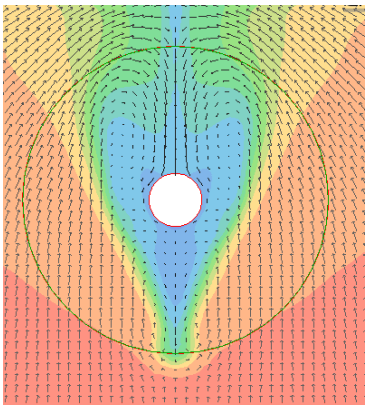
Fig. 5: Axial velocity component of wake flow

4 Numerical simulation of flow characteristics on POT and SPT conditions

Fig. 6 and Fig.7 show comparison results of oil flow visualization and calculation of limiting streamlines of Propeller C-2. Calculation results showed qualitative agreement with experimental results. Boundary radii between laminar and turbulent flow were slightly larger than experimental results. Full scale calculation result showed fully turbulent and separation region was negligible. Distributions of friction coefficient are shown in Fig.8. Flow characteristics of POT condition seemed to be mainly laminar in the range of Rn(K)= 1.5×10^5 to 7.5×10^5.

Oil flow visualization results in SPT condition are shown in Fig. 9. In the case of Rn(K)=1.1×10^5, large separation area was found and reattachment was not clearly confirmed. From this result, SPT should be conducted as high as possible Reynolds number.

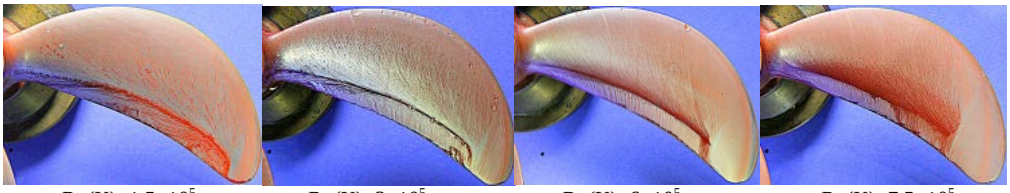

Rn(K)=1.5×10^5 Rn(K)=3×10^5 Rn(K)=6×10^5 Rn(K)=7.5×10^5

Fig. 6: Experimental results (Propeller C-2, Oil flow visualization, POT condition)

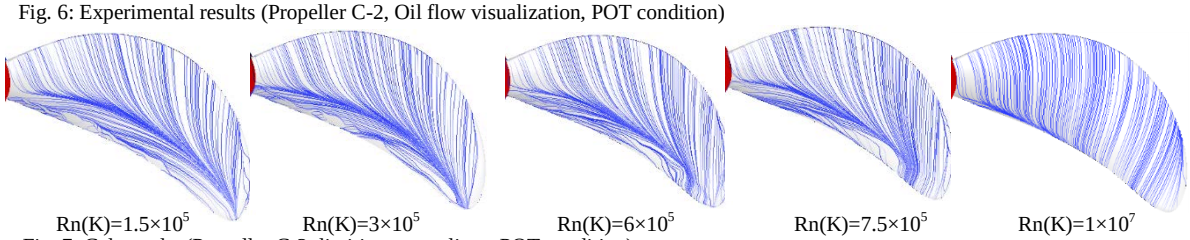

Rn(K)=1.5×10^5 Rn(K)=3×10^5 Rn(K)=6×10^5 Rn(K)=7.5×10^5 Rn(K)=1×10^7

Fig. 7: Cal. results (Propeller C-2, limiting streamlines, POT condition)

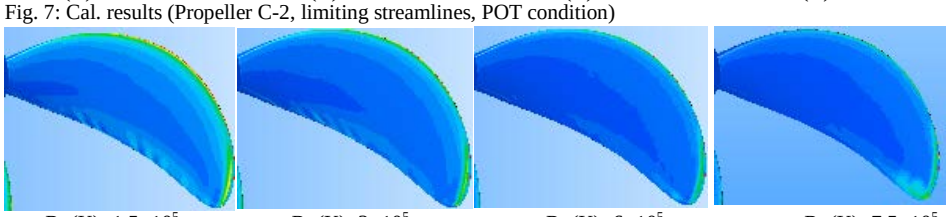

Rn(K)=1.5×10^5 Rn(K)=3×10^5 Rn(K)=6×10^5 Rn(K)=7.5×10^5

Fig. 8: Cal. results (Propeller C-2, distribution of friction coefficient, POT condition, yellow: higher friction, blue: lower friction)

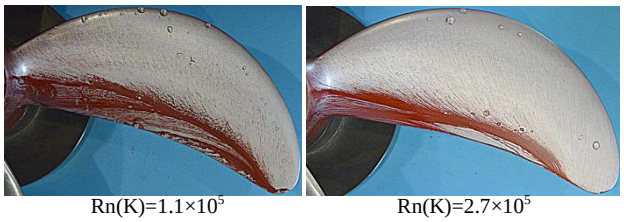

Rn(K)=1.1×10^5 Rn(K)=2.7×10^5

Fig. 9: Experimental results (Propeller C-2, Oil flow visualization, SPT condition)

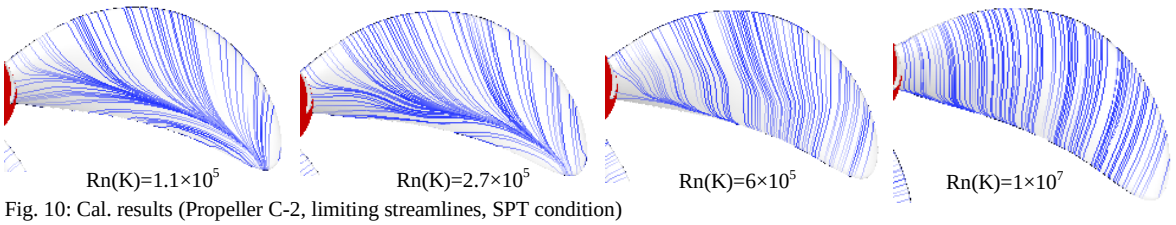

Rn(K)=1.1×10^5 Rn(K)=2.7×10^5 Rn(K)=6×10^5 Rn(K)=1×10^7

Fig. 10: Cal. results (Propeller C-2, limiting streamlines, SPT condition)

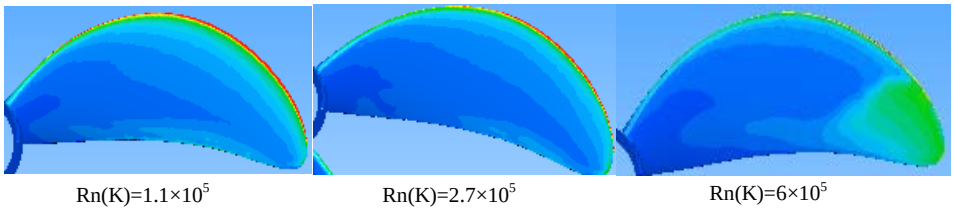

Rn(K)=1.1×10^5 Rn(K)=2.7×10^5 Rn(K)=6×10^5

Fig. 11: Cal. results (Propeller C-2, distribution of friction coefficient, SPT condition, yellow: higher friction, blue: lower friction)

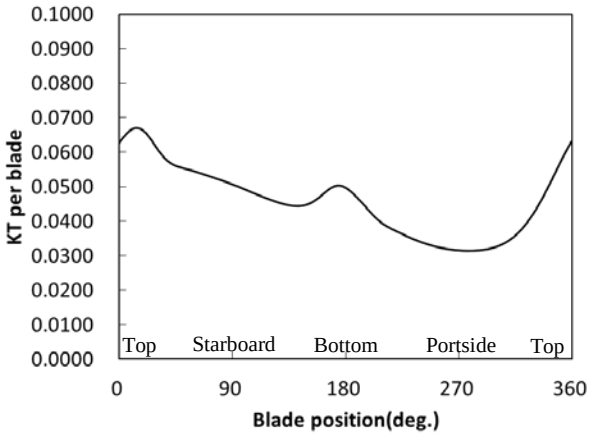

Fig. 12: Cal. results (Propeller C-2, thrust valiation in SPT condition, Rn(K)=6×10^5)

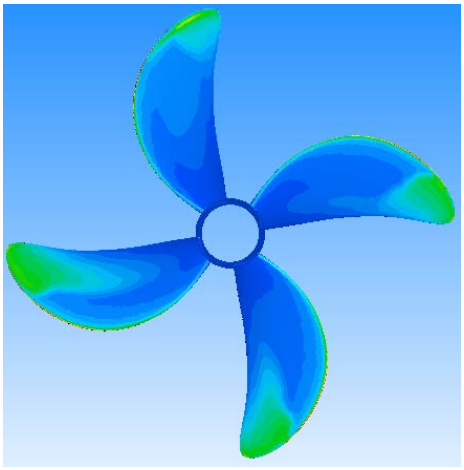

Fig. 13: Cal. results (Propeller C-2, distribution of friction coefficient, SPT condition, Rn(K)=6×10^5, yellow: higher friction, blue: lower friction)

Flow pattern at Rn(K)=2.7×10^5 was similar to flow pattern in POT condition at Rn(K)=3.0×10^5, which was typical Reynolds number in SPT condition. In detail, flow separation line near root located upper stream side in comparison with POT condition. Fig. 10 and Fig. 11 show limitting streamlines and friction coefficient respectively. Flow patterns in POT condition and SPT condition were similar at Rn(K)=abt. 3.0×10^5. However, flow pattern in SPT condition at Rn(K)=abt. 6.0×10^5 was more turbulent and higher friction region was found in comparison with POT condition, although SPT is not possible at Rn(K)=abt. 6.0×10^5. These seemed to be caused by the higher turbulence intensity in SPT condition in comparison with POT condition. The flow characteristics near the transitional Reynolds number are sensitive to the turbulence intensity. When Reynolds number is much smaller than the transitional Reynolds number, flow characteristics are not sensitive against the turbulence intensity. These tendencies were described in previous research[6].

Thrust variation of one blade is shown in Fig. 12. Thrust of one blade in one rotation was maximized near the top region due to the high attack angle with low axial velocity. Thrust at starboard side was greater than that of port side by upward wake flow. This tendency was well captured by calculation.Fig. 13 shows friction coefficient at each blade position. Turbulence region at starboard side is larger than top and portside position. This was caused by higher Reynolds number by high axial velocity at portside and increase of attack angle by upward stream of ship wake.

5 Conclusions

- Flow characteristics in model scale in POT and SPT conditions were still mainly laminar and include laminar flow separation which causes efficiency drop. Full scale extrapolation from model scale by model test should be improved with consideration of flow separation at model test.
- Flow patterns such as friction distributions and separation ranges in SPT condition at Rn(K)= abt.3.0×10^5 were similar to the flow patterns in POT condition at abt. Rn(K)= abt.3.0×10^5, which supports the validity of 2POT method.
- Full scale simulation showed less separation in comparison with model scale. Some of propeller designs may show high efficiency in full scale although the efficiency in model scale is low by flow separation.

These raise the importance of numerical estimation of high efficiency propeller design in full scale.

References

[1] Tamura, K. and Sasajima, T.,"Some Investigation on Propeller Open-Water Characteristics for Analysis of Self-Propulsion Factors", Mitsubishi Technical Bulletin, No.119, pp.1-12 (1977).
[2] ITTC-Recommended Procedures and Guidelines, Testing and Extrapolation Methods Propulsion, Propulsor Open Water Test, 7.5-02-03-02.1, Revision 02, (2008).

[3] Streckwall, H., Greitsch, L. and Scharf, M.," An advanced Scaling Procedure for Marine Propellers", Proc. of The 3rd International Symposium on Marine Propulsors smp'13, Launceston, Australia, (2013).
[4] Lee, S.-J., Kim, H.-R., Kim, W.-J., Van, S.-H., 2003. Wind tunnel tests on flow characteristics of the KRISO 3,600 TEU containership and 300K VLCC double- deck ship models. J. Ship Res. 47 (1), 24–38.
[5] Tsuda, T., Konishi, S., Asano, S., Ogawa, K. and Hayasaki, K.,"Effect of Propeller Reynolds Number on Self-Propulsion Performance", The Japan Society of Naval Architects and Ocean Engineers, 169, (1978).
[6]Hasuike, N., Okazaki, A., Yamasaki, S., Ando, J., "Reynolds effect on Propulsive Performance of Marine Propeller operating in wake flow", Nutts 2013, September, 2013
[7] Yamasaki, S., Hanaoka, M., Okada, Y., Hasuike, N., Yamamoto, M., Himei, K., Okazaki, A., Katayama, K., Mishima, T. and Kawasaki, M.,"Research on a Smallest Blade Area Propeller 1st Report : The Design and Model Tests of a Small Blade Area Propeller", Proc. of Conference Proceedings the Japan Society of Naval Architects and Ocean Engineers, Vol. 16, pp. 357-360, (2013).

A Development and Analysis of the New Energy Saving Device "USTD"

Yasuo Ichinose, Kenichi Kume, Yusuke Tahara
National Maritime Research Institute (NMRI), Mitaka, Tokyo/Japan
ichinose@nmri.go.jp kume@nmri.go.jp tahara@nmri.go.jp

1. Introduction

Energy Saving Devices (ESDs) are essential tools for design of eco-friendly and competitive ships. National Maritime Research Institute (NMRI), Japan developed a duct-type ESD called WAD equipped in front of Propeller. Over 40 ships installed the WAD have been delivered by 2015. Delivered power saving of WAD is estimated to be 3~7% by tank test results, and it strongly depends on the wake generated by hull forms (Kawashima (2014)). Fig.1 shows the correlation between delivered power saving of WAD and self-propulsion factor of ships without WAD. This figure indicates that WAD provides superior performance for hull form which yields low wake fraction (1-wt), which generally generates obvious hook shape in wake. Our challenge is to develop the new duct-type ESD to expand the applicable scope of ship to the hull form which yields weak hook shape in wake field, generally called V-type frame-line ship.

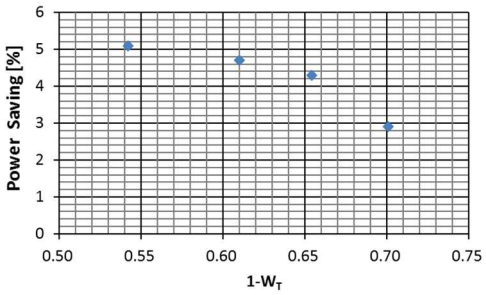

Fig.1 Correlation between Power Saving of WAD and self-propulsion factor of ships without WAD

In the present paper, we discuss the two development challenges of conventional circular-type duct "WAD" attached to the V-type frame-line hull based on the simulated flow filed data, and propose the new ESD, called "USTD", due to overcome the development challenges of WAD. Finally, the advantages of USTD against the conventional WAD is shown by the calculation and tank-test results.

2. The Development Challenge of WAD

A) Calculation method

The solver dedicated to the present study is NMRI CFD code surf ver.6.44 (Hino (1997) for unstructured grid. Unstructured Grids are generated by using HEXPRESS ver.5.1, and the total number of cells varies in 4.6M~9.0M and 6.8M~11.0M cells for model-scale and full-scale, respectively, depending on ESD geometry. Minimum Spacing of grids is set as y+~1 for model- and full-scales. Overview of surface grid of case with WAD is shown on Fig. 2. The turbulence model used in the present

work is modified Spalart-Allmaras (MSA Cvor=10) one-equation model without wall function in all cases of the present work. The presence of rotating propeller is represented by simplified body-force model based on an infinitely bladed-propeller theory.

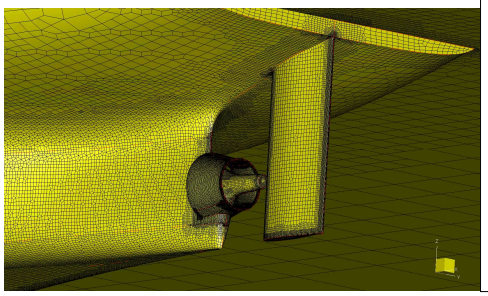

Fig. 2 Overview of surface grid of case with WAD

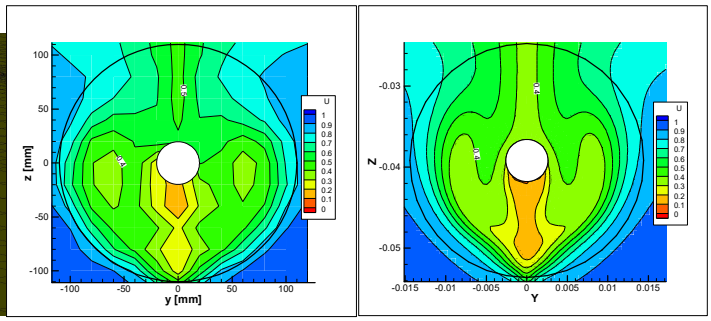

Fig. 3 Nominal wake distribution for 82BC test case for 7m model scale condition. Left: Measurements Right: surf MSA (4.6 Mil. Cells)

Before discussion on the flow field around ESDs, the CFD capability to predict powering parameters is investigated. Fig.3 shows comparison of nominal wake distribution for 82BC test case in NMRI between CFD and Measurement, and Fig.4 shows comparison of self-propulsion factors for various ESDs appended condition. Results shown in Fig.3 and Fig.4 indicate that wake fields in towing condition and thrust deduction friction (1-t) is generally well predicted by NMRI CFD what we normally use for design of hull form and ESD. However, we still observe difficulties in evaluate the wake coefficient in self-propulsion condition. Therefore, this recognition leads to our standpoint for CFD-based design and analysis of ESDs which focus on flow field characteristics.

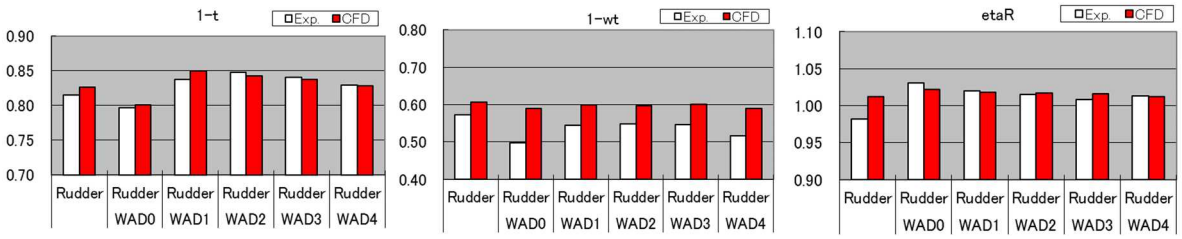

Fig. 4 Comparison of self-propulsion factors for 82BC test case for fully appended condition.

B) Comparison of flow field around WAD between ships with high and low wake coefficient.

Fig.5 shows pressure distributions and flow separation region (gray region in the figure, iso-surface of U~0) around WADs installed on the same-size over 80,000 DWT bulk carriers, which yield 0.1 wake-coefficient difference on tank test results. The ship at the left side in Fig.5 has U-type frame-lines, which are discussed in our previous work[4], and it yields strong hook-shape in wake. The hull form at right side in Fig.5 has V-type frame lines, which yield weaker hook-shape and higher wake coefficient than that by hull form with U-type frame-lines. As described above, the power saving

by WAD for U-type hull form, which evaluated by tank test results, is higher than that by WAD for V-type hull form, where the diameter at trailing edge of the both WADs are designed as 45% propeller diameter and the opening angle of WADs are designed as 11 and 10 degrees, for U-type and V-type hull form, respectively.

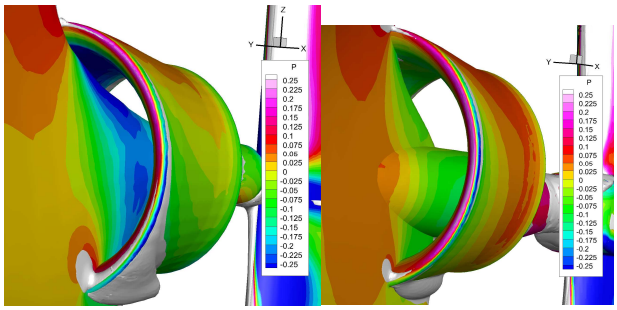

Fig. 5 Pressure Distributions and Flow Separation Regions (Gray iso-surface) around WADs. (Left: Ship with U-type Frame-line, Right Ship with V-type Frame-line)

The effects of the duct-type ESDs are classified as follows:

Eff.1 Improvement in the wake at propeller plane due to the flow separation and/or change of flow direction that occurred at/around the duct.

Eff.2 Improvement of propeller efficiency behind ship due to the same cause of Eff.1.

Eff.3 Improvement of thrust deduction factor due to the thrust produced by the duct.

Eff.4 Improvement of thrust deduction factor due to the change of hull pressure around the duct.

In the case that performance of the duct is not sufficiently demonstrated, thrust deduction factor is not improved or deteriorated, where the Eff.3 is evaluated too much small or opposite in CFD simulation results. Therefore, we focus on the Eff.3 in the WAD design to avoid a design of less effective or deteriorative WAD. It is noted that, in the case of the extremely strong hook-shape in wake field, extremely large improvement of the Eff.1 and 2 overcome the deterioration of Eff.3. However, this paper does not discuss this rare design case, because any design can generate effective power saving in this case due to the easier recovery of loss yielded by hull form.

It has been often discussed the Eff. 1 and 3 in terms of inflow angle at leading edge of duct cross section distributed in circumferential direction. (e.g., Inukai (2011) and sakamoto (2014)) In the present paper, we also discuss improving the thrust deduction factor and the wake coefficient which are yielded by thrust of duct and the speed loss of wake in axial direction, respectively. The findings from the discussion are very useful for design the opening angle and position of duct.

Fig. 6 shows distributions in circumferential direction of inflow angle at leading edge of wing section on WAD in self-propulsion conditions. The transverse axis represents circumferential position of wing section on WAD, where; 0 degree and 180 degrees indicate top and bottom, respectively, and positive value shows starboard-side. The vertical axis represents angle of inflow, where 0 degree indicates x-direction and positive value is flow from outside to inside of WAD. The blue-lines and red-lines show inflow angle for U-type and V-type hull form mentioned above, respectively. While the

angle of inflow for U-type hull form is changed uniformly in the whole position, that for V-type is changed steeply around 60 degrees and slowly recover from near the 80 degrees keeping the small angle. In addition, the flow in the position of near the 180 degrees becomes separated, which generate Eff.1 and 2, that also can be observed in Fig.5.

Then, Fig.7 indicates the calculated distribution of local thrust to x-direction at circumferential position, generated by the blade element from this inflow angle distribution, which is evaluated from equation (1).

$$C_{WTR} = C_L \times V_{inflow}^2 sin(\beta) + C_D \times V_{inflow}^2 cos(\beta) \quad (1)$$

Where:

C_L : Lift coefficient of the wing section of duct at local position. (evaluated from reference 6).

C_D : Drag coefficient of the wing section of duct at local position. (evaluated from reference 6).

β : Angle of inflow (positive : inflow from outside to inside of the duct).

The region of β in less than -30 and more than 40 are omitted from the calculation, which can be assumed as separated region.

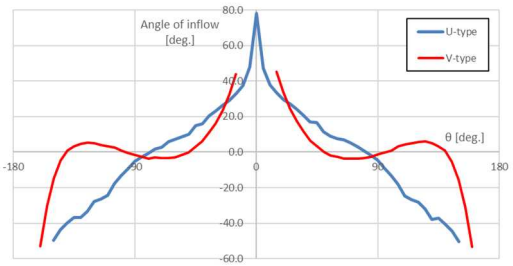

Fig.6 Distribution of in-flow angle (β) at leading edge of wing section in circumferential direction on WAD in self-propulsion conditions

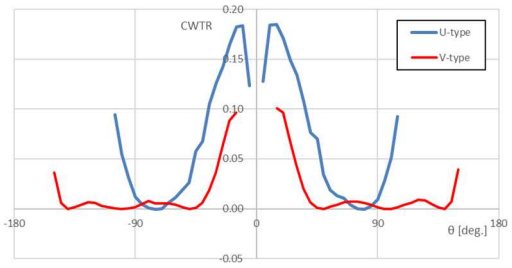

Fig. 7 Distribution of C_{WTR} for WAD in self-propulsion conditions.

As shown in Fig.7, whereas the duct equipped with the U-type hull form yields strong thrust to near 90 degrees, the duct equipped with the V-type hull form yields almost zero thrust from near 45 degrees to near 135 degrees. That is because the inflow angle has remained near zero. Therefore, one of the reasons why the energy saving effect of the duct mounted on V-type hull from is small, is the inflow angle yielded by wake with weak hook-shape. Thus, to enhance the energy saving effect of the duct mounted on V-type hull from, we utilize around top 0-degree position, which has large inflow angle, and reduce the location which has small inflow angle.

C) Interference between Circular-type Duct and Rudder Fin.

The effect of the rudder fin has been found to be particularly dependent on the thrust of the port side of the fin, however, the flow separation in the lower part of the circular-type duct disturbs the in-

flow to the rudder fin and make it worse. Thus, to reduce interference between circular-type duct and rudder fin, lower side of circular-type duct is removed.

3. Development and design of a new Duct-type ESD "USTD"

The design characteristics of the new design duct "USTD" are followings.

- ☐ Parallel part on the top side enhanced effective use of the inflow with large angle. (see. Fig.8)
- ☐ Semi-circular shape reduces the interference effect between duct and rudder fin.

Fig. 9 show effect of the parallel part for wake field yielded by V-type hull form, which evaluated by NMRI CFD code surf 6.44 with 8 ~ 9 million unstructured grid. Thrust deduction factor of USTD with parallel part is improved 0.4 % to that of USTD without parallel part. As a result, power saving of USTD with parallel part is improved 0.5 %. As shown in Fig.10, the top position of USTD, where we design parallel part, yields thrust to the forward direction of the ship.

As shown in Fig.11, based on the results of the tank test in 30,000 DWT class chemical tanker (left side figure) and 80,000 DWT class bulk carrier (center and right side figure), the power saving of USTD has 0.6% ~ 1.4 % advantage to that of WAD. The right side figure in Fig.11 shows the comparison of power saving in condition that both conventional duct and USTD are combined with the rudder bulb fin. The fact indicates that USTD has advantage to WAD even in consideration of the interference between duct and rudder bulb fin.

4. Concluding Remarks

In the present paper, we discussed the two development challenges of conventional circular-type duct WAD attached to the V-type frame-line hull based on the simulated flow filed data, and propose the new ESD, called USTD, due to overcome the development challenges of WAD.

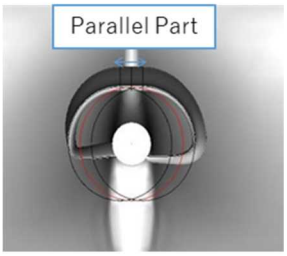

Fig.8 Parallel Part on USTD

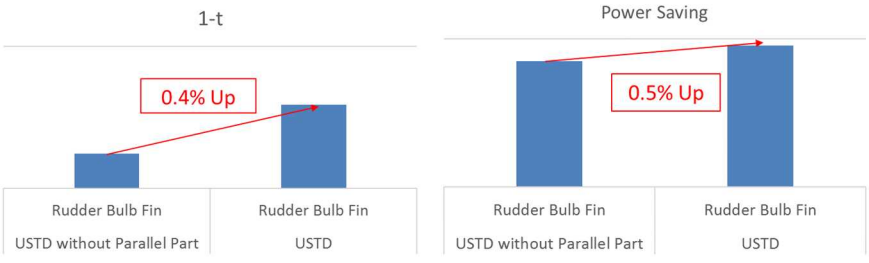

Fig.9 Comparison between USTD and USTD without Parallel Part

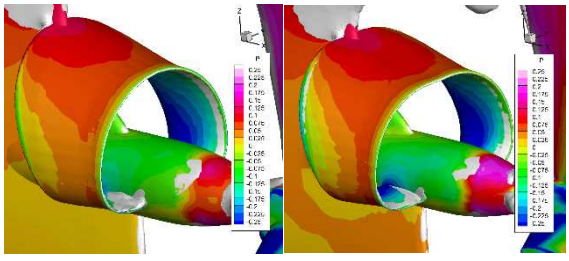

Fig.10 Comparison of Pressure Distributions and Flow Separation Regions (Gray iso-surface).
(Left: USTD without Parallel Part, Right: USTD with Parallel Part.)

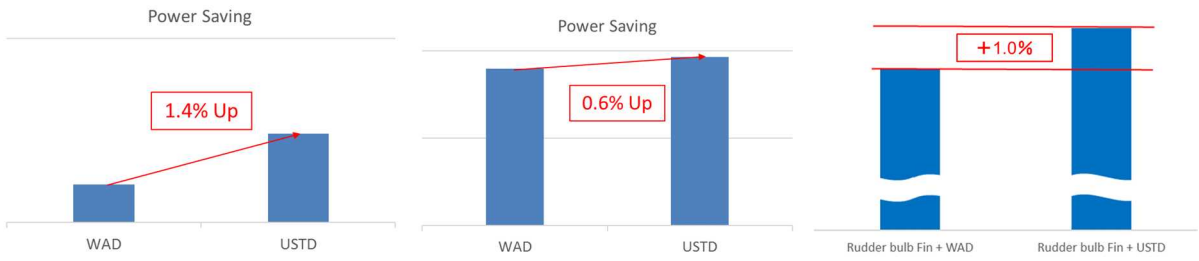

Fig. 11 Performances of WAD and USTD estimated by tank-test results

First of all, we discussed the low energy-saving effect in the hull with V-type hull form, which yields weak hook shape in wake field, from the point of view of the inflow angle to wing section on duct in circumferential direction. As a result, we proposed the parallel part on the top side to enhance the energy saving effect of the duct mounted on V-type hull from.

Secondly, we discussed the interference between the circular-type duct and the rudder fin. the flow separation in the lower part of the circular-type duct disturbs the inflow to the rudder fin and make the effect of rudder fin worse.

Based on the above, we propose a new duct-type ESD "USTD", which characterized by parallel part on the top side and semi-circular shape. The USTD has an advantage especially in improvement of thrust deduction factor to the convectional duct WAD. The tank test results show the 0.4 ~ 1.6% power-saving improvement to the conventional duct WAD even in consideration of the interference between duct and rudder bulb fin.

References

1. Y. Inukai, T. Kaneko, S. Nagaya, F. Ochi, 2011, Energy-Saving Principle of the IHIMU Semicircular Duct and Its Application to the Flow Field Around Full Scale Ships, IHI Engineering Review.
2. N. Sakamoto, Y. Kawanami, M. Hinatsu and S. Uto, 2014, Viscous CFD Analysis of Stern Duct Installed on Panamax Bulk Carrier in Model and Full Scale, 15th International Conference on Computer and IT Applications in the Maritime Industries.
3. H. Kawashima, K. Kume and N. Sakamoto, 2014, Study of Weather Adapted Duct (WAD), Papers of National Maritime Research Institute (in Japanese).
4. Y. Ichinose, Y. Tahara, Y. Kasahara, 2015, Numerical Study on Flow Field around the Aft Part of Hull Form Series in a Steady Flow, 18th Numerical Towing Tank Symposium.
5. T. Hino, 1997, A 3D Unstructured Grid Method for Incompressible Viscous Flows, Journal of the Society of Naval Architect, Japan
6. H. Yamaguchi, 1999, A Computer Program for Predicting the Hydrodynamic Characteristics of Two-Dimensional Foil or Cascade in Steady Flow with Boundary Layer Effects Taken into Account, http://www.1.k.u-tokyo.ac.jp/yama/prog/prblg/index.html

Numerical Simulation of an Ultrasonic Vibratory Cavitation Device

Byoung Guk Kim, Philip Wilson, Stephen Turnock
Fluid Structure Interactions group, Faculty of Engineering and Environment,
University of Southampton, Southampton SO16 7QF
bgk1g15@soton.ac.uk

1 Introduction

Cavitation erosion prediction is one of the most important tasks in the ship propeller design. While predominantly qualitative methods are used such as paint tests or high speed video image analyses, there have been efforts to quantify such risks especially in the field of computational fluid dynamics (CFD).

As an experimental quantitative method to assess erosion risk, the acoustic emission (AE) technique has been employed, for example, by Lloyds Register for more than a decade now to complement their borescopic cavitation observation at the ship scale. Boorsma and Fitzsimmons (2009) reported (see Fig. 1,) its correlation with borescope observed cavitation events appeared very positive and the location of cavitation impingement on the rudder (shown in the left image of Fig. 1) coincided with the estimated location by multiple synchronous measurements of AE at different locations. If it is possible to decipher how the AE connected with the pressure waves emitted from any given cavitation event, predicting the pressure waves we may be able to predict AE and eventually where and what intensity of cavitation events occur on any given propeller or ship structures. The transfer function can be useful for establishing quantitative correlations between CFD, full-scale trial data and with model test data.

As the first step in being able to model this process and gain greater understanding in links between acoustic signal and type/location of cavitation, an open source Computational Fluid Dynamics programme openFOAM (version. 3.0.1) has been used to simulate ultrasonic cavitation on a sonotrode and hence to predict cavitation phenomena and pressure impact loads on a test specimen under the ultrasonic horn. The aim of the work is to evaluate the physical realism required and the limitations of current cavitation models.

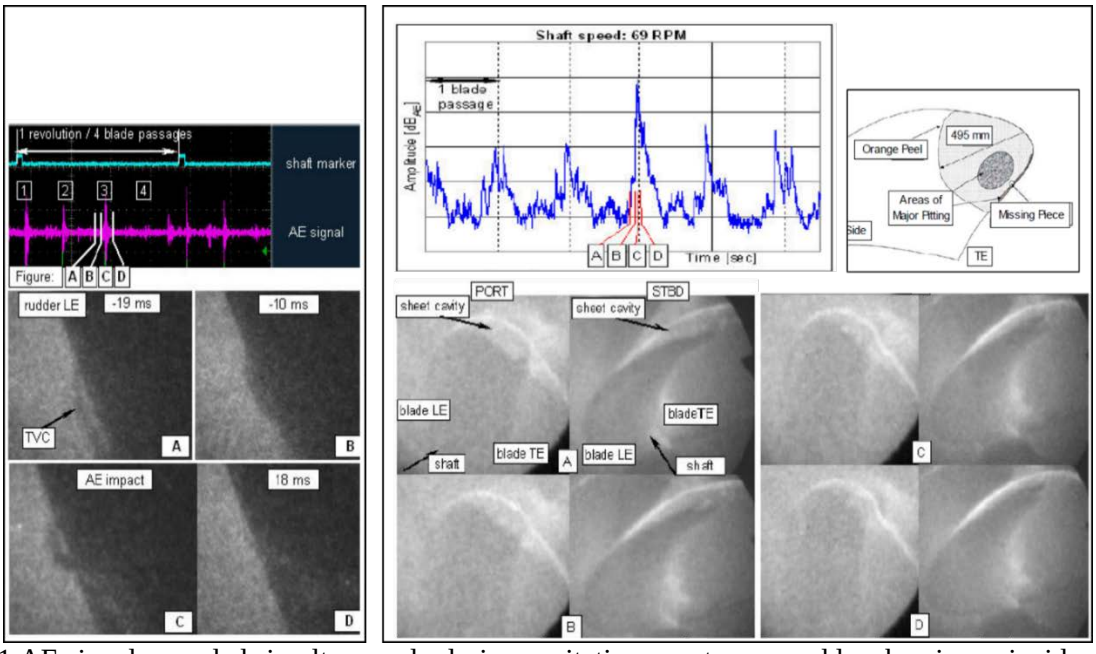

Fig. 1 AE signal recorded simultaneously during cavitation events on a rudder showing coincidence of AE burst and the tip vortex impingement moment in the image C (left) and a propeller also showing a good coincidence of AE burst and the propeller tip vortex bursting which was confirmed later by a visual inspection of the propeller (right). Boorsma and Fitzsimmons (2009).

2 Vibratory cavitation device (Sonotrode)

The device intended for the experiment is a Sonotrode. It consists of an ultrasonic transducer of which the horn tip is submerged in fresh water contained in a rectangular bath as shown in Fig. 2. Acoustic emission sensors will be placed just beneath the bottom of a rectangular test specimen. The technical specifications of the ultrasonic transducer and acoustic emission sensor as well as the approximate dimensions of the bath are described in Table 1.

Table 1 Technical specifications of the test equipment.

Sonotrode	
Manufactuer, model	Hielscher, UIP1000hd
Power output range	500 ~ 1000 W
Oscillation frequency and amplitude (peak-to-peak)	20 kHz ± 500 Hz (non-adjustable) Actual measurement results: 19.5 kHz, 43 (50 %) ~ 96 (100 %) ± 1 µm
Diameter of the ultrasonic horn	15.9 mm
Acoustic emission sensor	
Type	Ceramic-faced Piezoelectric
Frequency	150 kHz
Dimensions (mm)	20.0 x 23.7 x 10.1
Bath	
Material and shape	Transparent acrylic rectangular box
Dimensions (L x W x H, mm)	305 × 400 × 115
Liquid in the container	Fresh water at ambient temperature (5 litres)

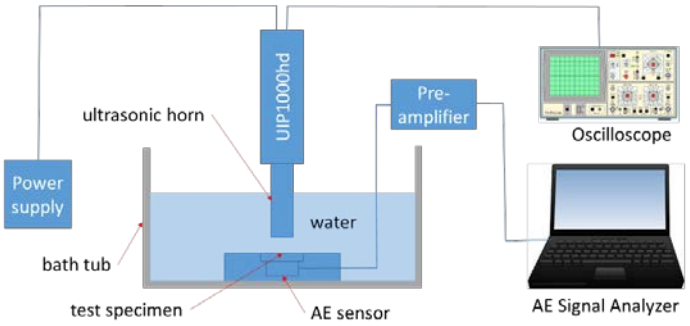

Fig. 2 Schematic instrumentation of the ultrasonic cavitation device.

3 Numerical simulation setup

There are a number of numerical validation studies on the acoustic cavitation simulation in an ultrasound field. Žnidarčič et al. (2015) reported a series of the homogeneous-mixture-based acoustic cavitation simulation results with different cavitation models. They reported failure of the conventional cavitation models in predicting the sub-harmonic oscillation of, namely the acoustic super-cavity in the ultrasound field and suggested importance of the inertia of the large cavity in describing its subharmonic oscillation in a rapidly changing pressure field. Mottyll and Skoda (2015) tried validation of their density-based compressible inviscid flow solver with barotropic cavitation model.

In this initial numerical study, to solve the unsteady Reynolds-Averaged Navier-Stokes equation, the PIMPLE (merged PISO-SIMPLE) algorithm was used together with the VoF-based Schnerr-Sauer cavitation model (in case of the two-phase simulation) and the k-ω SST (Shear Stress Transport) turbulence model as a start; the involved Reynolds number is in the order of 100 ~ 5000 suggesting laminar flow, however, considering the experimentation results of Žnidarčič et al. (2014) or Vít et al. (2014), a turbulent flow model appeared more appropriate.

An investigation was made for the flow features inside the gap between the ultrasonic horn and the test

specimen, pressure waves and the cavity development. Firstly, the solution sensitivity to the mesh size and the difference in solutions with the static mesh scheme and dynamic one were checked with an incompressible single-phase flow simulation case. The dynamic mesh scheme is to set the first cells on 'piston' and 'pistonSidewall' patches to move at a given oscillation speed of the patches. If the cells movement require re-alignment of the neighbour cells, the re-alignment is automatically done by the scheme skewing and displacing the neighbour cells. Otherwise, the size of the neighbour cells vary in the direction of the movement to compensate for the displacement of the moving cells. The flow was assumed as an incompressible single or two-phase flow to check how the pressure waves would be influenced by the development of a cavity volume.

The whole calculation domain was modelled as an axisymmetric one. The outer radius made the same as the distance from the ultrasonic horn to the shorter edge side of the rectangular bath. A schematic drawing of the model is shown in Fig. 3. The imposed boundary conditions are shown in Table 2. The simulation cases were performed for about 200 cycles (T ≈ 10 ms) based on a fixed test setup of the power setting at 50 % (peak-to-peak oscillation amplitude: 43 µm, frequency 19.5 kHz) with a fixed gap distance (= 2 mm) between the horn and the specimen.

The results of the calculation were evaluated based on the analogy of other similar published experimentation results like Žnidarčič et al. (2014) or Vít et al. (2014).

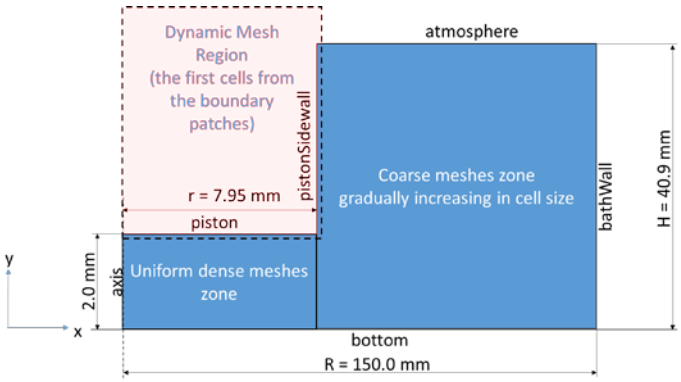

Fig. 3 Schematic drawing of the mesh.

Table 2. Finite volume boundary patches and the boundary conditions imposed on them.

Patch ID.	*p/ρ (ρ = 1000 kg/m³)*	*U*
piston & pistonSidewall	$\nabla p \cdot \vec{n} = 0$	$U_n = 2.634 * \sin(2\pi f * t)$ *where, f = 19500.*
bottom	$\nabla p \cdot \vec{n} = 0$	$\nabla \vec{U} \cdot \vec{n} = 0$, $\nabla \vec{U} \cdot \vec{\imath} = 0$
axis	empty	empty
atmosphere	p/ρ = 101.3	$\nabla \varphi \cdot \vec{n} = \overrightarrow{U_n} = \begin{cases} \nabla \varphi \cdot \vec{n}, & \vec{n} < 0 \\ 0, & \vec{n} > 0 \end{cases}$
bathWall	p/ρ = 101.3	$\nabla \varphi \cdot \vec{n} = \overrightarrow{U_n} = \begin{cases} \nabla \varphi \cdot \vec{n}, & \vec{n} < 0 \\ 0, & \vec{n} > 0 \end{cases}$

4 Results

The initial mesh sensitivity check with the static mesh scheme and five different mesh sizes of 530, 177, 106, 76 and 59 µm (total number of cells 3000, 11000, 17000, 36400 and 54400 respectively) showed all similar streamline patterns per cycle, pressure and velocity amplitudes and tendencies. Therefore, the solution appeared rather insensitive to the mesh resolution.

The mesh scheme appears to have an influence on the flow feature inside the gap between the ultrasonic horn and the bottom where a test specimen would be placed; while the predicted pressure amplitude and frequency was almost the same as each other, the size and location of the recirculating flow structure was different from each other as shown in Fig. 4. While the static mesh scheme predicted rather a consistent inward flow along the ultrasonic horn surface and therefore a large re-circulating structure residing inside the most of the gap space, the dynamic one predicted a smaller re-circulation flow moving up and down subject to the movement of the ultrasonic horn at near the throat of the gap between the horn and the bottom.

For the single-phase non-cavitating flow case, the pressure was oscillating with a single amplitude in the order of 4.5 MPa at the driving frequency of 19.5 kHz. Reality of such a high negative pressure was in question and a short investigation was made which will be discussed in the next section.

The interchangeable two-phase (cavitating) flow case showed the sub-harmonic cavity fluctuation at a half the excitation frequency. The pressure peaks fluctuated in between 0 and 3.5 MPa at every two cycles. This is shown in Fig. 6 and Fig. 7. The typical pressure peak occurrence and corresponding cavity during the sub-harmonic oscillation period is shown in Fig. 5. The produced cavity appeared very thin. An interesting observation was that there were two travelling vortices in opposite directions each other varying at the same sub-harmonic frequency as the cavity. The vortices appear to confine the boundaries of cavities as they move along the ultrasonic horn tip surface. This may be linked to a driving mechanism of sub-harmonic cavity oscillation in addition to the inertia of the acoustic cavity as suggested by Žnidarčič et al. (2015).

The above cavitating condition simulation was repeated without the turbulence model. The results were very similar with the one with the turbulence model. Thus appears the current problem can be treated in the laminar flow regime.

5 Discussion

While there is not any available experimentation data directly comparable with the current simulation results yet, it appears to show a similar feature as found from other precedent studies, like the sub-harmonic cavity fluctuation.

Regarding the different flow feature with the static mesh scheme, although it had not been expected at first, this was thought as a result from the absence of physical displacement of the solid boundary, which in reality would have played a role of blocking the inward flow during the moving-down phase of the ultrasonic horn rather than allowing the still strong inward flow as predicted. For realistic simulation, the dynamic mesh scheme was decided to be used for the rest of study.

The presence of very strong negative pressure peaks from the single-phase incompressible flow simulation was also in question. To investigate possible cause(s), several more calculations were performed with different boundary conditions; (1) change of ‘bathWall’ patch boundary condition from the far field to a wall, (2) change of the solver to incorporate free surface and gravity. The first case did not have any noticeable influence, which confirms the wall boundary of the current calculation domain can be regarded as the far field. Consideration of the free surface had a significant influence on the pressure peak prediction. The peak was reduced to about 2.9 MPa. However, still the amplitude was thought as too high to be realistic. Finally, the atmosphere patch was forced to oscillate in the vertical direction in accordance to the mass flux through the patch, which was calculated from the volume displacement by the ultrasonic horn movement. In that case, the oscillating pressure amplitude was reduced to the order of 20 % of the given internal pressure (atmospheric pressure) in the fluid domain. The reason of the high negative pressure is thought because of incompressibility of the fluid whereas the outlet (‘atmosphere’ patch) did not allow the fluid to be displaced accordingly.

Finally, observation of the travelling vortices is discussed. As shown in the sequence of images in Fig. 7, they seemed to confine the boundaries of cavities on the surface of the ultrasonic horn tip. Furthermore,

the frequency of such travelling vortices coincided with the sub-harmonic frequency of the cavitation. Therefore, although it is not clear enough yet if this is driving mechanism of the sub-harmonic oscillation of the acoustic super-cavity, it appears they are relevant with the phenomenon at least.

6 Conclusion

In spite of not being able to be supported by any directly comparable experimentation data yet, it appears to show some of important features like the sub-harmonic cavity fluctuation as reported by many other researchers.

There was a finding that may be relevant to a driving mechanism of the sub-harmonic cavity osciallation. It looks clear the travelling vortices behave at the same sub-harmonic frequency as the ultrasound cavitation and have a relevant link with the phenomenon.

Acknowledgements

This work is being performed as a part of a joint research among Lloyds Register, SSPA Sweden AB and DSME to establish a quantitative prediction method for cavitation erosion. Our deep appreciation for their consistent support goes to them and to our colleague, Mr. Artur Lidtke, who willingly shared his experiences with openFOAM and took his time to discuss and give advice.

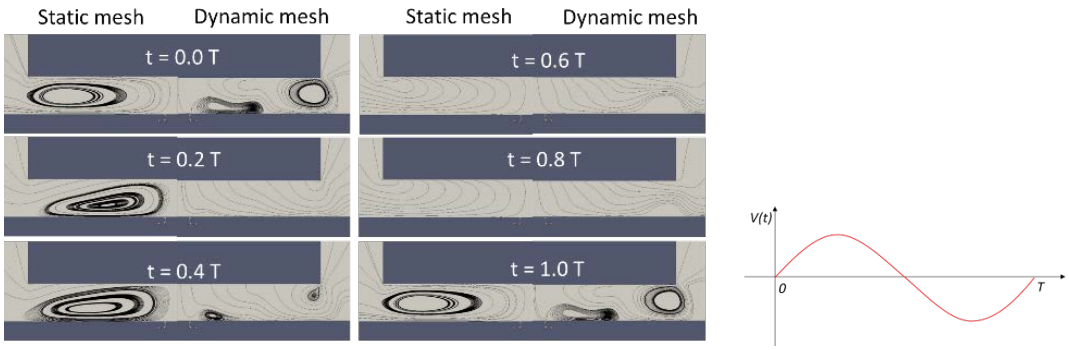

Fig. 4 Streamlines calculated with static and dynamic mesh schemes.

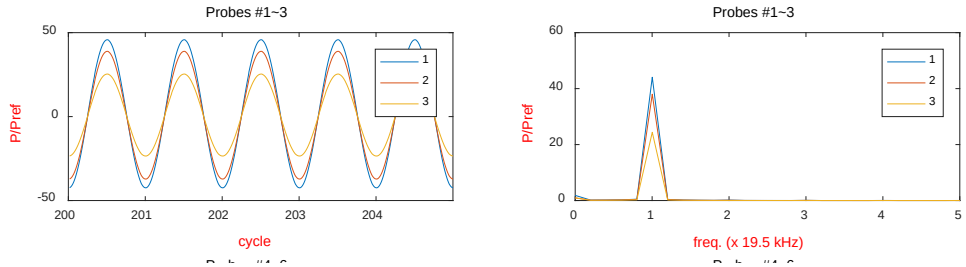

Fig. 5 Sampled time history of pressure pulses (left) and pressure harmonic analysis results (right) for an incompressible single phase flow. Probes #1~3 were located on the bottom of the gap from inside to outer edge of the gap with even spacing. The harmonic analysis results show the pressure peaks occur exactly at the same driving frequency of 19.5 kHz in the case of single-phase incompressible flow.

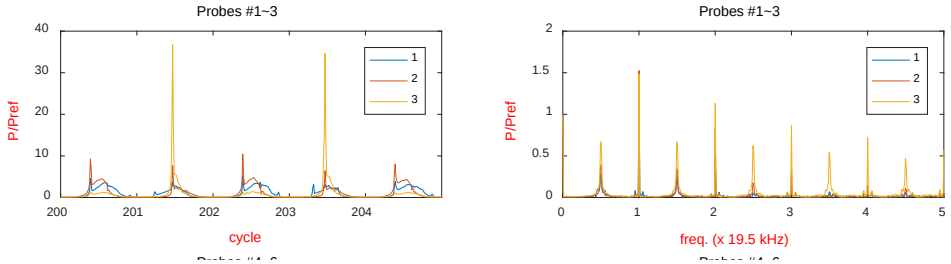

Fig. 6 Sampled time history of pressure pulses (left) and pressure harmonic analysis results (right), which shows strong power leakage over broad range of frequencies and subharmonic pulses at the frequencies corresponding to (n+1)/2 times the driving frequency (n = 0, 1, 2,...).

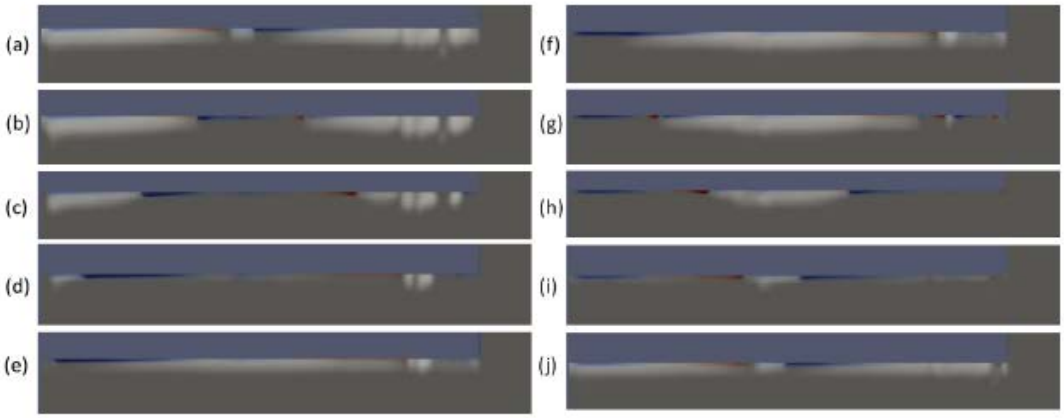

Fig. 7 Sequence of images of VoF and travelling vorticities at 0.2T interval for one sub-harmonic cycle from (a) to (j) (equivalent to the two cycles of the ultrasonic horn tip oscillation in this case). The bluish purple area shows the solid boundary of the ultrasonic horn tip and the grey part of the images show water-filled area. Travelling vortices appear to push the boundaries of cavities as they move along the surface of the ultrasonic horn tip.

References

A. Boorsma, & P. Fitzsimmons. (2009). *Quantification of Cavitation Impacts with Acoustic Emissions Techniques.*7th International Symposium on Cavitation, Ann Arbor, Michigan, USA.

S. Mottyll, & R. Skoda. (2015). Numerical 3D flow simulation of attached cavitation structures at ultrasonic horn tips and statistical evaluation of flow aggressiveness via load collectives. *Journal of Physics: Conference Series, 656*, 012052.

S. Müller, M. Fischper, S. Mottyll, R. Skoda, & J. Hussong. (2013). *Experimental investigation of the cavitating flow induced by an ultrasonic horn*.

T. Vít, S. Mottyll, S. Müller, P. Niederhofer, J. Hussong, S. Huth, . . . P. Novotný. (2014). Analysis of the cavitating flow induced by an ultrasonic horn – Numerical 3D simulation for the analysis of vapour structures and the assessment of erosion-sensitive areas. *EPJ Web of Conferences, 67*, 02078.

A. Žnidarčič, R. Mettin, C. Cairós, & M. Dular. (2014). Attached cavitation at a small diameter ultrasonic horn tip. *Physics of Fluids, 26*(2), 023304.

A. Žnidarčič, R. Mettin, & M. Dular. (2015). Modeling cavitation in a rapidly changing pressure field - application to a small ultrasonic horn. *Ultrason Sonochem, 22*, 482-492.

Modelling Natural Transition on Hydrofoils for Application in Underwater Gliders

Sébastien Lemaire[†,*], **Artur K. Lidtke**[*], **Guilherme Vaz**[†], and **Stephen R. Turnock**[*]

[†]MARIN, 6708 PM Wageningen, NL
[*]Fluid-Structure Interactions Group, University of Southampton, SO16 7QF, UK

1 Introduction

Underwater gliders are a class of autonomous underwater vehicles (AUV) used for long-endurance missions. They employ a buoyancy engine in order to induce vertical motion through the water column and by adopting an appropriate trim angle they propel themselves forward using hydrofoils. The velocities these vessels reach are typically less than $0.5\,ms^{-1}$. Efficiency of their hydrofoils is of course a key factor determining the overall system performance. Therefore, better understanding the nature of transition occurring on these foils is of significant importance for the design of next generation underwater gliders.

Standard turbulence models are known to predict transition onset too early in terms of Reynolds number, mainly because they were first developed with applications to fully turbulent flows in mind (Rosetti et al., 2016). For this reason a range of models designed to predict transition have been introduced in the literature (Van Ingen, 2008).

The aim of this paper is to assess the usefulness of the Local Correlation Transition Model (LCTM, also known as $\gamma - Re_\theta$, Langtry and Menter, 2009), implemented in the finite volume solver ReFRESCO (Rosetti et al., 2016), for application to engineering problems involving laminar and transitional Reynolds number regimes. The study will be focusing on modelling the flow around 3D infinite foils and underwater glider swept hydrofoils to analyse transition to turbulence as well as the nature of the separation bubble. Development of a better understanding of these phenomena will help to achieve a more efficient design in the future.

2 Methodology

2.1 ReFRESCO

ReFRESCO (`www.refresco.org`) is a community based open-usage CFD code for the Maritime World. It solves multiphase incompressible viscous flows using the Navier-Stokes equations, complemented with turbulence models, cavitation models and volume-fraction transport equations for different phases (Vaz et al., 2009).

ReFRESCO is currently being developed, verified and its several applications validated at MARIN (in the Netherlands) in collaboration with many Universities including University of Southampton (Hawkes et al., 2015).

2.2 Local Correlation Transition Model

This transition model was developed by Langtry and Menter, 2009 and has been validated multiple times since its full disclosure (Langel et al., 2016), also in ReFRESCO in Rosetti et al., 2016.

It involves solving the transport equations for turbulent kinetic energy, k, and specific dissipation rate, ω, similar to those presented by Menter et al., 2003. The model also solves two additional equations for intermittency, γ (Eq 1), and Reynolds momentum thickness, Re_θ,

$$\frac{\partial(\rho\gamma)}{\partial t} + \frac{\partial}{\partial x_j}(\rho U_j \gamma) = P_\gamma - E_\gamma + \frac{\partial}{\partial x_j}\left[(\frac{\mu_t}{\sigma_f} + \mu)\frac{\partial \gamma}{\partial x_j}\right], \tag{1}$$

$$P_\gamma = F_{length} c_{a1} \rho S [\gamma F_{onset}]^{0.5} (1 - c_{e1}\gamma). \tag{2}$$

The transport equation for Re_θ converts non local correlations into local variables. In equation 2, F_{onset} and F_{length} control respectively the transition location and its length; these variables are computed from empirical correlations based on Re_θ. The intermittency is then computed to yield the local turbulence state of the flow. The key feature brought by the LCTM is its local aspect.

Because this model adds two transport equations to the set convergence can be more challenging (Rosetti et al., 2016). Moreover, since the formulation is local the sensitiveness to external parameters is increased. Furthermore, because the empirical correlations were determined experimentally, its limits and suitability of application have to be studied with care.

2.3 Simulation set up

Steady and unsteady RANS simulations are first performed on the SD7003 foil section, shown in Fig. 1, using the $k - \omega$ SST model (Menter et al., 2003) with and without the LCTM. This infinite straight foil is set at an angle of incidence of 4° and sees a chord-based Reynolds number of 60,000. The resultant flow features are compared against PIV measurements by Ol et al., 2005

and Burgmann and Schröder, 2008. Moreover, data from ILES simulations by Visbal et al., 2009 and Uranga et al., 2011 are also referred to. Inlet turbulence intensity of 0.1% and eddy viscosity ratio of 50 are used to match the experimental conditions.

Then, steady flow past a swept wing based on the SD8020 foil (Fig. 1) similar to those used on underwater gliders is simulated at a number of angles of attack up to 4 degrees and at a fixed Reynolds number of 60,000. The undertaken analysis entails comparing computed forces to 2D data and analysis of the effect of sweep and tip vortex on transition.

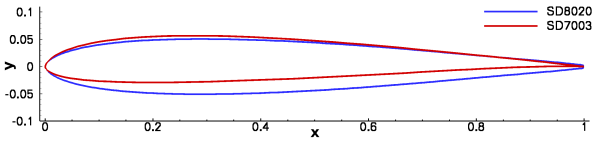

Fig. 1: Foil sections used for validation purposes (Selig, 1995)

2.4 Numerical set up

In all simulations discretisation is performed with the QUICK scheme for the momentum equations and a first order upwind scheme for turbulence and transition equations, both diffusion and discretisation in time uses a 2^{nd} order scheme.

Convergence is guaranteed by infinity norms of residuals below 10^{-7} for steady simulations and below $5{\cdot}10^{-4}$ for unsteady ones. For unsteady simulations the Courant number is kept around 1, time averaging is performed on at least 20 chord based dimensionless times. Because it is a requirement for transition models all generated grid satisfy $y^+ \leq 1$.

2.5 Grid set up

For the SD7003 study a large 3D C-type domain was generated ("L"). In this structured grid (Figure not shown), the inflow and the outflow are at 15 chords from the foil, and the top and bottom boundaries are separated by 32c. To simulate an infinite foil symmetric boundary conditions are set on both span-normal planes.

A grid convergence study has been conducted for this case using five 2D grids with cell counts from 32,000 to 500,000. Eventually, the grid with 130,000 was considered to be the best choice for balancing accuracy and simulation cost as it showed to differ from the finest grid only by 0.082% in terms of lift and 0.82% for drag.

A span size of 0.3 chord was chosen because 3D effects for this test case have been reported to be smaller than 0.2c (Burgmann and Schröder, 2008). Six span resolutions with z^+ from 360 to 1800 were tested but because no evident differences were found between these simulations a span-wise resolution of 15 cells (leading to a z^+ of 1200) was used to obtain the presented results. The resultant 3D mesh has 1,826,000 cells in total.

A second domain with a blockage ratio of 6.5%, the same as in the tests by Burgmann and Schröder, 2008, was prepared ("S"). This is shown in Fig. 2. The span size of the foil was chosen to be 0.3c, the inflow and outflow are respectively at 3c and 6c from the foil, the top and bottom boundaries are separated by 1.25c and simulated as slip walls; the outflow is treated as a pressure boundary condition. The same number of points along the foil was used as for the "L" domain, leading to 64,000 cells per a 2D plan, and 15 cells were used in the span-wise direction (z^+ of 1200). The total cell count in 3D was 895,000 elements.

For an underwater glider application a symmetric foil is needed, thus the second study is based on the SD8020 foil (Fig. 1) from Selig, 1995. The geometry has been modelled with a round trailing edge to be more representative of a real foil. A 2D O-grid with a radius of 14 chords and 32,000 cells is used (mesh not shown).

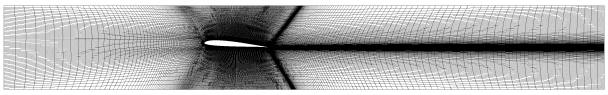

Fig. 2: Small domain (S) generated for the airfoil SD7003 following Burgmann and Schröder, 2008 experimental set up

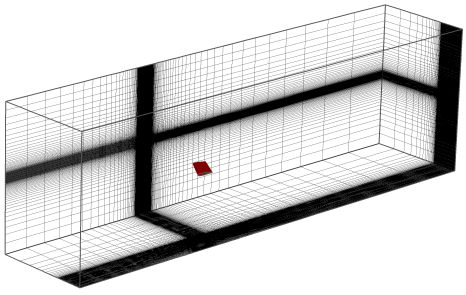

Fig. 3: Computational domain for the swept wing

The swept wing is based on the SD8020 foil with a round trailing edge, sweep angle of 35°, taper ratio of 0.9, and a span of 1.6c. The generated domain (Fig. 3), is 27c long, 7.7c high and 6c wide. A 5M cells structured hex mesh is used, with 125 cells

placed across the span and 170 along the chord of the foil. The wing is attached to one side of the domain simulated by a symmetry boundary condition, each of the remaining sides is modelled by a slip wall and the outflow is a pressure boundary condition.

3 Results and Discussion

3.1 Infinite straight foil

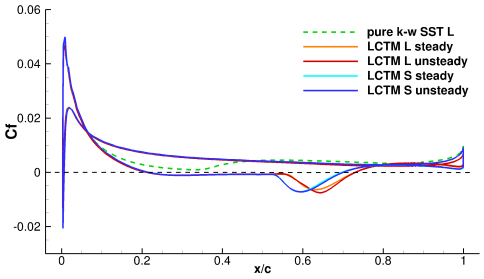

(a) Friction coefficient

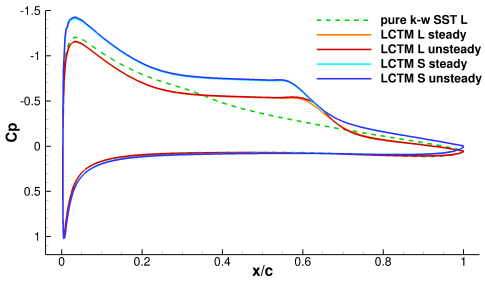

(b) Pressure coefficient

Fig. 4: Surface coefficients for simulations of the SD7003

According to Table 1, the present model shows similar trends to the measurements in terms of predicting the location of separation, which may also be seen in Fig. 5, although the experimental data shows a large amount of scatter and differences between various facilities. Onset of transition estimates from the present simulations, made using normalised Reynolds Stress of 0.001, analogously to how the analysis was made in the experimental studies, fall within the range described by the experimental studies. Reattachment is predicted at $x/c \approx 0.7$, which is slightly further downstream of the measured location.

Furthermore, the pure $k-\omega$ SST simulations trigger transition earlier than the LCTM, around $x_t/c \approx 0.3$. Consequently, they do not predict the presence of a separation bubble (Fig. 5a). It is also worth noting that the high blockage ratio of the small domain ("S") has a significant impact on the predicted force coefficients, leading to higher lift and drag (Fig. 4b). It does not, however, appear

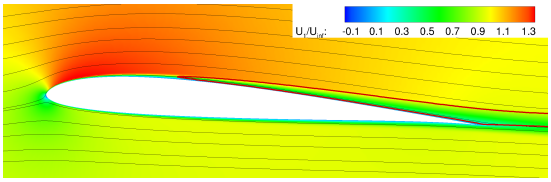

(a) pure $k-\omega$ SST

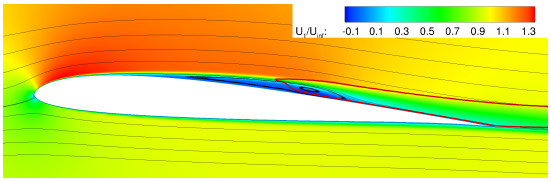

(b) LCTM

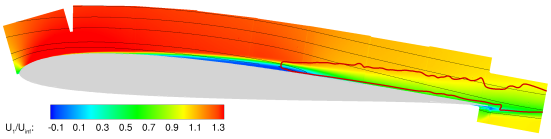

(c) Experiment TU-BS, Ol et al., 2005

Fig. 5: Velocity field around the foil SD7003, transition is shown by the red line (normalised Reynolds stress of 0.001)

to affect the nature of the separation bubble and downstream vortices.

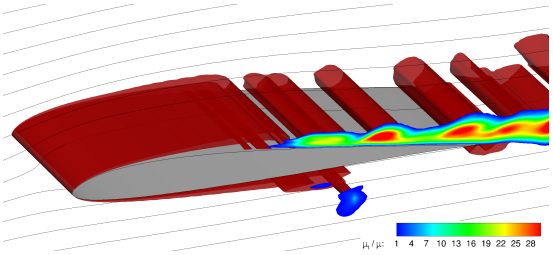

Fig. 6: Instantaneous surface of Q criterion around the SD7003 foil (in red), $\mu_t/\mu \geq 1$ displayed in the foreground to visualise the onset of transition for the LCTM simulation

Moreover, steady and unsteady simulations yielded similar results because turbulence is not solved directly and only modelled, and therefore the flow does not experience much unsteadiness. This is one of the fundamental and well understood limitations of the RANS approach. Experimental data by Burgmann and Schröder, 2008 show a lot of small flow features and unsteadiness, whereas the LCTM simulations predict only large drifting vortices with no 3D effects (Fig. 6). Moreover, these large vortices drift downstream faster and are created with a higher frequency compared to what was reported in the experiments, as seen Table 1.

Table 1: Integral quantities of SD7003 compared with experiments from Burgmann and Schröder, 2008 and Ol et al., 2005, XFOIL and ILES simulations (Visbal et al., 2009 and Uranga et al., 2011)

Type	Grid	C_L	C_D	Sep (x_s/c)	Trans (x_t/c)	Reattach (x_r/c)	vortex freq $(f_v \cdot c/u_{inf})$	vortex drift vel (u_v/u_{inf})
steady pure $k-\omega$ SST	L	0.561	0.0194	no	0.304	no		
steady pure $k-\omega$ SST	S	0.723	0.0214	no	0.290	no		
steady LCTM	L	0.5807	0.0239	0.2085	0.529	0.7299		
unsteady LCTM	L	0.5851	0.0239	0.2075	0.523	0.7307	5.2	0.675
steady LCTM	S	0.7357	0.0272	0.2121	0.503	0.6971		
unsteady LCTM	S	0.7401	0.0267	0.2132	0.496	0.6967	5.5	0.698
Visbal (ILES)				0.23	0.55	0.65		
Uranga (ILES)		0.6122	0.0241	0.21	0.53	0.67		
XFOIL		0.625	0.019	0.21	0.57	0.59		
Burgmann				0.390	0.470	0.515	7.8	≈0.55
IAR				0.33	0.57	0.63		
TU-BS				0.30	0.53	0.62		
AFRL				0.18	0.47	0.58		

The drift velocity has been computed using cross correlation of the velocity field in two mesh points on the vortex path.

Finally, ILES results by Visbal et al., 2009 and Uranga et al., 2011 (Table 1) agree quite well with the present LCTM simulations in terms of separation bubble characteristics and force coefficients.

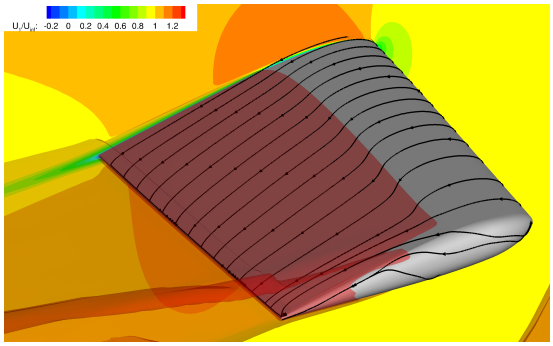

(a) pure $k-\omega$ SST

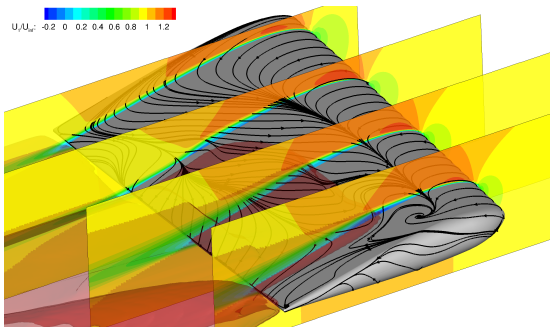

(b) LCTM

Fig. 7: Wall shear stress on the swept wing, stream wise velocity and $\mu_t/\mu = 1$ in red (turbulence onset) at an angle of attack of 4°.

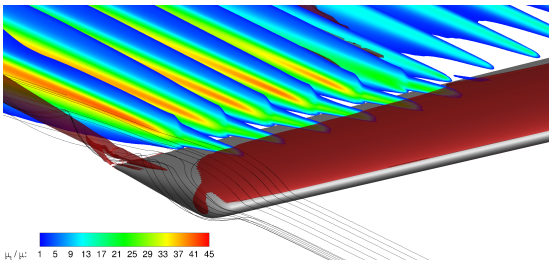

Fig. 8: Iso-surface of the Q criterion at the tip of the swept wing (in red) and $\mu_t/\mu \geq 1$ slices (showing turbulent flow location) from the LCTM simulation at an angle of attack of 4°.

3.2 Underwater glider swept wing

Fig. 7a shows wall shear stress on the wing as computed using the pure $k-\omega$ SST model at an angle of attack of 4°. Similarly to the SD7003 predictions, this simulation did not produce a separation bubble and the flow transitioned to turbulent at $x_t/c \approx 0.35$, as estimated using the eddy viscosity.

Fig. 7b presents the same data but computed using the LCTM. One may note that the root of the foil has been predicted to be subject to fully laminar flow and no separation bubble has been computed. At mid-span, however, the flow may be seen to separate at approximately 30% of chord, reattaches at $x/c \approx 0.75$ and becomes turbulent at $x/c \approx 0.45$, similarly to the 2D sections investigated before. This span-wise variation of the flow regime may also be seen in skin friction and pressure distributions sampled on the foil surface and shown in Fig. 9.

Finally, the tip of the wing has been predicted

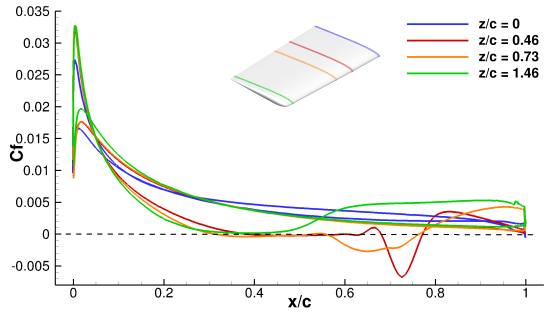

(a) Skin friction coefficient

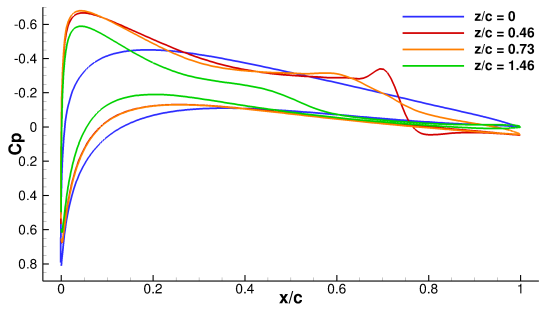

(b) Pressure coefficient

Fig. 9: Surface coefficients at various span locations from the LCTM simulation of the swept wing at an angle of attack of 4°.

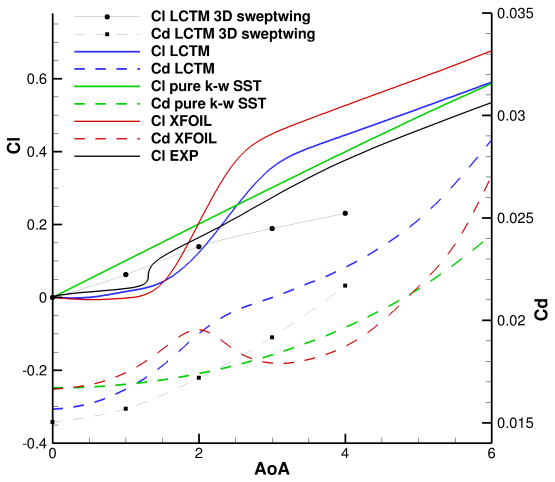

Fig. 10: Force coefficients at various angles of attack for LCTM and pure $k-\omega$ SST simulations of the swept wing and two-dimensional SD8020 foil. Experimental measurements and XFOIL predictions for the 2D scenario are also shown

to generate a substantial tip vortex (Fig. 8). This also has been observed to interact with the laminar separation, leading to a complex flow pattern on the suction side close to the tip, as seen in Fig. 7.

It is important to understand the exact outcome of three-dimensional effects on the performance of the wing. For this reason, the force coefficients of the swept foil are compared against 2D data obtained for the SD8020 using the both the LCTM and pure $k-\omega$ SST models in Fig. 10. It is noted that 2D LCTM and XFOIL simulations show a delayed increase of the lift compared to the experimental data. On the other hand, the pure $k-\omega$ SST simulations produce almost a linear curve for the lift, indicating that no laminar separation is predicted. For angles of attack above 3° the LCTM simulations tend to predict a linear relation between lift and the angle of attack which has also been reported in the experiments. All of the predictions consistently over estimate the lift coefficient but the LCTM appears to stand in a better agreement with the measured performance data than XFOIL. Noticeably, the lift coefficient of the swept wing appears to follow a linear trend with an increasing angle of attack, unlike the 2D predictions for the same foil section.

4 Concluding remarks

Overall, it has been noted that the use of the LCTM significantly improves the accuracy of predictions made for hydrofoils at Reynolds numbers below 100,000 in comparison to more standard RANS models. The key flow features, such as the laminar separation, transition taking place on top of the separation bubble, and reattachment have all been predicted with reasonable accuracy.

The considered SD7003 foil has been reported to experience substantial amounts of unsteady flow. Reportedly, it is possible to capture these features relatively well using advanced turbulence modelling techniques, such as ILES. The LCTM does not, however, solve the turbulent motions and thus even when a three-dimensional simulation is performed the unsteadiness is not captured well.

The LCTM model appears to account for the three-dimensional nature and the flow which has been predicted to significantly affect transition on the swept glider wing. However, because the RANS approach is used and due to the empirical relationships assumed, the influence of the tip vortex and span-wise instabilities may not be very well computed in detail. Overcoming this directly would require the turbulence to be resolved and not modelled, for instance through the use of methods such as LES or DNS, which is not yet feasible at practical Reynolds numbers. Further studies involving complex geometries are therefore necessary to truly understand the limitations of the

present model in this context and will likely need to be supported by dedicated experimental observations. Nonetheless, the acquired data has been seen to agree with experiments well enough to allow confident application to engineering problems.

Due to its sweep, the underwater glider wing has been predicted to experience a significant amount of span-wise flow running from the root towards the tip. The tip vortex has also been computed to act to induce circulation around the tip and thus induces local span-wise velocities, particularly on the suction side. The combination of the two phenomena disturbs the flow and affects the transition onset. Thus, modifying the tip shape to reduce the adverse impact of the tip vortex and controlling the span-wise sweep and chord distributions to encourage laminar flow are likely the two most important design decisions.

Although not considered here, the design of the joint between the wing and the glider hull may be expected to substantially affect the amount of laminar flow near the root of the foil. This may in turn induce turbulent flow over a much larger area of the appendage than what was predicted here for a simply supported foil. This highlights the importance of carefully analysing local design features when dealing with natural laminar flow.

Acknowledgements

The authors would like to acknowledge the use of ReFRESCO 2.3.0 and the Iridis 4 supercomputer of the University of Southampton for all of the presented simulations. The presented work has been funded as a part of the BRIDGES Project (`http://www.bridges-h2020.eu`). This Project has received funding from the European Unions Horizon 2020 research and innovation programme under grant agreement No 635359.

References

Burgmann, S. and Schröder, W. (2008). Investigation of the vortex induced unsteadiness of a separation bubble via time-resolved and scanning PIV measurements. *Experiments in fluids*, 45(4):675–691.

Hawkes, J. N., Turnock, S. R., Vaz, G., Cox, S. J., and Philips, A. B. (2015). Chaotic linear equation-system solvers for unsteady CFD. *VI International Conference on Computational Methods in Marine Engineering MARINE 2015*.

Langel, C. M., Chow, R., and Van Dam, C. C. P. (2016). A comparison of transition prediction methodologies applied to high Reynolds number external flows. In *54th AIAA Aerospace Sciences Meeting*, page 0551.

Langtry, R. B. and Menter, F. R. (2009). Correlation-based transition modeling for unstructured parallelized computational fluid dynamics codes. *AIAA journal*, 47(12):2894–2906.

Menter, F., Kuntz, M., and Langtry, R. (2003). Ten years of industrial experience with the SST turbulence model. *Turbulence, heat and mass transfer*, 4(1).

Ol, M. V., McAuliffe, B. R., Hanff, E. S., Scholz, U., and Kähler, C. (2005). Comparison of laminar separation bubble measurements on a low Reynolds number airfoil in three facilities. *AIAA paper*, 5149(1):2005.

Rosetti, G. F., Vaz, G., Hawkes, J., and Fujarra, A. (2016). Modeling transition using turbulence and transition models for a flat plate flow: Uncertainty, verification and sensitivity. *Journal of Fluids Engineering*.

Selig, M. S. (1995). *Summary of low speed airfoil data*, volume 1. SoarTech.

Uranga, A., Persson, P.-O., Drela, M., and Peraire, J. (2011). Implicit large eddy simulation of transition to turbulence at low Reynolds numbers using a discontinuous Galerkin method. *International Journal for Numerical Methods in Engineering*, 87(1-5):232–261.

Van Ingen, J. (2008). The e^N method for transition prediction. historical review of work at TU Delft. In *38th Fluid Dynamics Conference and Exhibit*, pages 23–26.

Vaz, G., Jaouen, F., and Hoekstra, M. (2009). Free-surface viscous flow computations: Validation of URANS Code FreSCo. In *ASME 2009 28th International Conference on Ocean, Offshore and Arctic Engineering*, pages 425–437. American Society of Mechanical Engineers.

Visbal, M. R., Gordnier, R. E., and Galbraith, M. C. (2009). High-fidelity simulations of moving and flexible airfoils at low Reynolds numbers. *Experiments in Fluids*, 46(5):903–922.

Simulation validation of a tidal turbine : comparison to Southampton's experiment

Corentin Lothode[*,†], Didier Lemosse[†], Emmanuel Pagnacco[†], Eduardo Souza[†], Augustin Hugues[*], Yann Roux[*]

[*]K-Epsilon, France, corentin@k-epsilon.com

[†]LOFIMS, France, eduardo.souza@insa-rouen.fr

1 Introduction

In this report, the mean power and thrust are compared between CFD computations and experimental data. The parameters are the flow speed, the blade pitch angle and the rotation speed. Then a surrogate model with a Latin Hypecube Sampling is used to find the optimal pitch angle and rotation speed.

The experiment used is the one made by Bahaj et al. 1 and was the first to be performed on tidal turbines. It contains many results for different pitch and is very useful to compare against. Though the experiment has a high blockage correction (up to $\simeq$ 18%), it is well documented and provide much insight. Many people used this experiment to validate codes, Blade Element Momentum Theory (BEMT) for example in 2.O Other experiments exist today but will not be used in this paper (Ifremer 3, Liverpool 4, 5, Manchester6). BEMT is a good approach to assess the performance of one turbine, but it fails to perform for multiple turbines.

To avoid this problem, other approach has been developed such as the Vortex Lattice Method (VLM) in 7. Their main focus is the wake of the turbine to study the interaction between two or more turbines 8. Their results are good until stall which is expected since their method force the flow to be attached until the trailing edge. Later 9 included turbulence.

Attempts to use Computational Fluid Dynamics (CFD) on wind or tidal has been performed in the past. To avoid too much computational efforts, many authors modeled the behavior of the turbine instead of resolve the full geometry. For instance, 10 has used Large Eddy Simulation (LES) with the turbine replaced by an approximated model of a concentrated drag force to study the wake development. Also using an approximated model for the turbine, 11 performed a LES computation using an actuator disk.

Fully resolved blade geometry CFD computations are computationaly expensive, but can give many more insight about the flow behavior and force distribution along the blade. 12 compared $k-\omega$ SST, Launder-Reece-Rodi turbulence model (LLR) and LES on the 20° pitch angle case of 1 as an unsteady simulation, including the mast and a simplified geometry of the cavitation tunnel. The results are very interesting but lack other pitch angles to further validate the models which is what we are adressing in this paper.

Name	Property	Name	Property
u	velocity	p	pressure
V	inlet velocity (m/s)	ρ	density of the fluide (kg/m^3)
r	radius of the turbine (m)	$S = \pi r^2$	tidal turbine area (m^2)
Q	turbine torque (Nm)	T	turbine drag (N)
Ω	turbine rotation speed (rad/s)	$TSR = \frac{\Omega r}{V}$	tip speed ratio
$C_P = \frac{P}{\frac{1}{2}\rho V^2}$	pressure coefficient	$C_p = \frac{Q \times TSR}{\frac{1}{2}\rho V^2 r S}$	power coefficient
$C_t = \frac{T}{\frac{1}{2}\rho V^2 S}$	thrust coefficient		

Table 1: Notations used

2 Description of the experiment

The experiment is fully described in 1. The tests were carried out in a cavitation tunnel at Southampton Institute (see FIGURE 1).

The rotor diameter of the turbine is 800mm. It was chosen as a compromise between maximising Reynolds number and not inducing too much tunnel blockage correction. The blockage correction is based on an actuator disk model of the flow through the turbine in which the flow is presumed to be uniform across any cross section

Fig. 1: Photo of the experiment

Pitch angle (°)	Flow speed
15°	1.40 m/s
20°	1.73 m/s
25°	1.54 m/s
27°	1.30 m/s
30°	1.54 m/s

Table 2: Pitch angle and flow speed corresponding

of the stream tube enclosing the turbine disc 13. For example, with a single rotor and a thrust coefficient of 0.8, the corrections amounted up to 18% decrease in power coefficient and 11% decrease in thrust coefficient for the cavitation tunnel and up to 8% and 5% decrease, respectively, for the towing tank.

The blades are made out of the NACA 63-8xx serie. The distribution of pitch and thickness can be found in 1. We kept the values used in 1 meaning that the pitch distribution is in fact the pitch of the element at radius 80mm (15° means taking the blade as the original blade pitch, 20° means imposing 5° pitch to the blade). Many tests were performed : varying the tip immersion, the blade pitch angle and yaw angle. In this study, mainly 5 batch are of interest for this study and are reported in TABLE 2.

3 Description of the simulation

The solver is FINE/Marine™which is distributed bu NUMECA International. It is developed by the LHEEA laboratory. It solves the Reynolds-Averaged Navier-Stokes Equations in a strongly conservative way. It is based on the finite volume method and can work on structured or unstructured meshes with arbitrary polyhedrons 14. The velocity field is obtained from the momentum conservation equations and the pressure field is obtained according to the incompressibility constraint. The pressure-velocity coupling is obtained using the SIMPLE algorithm. All the variables are stored in a cell-centered manner. Volume and surface integrals are evaluated according to second order schemes. The time integration is an explicit scheme of order two. At each time step, an internal loop is performed (called a non-linear iteration) associated with a Picard linearization in order to solve the non-linearities of the Navier-Stokes equations.

The equations are formulated according to the Arbitrary Lagrangian Eulerian paradigm and therefore can easily take into account mesh movements. In order to be able to rotate the geometry, we are using the sliding interface capability 15 of ISIS-CFD (see FIGURE 2b). Several turbulence models are implemented in ISIS-CFD. The turbulence models are here to avoid resolving completely the Navier-Stokes equations. In the case of LES, a low-pass filter is used to avoir resolving the smallest scale in space and time. For RANSE an additional viscosity term called eddy viscosity ν_t allows to use even less discretise grids and bigger time steps. In this study, we used the RANSE using the SST-$k-\omega$ model 16.

The computational domain is made of a box of width $L_x = 4m$, length $L_y = 6m$ and height $L_z = 4m$ (see FIGURE 2a). The size of the cylinder subdomain which is rotating is $L'_y = 0.6m$ and $r' = 0.6m$. The sides and outlet boundary condition use a zero-gradient boundary condition for both velocity and pressure. The inlet boundary condition is an imposed velocity of u_∞. The rotation velocity is added to the cylinder through the ALE formulation. The mesh has 4.1 million cells. Refinement boxes were placed to capture the tip vortices and the wake correctly.

4 Results discussion

For a blade pitch angle of 15°, the blade sections show a higher angle of attack compared to the blade pitch angle of 20°. As stated previously, the blade pitch angle of 20° is the design angle of the turbine. In other words, it mean that the blades apparent angle of attack is higher than for the design pitch angle of 20° by 5°. The apparent angle of attack is reduced by having an higher rotation. Hence to have the expected flow behaviour, the turbine will have to rotate faster than the design rotation speed in order to compensate the blade pitch angle. The pressure plots are showing the expected behaviour. The flow around the blade is fully separated at a TSR of 3 and still partially detached for TSR from 4 to 5. For a TSR ranged from 4.5 to 5.5, the error observed between the experimental data and the simulation is about 5% for the C_p and 2% for the C_t. Outside this range, the error is bigger, especially for high TSR where the C_p drops a lot faster than for the computation. The power

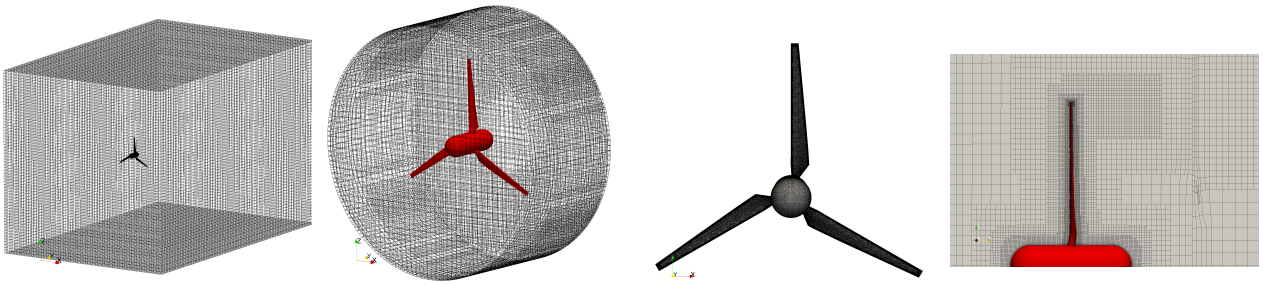

(a) View of the computational domain (b) View of the sliding interface (c) View of the surface mesh (d) Cut of the volume mesh

Fig. 2: Different views of the fluid mesh

coefficient by section shows that all the blade is propulsive for TSR from 4 to 6. For TSR 7 and 8, the tip starts to generate more drag than it generates propulsion. The observed C_p peak is observed for a TSR of 5, which is the result for the experiment, only the value differs (0.4626 for the simulation, 0.44 for the experiment).

For the design pitch angle of 20°, the flow is only partially detached for a TSR of 3 on the upper part of the blade, and fully separated for the other half of the blade. Some detached flow can still be seen for TSR up to 4.5, but is limited to a small area of the balde. The error made between the experimental and the simulation results is very small (about 1% for both C_p and C_t). It is probably due to an accurate blocage correction, and a nice flow behavior around the blades. The power coefficient by section shows that the whole blade is propulsive for all tested TSR, showing that the design is correct. The C_p peak is not as clear as for an angle of 15°, and occurs at a TSR of 5.5 (C_p = 0.4533), although the value obtained for a TSR of 5 and 6 are really close (0.4450 and 0.4531 respectively).

Blade pitch angles of 25° is starting to show a significant loss in term of power spike, and it is even worse for blade pitch angles of 27° and 30°. For the angle of 25°, the flow behaviour is similar to the blade pitch angle of 20° with only the lower third part of the blade showing separation. For blade pitch angles of 27° and 30°, this separation is even lower. For blade pitch angle of 30°, the flow starts to separate at the tip, on the front side. The difference observed between the simulation and the experiment is only significant for the blade pitch angle of 30°, otherwise the agreement is good (less than 5% difference). For blade pitch angles of 25°, 27° and 30°, the C_p peakes at a TSR of 5, 4 and 4 respectively, with a C_p of 0.3491,0.3012 and 0.2391. The power coefficient by section has progressive behaviour, the higher the blade pitch angle is, the faster the tip part of the blade stops generating power and starts to be counterproductive.

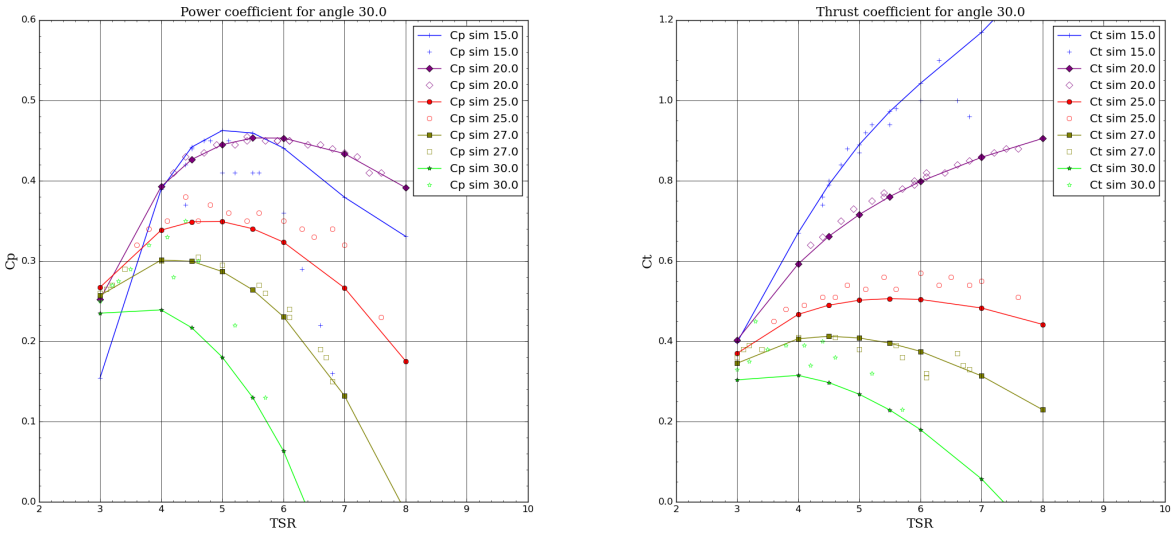

(a) Power coefficients for all angles (b) Thrust coefficients for all angles

5 Optimization of two parameters (TSR and pitch)

The goal is to optimize the power coefficient with two parameters (TSR and pitch). The first thing is to generate the couple of parameters in order to use a maximum of space. For this, a Latin Hypercube Sampling algorithm is used, this algorithm is base on the principle of the latin square, then it is extended to more dimensions. (The principle of the latin square, is that you plan is divided in square, and there one and only one value in each rows and each columns). A good sampling of the space is important, because we will see after that the evolutionary algorithm will have good results only on the area define by the sampling points, beside this area, the results are false. Scripts automatically mesh and setup the simulation of all the set of parameters obtained during the sampling.

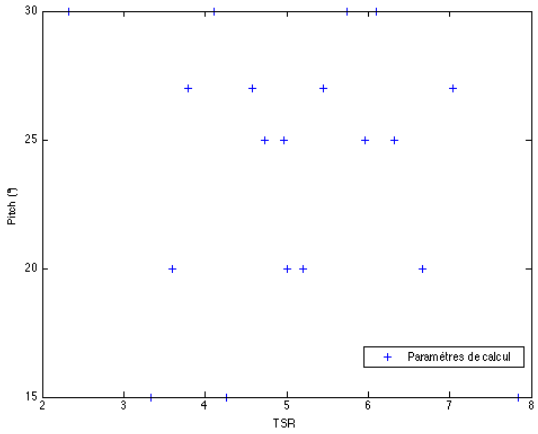

(a) Couple of values obtain with LHS algorithm

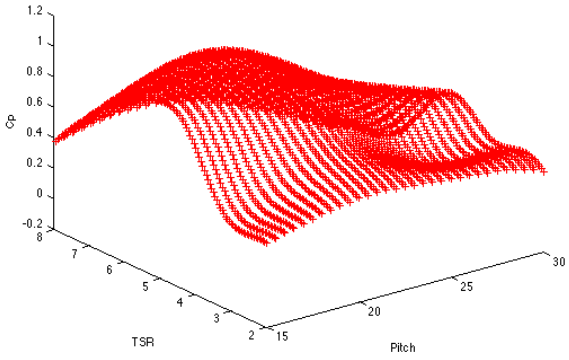

(b) Response Surface from Dakota

We then obtain a power coefficient for each couple (TSR, pitch), and from this we use a response surface method based on a Gaussian process 17. The response surface allows to use an optimisation algorithm on it without having to re-run computationaly expensive simulation., Here, the optimization of the power coefficient values are calculated with an evolutionary algorithm.

The figure 4b shows the surface obtained for the turbine. We have now a continuous surface, with only 20 couples of parameters at the beginning. The best parameters otbained through this process are 19.5° for the pitch and a TSR of 5.85. The calculation with those two optimum parameters shows an error of 7% between the calculation and the value on the surface. From this, an iterative process can be run by adding the new point to the set of parameters to obtain a new response surface and compute a new set of optimum parameters. After a few iterations, the optimum set of parameters shoud be found.

Conclusion

CFD results of a tidal turbine are shown for various conditions and are compared to experimental data. The results of the simulations show a very good agreement with the experiments. From these preliminary results, an optimisation methodology is developed with a surface response method coupled to a genetic algorithm. These initial results are promising and a follow up study, optimizing the reliability of the turbine subject to random current speeds and directions or the dynamic response of the blades with fluid-structure interaction would be interesting to pursue.

References

[1] AS Bahaj, AF Molland, JR Chaplin, and WMJ Batten. Power and thrust measurements of marine current turbines under various hydrodynamic flow conditions in a cavitation tunnel and a towing tank. *Renewable energy*, 32(3):407–426, 2007.

[2] WMJ Batten, AS Bahaj, AF Molland, JR Chaplin, Sustainable Energy Research Group, et al. Experimentally validated numerical method for the hydrodynamic design of horizontal axis tidal turbines. *Ocean Engineering*, 34(7):1013–1020, 2007.

[3] P Mycek, B Gaurier, G Germain, G Pinon, and E Rivoalen. Experimental study of the turbulence intensity effects on marine current turbines behaviour. part i: One single turbine. *Renewable Energy*, 66:729–746, 2014.

[4] SC Tedds, Ieuan Owen, and RJ Poole. Near-wake characteristics of a model horizontal axis tidal stream turbine. *Renewable Energy*, 63:222–235, 2014.

[5] TA de Jesus Henriques, SC Tedds, A Botsari, G Najafian, TS Hedges, CJ Sutcliffe, Ieuan Owen, and RJ Poole. The effects of wave–current interaction on the performance of a model horizontal axis tidal turbine. *International Journal of Marine Energy*, 8:17–35, 2014.

[6] E Fernandez-Rodriguez, TJ Stallard, and PK Stansby. Experimental study of extreme thrust on a tidal stream rotor due to turbulent flow and with opposing waves. *Journal of Fluids and Structures*, 51:354–361, 2014.

[7] G Pinon, P Mycek, G Germain, and E Rivoalen. Numerical simulation of the wake of marine current turbines with a particle method. *Renewable Energy*, 46:111–126, 2012.

[8] P Mycek, B Gaurier, G Germain, C Lothode, G Pinon, and E Rivoalen. Numerical and experimental characterisation of interactions between two marine current turbines. *Revue Paralia*, 6, 2013.

[9] C Carlier, G Pinon, B Gaurier, G Germain, and E Rivoalen. Numerical and experimental study of elementary interactions in marine current turbines array. In *11th European Wave and Tidal Energy Conference (EWTEC)*, 2015.

[10] A Jimenez, A Crespo, E Migoya, and J Garcia. Advances in large-eddy simulation of a wind turbine wake. In *Journal of Physics: Conference Series*, volume 75, page 012041. IOP Publishing, 2007.

[11] M Calaf, C Meneveau, and J Meyers. Large eddy simulation study of fully developed wind-turbine array boundary layers. *Physics of Fluids (1994-present)*, 22(1):015110, 2010.

[12] I Afgan, J McNaughton, S Rolfo, DD Apsley, T Stallard, and P Stansby. Turbulent flow and loading on a tidal stream turbine by les and rans. *International Journal of Heat and Fluid Flow*, 43:96–108, 2013.

[13] MJ Barnsley and JF Wellicome. Final report on the 2nd phase of development and testing of a horizontal axis wind turbine test rig for the investigation of stall regulation aerodynamics. carried out under etsu agreement e. *carried out under ETSU Agreement E. A*, 5, 1990.

[14] J Wackers, B Koren, HC Raven, A Van der Ploeg, AR Starke, GB Deng, P Queutey, M Visonneau, T Hino, and K Ohashi. Free-surface viscous flow solution methods for ship hydrodynamics. *Archives of Computational Methods in Engineering*, 18(1):1–41, 2011.

[15] P Queutey, G Deng, J Wackers, E Guilmineau, A Leroyer, and M Visonneau. Sliding grids and adaptive grid refinement for rans simulation of ship-propeller interaction. *Ship Technology Research*, 59(2):44–57, 2012.

[16] FR Menter, M Kuntz, and R Langtry. Ten years of industrial experience with the sst turbulence model. *Turbulence, heat and mass transfer*, 4(1), 2003.

[17] Anthony A Giunta, Laura P Swiler, Shannon L Brown, Michael S Eldred, Mark D Richards, and Eric C Cyr. The surfpack software library for surrogate modeling of sparse irregularly spaced multidimensional data. In *11th AIAA/ISSMO multidisciplinary analysis and optimization conference, AIAA*, pages 1708–1736, 2006.

Influence of grid setup on the prediction of hydrofoil cavitation

Carlo Negrato[*†], Thomas Lloyd[†], Tom van Terwisga[Ш], Rickard Bensow[*]
[*]Chalmers, Gothenburg/Sweden; [Ш]MARIN, [†]MARIN Academy, Wageningen/Netherlands.
negrato@chalmers.se

1 Introduction

The prediction of cavitation is of large interest for the design of ship propellers. Cavitation influences the propeller efficiency and causes undesired phenomena such as noise, vibrations and erosion. While potential flow solvers are routinely used for propeller design, viscous CFD calculations are used when a higher fidelity is needed. Within a finite volume framework, the flow domain is subdivided into grid cells and the governing equations are solved numerically in every cell. Essentially two approaches are possible to discretise the domain, with structured or unstructured meshes. In the former case, it is always possible to construct a mapping function between the physical grid and a uniform cartesian grid. In the unstructured mesh there is not such a correspondence. A structured mesh is easier to handle for a numerical solver, but for complex geometries it becomes difficult to generate. The size and quality of the mesh affect the quality of the flow solution. The objective of this work is to evaluate the effect of two different grid types when they are used to simulate cavitating flow using an unsteady Reynolds averaged Navier-Stokes (RANS) solver. The test case chosen is a 2D NACA0015 profile at 6 degrees angle of attack, confined in a water tunnel. Many numerical studies on the same test case are found in literature, e.g. Hoekstra (2011), Yakubov et al. (2015), and experimental tests, Arndt et al. (2000). After some preliminary wetted flow computations, which aim to investigate the numerical uncertainty, the main part of this work is a comparison of cavitating flow dynamics predicted with a structured and an unstructured mesh.

2 Methodology

2.1 Flow solver

The viscous flow solver ReFRESCO is used (`http://www.refresco.org/`). Unsteady RANS simulations of incompressible flow are performed. The $k - \sqrt{k}L$ two-equation model is used for turbulence closure, Menter et al.(2006), while the QUICK scheme is chosen for the convection term in the momentum equation. The time integration is performed using a first-order backward Euler scheme. To model multiphase flows, ReFRESCO implements a Volume of Fluid (VoF) approach. Mixture density and mixture viscosity are entered in the governing mass and momentum equations and an additional transport equation for the vapor volume fraction α_v is added, which includes source terms for evaporation and condensation. The source terms are computed by means of a modified version of the cavitation model of Sauer (2000). Here the concentration of nuclei is set to $n_0 = 10^8$ (100 particles per cm^3).

2.2 Test case

For the NACA0015 foil a chord length of $c = 0.2\,m$ was chosen and the origin of the axis is set at the center of gravity, at a relative chordwise position of 0.3086. The foil trailing edge is rounded. The water tunnel has a height of $2.85c$ and the domain extends $2c$ upstream of the leading edge and $4c$ downstream of the trailing edge; the computations are 2D (a nominal width w of one chord is set) and the inflow velocity is $6\,m/s$. The water properties $\rho_l = 998\,kg/m^3$, $\mu_l = 1.002 \times 10^{-3}\,kg/ms$ lead to a Reynolds number based on the chordlength of $Re = 1.2 \times 10^6$. The vapor density is $\rho_v = 0.024\,kg/m^3$. Figure 1 depicts schematically the domain size, the boundary conditions and the location of a pressure probe on the tunnel ceiling, indicated by a cross at $x = 0.5c$.

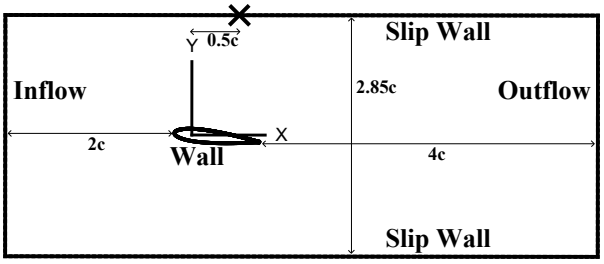

Fig. 1: Domain, boundary conditions, reference system and location of the pressure probe.

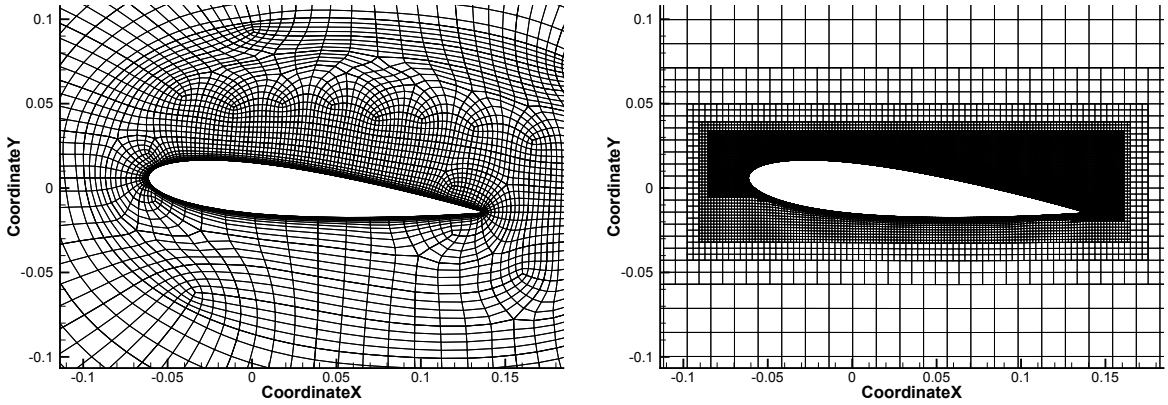

Fig. 2: Overview of the block-structured GridPro grid and the unstructured Hexpress grid.

2.3 Grid design

Two sets of grids were generated using the commercial packages GridPro® and Hexpress®. The former is based on a multi-block structured topology with nested refinement boxes at the foil suction side; the latter gives an unstructured grid which is aligned with the main coordinate axis, except in the wall region where additional flow-aligned 'boundary' layers are inserted. The grids were designed to have a good flow resolution at the suction side, where cavitation develops, without excessively increasing the number of grid cells in the whole domain. As a result, the number of cell nodes at the suction side is larger than the number of nodes at the pressure side. Figure 2 shows a close-up of the two (coarse) grids: the Hexpress one shows hanging nodes at the edges of the refinement regions. Furthermore, the coarsening towards the farfield is sharper than observed in the GridPro mesh. For the estimation of the numerical uncertainty a set of geometrically similar grids is preferred (i.e. the grid properties -skewness,orthogonality,etc.- should remain the same and the refinement ratio should be constant in the domain). This is achieved efficiently in GridPro by coarsening a fine grid with a constant factor, Kerkvliet (2013). In Hexpress it is more difficult to obtain geometrical similarity: a good similarity is achieved far from the foil and in close proximity of the wall. However, in the transition region between the wall layers and the outer grid, similarity is not guaranteed.

Table 1 lists the details of the grid sets. Effort was put into generating grids with a comparable number of cells. The boundary layer is fully resolved: the average value of y_1^+, as resulting from wetted flow calculations, is below one for all grids, expect for G1. A comparison of the two grid types reveals smaller average y_1^+, maximum y_1^+ and standard deviations for the unstructured grids.

Table 1: Details of the two grid sets: y_1^+ values result from wetted flow computations.

Gridpro	N	y_1^+				Hexpress	N	y_1^+			
	($\times 10^{-3}$)	min	max	avg	std		($\times 10^{-3}$)	min	max	avg	std
G1	29.6	0.12	2.65	1.17	0.47	G1	26.5	0.22	2.51	1.05	0.38
G2	66.3	0.007	1.71	0.78	0.31	G2	83.5	0.08	1.24	0.53	0.19
G3	118	0.03	1.24	0.57	0.23	G3	171	0.05	0.83	0.36	0.12
G4	263	0.04	0.85	0.39	0.15	G4	289	0.01	0.62	0.27	0.09
G5	468	0.01	0.62	0.29	0.11	G5	437	0.02	0.50	0.22	0.07

3 Wetted flow results

Wetted flow calculations were performed with the objective of estimating the numerical uncertainty and comparing preliminary results. The method of Eça and Hoekstra (2014) was used to estimate the numerical uncertainty. The influence of round-off error is commonly neglected. The iterative error is also neglected for these computations since the residuals remain well below 10^{-7} for all quantities. The discretisation error is computed from a series of systematically refined grids, from which the estimated exact solution is extrapolated. Then, the uncertainty range follows from the computed error, the standard deviation of the fit (i.e. a measure of the quality of the fit) and an additional safety factor. The wetted flow calculations were run in unsteady mode, with a normalized time step $t^* = \Delta t U_\infty / c = 4 \cdot 10^{-3}$. The solution quickly converges to a steady state, without flow separation.

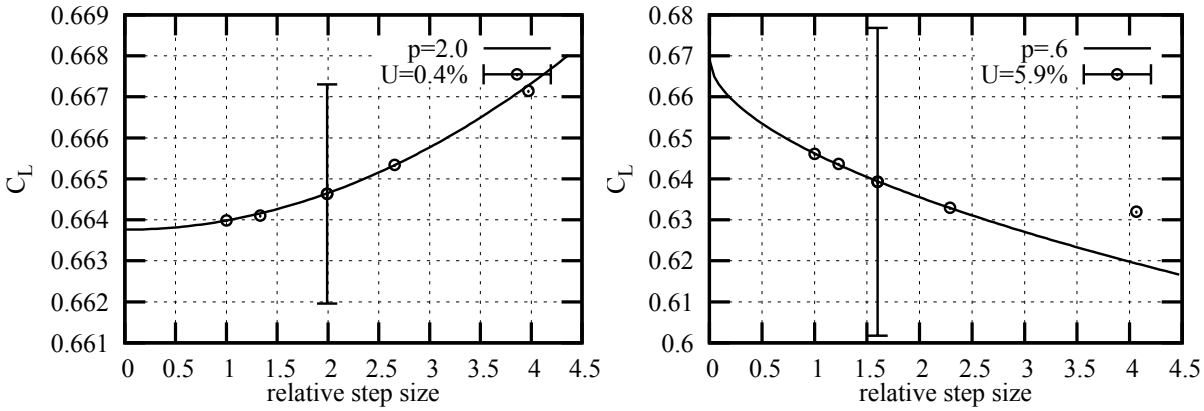

Fig. 3: Grid uncertainty for the lift coefficient. Structured mesh (left). Unstructured mesh (right)

Table 2: Uncertainty and computed order of convergence for G3. $C_p = 2p/(\rho U_\infty^2)$. For a force F, $C_F = 2F/(\rho U_\infty^2 cw)$. * indicates a first-plus-second order fit, as featured in the Eça and Hoekstra (2014) method.

		C_{Dp}	C_{Lp}	C_{Df}	C_D	C_L	$C_{p_{min}}$	$C_{p_{max}}$
GridPro	Value($\times 10^2$)	0.544	6.67	0.900	1.44	66.5	-204	101
	$U(\%)$	1.6	0.4	2.9	1.3	0.4	0.8	0.3
	p	1.7	2.0	2.0	2.0	2.0	2.0	2.0
Hexpress	Value($\times 10^2$)	0.574	6.39	0.848	1.42	63.9	-200	101
	$U(\%)$	11.2	5.9	2.5	2.1	5.9	10.8	0.1
	p	0.7	0.6	1 2*	1.1	0.6	1 2*	2.0

Figure 3 provides the fit, order of convergence and uncertainty for the lift coefficient, defined as $C_L = 2L/(\rho U_\infty^2 cw)$, with w the domain width. A low level of uncertainty of 0.4% is reached for the medium structured grid G3. As regards the unstructured grid set, the uncertainty is larger (5.9%) and the computed order of convergence is smaller; this is a symptom of lower grid quality, in combination with the difficulties to obtain fully similar grids with Hexpress. The drag coefficient exhibits a low uncertainty of 1.3% and 2.1% for the structured and unstructured mesh respectively. Overall, the set of structured grids has a higher quality, with an observed order of convergence of 2 for all quantities except C_{Dp}. The uncertainty for the unstructured G3 is larger for the minimum pressure coefficient (10.8%) and the lift (5.9%). Nevertheless, this medium grid provides a good compromise between accuracy and computational cost. The pressure and friction distributions over the foil surface are plotted in figure 4. For the unstructured grid there are small wiggles, that are more visible in C_f. Improvements can be obtained by increasing the number of cells or by trying different combinations of growth ratio and number of wall layers. Such investigations are not part of this study and are recommended for future work. The pressure distributions coincide and the minimum pressure coefficient differs by only 2% between the two topologies. The friction coefficient is larger at the suction side for the structured grid. This suggests a different boundary layer resolution at the suction side.

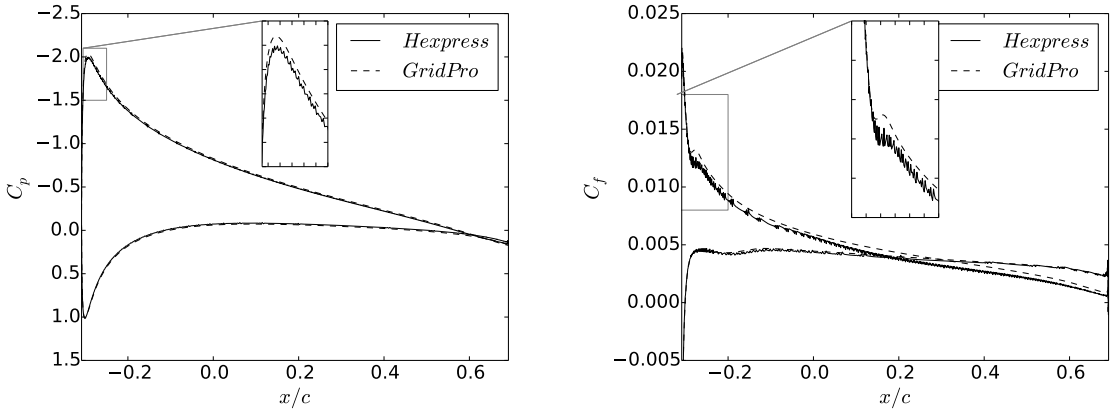

Fig. 4: Pressure coefficient and friction coefficient for the wetted flow condition.

Table 3: Drag, lift and Strouhal number. Relative differences ($\Delta\star$) between grids are included.

	$\overline{C}_D$	$\overline{C}_L$	St	$\Delta\overline{C}_D(\%)$	$\Delta\overline{C}_L(\%)$	$\Delta S_t(\%)$	$C_D wet$	$C_L wet$
GridPro	0.0604	0.524	0.134	2.1	0.38	6.7	0.0144	0.665
Hexpress	0.0591	0.526	0.125				0.0142	0.639

4 Cavitating flow results

From the results of the wetted flow study, the grids G3 (with 118k and 171k cells) are retained for cavitating flow calculations. The cavitation number is set to $\sigma = 2(p_{ref} - p_v)/(\rho U_\infty^2) = 1.0$. The time step is $t^* = 1 \times 10^{-3}$ for the structured mesh (approximately 8000 time steps per shedding cycle). The unstructured mesh is found to require smaller time steps to keep a good convergence behavior. Hence, the time step is halved to $t^* = 0.5 \times 10^{-3}$. The average quantities presented are obtained from the last 7 periods. Methods to estimate the statistical uncertainty typically require longer signals than the duration of the current simulations, which is roughly 12 shedding cycles. Although left out of this study, the statistical error is expected to be non-negligible and its estimation is recommended for future work. Table 3 provides an overview of the main integral quantities, including the relative difference between grid topologies. Noticeably, the Strouhal number differs by 6.7%. A large range of Strouhal numbers ($0.117 < St < 0.133$) is found also in literature, Hoekstra (2011). Here, the difference in St is attributed to an earlier collapse of the shed bubble in the unstructured mesh, which affects the development of the sheet cavity. Furthermore, the different time steps remains as another possible reason, so further verification studies including the effect of time discretization are suggested.

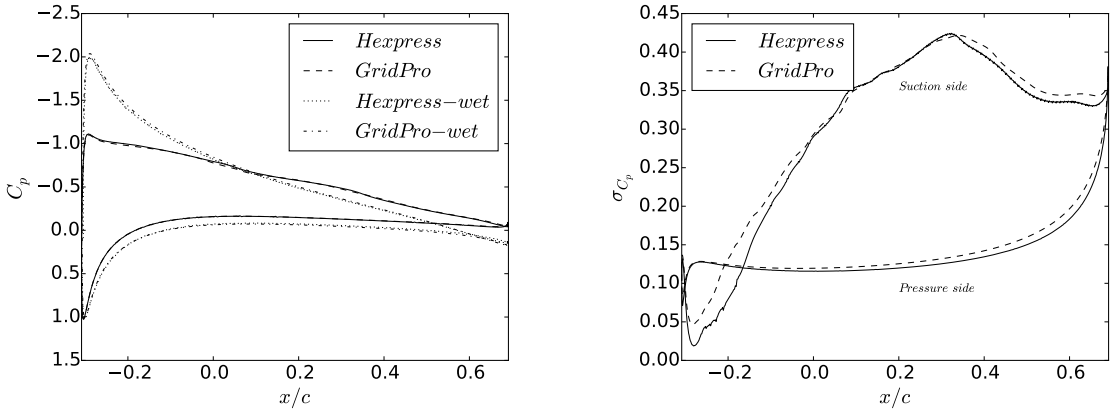

Fig. 5: Pressure coefficient distribution on the foil. Average for wetted and cavitating condition (left) and standard deviation for cavitating flow (right).

The average pressure coefficient and the standard deviation are plotted in Figure 5. The largest differences with the wetted flow occur at the suction side. In the first half of the foil the drop in pressure is limited by the inception of cavitation. The minimum pressure coefficient is lower than $-\sigma$. The same behavior is found in literature (e.g. Hoekstra and Vaz (2009)). Concerning the effect of grid topology, the differences are small and limited to the suction side between $-0.3 < x/c < -0.1$ and $0 < x/c < 0.1$. In the latter region, the unstructured mesh shows a lower pressure, which suggests a larger maximum length of the attached sheet cavity. The standard deviation in the right plot gives a measure of the influence of the dynamic cavitation cycle on the surface pressure. At the pressure side the unsteady cavitation influences the pressure especially towards the trailing edge. This is a consequence of the change in circulation when the shed vapor structure passes the trailing edge. At the suction side, the effect of cavitation is low up to $x/c = -0.1$ and then increases rapidly towards mid-chord and in the second half of the foil. The discrepancy between Hexpress and GridPro solutions is significant at $x/c < -0.1$, where the sheet cavity grows and shrinks; a smaller σ_{C_p} is observed for the unstructured mesh also at $x/c > 0.3$, which suggests a different prediction of the interaction between the trailing edge flow and the vapor bubble convected downstream. The time traces of the total vapor volume and the lift coefficient are plotted in the first and second rows of Figure 6. In addition, the last row shows the pressure signal at the point

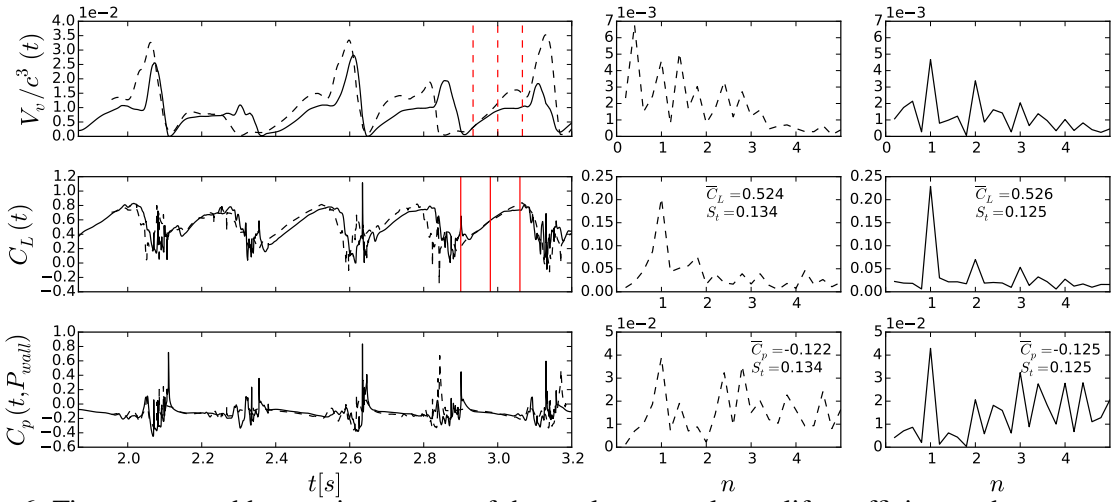

Fig. 6: Time traces and harmonic contents of the total vapor volume, lift coefficient and pressure at the probe. Structured (dashed) and unstructured (solid).

$P_{wall} = (0.5c, 1.425c)$ located on the top wall (see Figure 1). The first column shows the time trace in the last 5 periods. The shedding frequency differs by 6.7% between grids, hence the signals display a different duration. The second and third columns give the frequency contents, plotted as function of the harmonics of the shedding frequency. Neither of the solutions exhibits a regular periodicity. Looking at the total vapor volume, there are large and small peaks for both solutions. The peaks in vapor volume occur when the shed bubble passes by the trailing edge and interacts with the trailing edge flow, growing in size. More downstream, the bubble collapses and the total volume drops. The collapse of the bubble makes the new cavity shrink back. The peaks in total volume are narrower for the structured grid, which corresponds to an earlier collapse, affecting the shedding period. The earlier collapse relates to a sharper coarsening of the unstructured grid in the near wake. The lift force is maximum when the sheet is shrinking and the shed bubble becomes large. The collapse generates an instantaneous pressure jump such that the lift oscillates. The average lift differs by only 0.38% between the two grid types and the time traces are in good agreement. Looking at the pressure at the probe, it decreases slowly while the cavity develops, followed by a sharp but small increase when the vapor bubble detaches. Nevertheless, the time trace is dominated by the higher frequency oscillations at the moment of the collapse.
Concerning the frequency contents, for both solutions the first harmonic oscillation gives the main contribution to C_L, while for $C_p(P_{wall})$ there are high amplitudes for the larger harmonics as well. The alternation of small and large peaks in the vapor volume signals results in a significant component at half of the shedding frequency. The low frequency component is dominant in the trace of the vapor volume for the GridPro solution, and it is due to the collapsing bubble which affects the new shedding cycle. This behavior is less pronounced in the Hexpress grid, in view of the earlier bubble collapse.
Three contour plots of the pressure coefficient are presented in Figure 7. They correspond to the time steps shown as vertical red lines in Figure 6. The contours are selected at approximately $\frac{1}{4}$,$\frac{2}{4}$ and $\frac{3}{4}$ of shedding period T_S. The last frame also corresponds to the instant of maximum lift force. Green isolines show the location where $C_p = -\sigma = -1$ and black isolines show where the vapor fraction $\alpha_v = 0.5$. The latter is commonly considered as the edge of the cavity. The contour plot of the pressure coefficient gives an overview of the large low pressure area at the suction side which results from the development of cavitation. When the bubble is detached (in the third row of plots) there is a region of intermediate pressure between the shrinking cavity and the vapor bubble, more visible for the unstructured grid (right). The isolines do not coincide: the region where the pressure is below the vapor pressure are larger than the cavity/bubble size. When comparing the GridPro and the Hexpress grid, the same dynamic behavior is observed. However, there is a relevant difference in the size and shape of the shed bubble, which is larger and longer for the structured grid.

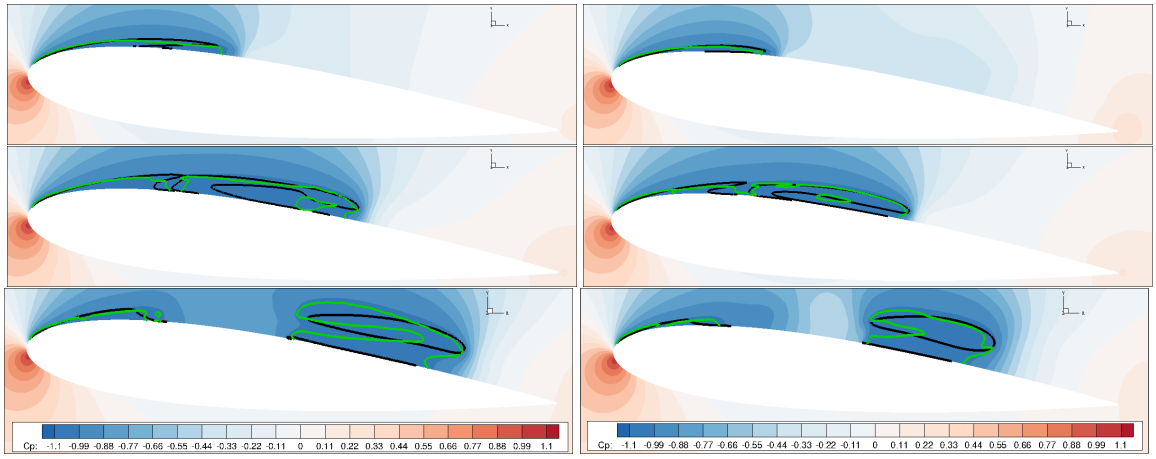

Fig. 7: Contour plots of pressure coefficient: isolines of $C_p = -\sigma = -1$ (green) and $\alpha_v = 0.5$ (black). Snapshots at $t = \frac{1}{4}T_S$, $\frac{2}{4}T_S$, $\frac{3}{4}T_S$. Structured grid (left); unstructured (right).

5 Summary

The influence of the grid setup on the prediction of cavitation dynamics was investigated in this study. Two grid sets were generated: one set of block-structured grids using GridPro® and one set of unstructured grids using Hexpress®. The first phase of the work addressed the numerical uncertainty for wetted flow. The uncertainty for the GridPro grid is very low (<2%) for all quantities considered. However, it is larger for the unstructured grid in view of the difficulties in obtaining full geometrical similarity with Hexpress®. The core of the work consists on the analysis of cavitating flow. Qualitatively, the two grid topologies predicts similar cavitation dynamics; however, the shape of the detached bubble and the location of the downstream collapse differ with the setups. Nevertheless, the variation of the lift force and the pressure at the tunnel ceiling are in good agreement: there is a 2% and <1% difference in average pressure and lift respectively. The main discrepancy is found in the shedding frequency, which is lower for the unstructured grid (-6.7%). Further work will involve a sensitivity study for the time step and the evaluation of the statistical error. This is desired to complete the study of uncertainties in the numerical simulation. Furthermore, it is interesting to check the pressure pulses at other locations. Finally, extension to 3D test cases is suggested to better capture the cavitation dynamics.

Acknowledgements
We thank Maarten Kerkvliet (MARIN) for providing the GridPro grids and Bart Schuiling (MARIN) for the guidance during part of this work.

References

R.E.A. Arndt, C.C.S. Song, M. Kjeldsen, J. He and A. Keller (2000). Instability of partial cavitation: a numerical/experimental approach. 23^{rd} Symp. on Naval Hydrodynamics, Val de Reuil, France (2000).

L. Eça, M. Hoekstra (2014). A procedure for the estimation of the numerical uncertainty of CFD calculations based on grid refinement studies. *Journal of computational physics*, **262**(2014), 104–130.

M. Hoekstra and G. Vaz (2009). The partial cavity in a 2D foil revisited. Proceedings of the 7^{th} International Symposium on Cavitation, CAV2009, Ann Arbor, Michigan, USA.

M. Hoekstra (2011). Exploratory RANS simulations of partial cavitation and its dynamics. International conference on computational methods in marine engineering, MARINE 2011.

M. Kerkvliet (2013). Influence on the numerical uncertainty of a generic submarine model by changing the wall-normal distribution of the wall-bounded grid cells. 16^{th} Numerical Towing Tank Symposium (NuTTS'13), Mülheim, Germany, 2013.

F.R.. Menter, Y. Egorov, D. Rush (2006). Steady and unsteady flow modelling using the k-kL model. Proceedings of the International Symposium in Turbulence, Heat and Mass Transfer. Pp. 403-406. 2006

J. Sauer. *Instationär Kavitierende Strömungen - Ein neues Modell, basierend auf Front-Capturing(VoF) und Blasendynamik.* PhD Thesis, University of Karlsruhe, Germany (2000).

S. Yakubov, T. Maquil, T. Rung (2015). Experience using pressure-based CFD methods for Euler-Euler simulations of cavitating flows. *Computer& Fluids*, **111**(2015), 91–104.

Steps towards fully nonlinear simulations of arrays of OWSC

Gerrit Olbert[*], **Pal Schmitt**[†]
[*] TU Harburg, Hamburg/Germany, [†]Queen's University Belfast
gerrit.olbert@tu-harburg.de

1 Introduction

OWSCs in waves reflect, refract and radiate waves in different directions depending on geometrical, structural and dynamic properties of the flap. Array interaction describes the changes induced on the excitation of flaps in an array compared to the excitation of a single flap.
Renzi and Dias, 2013, Renzi et al., 2014, investigated array effects of OWSCs using a linearised semi-analytical and a linearised FEM method. However, research suggests that the applicability of linear methods for the simulation of OWSCs is limited to very small flap angles (Crooks et al., 2014, Crooks et al., 2016). Linear inviscid assumptions seem to break down in typical operating conditions (Folley et al., 2004, Asmuth et al., 2014).
It can therefore be assumed that the accuracy of linear methods in predicting the characteristic wave pattern around a flap and the interaction between multiple such devices is limited when applied to realistic operating conditions with typical pitch motion amplitudes.
Although RANS CFD tools have been shown to reproduce the motion of single flaps in waves within the levels of experimental accuracy and can provide detailed data of all field variables like surface elevation, pressure or velocity (Schmitt and Elsässer, 2015a), the simulation of arrays of WECs remains an open challenge. Due to numerical dissipation water waves simulated using volume of fluid methods tend to diminish in height and require careful spatial and temporal discretisation.
The simulation of multiple moving bodies requires adaptation of the mesh and constitutes a considerable computational effort. As with physical test facilities numerical wave tanks require non-reflecting boundary conditions and wave makers.

2 Numerical Set-Up

To save computational effort a first estimate for time step and spatial resolution is made based on two-dimensional (2D) simulations. The domain is restricted to the y and z-direction. Waves of length 1.4m and height 9mm in a water depth of 0.346m (as expected in the experimental tests) are generated by a momentum-source term wave maker (Schmitt and Elsässer, 2015b) as shown in fig. 1. The wave elevation is recorded at predefined distances from the source area. These probes are represented by vertical cylinders in figure 1.
The data collected at these probes helps to give an estimation of diffusive losses for varying spatial and time discretisation settings. Maximum time steps were varied between a 100th and 500th of the wave period. The actual timestep was set by the limiting Courant Number of 0.3 depending on the cell size. Over one wavelength the wave height decreased more than 15% for a timestep of 100th or 200th of the wave period. Limiting the time step to 500th of the wave period reduces dissipation to 7.5%.

Variations of the mesh resolution were tested for 60, 80 and 100 cells per wave length and 10, 13 and 16 cells per wave height, but with approx. only 1% seem to have little influence on numerical diffusion. The runtime is only affected by the finest temporal discretisation, in the other cases the Courant condition limits the number of timesteps. An overview of the tested settings and the corresponding total run time of a 30s simulation can be seen in table 1.

The variable C_γ, defining the magnitude of interface compression, is tested for values between 0.5 and 1.5 to assess the influence of surface compression on the numerical diffusion of waves. The results show that the resulting variance is less than 0.1% of the incident wave height. As a higher value for C_γ leads to an increased compression and therefore a sharper interface, a value of 1.0 is used for the following simulations.
An impulse source type wave maker is used to create waves, while a numerical beach is implemented using a spatially varying dissipation term (Schmitt and Elsässer, 2015b). An implementation of the three-

Fig. 1: Side view of the 2D-simulation domain, showing the momentum source wave maker (center), waveprobes (grey cylinders) and damping regions (left and right corner)

Time step Cells per λ,H	$T/100$	$T/200$	$T/500$
60, 10	16.3%	16.3%	7.5%
Runtime	2472s	2472s	7044s
80, 13	16.3%	16.3%	6.64%
Runtime	4282s	4282s	10552s
100, 16	15%	15%	6.4%
Runtime	5310s	5310s	12641s

Table 1: Diffusive losses in percent of incident wave height for different resolutions of wavelength λ and waveheight H. Losses averaged over ten periods between simulations time of $20T$ and $30T$. $T = 1$s, H = 0.009m, $\lambda \approx 1.4$m

point-reflection analysis based on wave elevation and developed by Mansard and Funke, 1980, shows that less than 1% of the incident wave is reflected at the boundaries (see fig. 2). The wave maker developed by Higuera et al., 2013, was also tested and resulted in 12% wave amplitude reflection, which is deemed too large for the purpose of array investigations.

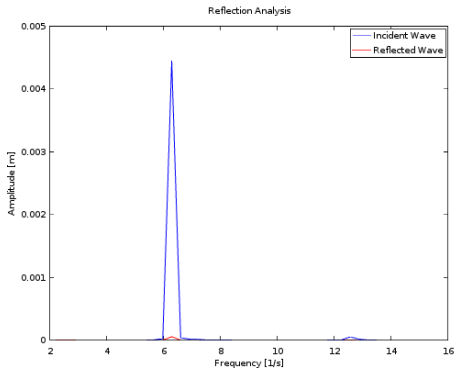

Fig. 2: Results of the three-point waveprobe analysis for $T = 1$s, $H = 0.009$m

In order to minimize the extensive computational effort required for the purpose of this investigation, an additional routine is implemented prior to 3D-simulations. The initialisation of the wave source region and the hereby induced influence on the flow field lead to oscillations in the wave height of the generated wave profile. These oscillations typically decreased to a negligible level after 30 to 40 wave periods of simulation time. Therefore, 40 wave periods of simulation time are computed in 2D. The resulting flow field is then saved and mapped onto a three-dimensional mesh, creating a long crested wave profile. Using this approach, only about 4-5 wave periods of simulation time are required prior to recording data, to allow the flow field to adapt to the presence of the flap geometries. An illustration of the mapping procedure is shown in figure 3.

(a) Side View of 2D-domain

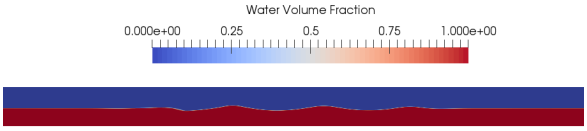

(b) 3D view on stretched 2D-domain

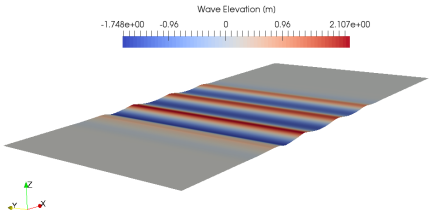

(c) 3D-domain after mapping, $t = 0$

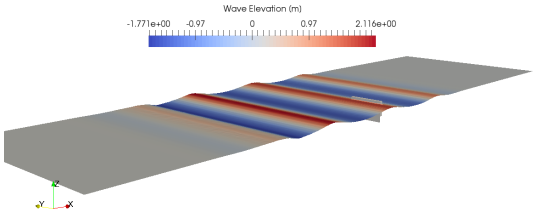

(d) 3D-domain at $t = 15T$

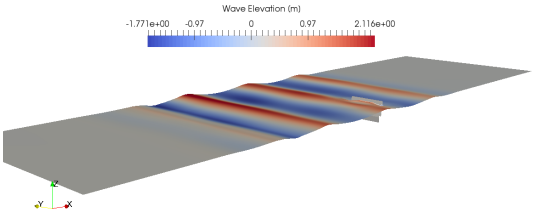

Fig. 3: Process of mapping the flow field beneath surface waves from a two-dimensional domain onto a three-dimensional grid. The 2D-grid is stretched until the lateral cell dimension corresponds to the width of the 3D-domain. The interpolation onto the grid creates a long crested wave profile, initially unaffected by the presence of the flap geometries. In this example: $T = 7$s, $H = 3$m, water depth= 13m. Flap corresponds to full scale model of Oyster© 800

2.1 Mesh distortion

The simulation of an OWSC in motion within a finite-volume-method (FVM) requires a mesh motion algorithm to account for the displacement of the body in each time step. Several approaches for the simulation of moving bodes exist, such as the overset grid solution presented by Meakin, 1998, or the sliding interface solution, e.g. Hadžić et al., 2005. Schmitt, 2013, developed a mesh motion tool for the simulation of flap type wave surge converters based on sliding interfaces and a custom field condition to account for the sea floor. Both models imply additional computational costs, requiring additional interpolation procedures and precautions to ensure mass continuity, as discussed for example by Tang et al., 2003.
A faster option is the application of mesh distortion methods. Though limited to flap rotation angles of up to 40°, they seem better suited for the envisaged array studies. *OpenFOAM* offers several dynamic mesh solvers available through its *interDyMFoam* toolkit. An explanation of the algorithm behind this method can be found in Pereira and Sequeira, 2010.
The mesh distortion caused by a moving boundary is computed using the Laplace equation (1).

$$\nabla(\gamma \nabla U) = 0 \tag{1}$$

Herein γ is the diffusion coefficient or stiffness of the mesh, regulating the spatial variation of the mesh deformation

$$\gamma(r) = \frac{1}{r^m}, \tag{2}$$

wherein r represents the distance from the moving wall and m the order of the approach. U, in this context, stands for the local mesh velocity.
A linear inverse distance definition leads to a reciprocal decrease of local distortion from a moving boundary. A quadratic inverse distance definition, in which the diffusivity is proportional to $1/l^2$, with l as

the distance to a selected boundary, results in a decrease of mesh distortion close to the boundary but leads to a larger overall number of distorted cells (see figures 4a, 4b and 4c, 4d) (Pereira and Sequeira, 2010).

As the Laplacian equation tends to show deficits for rotating deformations, a second approach will

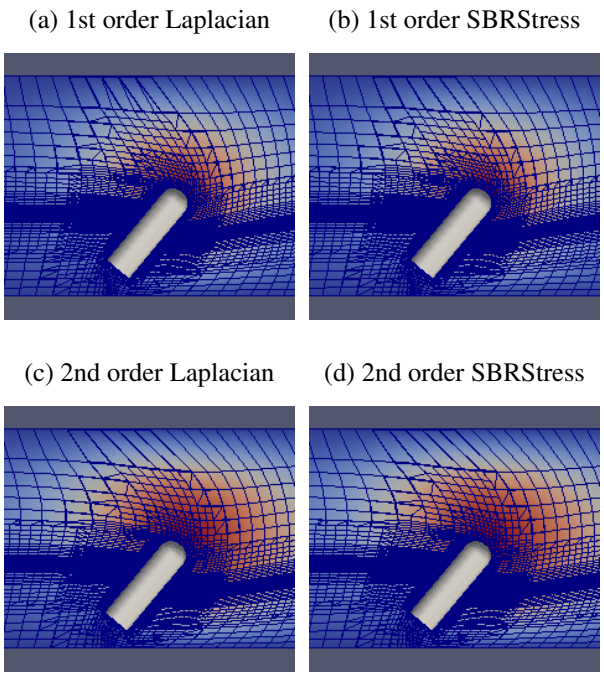

Fig. 4: Mesh distortion for first and second order approaches of Laplacian and SBRStress inverse distance diffusivity

be tested for both first and second order. The SBRStress mesh solver was developed to compute mesh deformation for rotating solid bodies and takes into account deformation due to shear while the laplace solver is based on translation (Dwight, 2006). Both approaches maintain valid meshes for flap angles $< 43°$.

3 First results

First simulations were run to compare a single flap with two, three or infinite number of devices. The devices are spaced on a line along the hinge, with one flap width distance in between. The infinite configuration was created using a symmetry condition on both laterally confining walls. Figures 5 $a - d$ show the different configurations and the surface elevation for waves of 11s period. The changes to the wave pattern are clearly visible when compared to the single flap case. These changes will be analysed and quantified in more detail in future work. To assess the array interaction, the interaction parameter q, defined as:

$$q = \frac{P'}{MP_s}, \tag{3}$$

with P' as the overall power output of the array, M as the number of devices in the array and P_s as the power output of a single device, is often used. Figure 6 shows the interaction factor for waves of 1m height over varying wave periods. The linear solution is plotted in lines, CFD results are only available for several points, due to constraints on computational power. Both datasets indicate that array interaction is positive for waves around 7s period and negative for longer waves. CFD results differ significantly from the linear solution for some periods or configurations, the exact cause will be investigated in future work.

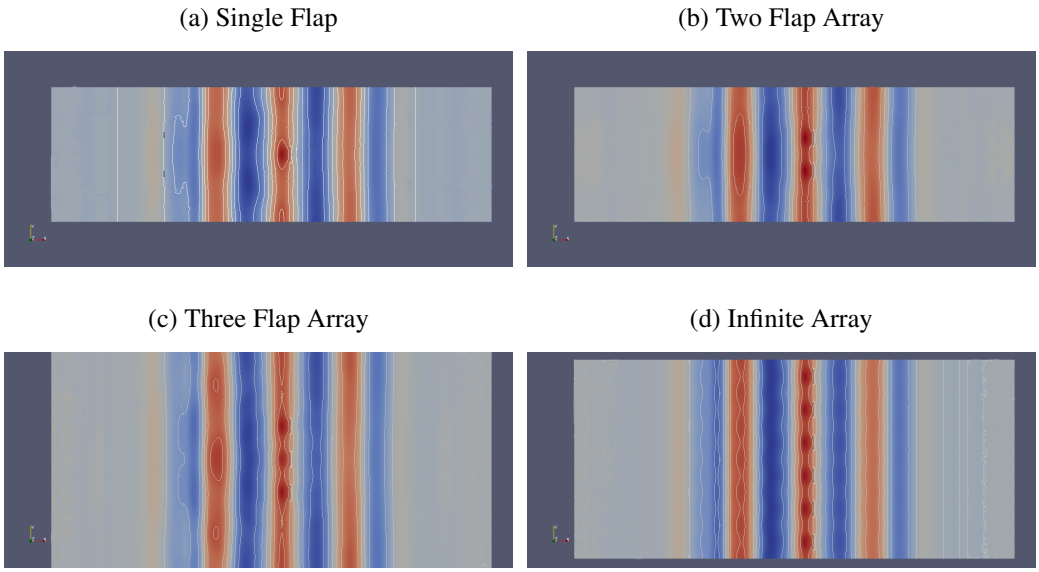

Fig. 5: Surface elevation after 605s for a single flap and three array configurations. Damping settings were defined in accordance with Renzi et al., 2014. $T = 11$s, $H = 1$m

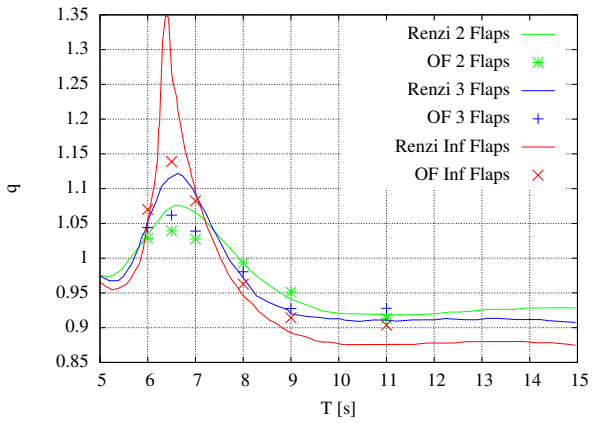

Fig. 6: Interaction factor q by Renzi (lines) in comparison to *OpenFOAM* results (points)

4 Conclusion

Careful testing and choice of appropriate mesh and timestep resolution is required for the correct application of VoF RANS simulations to the investigation of WEC arrays. First results show siginificant differences when compared to linear potential simulations, even higher deviations are expected for future simulations of more realistic sea states with wave heights of of up to three meters.

Acknowledgements

We thank the STG for funding Gerrit Olberts participation in NuTTS 2016 and the research team at Queen's University Belfast for their support in the course of this research.

References

Asmuth, H., Schmitt, P., and Henry, A.and Elsaesser, B. (2014). Determination of non-linear damping coefficients of bottom-hinged oscillating wave surge converters using numerical free decay tests. In Soares, G., editor, *Renewable Energies Offshore*. Taylor & Francis Group, London.

Crooks, D., van't Hoff, J., Folley, M., and Elsässer, B. (2016). Oscillating wave surge converter forced oscillation tests. In *Proceedings of the ASME 2016 35th International Conference on Ocean, Offshore and Arctic Engineering*.

Crooks, D., Whittaker, T. J., van't Hoff, J., and Cummins, C. (2014). Experimental validation of numericaly generated wave excitation torque on an owsc. In Soares, G., editor, *Renewable Energies Offshore*. Taylor & Francis Group, London.

Dwight, R. P. (2006). Robust mesh deformation using the linear elasticity equations. In *Proceedings of the Fourth International Conference on Computational Fluid Dynamics (ICCFD 4)*.

Folley, M., Whittaker, T., and Osterried, M. (2004). The oscillating wave surge converter. In *Proceedings of the 14th International Conference on Ocean and Polar Engineering, ISOPE 2004*.

Hadžić, I., Hennig, J., Perić, M., and Xing-Kaeding, Y. (2005). Computation of flow-induced motion of floating bodies. *Applied Mathematical Modelling*, 29(12):1196 – 1210.

Higuera, P., Lara, J. L., and Losada, I. J. (2013). Realistic wave generation and active wave absorption for navier-stokes models: Application to OpenFOAM. *Coastal Engineering*, 71(0):102 – 118.

Mansard, E. and Funke, E. (1980). The measurement of incident and reflected spectra using a least square method. In *ICCE'80*, pages 154–172. ASCE.

Meakin, R. L. (1998). *Handbook of Grid Generation*. CRC Press, Boca Raton.

Pereira, J. C. F. and Sequeira, A., editors (2010). *Dynamic Mesh Handling In Openfoam Applied To Fluid-structure Interaction Simulations*, European Conference on Computational Fluid Dynamics.

Renzi, E., Abdolali, A., Bellotti, G., and Dias, F. (2014). Wave-power absorption from a finite array of oscillating wave surge converters. *Renewable Energy*, 63:55 – 68.

Renzi, E. and Dias, F. (2013). Relations for a periodic array of flap-type wave energy converters. *Applied Ocean Research*, 39:31 – 39.

Schmitt, P. (2013). *Investigation of the near flow field of bottom hinged flap type wave energy converters*. PhD thesis, Queen's University Belfast.

Schmitt, P. and Elsässer, B. (2015a). On the use of OpenFOAM to model oscillating wave surge converters. *Ocean Engineering*, 108:98 – 104.

Schmitt, P. and Elsässer, B. (2015b). A review of wave makers for 3d numerical simulations. *MARINE 2015 - Computational Methods in Marine Engineering VI*, pages 437–446.

Tang, H., Jones, S. C., and Sotiropoulos, F. (2003). An overset-grid method for 3d unsteady incompressible flows. *Journal of Computational Physics*, 191(2):567 – 600.

Multi-Fidelity Adaptive Metamodel for Ship Hull Performance via CFD

Riccardo Pellegrini[*,†], Cecilia Leotardi[†], Stefano Zaghi[†], Riccardo Broglia[†], Emilio F. Campana[†], Umberto Iemma[*] and Matteo Diez[†]

[*]Department of Engineering, Roma Tre University, Via Vito Volterra 62, 00146 Rome, Italy

[†]CNR-INSEAN, National Research Council-Marine Technology Research Institute, Via di Vallerano 139, 00128 Rome, Italy

Email: matteo.diez@cnr.it

1 Introduction

The simulation-based design (SBD) process of complex engineering systems (such as ground, aerial, and marine vehicles) requires computationally expensive physic-based solvers, in order to achieve accurate solutions. Often, structural and/or computational fluid-dynamic (CFD) solvers are used in order to assess the design performance, *e.g.* the hydrodynamic performance of a ship hull with the resulting resistance force. The SBD process can integrate optimization algorithms in order to perform a fully-automated design optimization. In this case, a large number of computer simulations is required to converge to the optimal solution, and the computational cost of the process is usually very high. Furthermore, when dealing with real-life applications, uncertainties (stemming from environmental and operating conditions) must be taken into account in the design process, including uncertainty quantification (UQ) procedures and requiring very large computational resources.

Metamodels are used to reduce the computational cost of the SBD and have been successfully applied in diverse engineering fields (*e.g.* Giselle et al., 2016). Among others, accuracy and efficiency of radial basis functions (RBF) have been demonstrated for several engineering applications by Hardy, 1971. Furthermore, the assessment of RBF by analytical test problems has been discussed by Jin et al., 2001. Stochastic search in optimization by RBF has been shown in Regis, 2011, whereas the use of RBF in UQ problems has been discussed in Loeven et al., 2007. Volpi et al., 2015 have presented a dynamic RBF metamodel for UQ applications in ship hydrodynamics, with comparison to dynamic Kriging. Its extension to design optimization has been presented in Diez et al., 2015.

In order to combine the accuracy of high-fidelity solvers with the computational cost of low-fidelity solvers, several multi-fidelity approximation methods have been developed (*e.g.* Simpson et al., 2008). Combining metamodelling methods with multi-fidelity approximations potentially leads to a further reduction of the computational cost, such as in co-Kriging (Forrester et al., 2007). Correction methods, such as additive and/or multiplicative approaches, are used to build multi-fidelity metamodels combining high- and low-fidelity models (Ng and Eldred, 2012). High- and low-fidelity models may be determined by the physical model and/or the size of the computational grid (Sun et al., 2010a). Multi-fidelity metamodels have been used for both design optimization (Sun et al., 2010b) and uncertainty quantification (Ng and Eldred, 2012).

The objective of the present work is to apply and assess the effectiveness and efficiency of a multi-fidelity global metamodel (Pellegrini et al., 2016a, Pellegrini et al., 2016b) able to manage high- and low-fidelity solvers through a multi-fidelity adaptive sampling procedure. The metamodel is used here to evaluate the ship hull performance versus the operating conditions.

The multi-fidelity approximation is built as the sum of a low-fidelity-trained metamodel and the metamodel of the difference (error) between high- and low-fidelity simulations, using the stochastic RBF method. Both the prediction and the associated uncertainty are provided by the method. The adaptive sampling procedure is based on the maximum value of the prediction uncertainty. The prediction uncertainty of both the low-fidelity and the error metamodel is used for the adaptive refinement of the low- and high-fidelity training set, respectively.

The method is demonstrated through one analytical test problem and one industrial application. The examples are one-dimensional and address one function of interest at the time. The industrial problem addresses the total resistance of an unmanned small waterplane area twin hulls (SWATH) vehicle (Zaghi et al., 2015), advancing in calm water, versus the cruise speed. The high-fidelity simulations of the SWATH are performed using the CNR-INSEAN in-house Reynolds average Navier-Stokes equations

(RANS) solver χnavis (*e.g.* Di Mascio et al., 2009). The low-fidelity simulations are performed using the CNR-INSEAN in-house steady potential flow solver wave resistance program (WARP).

2 Multi-fidelity adaptive metamodel

Considering n functions (relevant outputs), the multi-fidelity metamodel is defined as

$$\begin{aligned} \hat{f}_i(\mathbf{x}) &= \tilde{f}_{i,L}(\mathbf{x}) + \tilde{\delta}_i(\mathbf{x}),\ i = 1, \ldots, n \\ \delta_i(\mathbf{x}) &= f_{i,H}(\mathbf{x}) - f_{i,L}(\mathbf{x}),\ i = 1, \ldots, n \end{aligned} \tag{1}$$

where $\mathbf{x} \in \mathbb{R}^n$ is the independent variable (or uncertain parameter), superscript $\sim$ denotes the RBF prediction, and δ_i is the difference (error) between high- and low-fidelity simulations (respectively, $f_{i,H}$ and $f_{i,L}$ with $i = 1, \ldots, n$).

The uncertainty associated with the prediction provided by the multi-fidelity metamodel of the i-th function is defined as

$$U_{\hat{f}_i}(\mathbf{x}) = \sqrt{U^2_{\tilde{f}_{i,L}}(\mathbf{x}) + U^2_{\tilde{\delta}_i}(\mathbf{x})} \tag{2}$$

where $U_{\tilde{f}_{i,L}}$ and $U_{\tilde{\delta}_i}$ are the uncertainties associated to the prediction of the i-th function, provided by the low-fidelity and error metamodels ($\tilde{f}_{i,L}$ and $\tilde{\delta}_i$), respectively Volpi et al., 2015.

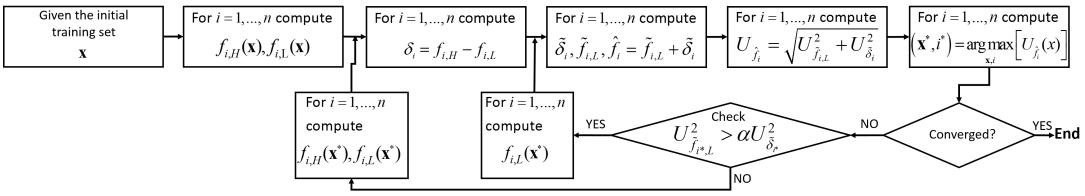

Fig. 1: Multi-fidelity metamodel adaptive sampling procedure.

The multi-fidelity metamodel is trained using the adaptive procedure shown in Fig. 1. After initialization, a new sample is added to the training set at each iteration, solving the following problem:

$$(\mathbf{x}^*, i^*) = \underset{\mathbf{x},i}{\text{argmax}}[U_{\hat{f}_i}(\mathbf{x})] \tag{3}$$

Once $\mathbf{x}^*$ and i^* are evaluated, the training sets H and/or L (high- and low-fidelity, respectively) are updated as

$$\begin{cases} \text{If } U^2_{\tilde{f}_{i^*,L}}(\mathbf{x}^*) \geq \alpha U^2_{\tilde{\delta}_{i^*}}(\mathbf{x}^*), \text{ then add } \mathbf{x}^* \text{ to } L \\ \text{If } U^2_{\tilde{f}_{i^*,L}}(\mathbf{x}^*) < \alpha U^2_{\tilde{\delta}_{i^*}}(\mathbf{x}^*), \text{ then add } \mathbf{x}^* \text{ to } H \text{ and } L \end{cases} \tag{4}$$

where $\alpha \in [0, 1]$ is an arbitrary tuning parameter, related to the ratio of the computational cost of the low- and high-fidelity simulations.

Herein, only one function is considered, therefore $n = 1$.

3 Stochastic radial basis functions

The prediction $\tilde{f}$ is evaluated as the expected value of a set of stochastic RBF predictions (Volpi et al., 2015), which depend on the stochastic parameter $\epsilon \sim \text{unif}[1, 3]$:

$$\tilde{f}(\mathbf{x}) = E[g(\mathbf{x}, \epsilon)]_\epsilon, \quad \text{with } g(\mathbf{x}, \epsilon) = \sum_{i=1}^{m} w_i\, \varphi(\mathbf{x} - \mathbf{x}_i) \tag{5}$$

where m is the size of the training set, $\mathbf{x}_i$ are the training points, $\varphi(\cdot) = \|\cdot\|^\epsilon$, and $\|\cdot\|$ is the Euclidean norm. The coefficients w_i are obtained solving the linear system $\mathbf{Aw} = \mathbf{y}$ with $\mathbf{w} = \{w_i\}$. The elements of the matrix $\mathbf{A}$ are $a_{ij} = \varphi(\mathbf{x}_i - \mathbf{x}_j)$ and the vector $\mathbf{y} = \{y_i\}$ collects the function evaluations at the training points, $y_i = f(\mathbf{x}_i)$.

The uncertainty associated to the metamodel prediction, $U(\mathbf{x})$, is quantified at each $\mathbf{x}$ as the 95%-confidence interval of $g(\mathbf{x}, \epsilon)$.

4 Applications

A one-dimensional analytical test function is used for the demonstration of the method, providing also a comparison between the computational effort required by multi-fidelity metamodel (trained by high- and low-fidelity evaluations) and a high-fidelity metamodel (trained by high-fidelity evaluations only). The one-dimensional industrial problem addresses the evaluation of the total resistance (R_T) of the SWATH advancing in calm water (no motions considered), within the speed range [3;6] kn. The normalized root mean square error (NRMSE) versus high-fidelity evaluations is used as a convergence criterion of the adaptive sampling. The NRMSE is also used as evaluation metric for the accuracy of the method.

4.1 Analytical test problem

Consider the following high-fidelity function (which is going to be approximated by the multi-fidelity metamodel)

$$f_H(x) = a\, e^{-\frac{(x-\mu)^2}{2\sigma^2}} + 0.065x, \quad \text{with } \mu = 5,\ \sigma = 2,\ a = \left(\sigma + \sqrt{2\pi}\right)^{-1} \tag{6}$$

and the corresponding low-fidelity function $f_L(x) = f_H(x) - \delta(x)$, with δ provided by the quadratic form $\delta(x) = 0.0007x^2 - 0.0208$. In order to evaluate the efficiency of the multi-fidelity method, a nominal computational cost of 10 is assigned to f_H and 1 to f_L, resulting in $\alpha = 1/10$.

4.2 Industrial problem

The SWATH is designed as two torpedoes connected to the upper platform by a couple of NACA 0012 profiled twin narrow struts for each hull (for a total of four struts). Its main geometric particulars, as shown in Fig. 2, are: length between perpendiculars, $L_{pp} = 5m$; torpedoes diameter, $D = 0.45m$; interaxis distance, $DH_{sep} = 2.5m$; first strut leading edge position, $L1 = 1.238m$ and struts clearance, $D_S = 0.686m$.

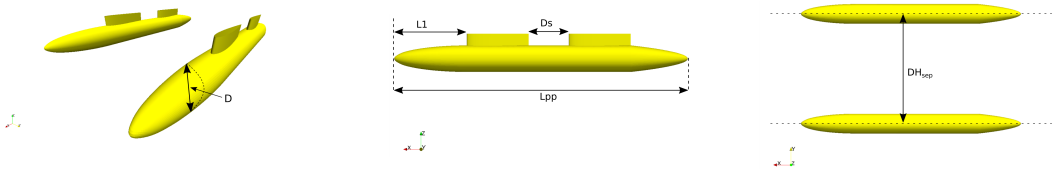

Fig. 2: Perspective, lateral and top view of the SWATH.

The high-fidelity solver, namely χnavis, yields the numerical solution of the RANS equations with proper boundary and initial conditions. The algorithm is formulated as a finite volume scheme, with variable co-located at cell centers. Turbulent stresses are taken into account by the Boussinesq hypothesis. Spalart-Allmaras turbulence model is used. Free surface effects are taken into account by a single phase level-set algorithm. A computational grid with 5.6M nodes is used. Each high-fidelity evaluation requires 1216 minutes wall-clock time, running on 8 Intel(R) Xeon(R) CPU X3230 @ 2.66GHz.

The low-fidelity solver is the steady potential flow (PF) code WARP. The wave resistance computations are based on the linear potential flow theory with the double-model linearization (Dawson, 1977) and is evaluated using a pressure integral over the body surface, whereas the frictional resistance is estimated using a flat-plate approximation based on the local Reynolds number . A computational grid with 11k panels is used. Each low-fidelity evaluation requires 2 minutes wall-clock time, running on 1 Intel(R) Xeon(R) E5-1620 v2 @ 3.9 GHz. The resulting α is equal to 0.0016.

5 Numerical results

The results of the analytical test problem and the total resistance of the SWATH are presented in section 5.1 and 5.2 respectively, showing: (i) the convergence of the NRMSE versus the computational cost and (ii) the multi-fidelity metamodel training at the initial and final iterations. The training sets L and H are initialized using three points, which are namely the lower and upper bounds, and the mid point of the variable range. An arbitrary convergence value of 0.01 is set for the NRMSE.

5.1 Analytical test problem

Figure 3a shows the NRMSE convergence of the multi- and high-fidelity metamodels, along with their respective maximum uncertainty, versus the computational cost. The NRMSE is computed between the metamodel predictions (multi-fidelity $\hat{f}$ and high- $\tilde{f}_H$) and the high-fidelity function (f_H).

The convergence of the multi-fidelity metamodel is obtained after 17 iterations, with 6 high- and 19 low-fidelity evaluations. The computational cost is lower than that of the high-fidelity metamodel, which requires 13 high-fidelity evaluations.

Figure 3b shows the high-fidelity, low-fidelity, and error functions, along with the multi-fidelity, low-fidelity and error metamodels, at the initial iteration. Diamonds and circles represent the H and L training points. The error metamodel is in good agreement with the analytical function. Conversely, the multi-fidelity metamodel does not show an accurate prediction. The associated prediction uncertainties are shown in the bottom box.

Figure 3c shows the final iteration. The multi-fidelity metamodel is in good agreement with the high-fidelity function. The uncertainty is shown in the bottom box and is considerably lower than that shown in Fig. 3b, achieving a maximum of 0.42% of the function range.

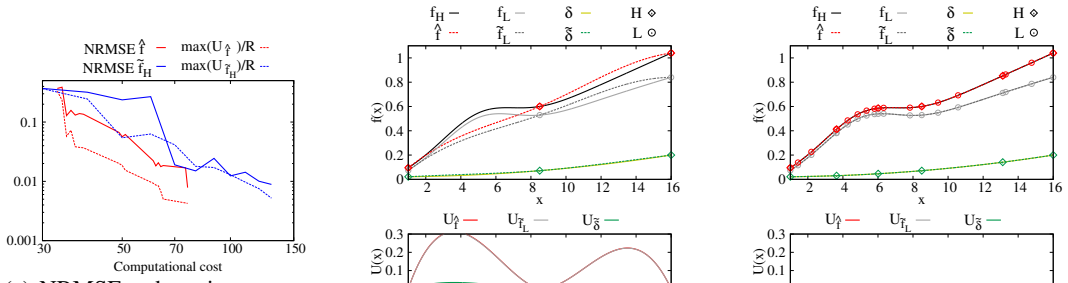

(a) NRMSE and maximum normalized uncertainty versus the computational cost

(b) Initial iteration

(c) Final iteration

Fig. 3: Analytical problem: multi-fidelity metamodel convergence.

5.2 Industrial problem

In order to provide the high- and low-fidelity values for the current test case, two functions are built by spline interpolation of the available RANS and PF simulations, and used as surrogate of the real RANS and PF. High-fidelity spline is trained with six RANS simulations performed at $\{3, 4, 4.5, 5, 5.5, 6\}$ kn. Low-fidelity spline is trained with 13 simulations performed at evenly spaced velocities between 3 kn $\leq v \leq$ 6 kn.

Figure 4 shows the computational grid the wave elevation at 6 kn computed by the RANS solver. PF (not reported here) tends to overestimate the resistance, compared to the RANS solver, in the region between [3.5;5] kn.

Figure 5a shows the NRMSE convergence of the multi- and high-fidelity metamodels, along with their respective maximum uncertainty, versus the computational cost. The convergence of the multi-fidelity metamodel is obtained after 14 iterations, with 7 high- and 17 low-fidelity evaluations. The comparison with the high-fidelity solver is not reported since, for the current demonstration, the high-fidelity function is derived from spline, resulting in an artificial evaluation.

Figure 5b shows the high-fidelity, low-fidelity, and the multi-fidelity metamodels, at the initial iteration. The multi-fidelity metamodel is not in agreement with the high-fidelity metamodel, due to the shape of f_H. The associated prediction uncertainties are shown in the bottom box.

Figure 5c shows the final iteration. The multi-fidelity metamodel is in good agreement with the reference solution. The associated uncertainty is considerably lower than that shown in Fig. 5b, achieving a maximum of 0.98% of the function range.

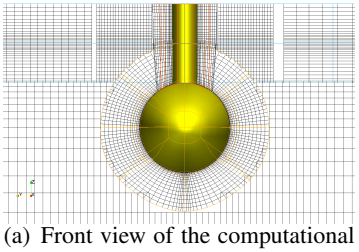

(a) Front view of the computational grid

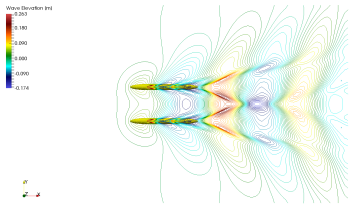

(b) Wave elevation at 6 kn

Fig. 4: Industrial problem: RANS computational grid and hydrodynamic results.

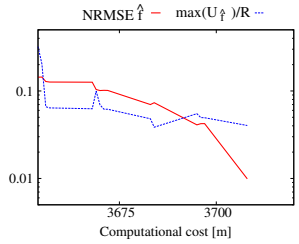

(a) NRMSE and maximum normalized uncertainty versus the computational cost

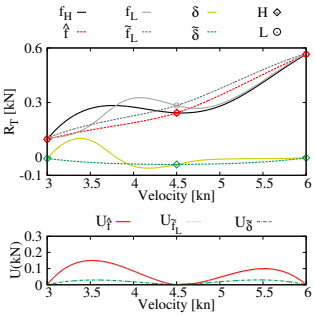

(b) Initial iteration

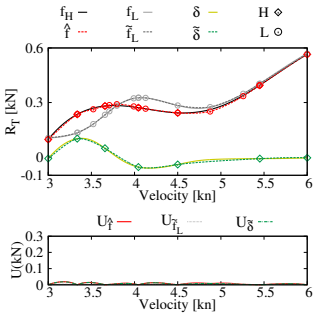

(c) Final iteration

Fig. 5: Industrial problem: multi-fidelity metamodel convergence.

6 Conclusions

A multi-fidelity global metamodel has been presented and assessed. High- and low-fidelity solvers are managed through an adaptive sampling procedure. The multi-fidelity approximation is obtained as the sum of the low-fidelity-trained metamodel and the metamodel of the difference (error) between high- and low-fidelity simulations. The metamodel is based on the dynamic stochastic RBF method, which provides the prediction and the associated uncertainty. The prediction uncertainty of both the low-fidelity and the error metamodel is used for the adaptive refinement of the low- and high-fidelity training set, respectively.

The method is demonstrated for an analytical one-dimensional test problem. The current method provides a reduction of the computational cost (artificially defined for the high- and low-fidelity evaluations) close to 40%, compared to a metamodel trained by high-fidelity evaluations only.

The method has been also demonstrated for a simple one-dimensional industrial problem, addressing the total resistance of an unmanned SWATH vehicle in calm water, versus the cruise speed. High- and low-fidelity simulations have been performed using RANS and PF solvers respectively, showing promising results.

Ongoing activities focus on applying the method to multi-dimensional and multiple function problems. Future work will include the application of the methodology to multi-objective simulation-based design optimization.

References

Dawson, C. W. (1977). A practical computer method for solving ship-wave problems. In *Proceedings of the 2nd International Conference on Numerical Ship Hydrodynamics*, pages 30–38, Berkeley.

Di Mascio, A., Broglia, R., and Muscari, R. (2009). Prediction of hydrodynamic coefficients of ship hulls by high-order Godunov-type methods *Journal of Marine Science and Technology*, 14(1):19–29.

Diez, M., Volpi, S., Serani, A., Stern, F., and Campana, E. F. (2015). Simulation-based design optimization by sequential multi-criterion adaptive sampling and dynamic radial basis functions. In *EUROGEN*

2015, International Conference on Evolutionary and Deterministic Methods for Design, Optimization and Control with Applications to Industrial and Societal Problems, Glasgow, UK, September.

Forrester, A. I., Sóbester, A., and Keane, A. J. (2007). Multi-fidelity optimization via surrogate modelling. In *Proceedings of the royal society of london a: mathematical, physical and engineering sciences*, volume 463, pages 3251–3269.

Giselle, M. F.-G., Park, C., Kim, N. H., and Haftka, R. T. (2016). Review of multi-fidelity surrogate models. In *Proceedings of the VII European Congress on Computational Methods in Applied Sciences and Engineering, ECCOMAS 2016*, Crete Island, Greece, 5–10 June.

Hardy, R. L. (1971). Multiquadric equations of topography and other irregular surfaces. *Journal of geophysical research*, 76(8):1905–1915.

Jin, R., Chen, W., and Simpson, T. W. (2001). Comparative studies of metamodelling techniques under multiple modelling criteria. *Structural and Multidisciplinary Optimization*, 23(1):1–13.

Loeven, G., Witteveen, J., and Bijl, H. (2007). A probabilistic radial basis function approach for uncertainty quantification. In *Proceedings of the NATO RTO-MP-AVT-147 Computational Uncertainty in Military Vehicle design symposium*.

Ng, L. W. T. and Eldred, M. (2012). Multifidelity uncertainty quantification using nonintrusive polynomial chaos and stochastic collocation. In *Proceedings of the 14th AIAA Non-Deterministic Approaches Conference, number AIAA-2012-1852, Honolulu, HI*, volume 43.

Pellegrini, R., Leotardi, C., Iemma, U., Campana, E. F., and Diez, M. (2016a). Multi-fidelity adaptive global metamodel of expensive computer simulations. In *Proceedings of the IEEE World Congress on Computational Intelligence, IEEE WCCI 2016*, Vancouver, Canada, 24–29 July.

Pellegrini, R., Leotardi, C., Iemma, U., Campana, E. F., and Diez, M. (2016b). A multi-fidelity adaptive sampling method for metamodel-based uncertainty quantification of computer simulations. In *Proceedings of the VII European Congress on Computational Methods in Applied Sciences and Engineering, ECCOMAS 2016*, Crete Island, Greece, 5–10 June.

Regis, R. G. (2011). Stochastic radial basis function algorithms for large-scale optimization involving expensive black-box objective and constraint functions. *Computers & Operations Research*, 38(5):837–853.

Simpson, T. W., Toropov, V., Balabanov, V., and Viana, F. A. (2008). Design and analysis of computer experiments in multidisciplinary design optimization: a review of how far we have come or not. In *12th AIAA/ISSMO Multidisciplinary Analysis and Optimization Conference*, volume 5, pages 10–12.

Sun, G., Li, G., Stone, M., and Li, Q. (2010a). A two-stage multi-fidelity optimization procedure for honeycomb-type cellular materials. *Computational Materials Science*, 49(3):500–511.

Sun, G., Li, G., Zhou, S., Xu, W., Yang, X., and Li, Q. (2010b). Multi-fidelity optimization for sheet metal forming process. *Structural and Multidisciplinary Optimization*, 44(1):111–124.

Volpi, S., Diez, M., Gaul, N. J., Song, H., Iemma, U., Choi, K., Campana, E. F., and Stern, F. (2015). Development and validation of a dynamic metamodel based on stochastic radial basis functions and uncertainty quantification. *Structural and Multidisciplinary Optimization*, 51:347–368.

Zaghi, S., Leotardi, C., Muscari, R., Dubbioso, G., Diez, M., and Broglia, R. (2015). RANS hydrodynamic characterization of a USV SWATH configuration including design optimization. In *18th Numerical Towing Tank Symposium*, Cortona, Italy, September.

Comparison of uRANS and BEM-BEM for propeller pressure pulse prediction: E779A propeller in a cavitation tunnel

Paolo Perali[*,†], **Thomas Lloyd**[†] **and Guilherme Vaz**[‡]
[*] ECN, Nantes/FR, [†]MARIN Academy, Wageningen/NL, [‡] MARIN, Wageningen/NL
t.lloyd@marin.nl

1 Introduction

Studying pressure fluctuations from marine propellers is important when hull fatigue and comfort onboard are of interest. While potential flow tools, based on boundary element methods (BEM), are still commonplace for propeller design, viscous flow codes, solving the unsteady Reynolds-averaged Navier Stokes (uRANS) equations, are nowadays mature enough to study cavitation, as well as pressure pulses. This work is a deeper investigation of the wetted and cavitating flow around the INSEAN E779A propeller in a cavitation tunnel as studied within the CRS SHARCS working group (Vaz *et al.*, 2015). Previously, MARIN was only able to perform one wetted and one cavitating computation using the uRANS code ReFRESCO. In this paper, the sensitivity of such computations to timestep and turbulence model will be examined. In addition, further simulations using a BEM-BEM coupling of MARIN's PROCAL and EXCALIBUR codes, will be presented and evaluated, including comparison to experimental data and results from a RANS-BEM-BEM coupling performed by DRDC during CRS SHARCS .

2 Computational methods

The viscous flow results presented in this paper are obtained using ReFRESCO (www.refresco.org). For brevity full details of the code are omitted here; we refer the reader to, for example, Lloyd *et al.* (2015) for full details of the code, especially related to propeller applications. All computations were performed in unsteady mode, using sliding interfaces for communication between the rotating and non-rotating grid regions. The two turbulence models used in the comparison were the $k-\omega$ SST (Menter *et al.*, 2003) and $k-\sqrt{k}L$ (Menter *et al.*, 2006) models. Cavitation was included using a homogeneous mixture approach based on a modified version of the model of Sauer and Schnerr (2001).

Potential flow computations were also performed using PROCAL (Vaz, 2005) and EXCALIBUR (van Wijngaarden, 2011). PROCAL is an unsteady boundary element code, which can read a prescribed inflow velocity distribution (as carried out here, using an effective wake computed by DRDC) or coupled with a RANS solver (see, for example, the results of DRDC in Hally (2015)). EXCALIBUR meanwhile, solves the frequency domain Laplace or Helmholtz equation to compute the scattered pressure due to the presence of solid boundaries in the flow. The resulting harmonic amplitudes and phases are then used to reconstruct time traces of the pressure signals for comparison to ReFRESCO results.

3 Test case setup

The test case is based on the experiments described in Salvatore (2007), for the INSEAN E779A propeller operating behind an artificial wake in a cavitation tunnel. Pressure fluctuations were measured using sensors (P1-P4) located on the tunnel walls and in-flow hydrophones (H1-H4), as shown in Fig. 1. Computations were performed for one operating condition, characterised by an advance coefficient $J = 0.897$ and cavitation number $\sigma = 2.5$, where $J = U_0/nD$ and $\sigma = 2(p_0 - p_v)/\rho_l U_0^2$, with U_0 the inflow velocity, ρ_l liquid density, n propeller rotation rate, D propeller diameter, and p_0 and p_v the reference and vapour pressures. Results for the thrust coefficient ($K_T = T/\rho_l n^2 D^4$, where T is the axial propeller thrust), cavity volume and pressure fluctuations will be compared to those obtained by DRDC using a RANS-BEM-BEM coupling (see (Vaz *et al.*, 2015)) as well as experimental data (where available).

ReFRESCO computations used a grid designed to give improvements over the results originally obtained by MARIN within the CRS SHARCS project. The structured propeller grid consisted of 1.5M cells, while an unstructured grid generator was used to produce the tunnel grid, focussing on improved resolution of the propeller inflow and pressure probes. This resulted in 12.6M cells for the non-rotating grid region. For PROCAL, 96 chordwise and 48 spanwise panels were used. The EXCALIBUR computations used a discretised tunnel geometry of 3200 panels. Pictures of the ReFRESCO and PROCAL grids are given in Fig. 2.

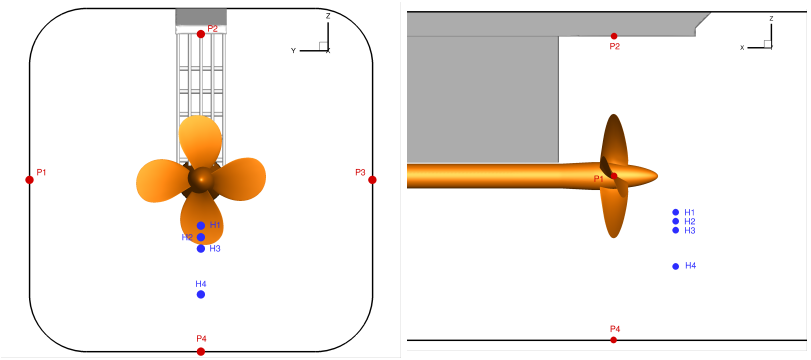

Fig. 1: Locations of the sensors and hydrophones within cavitation tunnel setup.

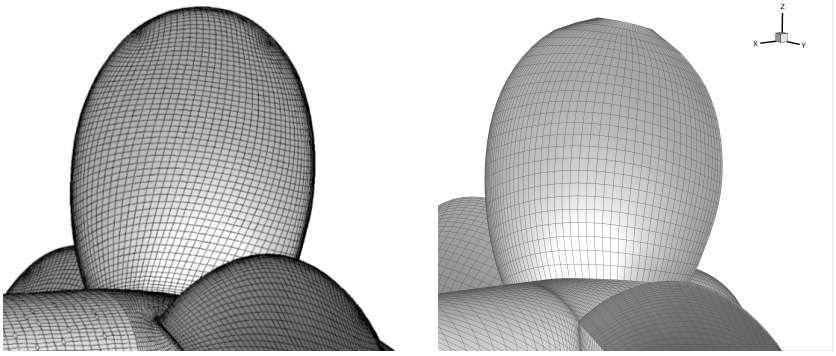

(a) ReFRESCO (b) PROCAL

Fig. 2: Propeller surface grids for the ReFRESCO and PROCAL computations.

4 Wetted flow

Fig. 3 shows comparison of the new and old grids, using the $k-\omega\ SST$ turbulence model and a timestep equivalent to $\Delta\theta = 3°$. The improved grid used in this work allowed to better solve the tip vortex than the original grid used in the CRS SHARCS project, as well as better capturing the vortex shedding from the baffle support rods. In order to investigate the influence of the timestep a computation was also performed using $\Delta\theta = 1°$. Although differences in the thrust coefficient were seen to be minimal, the pressure fluctuations were more sensitive, as shown in Fig. 4 for probe P4. The pressure amplitudes are seen to decrease with the timestep. For wetted flow conditions, no noticeable differences were observed between the $k-\omega\ SST$ and $k-\sqrt{k}L$ models.

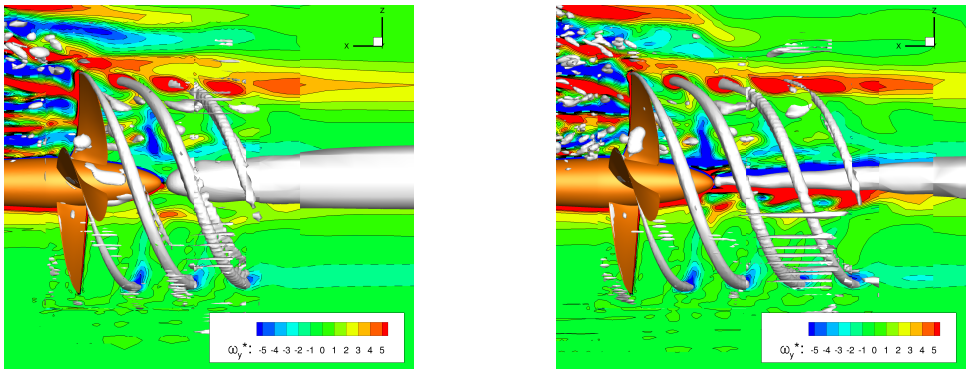

(a) CRS SHARCS grid (b) New grid

Fig. 3: Centerline slices of normalised vorticity and isosurfaces of the Q criterion ($Q = 1$).

A BEM-BEM computation was performed for the wetted flow using $\Delta\theta = 2.5°$. The averaged thrust coefficient obtained with PROCAL is smaller than the ones found with ReFRESCO and by DRDC as shown on Fig 5. This might be due to blockage of the tunnel walls which is not taken into account with PROCAL. A phase shift was obtained between the viscous flow computation and the potential flow

computations which is also found in the pressure fluctuations presented in Fig. 5. The amplitudes of the pressure fluctuations were found to be very similar between ReFRESCO and EXCALIBUR computations and almost identical between fully BEM approach and RANS-BEM-BEM coupling of DRDC.

5 Cavitating flow

Next comparison is made between the two turbulence models for cavitating flow conditions. The computation performed within the CRS SHARCS project (using the $k-\omega\ SST$ turbulence model) is named $CC0$ while this new computation (using the $k-\sqrt{k}L$ turbulence model) is named $CC1$ in the following figures. Hub cavitation occurs with the new computation which was not seen previously. The amplitudes of the cavity volume fluctuations are also smaller for the computation using the $k-\sqrt{k}L$ model as shown on Fig. 6. Since the propeller grid is the same for the two computations, those differences are mainly due to the turbulence model; the $k-\sqrt{k}L$ model is expected to better predict cavity dynamics because it produces less eddy viscosity, as shown in Fig. 7.

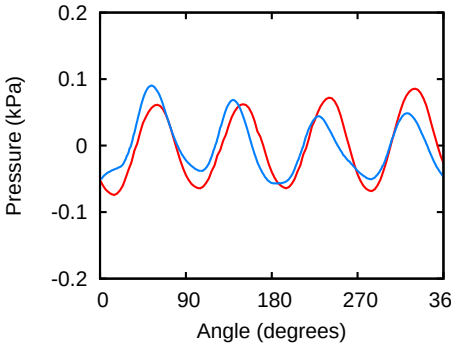

Fig. 4: Pressure fluctuations at P4 for wetted flow computed using ReFRESCO, with $\Delta\theta = 3°$ (red) and $\Delta\theta = 1°$ (blue).

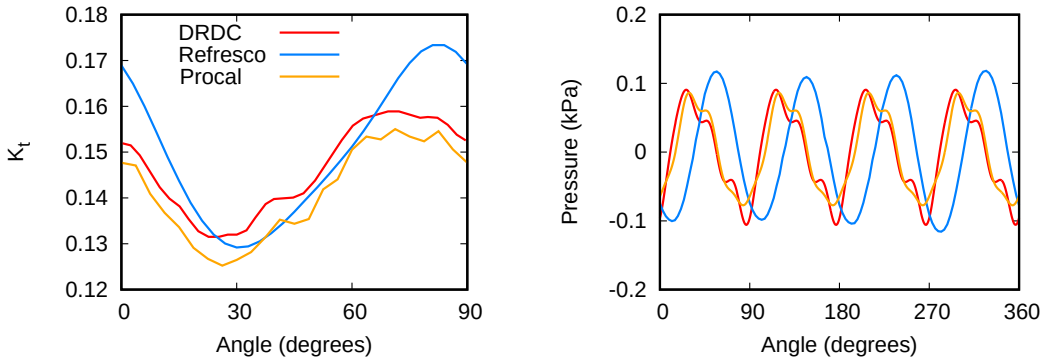

Fig. 5: Thrust coefficients and pressure fluctuations at P1 for wetted flow computed by MARIN (with ReFRESCO and PROCAL-EXCALIBUR) and RANS-BEM-BEM coupling from DRDC.

The effect of changing the timestep on the cavity volume and pressure fluctuations at sensor 3 is revealed in Fig. 8. According to basic theory the amplitudes of the pressure pulses are proportional to the second temporal derivative of the cavity volume. As presented in Fig. 8, with the coarser timestep the amplitude of the cavity volume fluctuations is smaller and thus the same trend is observed for the pressure pulse as shown for P3.

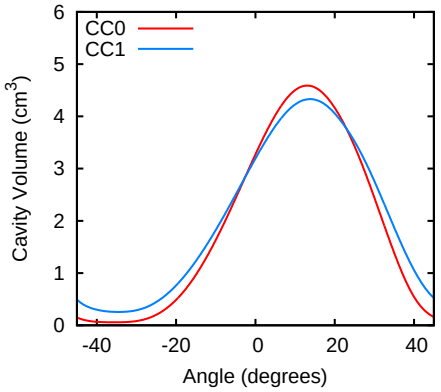

Fig. 6: Cavity volumes computed using ReFRESCO for computations CC0 and CC1.

In Fig. 9, comparisons of the thrust coefficients and cavity volumes obtained by MARIN with ReFRESCO and PROCAL are presented as well as the results obtained by DRDC. The average thrust coefficients obtained with the potential flow approaches are again smaller than that from ReFRESCO. While the maximum of cavity occurs around $\theta = 17°$ for ReFRESCO, results obtained with PROCAL and by DRDC show a maximum around $\theta = 5°$. The differences in the cavity volume between the DRDC and MARIN PROCAL computations might be due to the timestep or the grid, and requires further investigation.

Pressure fluctuations obtained at the sensors with the three approaches are compared with experimental values in Fig. 10. Results from ReFRESCO agree very well with experiments. Note that for P2, the experimental data are not considered reliable. A phase shift is obtained between the results obtained by the potential flow approaches and experiments which is not yet understood. Amplitudes of the fluctuations obtained by DRDC are of the same order as the experiments, while those from the PROCAL-EXCALIBUR coupling are sometimes higher than the experimental values and DRDC results. These differences might be due to differences in the grid and should be investigated further.

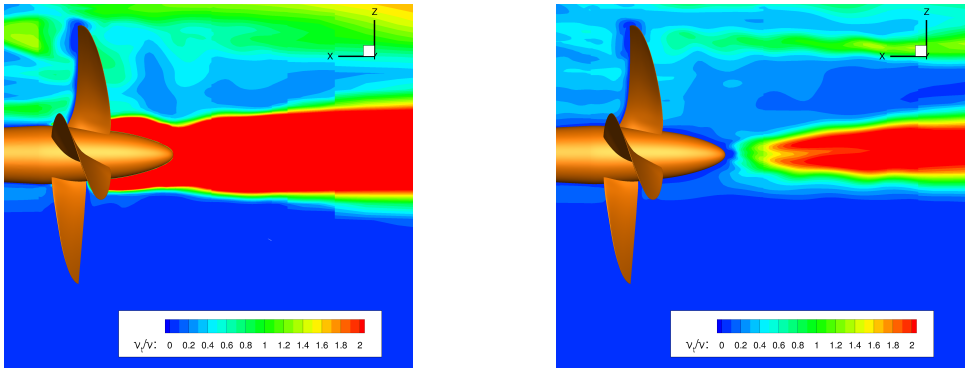

(a) CC0 (b) CC1

Fig. 7: Slices of the normalised eddy viscosity in the propeller wake for compuations CC0 and CC1.

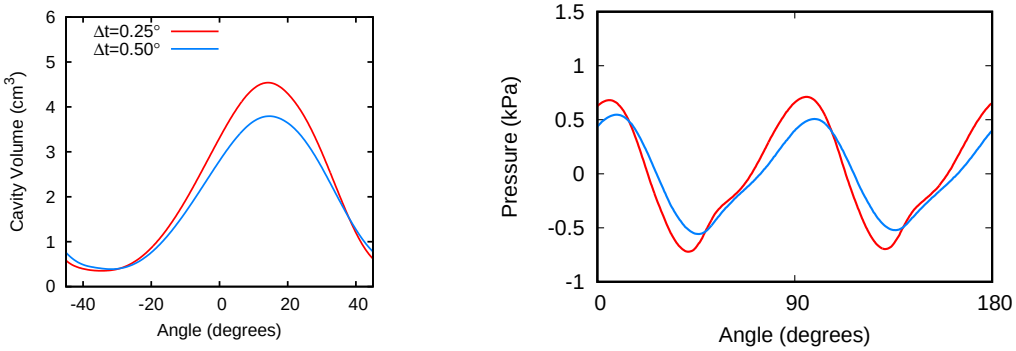

Fig. 8: Cavity volume and pressure fluctuation at P3 using ReFRESCO with $\Delta\theta = 0.5°$ and $0.25°$.

The cavity patterns obtained for three angles using ReFRESCO ($\Delta\theta = 0.25°$) and PROCAL are compared with experiments on Fig. 11. For all angles the cavity shape computed by ReFRESCO agrees very well with the experiments, although the extent is slightly underpredicted. The PROCAL computation was not able to predict cavitation at low radii. The best agreement with experiments is obtained for $\theta = 0°$ while for $\theta = -20°$ and $\theta = 20°$ less cavitation is predicted by PROCAL. This clearly shows that the maximum cavity extent occurs around $\theta = 0°$ for the PROCAL computations.

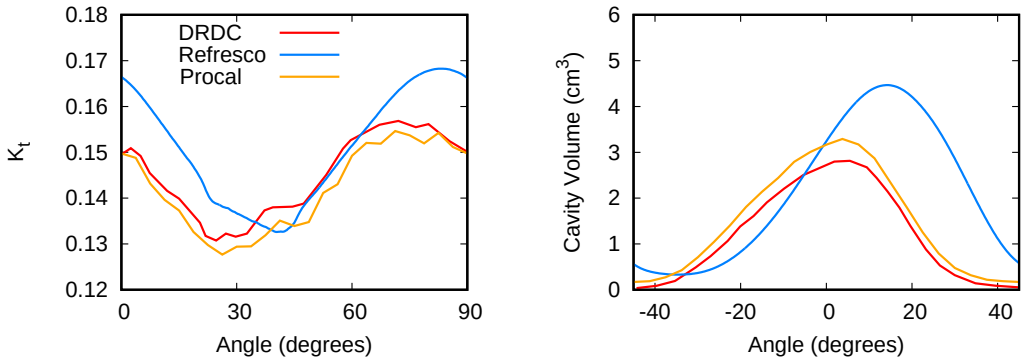

Fig. 9: Thrust coefficients and cavity volumes computed using ReFRESCO and PROCAL-EXCALIBUR coupling, and compared to RANS-BEM-BEM results from DRDC.

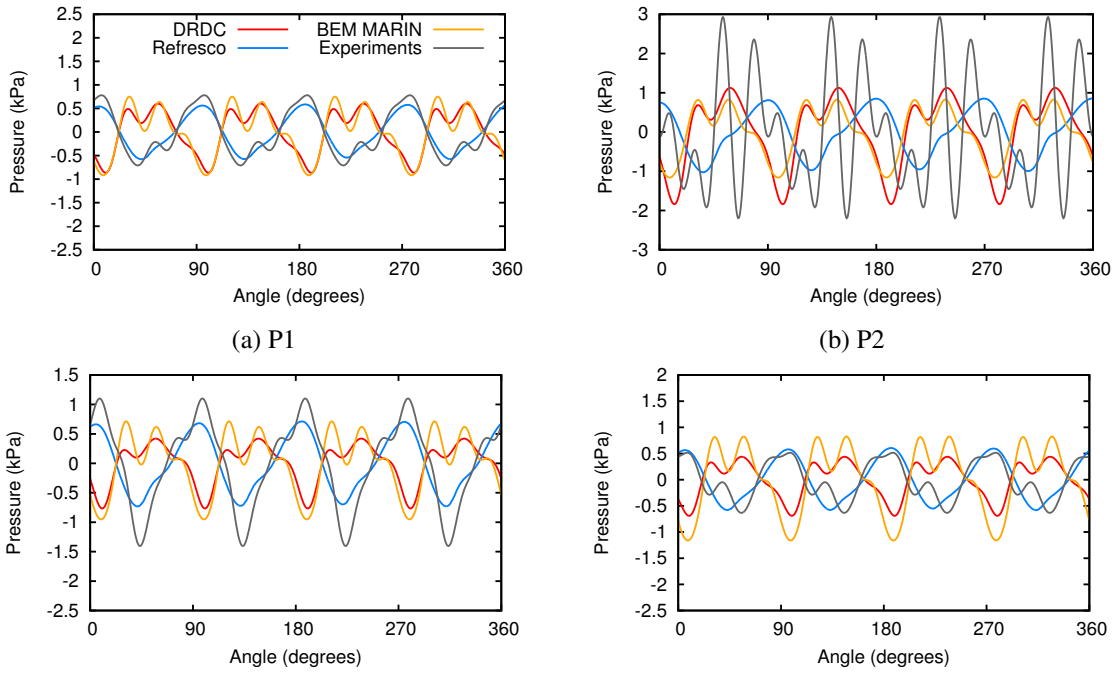

(a) P1 (b) P2

(c) P3 (d) P4

Fig. 10: Pressure fluctuations at the sensors computed using ReFRESCO and PROCAL-EXCALIBUR coupling, compared to RANS-BEM-BEM results from DRDC and experiments.

6 Summary

In this work a comparison between the uRANS code ReFRESCO and a coupling between the BEM codes PROCAL and EXCALIBUR was made for wetted and cavitating flows. PROCAL computations took ~hours on a PC, while ReFRESCO required approximately one week using 128 cores on MARIN's computing cluster. The results here can be considered as an investigation of the sensitivity to grid density, timestep and turbulence model, and provide a basis for further verification studies.

For wetted flow, while the thrust coefficient predicted by ReFRESCO was not seen to be sensitive to the timestep, this was not true for the amplitudes and phases of the pressure fluctuations. The thrust predicted by PROCAL was found to be smaller than with ReFRESCO and a phase shift was present. However, amplitudes of the pressure fluctuations obtained using the two approaches were similar.

Cavitating flow results from ReFRESCO showed strong sensitivity to the timestep. Despite this, the cavity patterns and pressure fluctuations were in good agreement with experiments. The pressure pulses obtained with PROCAL and EXCALIBUR showed a large phase shift compared to the experimental results. The cavity volume obtained with PROCAL was found to be very sensitive to the grid and timestep, and thus led to higher pressure fluctuations. Therefore an uncertainty analysis should be performed for PROCAL cavitating computations.

Acknowledgements

We thank DRDC for allowing us to use the results they obtained within the CRS SHARCS working group.

References

Hally, D. (2015), Propeller analysis using RANS/BEM coupling accounting for blade blockage. In: *Proceedings of the 4th International Symposium on Marine Propulsors*, 31st May-4th June, Austin.

Lloyd, T.P., Vaz, G., Rijpkema, D.R. and Schuiling, B. (2015), The Potsdam Propeller Test Case in oblique flow: prediction of propeller performance , cavitation patterns and pressure pulses. In: *Proceedings of the 2nd International Workshop on Cavitating Propeller Performance*, 4th June, Austin.

Menter, F.R., Kuntz, M. and Langtry, R. (2003), Ten years of industrial experience with the SST turbulence model.

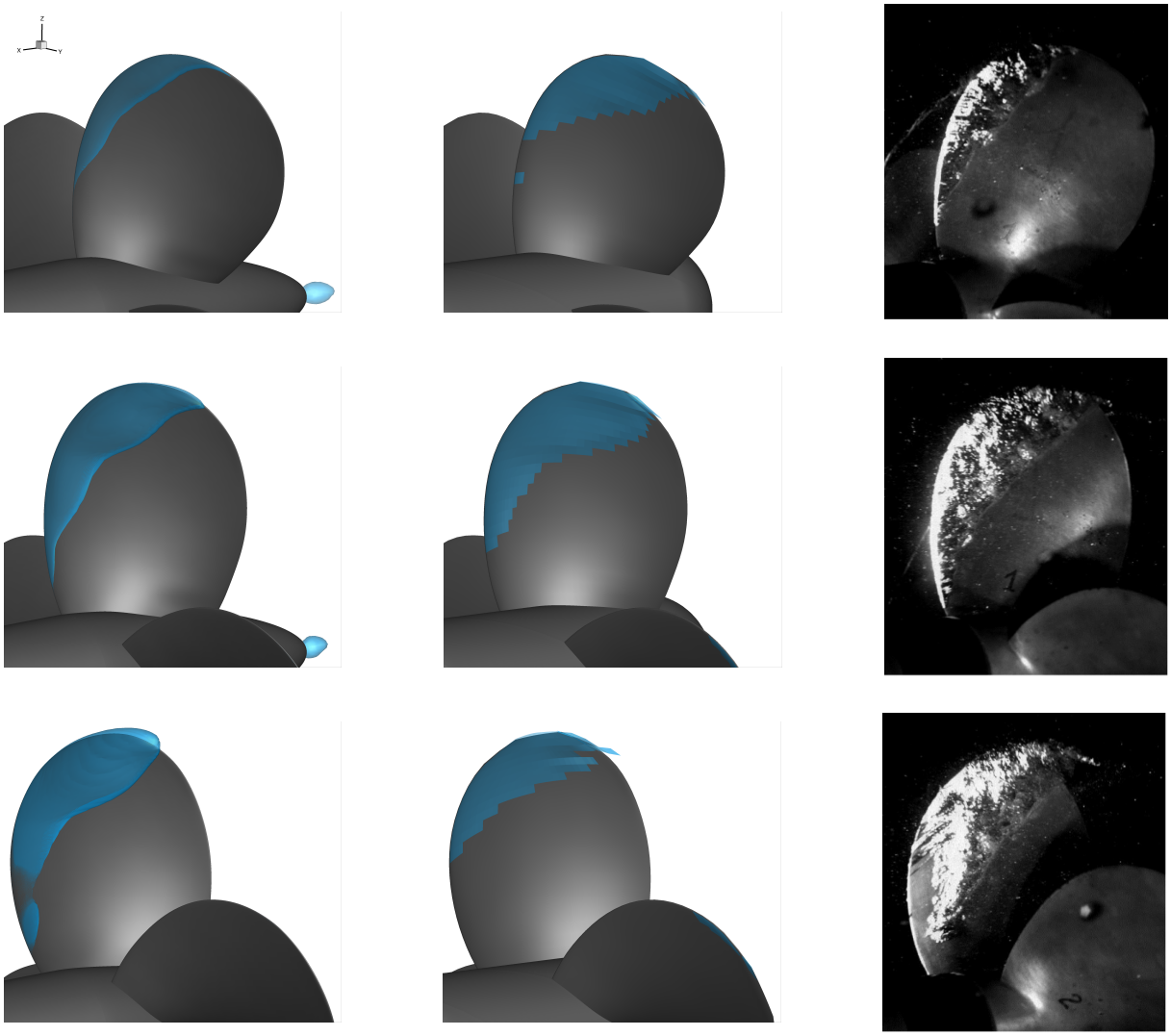

(a) ReFRESCO (b) PROCAL (c) Experiments

Fig. 11: Cavity patterns computed using ReFRESCO and PROCAL, compared to experiments for rotational positions: $\theta = -20°$ (top), $\theta = 0°$ (middle) and $\theta = 20°$ (bottom).

In: K. Hanjalic, Y. Nagano and M. Tummers (eds.), *Turbulence, Heat and Mass Transfer 4*, Begell House, pp. 625–632.

Menter, F.R., Egorov, Y. and Rusch, D. (2006), Steady and unsteady flow modelling using the k-kL model. *Proceedings of the International Symposium on Turbulence, Heat and Mass Transfer*: pp. 403–406, doi: 10.1615/ICHMT.2006.TurbulHeatMassTransf.800.

Salvatore, F. (2007), The INSEAN E779A propeller experimental dataset. *Tech. rep.*, INSEAN, Report No. D4.1.3.

Sauer, J. and Schnerr, G.H. (2001), Development of a new cavitation model based on bubble dynamics. *Zeitschrift für Angewandte Mathematik und Mechanik*, **81**(S3): pp. 561–562, doi:10.1002/zamm.20010811559.

van Wijngaarden, E. (2011), *Prediction of propeller-induced hull-pressure fluctuations*. Ph.D. thesis, Maritime Research Institute Netherlands.

Vaz, G. (2005), *Modelling of sheet cavitation of hydrofoils and marine propellers using boundary element methods*. Ph.D. thesis, Instituto Superior Technico, Lisbon.

Vaz, G., Hally, D., Huuva, T., Bulten, N., Muller, P., Becchi, P., Herrer, J.L.R., Whitworth, S., Mace, R. and Korsström, A. (2015), Cavitating Flow Calculations for the E779A Propeller in Open Water and Behind Conditions: Code Comparison and Solution Validation. In: *4th International Symposium on Marine Propulsors*, 31st May-4th June, Austin, pp. 330–345.

Damping of Free Surface Waves - State of the Art and Future Developments

Robinson Perić, Moustafa Abdel-Maksoud
Institute for Fluid Dynamics and Ship Theory (M-8), Hamburg University of Technology (TUHH), Germany
robinson.peric@tuhh.de

1 Introduction

For flow simulations, it is usually desired to choose the computational domain as small as possible to reduce the computational effort. However when simulating wave propagation, undesired wave reflections at the domain boundaries must be minimized. If this is not achieved, it can lead to large errors in the results. For practical purposes, it is desired to be able to estimate the amount of undesired reflection before running the simulation. The same problem holds when coupling different flow solvers. Of the various techniques for reducing undesired reflections (see Perić and Abdel-Maksoud (2016)), this paper is concerned with the ones that apply source terms to the governing equations in a zone adjacent to the corresponding domain boundaries. This includes wave damping zones (also called absorbing layers, sponge layers, porous media layer) and forcing zones (also called coupling zones, relaxation zones, Euler overlay method), see e.g. Cao et al. (1993), Choi and Yoon (2009), Ferrant et al. (2008), Guignard et al. (1999), Israeli and Orszag (1981), Kim et al. (2012), Park et al. (1999), Wöckner-Kluwe (2013). A possible distinction could be that *forcing zones* apply a forcing term to several or all of the governing equations, while *damping zones* apply a forcing term (formulated so that it can be interpreted as damping term) in only one of the governing equations. However, these approaches can all be generalized as forcing approaches as outlined below, so in the following the term '*forcing*' will be used.

The aim of this paper is to point out the necessity to adjust the forcing coefficients according to the wave parameters. The default values do not provide reliable damping. This holds for wave damping, coupling of different flow solvers and for speeding up convergence in ship resistance computations. The current state of the art and future developments are outlined. Recommendations how to reliably produce (close-to) optimum setup of these approaches are given. The findings are presented for free surface waves, but are expected to apply to potential flow simulations as well, and also to wave simulations in other disciplines (electromagnetic waves, gravitational waves, etc.).

2 General Description of Forcing Approaches

The governing equations consist of the equation for mass conservation, the three equations for momentum conservation and the equation for the volume fraction, which describes the distribution of the phases:

$$\frac{\mathrm{d}}{\mathrm{d}t}\int_V \rho \,\mathrm{d}V + \int_S \rho(\mathbf{v}-\mathbf{v}_g)\cdot\mathbf{n}\,\mathrm{d}S = 0 \quad , \tag{1}$$

$$\frac{\mathrm{d}}{\mathrm{d}t}\int_V \rho u_i \,\mathrm{d}V + \int_S \rho u_i(\mathbf{v}-\mathbf{v}_g)\cdot\mathbf{n}\,\mathrm{d}S = \int_S (\tau_{ij}\mathbf{i}_j - p\mathbf{i}_i)\cdot\mathbf{n}\,\mathrm{d}S + \int_V \rho\mathbf{g}\mathbf{i}_i \,\mathrm{d}V + \int_V \rho q_i \,\mathrm{d}V \quad , \tag{2}$$

$$\frac{\mathrm{d}}{\mathrm{d}t}\int_V \alpha_{\mathrm{water}} \,\mathrm{d}V + \int_S \alpha_{\mathrm{water}}(\mathbf{v}-\mathbf{v}_{\mathrm{g}})\cdot\mathbf{n}\,\mathrm{d}S = \int_V q_\alpha \,\mathrm{d}V \quad . \tag{3}$$

Here V is the control volume (CV) bounded by the closed surface S, $\mathbf{v}$ is the velocity vector of the fluid with the Cartesian components u_i, $\mathbf{v}_g$ is the grid velocity, $\mathbf{n}$ is the unit vector normal to S and pointing outwards, t is time, p is the pressure, ρ are fluid density, τ_{ij} are the components of the viscous stress tensor, $\mathbf{i}_j$ is the unit vector in direction x_j, with volume fractions α_{air} and α_{water} for air and water,

respectively. It holds $\alpha_{\text{water}} + \alpha_{\text{air}} = 1$. Unless severe wave breaking occurs, the propagation of ocean waves is a nearly inviscid phenomenon. Thus the present results apply regardless which formulation for τ_{ij} is chosen or whether it is neglected altogether. Undesired wave reflections can by minimized by applying source terms e.g. for volume fraction, q_α, and momentum, q_i. Their general form[1] is

$$q_\alpha = \gamma b(x) \left(\alpha_{\text{water,ref}} - \alpha_{\text{water}}\right) \quad , \tag{4}$$

$$q_{\text{i}} = \gamma b(x)(u_{i,\text{ref}} - u_i) \quad , \tag{5}$$

with reference volume fraction $\alpha_{\text{water,ref}}$, reference velocity component $u_{i,\text{ref}}$, forcing strength γ and blending function $b(x)$. The unit of γ is $\left[\frac{1}{\text{s}}\right]$. It regulates the magnitude with which the solution at a given cell is forced against the reference solution. The optimum value for γ is case-dependent.

When no coupling to other flow solvers is intended, the classical '*wave damping*' corresponds to a forcing, where the reference solution is the hydrostatic solution for the undisturbed free surface; often, this corresponds to the initial condition. The blending term $b(x)$ regulates the distribution of the source term over the domain, where x is the wave propagation direction. Many different types of blending functions can be applied. Common choices are constant blending $b(x) = 1$, linear blending $b(x) = \frac{x - x_{\text{sd}}}{x_{\text{ed}} - x_{\text{sd}}}$, quadratic blending $\left(\frac{x - x_{\text{sd}}}{x_{\text{ed}} - x_{\text{sd}}}\right)^2$, cosine-square blending $b(x) = \cos^2\left(\frac{x - x_{\text{sd}}}{x_{\text{ed}} - x_{\text{sd}}}\right)$, as illustrated in Fig. 1. Though so far the optimum blending function is not known, generally higher order blending functions are preferred, since they proved more effective in several investigations (e.g. Israeli and Orszag (1981)). In the following, an exponential blending is used:

$$b(x) = \left(\frac{e^{\left(\frac{x - x_{\text{sd}}}{x_{\text{ed}} - x_{\text{sd}}}\right)^2} - 1}{e^1 - 1} \right) \quad , \tag{6}$$

with start coordinate x_{sd} and end coordinate x_{ed} of the forcing zone. The thickness of the forcing zone is $x_{\text{d}} = |x_{\text{ed}} - x_{\text{sd}}|$. In this work, the reflection coefficient is calculated as in experiments according to

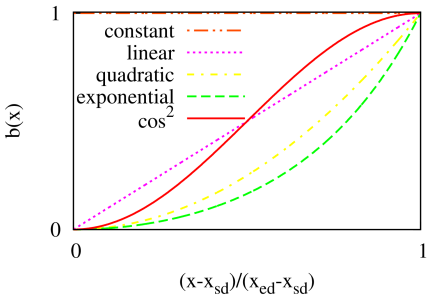

Fig. 1: Different blending functions $b(x)$ over location in forcing zone

Ursell et al. (1960) as

$$C_{\text{R}} = (H_{\text{max}} - H_{\text{min}}) \,/\, (H_{\text{max}} + H_{\text{min}}) \quad , \tag{7}$$

with minimum and maximum wave height, H_{min} and H_{max}, which result from the superposition of generated and reflected wave in the domain during one wave period, as seen in Fig. 2. However in practice, reflection coefficients are seldomly calculated for CFD simulations. Therefore it is important to be able to reliably predict the damping performance of the layer.

3 Optimum Setup of Forcing Approaches

Consider the case where a flow simulation for a regular wave has been completed, and the forcing setup provided satisfactory damping. Then, a second simulation is to be be carried out, but for a different wave.

[1]There exist also source terms which are not directly proportional to the forced quantity, e.g. $q_{\text{i}} = \gamma b(x)\rho(u_{i,\text{ref}} - u_i)|(u_{i,\text{ref}} - u_i)|$ as in Eq. (14). These are discussed in Sect. 4.

Since the wave parameters must scale consistent to Froude scaling, this has to hold for the parameters of the forcing zone as well. Thus γ and x_d scale as

$$\gamma \propto \omega, \quad x_\mathrm{d} \propto \lambda \quad , \tag{8}$$

with angular wave frequency $\omega = \frac{2\pi}{T}$ and wavelength λ. Thus to achieve similar damping[2], the parameters γ and x_d for the second simulation have to be adjusted as

$$x_\mathrm{d} = x_\mathrm{d,ref} \cdot \frac{\lambda}{\lambda_\mathrm{ref}} \quad , \tag{9}$$

$$\gamma = \gamma_\mathrm{ref} \cdot \frac{\omega}{\omega_\mathrm{ref}} \quad , \tag{10}$$

where the $x_\mathrm{d,ref}$, λ_ref, ω_ref and γ_ref are the corresponding parameters from the first simulation.

Note that recommendations for the optimum forcing setup depend on the kind and number of governing equations to which forcing is applied. This is illustrated in the following.

The classical '*wave damping*' implemented in most commercial and research flow solvers consists of a forcing according to Eq. (5), which is only applied to the vertical fluid velocity component. Existing implementations differ in the choice of $b(x)$, as discussed in the following Sect. 4.

Perić and Abdel-Maksoud (2016) showed that the optimum value γ_opt and the corresponding reflection coefficient C_R turned out to be independent of the wave steepness and also, for practical configurations[3], independent of the discretization (time step, order and choice of discretization scheme, mesh size). Further, γ_opt showed no significant dependency on the thickness x_d of the forcing zone for practical choices like $1\lambda \leq x_\mathrm{d} \leq 2\lambda$. Increasing x_d decreases the reflection coefficient C_R exponentially, and broadens the window of wave frequencies which are damped satisfactorily.

However, γ_opt depends on the choice of blending function $b(x)$. Via 2D-simulations of a wave with given period for different values of γ, it is possible to determine γ_opt and the corresponding reflection coefficients with low computational effort. Using Eqs. (9) and (10), γ_opt and x_d can be scaled so that the results can be applied to waves of any given period. In this manner, e.g. for $x_\mathrm{d} = 2\lambda$, reflection coefficients of $C_\mathrm{R} < 1\%$ can be reliably produced using the recommendation given below.

Practical Recommendation - Wave Damping
When forcing is only applied to the vertical velocities, as q_z according to Eq. (5), the following forcing setup can be recommended:

$$\gamma_{opt} \approx \Psi\omega \quad , \tag{11}$$

with $\Psi = \pi$, wave frequency ω, $x_\mathrm{d} = 2\lambda$ and $b(x)$ according to Eq. (6).

For irregular waves, ω and λ can be based on the peak angular wave frequency. A more detailed description of the information in this section is given in Perić and Abdel-Maksoud (2016).

When forcing is applied to a different and/or other governing equations, then the above recommendation needs to be adjusted. To illustrate this, preliminary results are presented for the damping of a wave with period $T = 1.6\,\mathrm{s}$ and height $H = 0.15\,\mathrm{m}$, linear blending $b(x) = \frac{x - x_\mathrm{sd}}{x_\mathrm{ed} - x_\mathrm{sd}}$ and damping layer thickness $x_\mathrm{d} = 2\lambda$. The 2D simulations are run with the commercial flow solver STAR-CCM+ from CD-adapco, using the implicit segregated flow solver with second order approximations in space and time. The governing Eqs. are (1) to (3) with SIMPLE method for pressure correction and no further simplifications. In deep water conditions, the wave is generated at $x = 0\,\mathrm{m}$ propagates in positive x-direction, enters the forcing zone at $x = 4\lambda$, and at $x = 6\lambda$ there is a perfectly reflecting wall boundary. The wave is discretized by > 500 time steps per period and by ≈ 100 cells per wavelength and ≈ 16 cells per wave height. Local

[2]This means same reflection coefficient and similar free surface elevation everywhere within the forcing zone.

[3]This was confirmed for discretizations with $30 - 200$ cells per wavelength and $8 - 20$ cells per wave height. Coarser discretizations were considered impractical and not investigated.

vertical grid coarsening is used to reduce the total number of cells to ≈ 40 000. Simulations are run with different forcing strengths $\gamma \in [0.625\,\mathrm{s}^{-1}, 10240\,\mathrm{s}^{-1}]$, for forcing of x-momentum (q_x), z-momentum (q_z), both x- and z-momentum (q_x, q_z), and finally for forcing of volume fraction α and both x- and z-momentum (q_α, q_x, q_z). All forcing is done according to Eqs. (4) and (5). The results are depicted in Figs. 2 and 3. They can be applied to any regular wave of arbitrary period when scaling according to Eqs. (9) and (10).

However, the values for optimum forcing strength γ_opt are different for the different approaches. This can be explained using the distribution of the energy components. According to linear wave theory, the average energy $\bar{E} = \int_0^\lambda \int_{-h}^{\eta} \int_0^{1\,\mathrm{m}} E \,\mathrm{d}y\mathrm{d}z\mathrm{d}x$ in a regular deep water ocean wave can be subdivided as

$$\bar{E} = \bar{E}_\mathrm{pot} + \underbrace{\bar{E}_\mathrm{kin}}_{=\bar{E}_\mathrm{kin,x}+\bar{E}_\mathrm{kin,z}} \quad , \text{ where } \quad \bar{E}_\mathrm{pot} = \bar{E}_\mathrm{kin} \quad \text{and} \quad \bar{E}_\mathrm{kin,x} = \bar{E}_\mathrm{kin,z} = \frac{1}{2}\bar{E}_\mathrm{pot} \quad , \tag{12}$$

with location of the free surface η above still water level, water depth h, average potential and kinetic energy $\bar{E}_\mathrm{pot}$ and $\bar{E}_\mathrm{kin}$, and the x- and z-component $\bar{E}_\mathrm{kin,x}$ and $\bar{E}_\mathrm{kin,z}$ of the average kinetic energy.[4]

Average potential and kinetic energy in the wave have the same magnitude. Therefore applying forcing with same γ to both potential and kinetic energy (q_α, q_x and q_z) produces a forcing of twice the strength as when applying forcing with same γ only to the kinetic energy (i.e. q_x and q_z); thus $\gamma_{(\mathrm{opt},E_\mathrm{kin})} = 2\gamma_{(\mathrm{opt},E_\mathrm{pot}+E_\mathrm{kin})}$, so the curves for forcing of kinetic energies is shifted to the right in Fig. 3.

Similarly, since the x- and z-components of the kinetic energy have on average the same magnitude (i.e. $\bar{E}_\mathrm{kin,x} = \bar{E}_\mathrm{kin,z}$), applying forcing to only one of these (i.e. either q_x or q_z) shifts the optimum of γ even further to the right. Therefore, it generally holds that

$$\gamma_{(\mathrm{opt},E_\mathrm{kin,z})} = \gamma_{(\mathrm{opt},E_\mathrm{kin,x})} = 2\gamma_{(\mathrm{opt},E_\mathrm{kin})} = 2\gamma_{(\mathrm{opt},E_\mathrm{pot})} = 4\gamma_{(\mathrm{opt},E_\mathrm{pot}+E_\mathrm{kin})} \quad , \tag{13}$$

with optimum forcing strengths for the cases of forcing of w-velocity, $\gamma_{(\mathrm{opt},E_\mathrm{kin,z})}$, forcing of u-velocity, $\gamma_{(\mathrm{opt},E_\mathrm{kin,x})}$, forcing of both u- and w-velocities, $\gamma_{(\mathrm{opt},E_\mathrm{kin})}$, as well as forcing of u- and w-velocities and volume fraction α, $\gamma_{(\mathrm{opt},E_\mathrm{pot}+E_\mathrm{kin})}$.

The choice of governing equations, to which forcing is applied, results in similar reflection coefficients for $\gamma < \gamma_\mathrm{opt}$ (see shifted curves in Fig. 3, right). The wave energy components are coupled, so that e.g. a damping of the kinetic energy will also result in damping of the potential energy. However for $\gamma >> \gamma_\mathrm{opt}$ there are noticeable differences in the reflection coefficients. In this case, it does make a difference to which governing equations the forcing is applied. For example, q_x produces more reflection than q_z if the forcing is too strong. This behavior will be investigated in future studies.

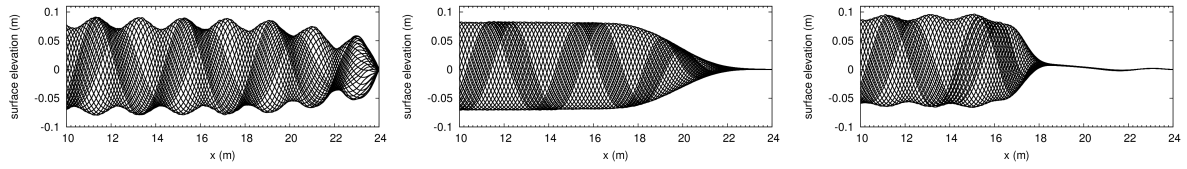

Fig. 2: Free surface elevation over location in wave propagation direction for several equally spaced time-instances during ≈ 1T with forcing terms q_x and q_z; left: $\gamma = 1.25\,\mathrm{s}^{-1}$ (too weak forcing); middle: $\gamma = 10\,\mathrm{s}^{-1}$ (≈ optimum forcing); right: $\gamma = 320\,\mathrm{s}^{-1}$ (too strong forcing)

4 Discussion of Common Implementations and Different Forcing Approaches

Examples of widely used wave damping implementations are the approaches by Choi and Yoon (2009) (implemented in STAR-CCM+ by CD-adapco) and by Park et al. (1999) (implemented in ANSYS Flu-

[4] In intermediate to shallow water $\bar{E}_\mathrm{kin,x} \neq \bar{E}_\mathrm{kin,z}$, but corresponding adjustments are expected to be straight forward.

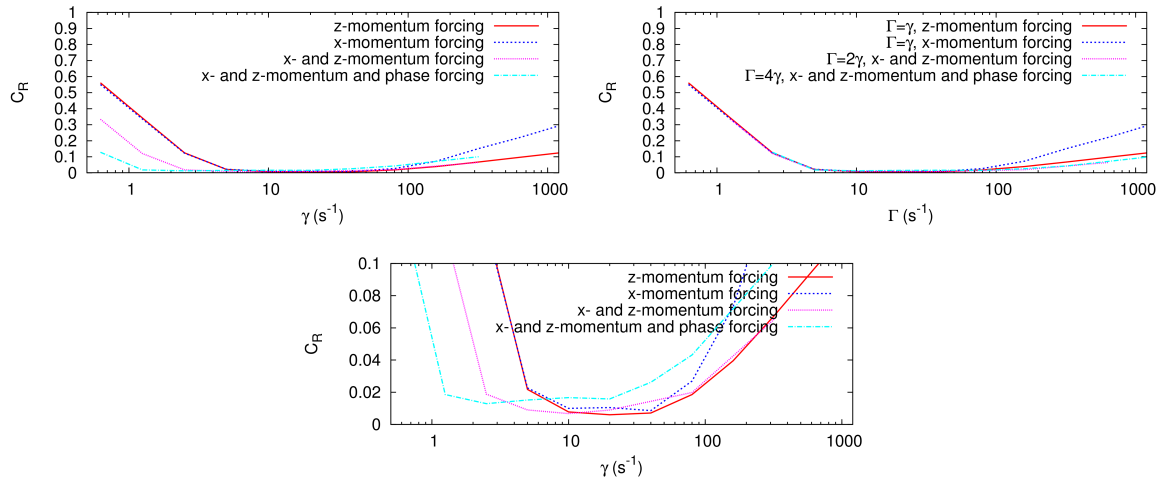

Fig. 3: Reflection coefficient C_R over forcing layer thickness x_d for a wave with period $T = 1.6\,\mathrm{s}$ and height $H = 0.15\,\mathrm{m}$, linear blending $b(x) = \frac{x-x_{sd}}{x_{ed}-x_{sd}}$ and forcing zone thickness $x_d = 2\lambda$, with wavelength λ; simulation results for x-momentum forcing, z-momentum forcing, x- and z-momentum forcing, x- and z-momentum and phase forcing; top right plot shows shifted curves according to energy (cf. Eq. (13))

ent), which are

$$q_{z_{\mathrm{CCM+}}} = \underbrace{\gamma b(x)(-w)}_{\text{forcing} \propto w} + \underbrace{f_2 b(x)(-w)|w|}_{\text{forcing} \propto w|w|} \quad , \tag{14}$$

$$q_{z_{\mathrm{ANSYS}}} = \underbrace{0.5\left(1 - \frac{z - z_{fs}}{z_b - z_{fs}}\right)}_{\text{additional factor}} \underbrace{f_3 b(x)(-w)|w|}_{\text{forcing} \propto w|w|} \quad , \tag{15}$$

with vertical velocity w, forcing strengths γ, f_2 and f_3, vertical coordinate z, with domain bottom at z_b and free water surface at z_{fs}. Further $b(x)$ is Eq. (6) for Eq. (14), while $b(x) = \left(\frac{x-x_{sd}}{x_{ed}-x_{sd}}\right)^2$ in Eq. (15). In Eq. (14), the first term corresponds to Eq. (5) and is therefore directly proportional to the vertical velocity, while the second term contains an additional factor $|w|$, which renders this forcing term proportional to $w|w|$. Equation (15) corresponds to the second term in Eq. (14) with only slightly different blending (see Fig. 1), a factor 0.5 and an additional vertical blending $\left(1 - \frac{z-z_{fs}}{z_b-z_{fs}}\right)$.

At the time of writing, the default values in the commercial codes for forcing strengths in Eqs. (14) and (15) are $\gamma = 10.0\,\mathrm{s}^{-1}$, $f_2 = 10.0\,\mathrm{m}^{-1}$ and $f_3 = 10.0\,\mathrm{m}^{-1}$. As given in Perić and Abdel-Maksoud (2016), for a $w|w|$-proportional forcing as in the second term in Eq. (14) and in Eq. (15), the optimum values for f_2 and f_3 are more than one order of magnitude larger than γ_{opt}. Thus with default settings in STAR-CCM+, the second term in Eq. (14) has a negligible effect compared to the first term. Both forcing applied directly-proportional and quadratically-proportional to the velocity produced comparable reflection coefficients at optimum settings, so both approaches may be used to damp waves successfully. However for a fixed forcing strength, directly-proportional forcing as in Eq. (5) has a wider range of wave frequencies which are damped satisfactorily, as illustrated in Fig. 4. Historically, $w|w|$-proportional forcing terms may have been introduced as analogy to porous media flows, where for larger flow rates effects like turbulence lead to nonlinearities which can be expressed as quadratically dependent on the flow velocity, such as the Forchheimer or Brinkman extension to Darcy's law, see Straughan (2008). However, this analogy is not entirely valid.[5] Even in steep nonlinear ocean waves, turbulent effects are insignificant unless there is wave breaking, which especially with regard to coupling of different flow solvers should not be provoked inside the forcing zone. Moreover, Fourier approximation methods allow to split nonlinear waves into

[5] A possibly more adequate analogy to wave damping with porous plates in wave tank experiments may be to force the turbulent viscosity to high values in the forcing zones for Reynolds Averaged Navier-Stokes (RANS) solvers.

different regular harmonics, so applying a forcing directly proportional to the velocity according to Eq. (5) already fully describes the damping also of nonlinear surface waves. Thus $w|w|$-proportional forcing terms are neither necessary nor physical for free surface wave damping.

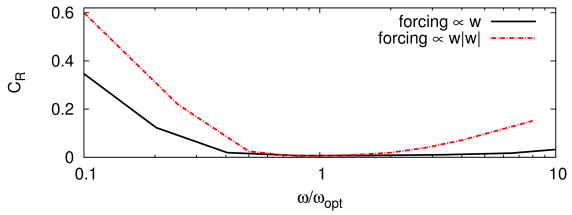

Fig. 4: Reflection coefficient C_R over wave frequency ω scaled by optimum wave frequency ω_{opt} for a fixed forcing strength γ or f_2 and forcing zone thickness $x_d = 2\lambda$; for forcing using Eq. (5) (continuous line) versus using only the second term in Eq. (14) (dotted line)

Vertical blending terms like $\left(1 - \frac{z-z_{fs}}{z_b-z_{fs}}\right)$ in Eq. (15) are not recommended. Their effect is negligible in water of several wavelengths depth. When forcing vertical velocity w they may not critically decrease the damping quality, however for horizontal velocities u and v such terms may produce unphysical shearing in the flow, especially for shallow water waves, where the particle velocities do not vary with water depth.

5 Conclusion

When using forcing zones, both forcing strength and forcing zone thickness *must* be adjusted for every simulation. Forcing terms which are directly proportional to their corresponding quantity (like velocity, volume fraction, etc.) as in Eqs. (4) and (5) are recommended, because they provide satisfactory forcing for a wider range of wave frequencies. Since the forcing used in this work can be considered a one-way-coupling of a flow solver to an analytical solution, the results are expected to be applicable also to the coupling of different flow solvers, like potential flow codes. This will be a topic of future research.

References

Y. Cao, R.F. Beck, and W.W. Schultz (1993). An absorbing beach for numerical simulations of nonlinear waves in a wave tank, *Proc. 8th Intl. Workshop Water Waves and Floating Bodies*, 17–20.

J. Choi, and S.B. Yoon (2009). Numerical simulations using momentum source wave-maker applied to RANS equation model. *Coastal Engineering*, 56, (10), 1043–1060.

P. Ferrant, L. Gentaz, C. Monroy, R. Luquet, G. Ducrozet, B. Alessandrini, E. Jacquin, and A. Drouet (2008). Recent advances towards the viscous flow simulation of ships manoeuvring in waves, *Proc. 23rd Int. Workshop on Water Waves and Floating Bodies*, Jeju, Korea.

S. Guignard, S.T. Grilli, R. Marcer, and V. Rey (1999). Computation of shoaling and breaking waves in nearshore areas by the coupling of BEM and VOF methods. *Proc. ISOPE1999*, Brest, France.

M. Israeli and S.A. Orszag (1981). Approximation of radiation boundary conditions. *Journal of Computational Physics*, 41(1), 115–135.

J. Kim, J. O'Sullivan, and A. Read (2012). Ringing analysis of a vertical cylinder by Euler overlay method. *Proc. OMAE2012*, Rio de Janeiro, Brazil.

J.C. Park, M.H. Kim, and H. Miyata (1999). Fully non-linear free-surface simulations by a 3D viscous numerical wave tank. *International Journal for Numerical Methods in Fluids*, 29, 685–703.

R. Perić, and M. Abdel-Maksoud (2016). Reliable damping of free-surface waves in numerical simulations. *Ship Technology Research*, 63(1), 1–13.

B. Straughan (2016). *Stability and Wave Motion in Porous Media*. Springer.

F. Ursell, R.G. Dean, and Y.S. Yu (1960). Forced small-amplitude water waves: a comparison of theory and experiment. *Journal of Fluid Mechanics*, 7, (01), 33–52.

K. Wöckner-Kluwe (2013). Evaluation of the unsteady propeller performance behind ships in waves. PhD thesis at Hamburg University of Technology, *Schriftenreihe Schiffbau*, 667, Hamburg.

Optimization of a ship with a large diameter propeller

Auke van der Ploeg,
A.v.d.Ploeg@MARIN.NL
Guus van der Bles and Jan van Zelderen,
Conoship International BV

1. Introduction

From several studies in the past it has been demonstrated that the fuel consumption of a ship can be decreased by enlarging the propeller and reducing its rotation rate. One of the work packages in the EU project "LeanShips" aims to integrate the design of the aft ship and a large area propeller. As a test case and demonstrator, we consider a container ship in which the propeller diameter was enlarged from 5.85m to 7.00m. As a first step, the nominal wake fields at both model and full scale were computed with the RANS-code PARNASSOS (Hoekstra, 1999), in which the SST k-ω turbulence model was used. The model and full-scale Reynolds numbers are, respectively, 1.1e7 and 1.2e9. It was assumed that modifications of the aft part of the hull will only slightly influence the wave resistance. Therefore, the computations were performed without taking into account the ship's generated wave system. However, the dynamic trim and sinkage as computed by a panel code were taken into account.

Figure 1 shows the aft part of the original hull, together with the flow separation computed at full scale. The figure demonstrates the tunnel form of the hull and the region of flow separation just upstream of the lower part of the propeller plane. The computed wake fields are shown in Figure 2. The region with flow separation extends into the propeller plane, causing a rather large area with low inflow velocity towards the propeller. Scale effects in the computed wake fields are rather strong.

It is expected that the increase of the propeller diameter decreases the required power by approximately 4%. A further decrease is expected from a combined optimization of the aft part of the hull and the propeller. In this paper, we focus on the method that can be used to optimize the hull form, in which candidate hull forms will be evaluated by full-scale RANS-computations .

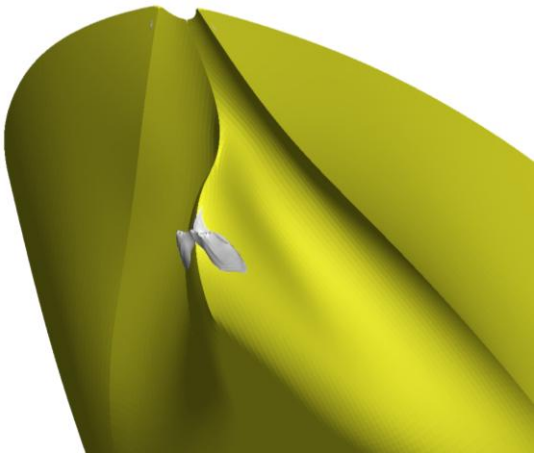

Figure 1 Fish-eye view of the aft part of the hull and flow separation at full scale.

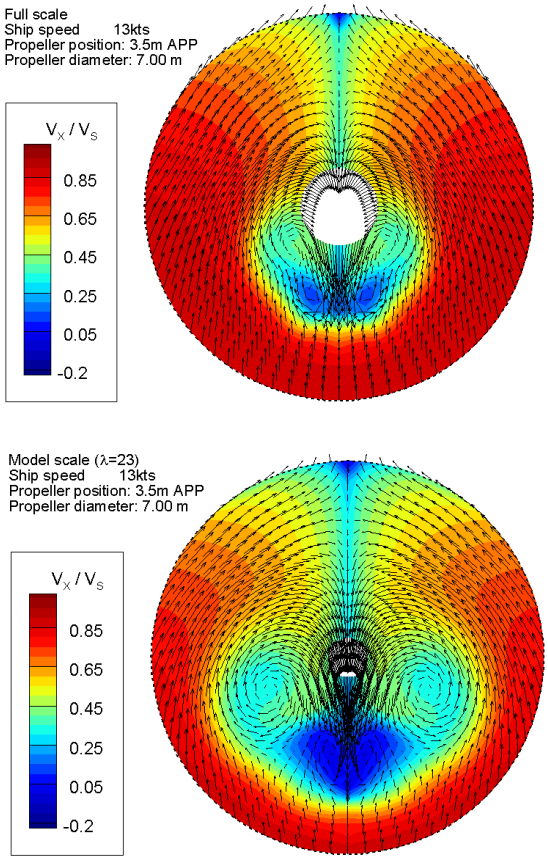

Figure 2 Computed wake fields for the original hull. Top: full scale. Bottom: model scale.

The rudder is not taken into account in the RANS-computations. The displacement is not allowed to decrease more than 0.2% and the propeller location as well as the ship's main dimensions are fixed. In this particular propeller/hull optimization project, the propeller clearance makes it challenging to compute the propulsive parameters accurately.

2. RANS method

The hull forms are evaluated with the RANS code PARNASSOS, a code developed & applied by MARIN and IST (Hoekstra, 1999). It computes the steady, turbulent flow around ship hulls by solving the discretised Reynolds-averaged Navier-Stokes equations for steady, incompressible flow.
For the optimization of the hull we use Menter's one-equation turbulence model (Menter, 1997) with the Dacles-Mariani correction (Dacles-Mariani, 1995).
The inflow boundary is located $0.5L_{pp}$ in front of the bow, and the outflow boundary at $1.5L_{pp}$ behind the transom. Due to symmetry considerations, only the starboard side is taken into account. In a *(x,y,z)*-co-ordinate system fixed to the ship, with *y=0* being the symmetry plane, *x* positive aft, and *z* upward, the lateral outer boundary is a quarter of a cylinder with axis *y=z=0* and radius $1.0L_{pp}$. At this boundary tangential velocities and pressure found from a potential-flow computation are imposed.
We use a boundary fitted, structured grid in which the number of nodes in longitudinal, girthwise and wall-normal direction is, respectively, 569, 53 and 161, leading to a total of 4.9 million nodes. A strong contraction of nodes towards the hull is used such that wall functions are not necessary, not even in full-scale computations. The grid nodes are contracted in longitudinal direction towards the propeller plane, as is demonstrated in Figure 3.
A finite-difference discretization is used with second and third-order schemes for the various terms. The resulting system of non-linear equations is solved very efficiently with respect to both CPU-time and memory usage (van der Ploeg et al, 2000).

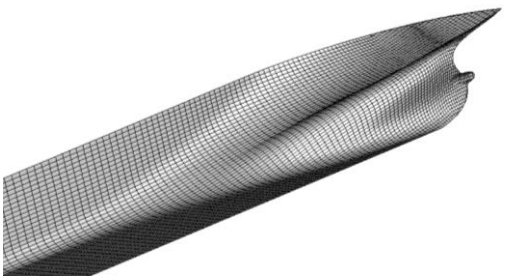

Figure 3 Wall grid around the aft part of the original hull.

Automatic grid generation
Grids need to be generated around each variant and a fully automatic grid generation procedure is therefore required. To minimize the scatter in the computed trends caused by discretization errors, these grids have to be as similar as possible. As a first step in the construction of the grid for a hull form variant, the wall grid for the original hull form is projected on the variant. Next, the 3D-grid is obtained using the usual grid-generation techniques: for this we use in-house developed elliptic grid generation software. The settings for the generation of the 3D-grid are chosen the same for all hull forms.

3. Initial RANS-BEM computation

As will be explained in the next section, for each hull form two RANS computations are performed, one without propeller action, and one RANS computation in which the propeller action is modelled as a force field. In order to obtain this force field, a RANS-computation will be performed for the original hull form, in which a boundary element method (BEM) is used to model a propeller which was designed based on the nominal wake computed at full scale (Figure 1).

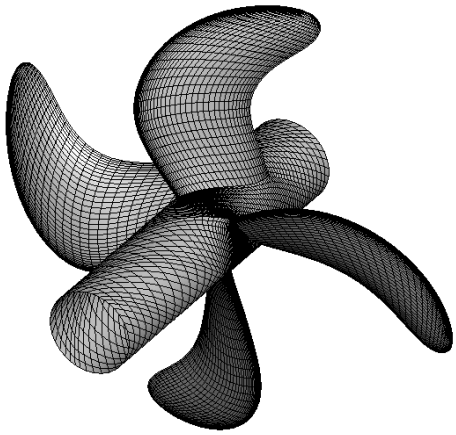

Figure 4 Large diameter propeller and panel distribution for the original hull.

The BEM-method solves the incompressible potential flow equations for lifting surfaces. The method, designated PROCAL, is being developed within MARIN'S Cooperative Research Ships (CRS) for the unsteady analysis of cavitating propellers operating in a prescribed ship wake. It has been validated for open water characteristics, shaft forces, and sheet cavitation inception and extent. The code is a low-order BEM that solves for the velocity disturbance potential. Initial validation studies

and details on the mathematical and numerical model can be found in *Vaz & Bosschers (2006)*. The panel distribution on the propeller and the hub is shown in Figure 4.

3.3 RANS-BEM coupling

The RANS-BEM computation consists of the following steps: an initial RANS computation without propeller action is performed to obtain a first estimate of the effective wake field which is used as input for the first BEM-computation. Next, a second RANS computation is performed, in which the thrust and loading distribution from the previous BEM computation, after averaging over all blade positions, is used. The rotation rate of the propeller is then adjusted using the imbalance between the resistance force from the RANS computation and the thrust predicted by the BEM computation. The effective wake is updated by subtracting the propeller induced velocities from the wake field computed by the RANS method. This process is repeated until the above-mentioned imbalance in the forces as well as the updates in the effective wake field become negligible. For all hull forms, the same correction for wave resistance, roughness etc. is imposed.

4. Object functions

The choice of the object functions is very important in hull form optimization. Minimizing the resistance is usually accompanied by a decrease of the propeller efficiency and minimizing fuel consumption brings the risk of increasing vibration hindrance. Those effects have to be taken into account. We use two object functions, decreasing the first minimizes fuel consumption and minimizing the second object function reduces the risk of erosive cavitation or vibration hindrance.

4.2 Object function for the power

we use an estimate of the power delivered to the propulsor:

$$P_D = \frac{R_T \cdot V_S}{\eta_H \cdot \eta_R \cdot \eta_O} = \frac{1-w_{eff}}{1-t}\frac{R_T \cdot V_S}{\eta_R \cdot \eta_O} \qquad (1)$$

in which R_T is the towing resistance, w_{eff} the estimated effective wake fraction, V_S the ship speed, t the thrust deduction fraction, η_o the propeller efficiency in open water, and η_R the relative rotative efficiency, approximated by 1. The behind efficiency of the propeller is defined as $\eta_B = \eta_0 \times \eta_R$. It is essential to estimate η_B, as this efficiency can vary significantly between design variations. The behind efficiency could be evaluated by a coupling with a panel code for the propeller or by incorporating the propeller in the RANS computation. However, this would mean that one optimizes the hull form for the particular propeller chosen, instead of optimising both in combination. In order to estimate better the achievable performance, η_B is obtained from the B-series of propellers (Kuiper, 1992). The thrust, wake fraction, number of blades, propeller diameter and revolution rate are fixed, while the blade area ratio and pitch ratio for each hull form are found from the B-series.

To compute the thrust deduction fraction we perform a second RANS computation including a force distribution representing the propeller with an imposed thrust T_0. This imposed thrust should be a reasonable estimate of the thrust T required for self propulsion. Assuming a linear behaviour between the resistance force on the hull and T_0, the thrust deduction coefficient can then be computed from $t=(R_0-R_T)/T_0$ with R_0 the resistance force from the second RANS computation.

The second RANS computation also computes a wake field including the propeller action: the so-called total wake. From the initial RANS-BEM computation described in section 3 we also obtain the propeller-induced velocity field. The estimated effective wake is obtained by subtracting this induced velocity field from the total wake. Hence the assumption is that the induced velocity field is the same for all hull forms.

4.2 Object function for the wake

In case of danger of erosive cavitation, one would like to prevent strong variations of the wake in circumferential direction, especially in the top half of the propeller plane. We will use the L_1-norm of the variation of

$$\beta = \tan^{-1}\left(V_x / \left(\omega \tfrac{r}{R} - V_\theta\right)\right)$$

with V_x and V_θ the axial and tangential velocity components respectively, θ the angular position in rad. and ω the propeller rotation rate in rad/s. β is the undisturbed propeller inflow angle and its variation in circumferential direction as the propeller rotates is $\partial\beta/\partial\theta$. The Wake Object Function

(WOF) is determined from integration in circumferential direction and over a range of radii from the hub to the tip and the propeller radius.

5. Required modifications

Due to the relatively small propeller clearance two modifications in the procedure for the hull form evaluation were required: 1. The determination of the effective wake in the RANS-BEM method and 2. The interpolation of the propeller force field to the 3D-grid used for every variant.

Originally, the effective wake was obtained from an extrapolation using several planes upstream of the propeller. An example in which two of such planes are used is shown in Figure 5.

In this particular case, it is not possible to choose those planes in such a way that they do not intersect with the hull. As a result, unrealistic velocity distributions for both the inner- radii and in the top of the propeller plane could be obtained.

During the LeanShips project, an alternative coupling procedure for the RANS-BEM computations became available. In this new procedure, the effective wake is obtained by evaluating the propeller-induced velocities within the volume swept by the propeller and averaging over all blade positions. We have adapted this new method in the initial RANS-BEM computation. The computed effective wake fields obtained with both the 'old' and the 'new' method for one of the variants is shown in Figure 6. The figure illustrates that the strange velocity components mentioned above obtained with the old method are not present when the new method is used.

The force distribution that represents the propeller is stored in a so-called External Force Distribution (EFD)-file that contains the three force components for every grid point. In the original method, the same EFD-file was used for every hull form.

However, with large hull form deformations, the 3D-grid used for a variant can differ significantly from the 3D-grid used for the original hull form. Therefore, in the new method the EFD-file is updated for every variant, by interpolating the force field once the 3D grid is determined. Some changes were made in the interpolation routine to make it computationally more efficient: the routine was parallelized by using open MP statements, and the 3D grid is temporarily coarsened in those locations where a boundary layer resolution was required for the RANS computation. In the next section, we will compare the result obtained with the original EFD-file for every variant, and those obtained with an updated EFD-file.

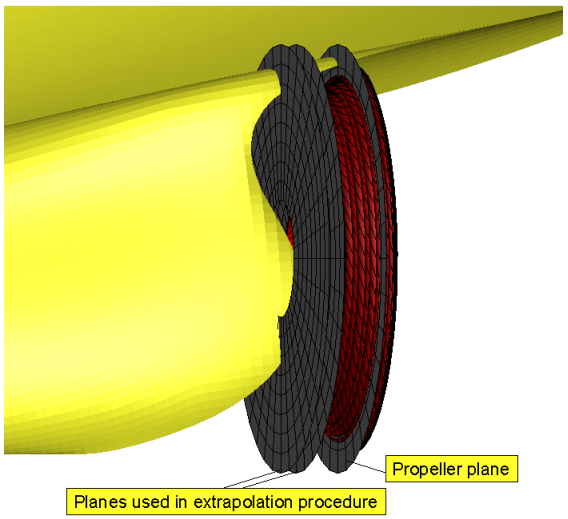

Figure 5 Yellow: ship. Red: gid cells with propeller forces. Grey: planes used to extrapolate the effective wake.

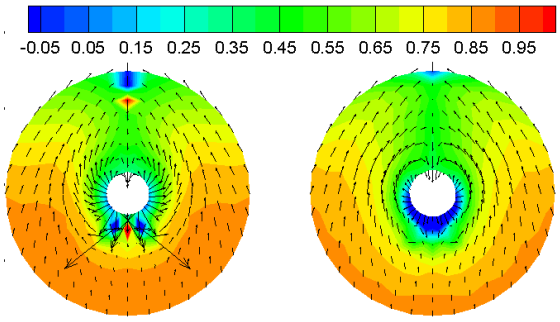

Figure 6 Comparison of effective wake fields. Left: old method. Right: new method.

6. Results

Based on RANS-BEM computations for some variants of the initial hull form, we constructed two basis hull forms (denoted by A and B) that span the design space. Parametric deformations of the geometry are obtained by interpolating between the original hull form and the basis hulls. Figure 7 shows a comparison between hull form B and the original form. Hull form B

has only a minor decrease (0.01%) of displacement.

Effect of interpolating the propeller force field. To study the effect of the interpolation of the force field that represents the propeller, Table 1 shows the results computed for several hull forms obtained with the 'old' method, in which the External Force Field (EFD)-file was the same as the EFD-file used for the original hull. Table 2 shows the same results, but now obtained with the EFD-file updated for every hull form, as explained in the previous section.

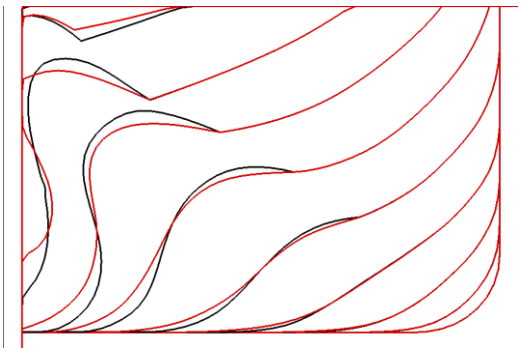

Figure 7 Comparison of the body plans of basis hull form B (red) compared with the original geometry (black).

Table 1 Relative results [%] compared to original. Same EFD-file for every hull form.

	0.6(A+B)	A	B
ΔP_D	-2.6	-2.1	-2.5
Δw_{eff}	-7.3	-10.0	-1.2
ΔT	-4.2	-3.3	-1.9
ΔR_T	-0.76	-0.22	-0.79
Δt	-14.0	-17.0	-7.0
$\Delta \eta_o$	+2.0	+2.5	+0.7
$\Delta \eta_H$	-0.9	-0.6	+1.0

Table 2 Relative results [%] compared to original. New EFD-file for every hull form.

	0.6(A+B)	A	B
ΔP_D	-2.7	-2.7	-1.4
Δw_{eff}	-7.3	-10.0	-1.2
ΔT	-3.3	-3.8	-1.1
ΔR_T	-0.76	-0.22	-0.79
Δt	-14.3	-19.5	-2.7
$\Delta \eta_o$	+2.0	+2.6	+0.5
$\Delta \eta_H$	-0.0	-0.0	+0.1

Especially for the variant B the computed decrease in the thrust deduction coefficient is significantly influenced by the interpolation of the force field that models the propeller action. When the same EFD-file is used for every hull form, this decrease is significantly higher than in case the EFD-file is updated. In addition, the change in open water efficiency $\Delta\eta_o$ is slightly overestimated in case the EFD file is not updated. In that case, the computed decrease in required power P_D is significantly higher. It is therefore recommended to perform the interpolation of the force field to the 3D-grid used in the RANS computation for every hull form.

To illustrate the difference in the 'distribution of the thrust deduction coefficient' for hull form B, Figure 8 shows the distribution of contributions to the resistance obtained with propeller action (modelled as a force field using the EFD-file) minus these contributions without propeller action.

The top picture shows the results obtained with the same EFD-file as used for the original hull form, and the bottom picture shows the same obtained with the updated EFD-file. Differences are notable especially upstream of the propeller and above the propeller shaft. For the other hull forms, the influence of the interpolation of the force field to the updated 3D-grid is smaller, although not negligible.

The results in Table 2 already show that although hull form B has a lower resistance than hull form A, hull form A is more successful in decreasing both object functions. This trend has been found for other ships as well (van der Ploeg and Raven, 2010).

We performed a systematic variation in which hull forms were varied 'around' hull form A. The results are summarized in Figure 9 in which each symbol corresponds with an evaluated hull form. The more 'optimal' hull forms are closer to the lower-left corner of the chart. As can be seen from the figure, there is a set of hull forms (the Pareto front) that show the best compromise between decreasing the required power and the wake object function. It appears that the 'best' hull form is the basis hull form A. A combined improvement of both object functions is obtained, and the decrease of displacement is only 0.17%.

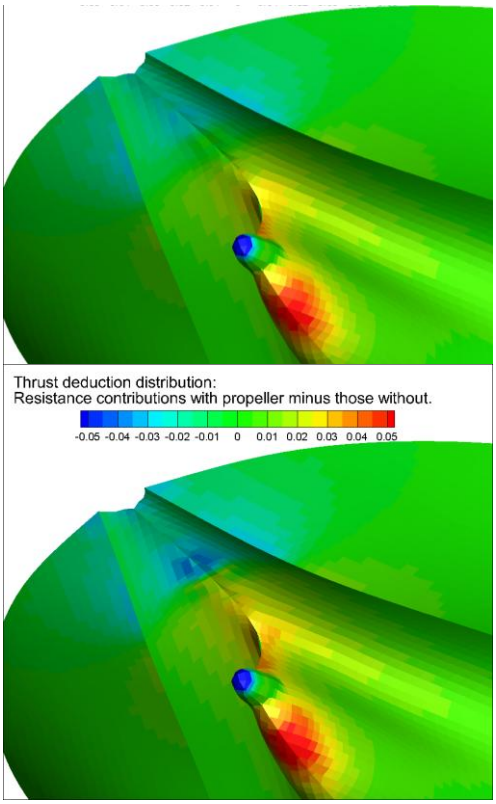

Figure 8 Distribution to the thrust deduction coefficient for hull form B. Top: EFD file from the original hull. Bottom: updated EFD file.

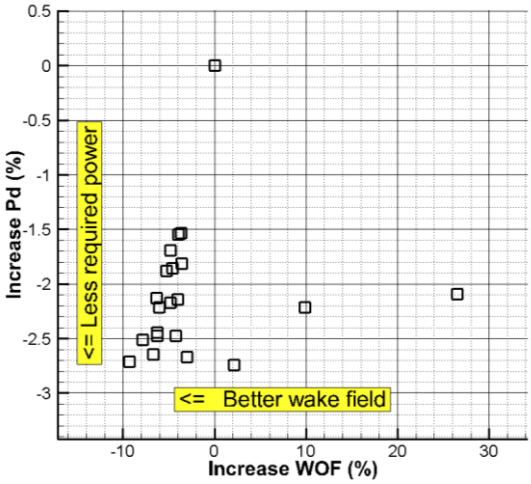

Figure 9 Pareto front computed using a two-parameter variation.

7. Conclusions

To minimize fuel consumption, it is important not only to minimize the nominal resistance but to take into account other propulsion parameters like propeller efficiency and the thrust deduction n coefficient.

A small propeller clearance can cause some extra challenges for the quality of the hull form evaluations. The evaluation of the effective field has to be done in the volume swept by the propeller, instead of obtaining the effective field from an extrapolation using the velocity field upstream of the propeller. In addition, the propeller force field has to be interpolated to the 3D-grid for every hull form.

It appeared to be possible to obtain a combined improvement of both object functions. Hence on top of the expected decrease in required power of about 4% due to only the increase of the propeller diameter we can expect an extra decrease of about 2.7% due to the modification of the gondola.

Acknowledgement

LeanShips has received funding from the European's Horizon 2020 research and innovation programme (Contract No.: 636146).

References

Dacles-Mariani, J., Zilliac, G.G., Chow, J.S., and Bradshaw, P., (1995), "Numerical/ experimental study of a wingtip vortex in the near field", AIAA Jnl, Vol. 33-9, pp. 1561-1568.

Gent W. van and Hoekstra M., (1985), "Force field approach for propeller-wake interaction", MARIN Report No. 44303-7-SR.

Hoekstra M., (1999), "Numerical simulation of ship stern flows with a space-marching Navier Stokes method", Thesis, Technical University of Delft.

Kuiper, G., (1992), "The Wageningen Propeller Series" MARIN publication 92-001. Published on the occasion of its 60th anniversary.

Menter, F.R., (1997), "Eddy-viscosity transport equations and their relation to the k-ε model", Journal of Fluids Engineering,Vol. 119, pp. 876-884.

Ploeg A. van der, Hoekstra M., and Eça L., (2000), "Combining accuracy and efficiency with robustness in ship stern flow computation", Proc. 23rd Symp. Naval Hydrodynamics, Val de Reuil, France.

Ploeg A. van der and Raven H.C., (2010), "CFD-based Optimization for Minimal Power and Wake Field Quality", Proceedings 11th International Symposium on Practical Design of Ships and other Floating Structures, Rio de Janeiro, pp. 92-101.

Vaz G. and Bosschers J., (2006), "Modelling Three Dimensional Sheet Cavitation on Marine Propellers using a Boundary Element Method", , In Cav2006 Proceedings, Wageningen, The Netherlands.

RANS and Hybrid RANS-LES simulations around the Japan Bulk Carrier of the Tokyo 2015 CFD Workshop

Patrick Queutey, Emmanuel Guilmineau, Michel Visonneau, Jeroen Wackers and Gan Bo Deng
LHEEA Lab., UMR 6598 du CNRS, Ecole Centrale de Nantes. France.
patrick.queutey@ec-nantes.fr

1 Introduction

This paper presents a computational study of the flow around the Japan Bulk Carrier (JBC) with the help of RANS and Hybrid RANS-LES modelling. The JBC hull was selected as one of the test cases in the framework of the Tokyo 2015 Workshop on Numerical Ship Hydrodynamics (T2015) [1]. Nine configurations of the JBC were considered for comparisons between the participants; experiments for these cases were conducted at NMRI (National Maritime Research Institute), SRC (Ship Building Research Centre of Japan) and Osaka University. These experiments include resistance tests, self-propulsion tests and PIV measurements of stern flow fields. Also, LDV measurement data in the wind tunnel are available from TUHH (Technical University of Hamburg-Harburg). Among the various simulations performed by our group, see Deng et al. (2015) and Visonneau et al. (2016), the emphasis of this paper is on the analysis of the local flow for the simplest configuration in resistance test conditions, namely the case C1.

The investigation is conducted with RANS ($k-\omega$ SST and anisotropic EARSM) and hybrid RANS-LES (DES-SST) models. The latter was used recently to shed some light on the flow physics. Simulations have been performed with the ISIS-CFD flow solver, which is developed by Ecole Centrale de Nantes and CNRS. In the core of the bilge vortex, it is shown that the hybrid RANS-LES model can predict the co-existence of high levels of the turbulent kinetic energy (TKE) with large levels of longitudinal vorticity which is in agreement with the experiments.

2 The Japan Bulk Carrier

The Japan Bulk Carrier (JBC) is a capesize bulk carrier, represented in Figure 1. Its length between perpendiculars at full scale is L_{PP} = 280 m, its service speed is 14.5 knots and the draft is 16.5 m, leading to a Froude number Fn = 0.142. This geometry is investigated at model scale, where its length is L_{PP} = 7 m and the Reynolds number is Re = 7.46×10^6, based on the length L_{PP} and the velocity U = 1.179 m/s. Local LDV velocity profiles at three sections S2, S4 and S7 (i.e. X/L_{pp}=0.9625, X/L_{pp}=0.9843 and

Fig. 1: Geometry of the JBC hull

X/L_{pp}=1.0000) before and after the propeller and duct were provided by the organizers. Fig. 2 shows a view of the stern with the location of the local measurement sections.

With test case C1, the main vortical structures are located at the aft-ship. An overview of the bilge vortices as obtained from RANS computation is shown in Fig. 3.

3 The ISIS-CFD flow solver

ISIS-CFD solves the incompressible unsteady Reynolds-averaged Navier-Stokes equations (URANS). It is developed by Ecole Centrale de Nantes and CNRS and available as a part of the FINE$^{\mathrm{TM}}$/Marine computing suite. The solver is based on the finite volume method to build the spatial discretization of the transport equations. The unstructured discretization is face-based, which means that cells with an arbitrary number of arbitrarily shaped faces are accepted. A second order backward difference scheme is used to discretize time. The solver can simulate both steady and unsteady flows. The velocity field is

[1] http://www.t2015.nmri.go.jp/

Fig. 2: Side view of the JBC hull with location of three measurement sections

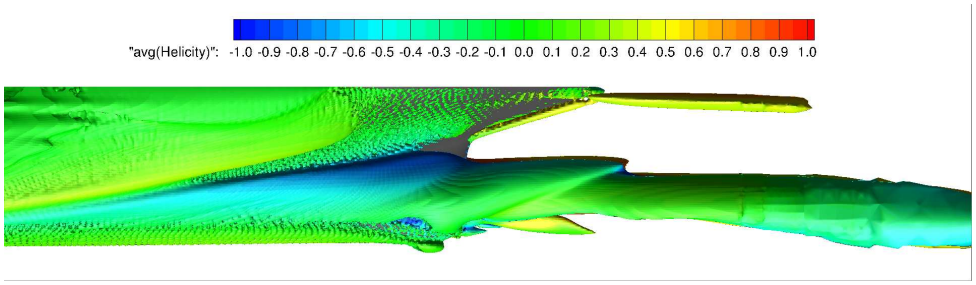

Fig. 3: Side view of the main aft-body vortex visualized by iso-surface of dimensionless invariant Q=25

obtained from the momentum conservation equations and the pressure field is extracted from the mass equation constraint, or continuity equation, transformed into a pressure equation. In the case of turbulent flows, transport equations for the variables in the turbulence model are added to the discretization. A detailed description of the solver is given by Queutey and Visonneau (2007).

The solver features sophisticated turbulence models: from the classical two-equation k-ε and k-ω models to the anisotropic two-equation Explicit Algebraic Reynolds Stress Model (EARSM), as well as Reynolds Stress Transport Models, see Duvigneau et al. (2003) and Deng and Visonneau (1999). All these are RANS models. A Detached Eddy Simulation (DES) approach based on Menter et al. (2003), DES-SST, has been introduced, see Guilmineau et al. (2011).

To enable relative motions of appendages, propellers or multiple bodies, sliding and overlapping grids approaches have been implemented. Finally, an anisotropic automatic grid refinement procedure (AGR) has been developed which is controlled by various flow-related criteria, see Wackers et al. (2014)a. Moreover, the AGR procedure is fully parallelized with a dynamic load balancing working transparently.

4 RANS simulations

The first studies carried out for the workshop involved a verification and validation study (V&V) for the resistance test including free-surface effects with RANS. The least-squares approach was used for Richardson extrapolation, see Hoekstra and Eça (2008). It is perilous to use Richardson extrapolation to conduct a solution verification exercise when the computations are performed on fully unstructured grids. However, with a special set-up, see Visonneau et al. (2016) for details, it is possible to ensure grid similarity before the insertion of viscous layer. For the total resistance prediction, a series of four grids for the half domain from 0.86M (G4) cells to 9.2M cells (G1) was used to estimate the order of convergence (1.94 with wall resolved EARSM), extrapolation error (2%) and comparison error (1.8%) for the finest grid G1. On this grid, with spatial resolution about $0.00086 L_{pp}$, the numerical discretization error is shown to be smaller than the difference between the SST k-ω and EARSM models. But looking at the predicted mean longitudinal component of the velocity in section S2 from various embedded grids, Fig. 4, the observed differences clearly indicate that a grid-independent solution has not been reached for the local flow field.

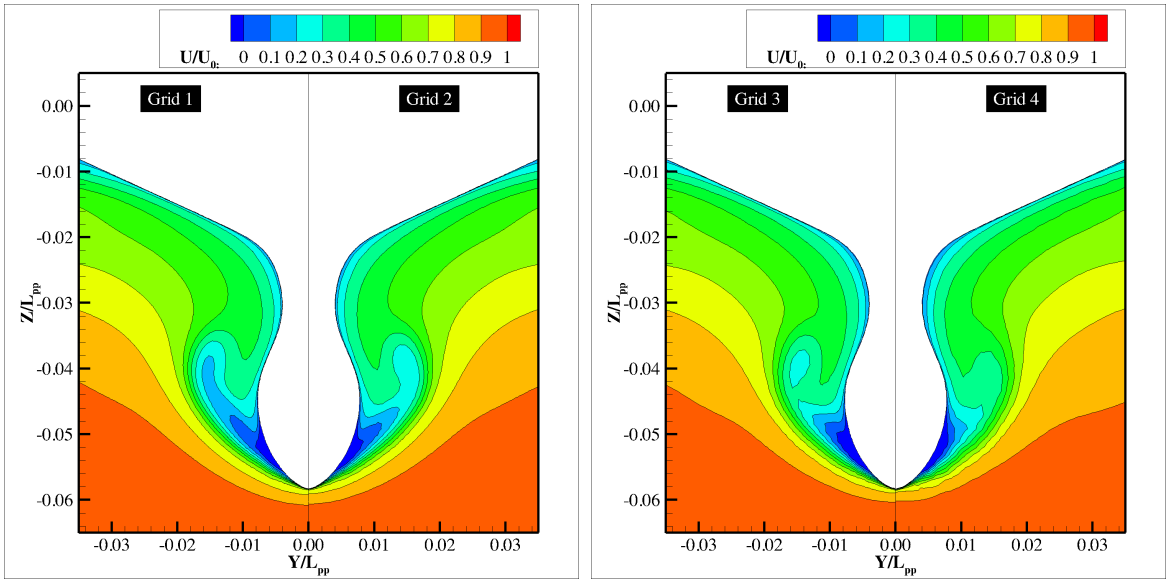

Fig. 4: U velocity contours at section S2 - Grid influence with wall resolved RANS from coarse (far right G4) to fine (far left G1)

On a similar test case, namely the KVLCC2 tanker, it was recently shown by Wackers et al. (2015) that anisotropic adaptive grid refinement with metric-based refinement criteria is suitable for the creation of the geometrically similar grid series needed in convergence studies. With the use of the Flux-component Hessian (FCH) criterion introduced in Wackers et al. (2014)b it was possible to produce grid-independent solutions in this similar situation, not only for the forces but also for the wake flow which is mandatory for advanced design of the propulsive system.

With this in mind, computations with AGR and the FCH criterion were performed tentatively to obtain a more accurate solution for the JBC. The minimum cell size was refined to about $0.00009L_{pp}$. But with such a fine grid, a flow instability developed leading to an unsteady behaviour of the large vortex structure, Fig. 5. Due to this unexpected unsteadiness, the predicted wake flow becomes quite different from what is obtained on the previous series of meshes.Such unsteadiness is also observed when the mesh is refined manually in the wake with similar grid resolution, although in that case, the amplitude of the unsteady fluctuation is not exactly the same.

During the T2015 workshop, see analysis by Visonneau (2015), at least for those who found RANS solutions which appear to be converged, a satisfactory agreement between computations and experiments was observed for the mean longitudinal component of the velocity in the core of the JBC bilge vortex. On the other hand all the RANS contributions underestimate the turbulence kinetic energy (TKE) by a factor three to ten. As our AGR results indicate, this difficulty to predict the flow around the naked JBC hull may come from a likely unsteady behaviour of the main vortex structure. Additional unsteady computations based on hybrid RANS-LES modelling are analysed in the next section in order to shed some light on this flow with complex physics.

5 Hybrid RANS-LES simulations

A time-accurate DES-SST computation is compared to statistical turbulence closure on the same case, neglecting the free-surface effects and using a symmetry plane instead (double-body). This choice was justified by additional RANS simulations showing that the mean flow topology remains the same in the core of the aft-body vortex. In double-body flow configuration the predicted axial velocity in the core of the vortex is higher than measured ($0.3U$), while for free-surface computations, the predicted value is lower ($0.2U$) and closer to experiments. The grid around the complete double-body hull contains $66{\times}10^6$ cells with typical isotropic cell sizes of $0.0008L_{\mathrm{PP}}$ complying with the Taylor scale. For the hybrid RANS-LES simulations time step is 0.006s and averaging time 24.2 (about 144s); this means that

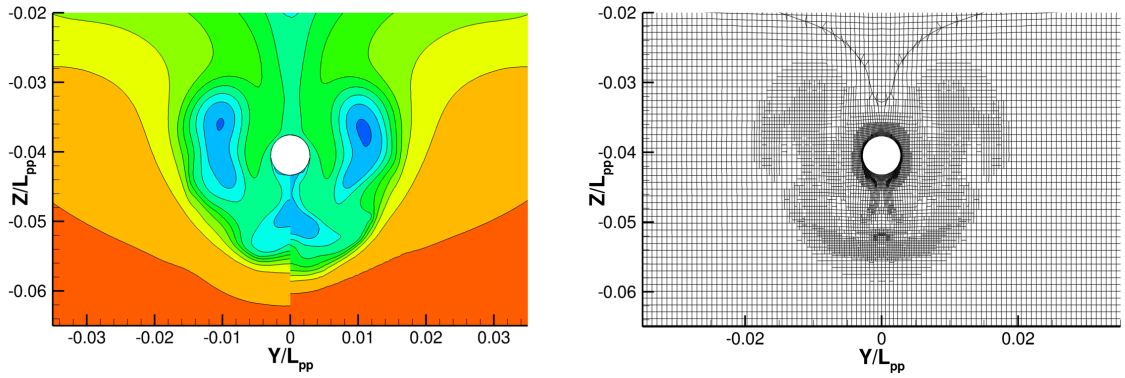

Fig. 5: Section S4 with AGR. Left: U velocity contours at two different instants - Right: corresponding AGR grid cut for the complete hull

the CPU cost is multiplied by ten compared to a similar RANS case.

Fig. 6 presents an instantaneous view of the iso-surfaces of the Q invariant colored by the helicity. The figure clearly shows a succession of ring vortices which are created after the onset of an open separation linked with the initial thickening of the boundary layer. This large scale unsteadiness is likely to be due to the peculiar design of JBC (block coefficient C_B 0.858). The rapid reduction of the hull sections at the stern, implied by the high value of C_B, creates the condition of open separation followed by a flow reversal and a strong unsteadiness revealed by the shedding of ring vortices. This underlying physical unsteadiness may explain why the grid convergence on the local flow is difficult to reach with a RANS approach and consequently, the mixed success of anisotropic EARSM turbulence closures.

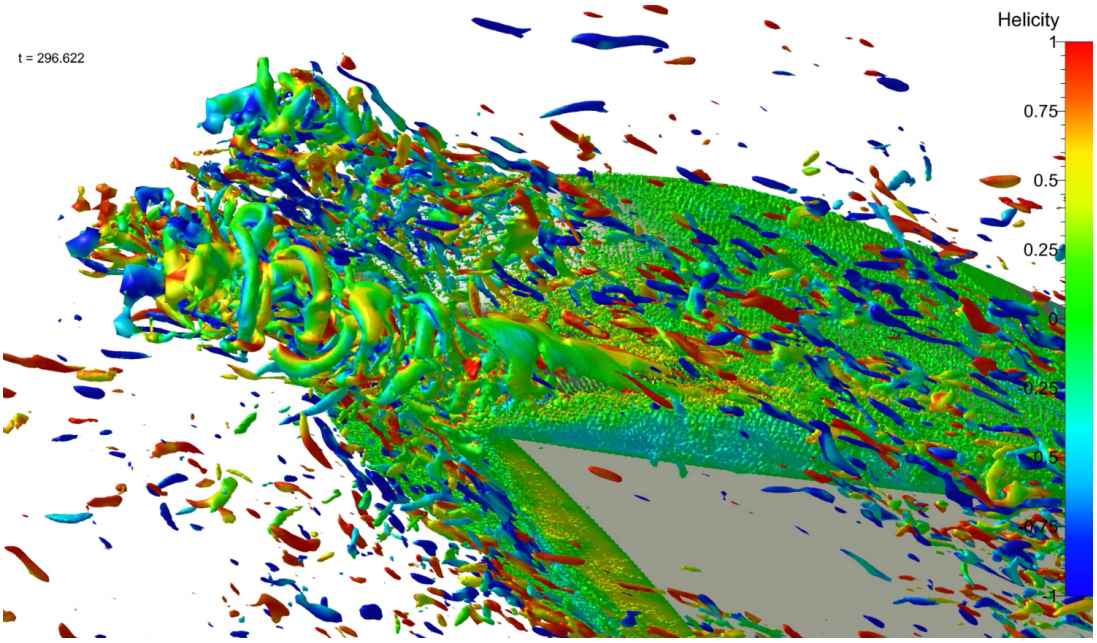

Fig. 6: Side view of the main aft-body vortex visualized by iso-surface of dimensionless invariant Q=25

As shown in Fig. 7 for section S4 with two DES-SST snapshots separated in time by 0.6s, it appears that averaged bilge vortex obtained is actually a superposition of intense and strongly unsteady smaller vortical structures. Transversal evolutions along Y and Z lines across the vortex centre (Y_{V1},Z_{V1}) defined as the local maximum value of the time-averaged Q (see the cross in Fig. 7) are computed and compared to NMRI measurements: Figs. 8 with the averaged axial velocity component; and Figs. 9 for averaged TKE (both resolved and modelled for DES). While RANS and DES-SST simulations produce similar

mean axial velocity component in agreement with the experience, only the DES-SST simulation predicts the unsteady motion of smaller scale vortical structures which leads to higher levels of TKE associated with large-scale, low-frequency fluctuations. These results are consistent with the results obtained by Abbas and Kornev (2015) with a Hybrid RANS-LES approach.

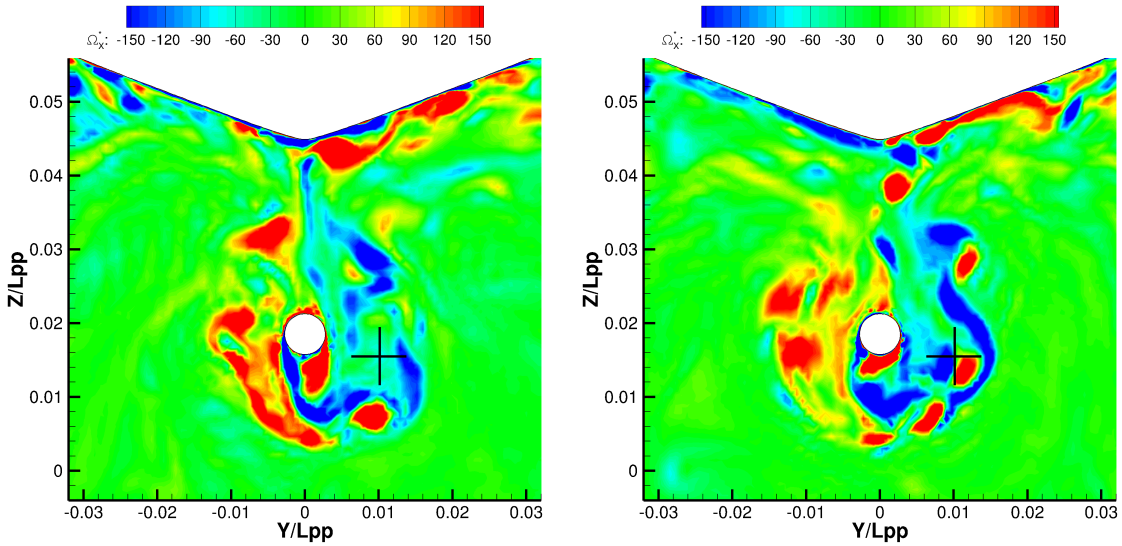

Fig. 7: Instantaneous vorticity distribution in section S4 at two arbitrary time instants: on the right 0.6s after that left one - DES-SST simulation

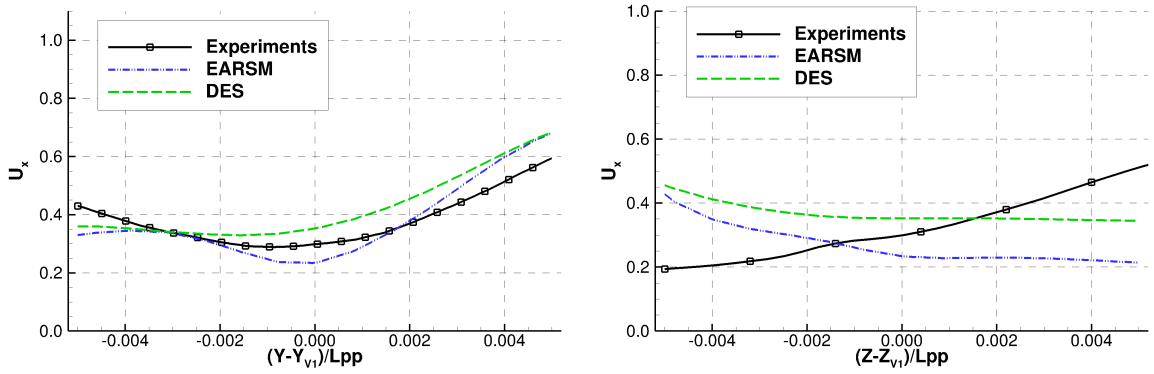

Fig. 8: Evolution (left Y, right Z) of the streamwise velocity component across the vortex centre

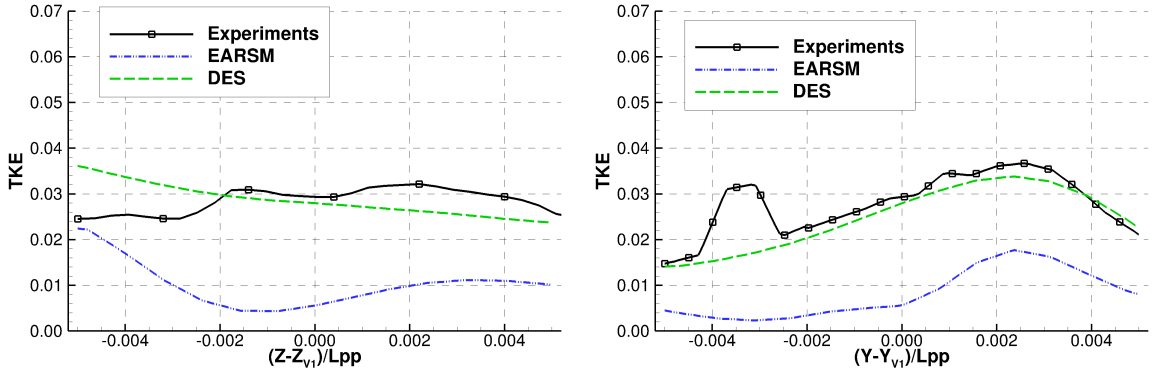

Fig. 9: Evolution (left Y, right Z) of the turbulent kinetic energy across the vortex centre

6 Conclusion

The flow around the naked JBC hull of the Tokyo 2015 CFD Workshop appears to be difficult to predict accurately with statistical turbulence closures because of the unsteady behaviour of the main vortex structure as seen by RANS modelling. This unsteadiness, detected with the advanced AGR method, explains the difficulty to conduct a Richardson extrapolation from series of embedded grids. Furthermore, even Unsteady RANS solutions have a systematic deficiency by a factor three to ten of the turbulent kinetic energy whereas a time-accurate DES-SST computation produces consistent results, both for the velocity and the turbulence of the time-averaged flow.

Moreover, the DES-SST computation provides a new interpretation of the averaged stern flow which removes the apparent contradiction between high levels of vorticity and turbulent kinetic energy in the core of the averaged vortex. In the case of the JBC, what is called an averaged bilge vortex is actually a superposition of intense and strongly unsteady and coherent structures structures that contribute dominantly to the turbulent kinetic energy.

Acknowledgements

This work was granted access to the HPC resources of CINES and IDRIS under the allocations 2015-2a0129, 2016-2a1308 and 2016-2a0129 made by GENCI (Grand Equipement National de Calcul Intensif).

References

N. Abbas and N. Kornev (2016). Computations of the Japan Bulk Carrier using URANS and URANS/LES methods implemented into OpenFoam Toolkit. Proceedings of Tokyo 2015 Workshop on CFD in Ship Hydrodynamics.

G.B. Deng and M. Visonneau (1999). Comparison of explicit algebraic stress models and second-order turbulence closures for steady flow around ships. Proceedings of the 7th Symposium on Numerical Ship Hydrodynamics. Nantes, France.

G.B. Deng, A. Leroyer, E. Guilmineau, P. Queutey, M. Visonneau, J. Wackers and A. del Toro Llorens (2015). Verification and validation of resistance and propulsion computation. Proceedings of Tokyo 2015 Workshop on CFD in Ship Hydrodynamics.

R. Duvigneau, M. Visonneau and G.B. Deng (2003).On the role played by turbulence closures in hull ship optimization at model and full scale. *Journal of Marine Science and Technology*, **8**, 11–25.

E. Guilmineau, G.B. Deng and J. Wackers (2011). Numerical simulation with a DES approach for automotive flows. *Journal of Fluids and Structures*, **27**, 807–816.

M. Hoekstra and L. Eça (2008). Testing Uncertainty Estimation and Validation Procedures in the Flow Around a Backward Facing Step. Proceedings of the 3rd Workshop on CFD Uncertainty Analysis, Lisbon, Portugal.

F.R. Menter, M. Kuntz and R. Langtry (2003). Ten years of industrial experience with the SST turbulence model. K. Hanjalić, Y. Nagano, M. Tummers (eds.) (2013). *Turbulence, Heat and Mass Transfer 4*, **19**, 339–352. Begell House, Inc.

P. Queutey and M. Visonneau (2007). An interface capturing method for free-surface hydrodynamic flows. *Computers and Fluids*, **36**, 1481–1510.

M. Visonneau (2015). JBC local flow analysis. Website of the Tokyo 2015 Workshop on CFD in Ship Hydrodynamics. http://www.t2015.nmri.go.jp/Presentations/Day1-PM1-JBC-LocalFlow-Visonneau.pdf

M. Visonneau, G.B. Deng, E. Guilmineau, P. Queutey and J. Wackers (2016). Local and Global Assessment of the Flow around the Japanese Bulk Carrier with and without Energy Saving Devices at Model and Full Scale. Proceedings of the 31st Symposium on Naval Hydrodynamics. Monterey, California, 11-16 September 2016.

J. Wackers, G.B. Deng, E. Guilmineau, A. Leroyer, P. Queutey and M. Visonneau (2014). Combined refinement criteria for anisotropic grid refinement in free-surface flow simulation. *Computers and Fluids*, **92**, 209–222.

J. Wackers, E. Guilmineau, A. Palmieri and P. Queutey (2014). Hessian-based grid refinement for the simulation of surface-piercing hydrofoils. Proceedings of the 17h Numerical Towing Tank Symposium (NuTTS 2014), Marstrand, Sweden.

J. Wackers, G.B. Deng, E. Guilmineau, A. Leroyer, P. Queutey and M. Visonneau (2015). What is happening around the KVLCC2? Proceedings of the 18th Numerical Towing Tank Symposium (NuTTS 2015), Cortona, Italy.

Numerical features of cavitation models based on the simplified Rayleigh-Plesset equation

Catherine Ramirez, Alban Leroyer, Emmanuel Guilmineau, Patrick Queutey
LHEEA, UMR-CNRS 6598, Ecole Centrale Nantes
lcramire@ec-nantes.fr

1 Introduction

To reproduce and investigate cavitation phenomena, several numerical models have been developed and implemented in Computation Fluid Dynamics (CFD) solvers in the last two decades. From those models, a large number uses calibration coefficients that are mainly empirical, and even though they are set for a large set of conditions, coefficients are mostly undesirable due to the work it implies to find proper values. In this work, we propose to investigate the model of [Sauer, 2000], based on a simplified Rayleigh-Plesset equation, because it does not use coefficients. Nonetheless, it was found that the ISIS-CFD implementation of this model presents a problematic feature. Under some physical configurations, Sauer's model exhibits a short cavitation pocket with a minimum pressure much lower than the vapor pressure, which additionally is not predicted by the experimental results neither by the models of [Merkle et al., 1998] and [Kunz et al., 2000].

Although it is not largely commented, this issue can also be depicted by some other models besides the Sauer's one, either because of a lack of physics in the model or due to wrong numerical parameters. For instance, in the case of a foil, [Bauer and Abdel-Maksoud, 2001] show that a model based on a potential method is unable to reproduce experimental data and the results of a more sophisticated model. Or, as it is shown by [Yakubov et al., 2015], a model may present a loss in accuracy depending on the calibration coefficients used. Furthermore, it has been seen that this phenomena can be a real physical condition, as it is the case for injection nozzles due to the liquid tension, work presented by [Martynov et al., 2006]. Within this work, the studied models were compared and different mechanisms were proposed and tested in order to improve the implementation of the Sauer's model. It was found that a modification in the Rayleigh-Plesset model exhibited good results, and additionally it was proved that there is a direct influence of the source term on the pressure response.

2 Numerical simulation of cavitation

Among the different cavitation models, two main approaches can be recognized: the heterogeneous approach and the homogeneous equilibrium. The present study is focused on models within the framework of the second approach. This approach defines a single fluid model for both phases and interaction between them is taken into account by means of a barotropic state law or by solving an advection equation for the liquid or vapor fraction, with a source term modeling the vaporization/condensation process. In this approach, density and viscosity are computed as a weighted average of the volume fraction of the two phases. The governing equations of the multiphase flow will then include, conservation of mass and momentum, and a transport equation for the cell fraction of one of the phases, as the one shown below:

$$\frac{\partial}{\partial t}(\alpha_v \rho_v) + \frac{\partial}{\partial x_i}(\alpha_v \rho_v u_j) = S. \tag{1}$$

In this equation the source term can be understood as composed by two terms as $S = \dot{m}^{vap} + \dot{m}^{cond}$, each term related to the active process, i.e. $\dot{m}^{vap}$ stands for the vaporization process and $\dot{m}^{cond}$ for the condensation one. As shall be seen later, the source term S is formulated mainly as a function of the pressure and the fraction of a donor phase. The advection equation (1) can be seen as a continuity equation, where the vapor fraction α_v defines the ratio of the vapor volume within the cell volume.

In this work, the solution strategy for the advection equation of the vapor fraction (1) and the turbulence model are common for all the studied models, and the cavitation models are distinct from each other only by the definition of the source term S. In that regard, turbulence effects on the cavitation process are

included through the use of the shear stress transport (SST) turbulence model of [Menter et al., 2003], and the dynamic of the mixture is predicted using a standard mono-fluid multiphase method, which is in turn related to a given mass transfer model allowing the evolution between the phases.

3 Rayleigh-Plesset equation based models

This section presents a brief description of some homogenized models that use the Rayleigh-Plesset equation as a closure for the motion equations. These models assume that micro-bubbles or cavitation nuclei n_0 exist in the liquid and are carried by it during the motion. When the liquid pressure is lowered below the vapor pressure those cavitation nuclei expand generating regions of vapor. Particularly, in a hydrofoil, the pressure decreases along the suction side, inducing the process of vaporization in the low pressure regions (near the leading edge), and the breakage of the vapor pocket downstream where the pressure recovers. Even though the model of interest is the model of Sauer, the models of Kubota and Zwart are also presented since they are useful to highlight some features of Sauer's one.

The table 1 presents an overview of the models. It shows, for each of the models, the definitions for the nuclei density n_0, the vapor fraction α_V and the mass transfer between the phases, expressed either by the particular term according to the active process, $\dot{m_v}^{vap}$ or $\dot{m_v}^{cond}$, or by the general source term S.

Table 1: Synopsis of some Rayleigh-Plesset equation based models

	Kubota et al., 1992	**Zwart et al., 2004**	**Schnerr and Sauer, 2001**
n_0	N_B/V		N_B/V_L
α_V	$V_B n_0 = \frac{4}{3}\pi R_B^3 n_0$		$\frac{Vv}{V} = \frac{n_0 4/3\pi R^3}{1 + n_0 4/3\pi R^3}$
$\dot{m_v}^{vap}$	$C_{vap}\frac{3\alpha_v\rho_v}{R_B}\dot{R}$	$C_{vap}\frac{3\alpha_{nuc}(1-\alpha_V)\rho_v}{R_B}\dot{R}$	$3\frac{\rho_l}{\rho}(1-\alpha_v)\alpha_v\frac{\dot{R}}{R}$
$\dot{m_v}^{cond}$	$C_{cond}\frac{3\alpha_v\rho_v}{R_B}\dot{R}$	$C_{cond}\frac{3\alpha_v\rho_v}{R_B}\dot{R}$	$3\frac{\rho_l}{\rho}(1-\alpha_v)\alpha_v\frac{\dot{R}}{R}$
$\dot{R}$	$\sqrt{\frac{2}{3}\frac{P_R-P_\infty}{\rho_l}} = sgn(P_v - P_c)\sqrt{\frac{2}{3}\frac{\lvert P_v-P_c\rvert}{\rho_l}}$		

Furthermore, the last line of the table presents the simplified Rayleigh-Plesset equation $\dot{R}$, which seeks to characterize the size evolution of a single bubble due to the change in the local pressure. This formulation assumes that bubble-bubble interactions and bubble coalescence can be neglected, and also that bubbles remain spherical all along their life. In this equation P_R is the liquid pressure at the bubble boundary, P_∞ is the one in the far field and ρ_l the density of the domain surrounding the bubble. However, in practice, P_R and P_∞ are taken as saturation vapor pressure P_v and cell pressure P_c, respectively. The models under studying additionally neglect the liquid viscosity the surface tension and the second order terms within the original equation.

One of the first models to predict cavitation by means of a multiphase mixture model based on a transport equation is the one of [Kubota et al., 1992]. This model proposes a pseudo-density calculation for the mixture and determines the volume vapor fraction using a constant nuclei density n_0, a fixed radius R_B per unit volume and the Rayleigh-Plesset model. However, some issues are present at low void fractions for this model, which is why the model of [Zwart et al., 2004] proposes to replace the term α_v, present in $\dot{m_v}^+$, by $\alpha_{nuc}(1-\alpha_v)$. Change that allows overcoming the issue by considering that as the vapor volume fraction increases, the nucleation site density decrease accordingly. Within this model, α_{nuc} is the nucleation site volume fraction and likewise R_B is the radius of a nucleation site.

On the other hand, conversely to the models of Kubota and Zwart, [Schnerr and Sauer, 2001] propose a particular definition of the nuclei density that leads with a different expression of the source term. This model similarly adopts a constant nuclei density *no* and bubble radius R_0 to describe the liquid quality,

nonetheless in the definition of the nuclei density, the number of bubbles is explicitly linked to the liquid volume and not to the mixture one. By doing this, the conservation of the defined quality of the liquid is guaranteed along the cavitation process. That is to say that, if the nuclei grow the vapor fraction rises and hence the water fraction decreases, and so does the number of bubbles in the cell, argument that is in accordance with the one of Zwart to improve Kubota's model.

4 Extended model of Sauer

This section presents a mechanism that was found to improve the prediction of Sauer's model, increasing the pressure so that it remains within the physical limit, and at the same time extending the cavity pocket. In order to introduce the mechanism the following analysis is done. If a homogeneous nuclei distribution is considered, for low vapor fraction values the assumption of non-interaction and non-coalescence might be correct since the bubbles contained in the computational cell would be small enough and might not be interacting with each other. Therefore, in this case, it is correct to use the liquid density to characterize the domain in which a single bubble evolves, as it stated by the Rayleigh-Plesset model. Nonetheless, when bubbles grow and the vapor fraction of a cell increases, a bubble is not anymore evolving in a purely liquid medium, which is why this work proposes to use the cell density (mixture density), instead of the pure liquid one, to characterize the surrounding domain of a bubble evolving. In this way, the initial assumption is met and the physical sense within the model is extended for high values of the vapor fraction.

Additionally, to compute the cell density instead of using an arithmetic mean, between liquid and vapor density, a modified mean was used. A function between and arithmetic and a generalized mean (with exponent $p = 0.1$) was finally implemented. Figure 3 shows that the density of the cell will be almost considered as the vapor density for vapor fractions below 0.5, it means $\rho_{cell} = \rho_v$ for $0 < \alpha_v \approx 0.5$.

Despite an extensive revision of [Sauer, 2000] aspects of the model, such as use of dynamic bubble radius or the assumption regarding the vapor density, remained unclear and were thus studied within this work. Regarding the bubble radius, it was questioned whether to fix it along the computation to the value R_0, which corresponds to the liquid quality defined, or to compute and use an actualized radius at each iteration using the current value of the vapor fraction, as defined by the expression of the radius R in section 3. Even though the effect of a fixed radius was studied, the results are not presented here, instead, the radius R is computed at each iteration according to the original implementation of Sauer's model in the ISIS-CFD solver. Under this assumption, the model of Sauer should depict not only the mechanism of the inception, but the growing of the bubbles and the inverse process. Additionally the vapor density is neglected in the formulation of the source term.

5 Influence of the source term on the balance of the system

As mentioned before, transient effects given by the mass transfer between phases are taken into account by considering a source term in both, the VOF transport equation (1) and the pressure-equation. Using an algorithm (SIMPLE-type), this section illustrates the influence of the sign and magnitude of the source term on the pressure field. Given the algorithm used determine and couple the pressure and velocity fields for incompressible flows, using the Navier-Stokes equations, as:

$$\begin{aligned}
&\text{Prediction of the velocity} && (E - A)U^k + Gp^{k-1} = f\ ,\\
&\text{Prediction of the pressure} && DE^{-1}Gp^k = DU^{*k}\ ,\\
&\text{with} && U^{*k} = E^{-1}(AU^k + f)\ ,\\
&\text{Correction of velocity} && U = U^{*k} - E^{-1}Gp^k\ .
\end{aligned}$$

Applying the divergence operator on the velocity correction equation and assuming the E matrix to be diagonal, yields the relation $DE^{-1}Gp = DU^* - DU$. There, the terms DU and DU^* are considered to be source of change for the pressure, and the behavior of the left hand side term is assimilated as proportional to the Laplacian of the pressure, i.e. $DE^{-1}Gp \approx \beta\Delta p$.

It is recalled that for a non-cavitating flow, the continuity equation yields $\nabla\vec{u} = 0$. However, when cavitation is presented, the source term on the continuity equation (1) is active and $\nabla\vec{u}$ is no longer zero,

instead the expression $\nabla\vec{u} = \frac{\rho_l - \rho_v}{\rho_v \rho_l} S$ yields. Under cavitation condition, the term DU can be directly linked to the cavitation and DU^* to the changes in the velocity. Furthermore, the resultant pressure can be determined by the linear contribution of two sources, one related to the cavitation (Δp^c) and other to the change in velocities (Δp^v), as noted below:

$$\begin{array}{rcccc} \beta\Delta p & \approx & \underbrace{\beta\Delta p^v} & + & \underbrace{\beta\Delta p^c} \\ \beta\Delta p & \approx & \text{velocity Src} & + & -\text{cavitation Src.} \end{array} \tag{2}$$

Finally, if it is considered that $\rho_v << \rho_l$, it is possible say that $\Delta\vec{u} \approx \dot{m}_v$, and therefore a simplified relation between the pressure evolution and the source term can be expressed as $\Delta p^c \approx -\dot{m}_v/\beta$.

5.1 1D Analytical example

To study the influence of the source term on the pressure, the following set of two 1D polynomial equations is proposed. It consists of an analogical term for the cavitation source $\ddot{f}(x)$ and the resultant analog pressure obtained after double integration $f(x)$, for the process of vaporization and condensation.

$$\begin{array}{rcll} \ddot{f}(x)^{vap} & = & x(1-x) & ,(\dot{m}_v{}^{vap}) \\ -f(x)^{vap} & = & -\left(x^4/12 - x^3/6 + x/12\right) & ,(p^{c^{vap}}) \end{array} \qquad \begin{array}{rcll} \ddot{f}(x)^{cond} & = & x(x-1) & ,(\dot{m}_v{}^{cond}) \\ -f(x)^{cond} & = & -\left(x^3/6 - x^4/12 - x/12\right) & ,(p^{c^{cond}}) \end{array}$$

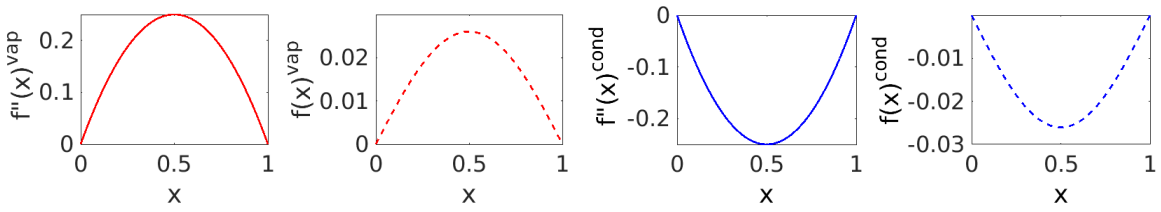

(a) Vaporization (b) Condensation

Fig. 1: Analog expression of the source term $\ddot{f}(x)$ and the response, or analog expression of the pressure, $f(x)$.

It is highlighted here that the sign obtained for the function $f(x)$ is changed after the integration in order to consider the negative sign shown in equation (2), and directly see the effect of the source term . As it is shown in the Figure 1, it can be stated that a positive source term $\dot{m}_v{}^+$, as is the case during the vaporization process, will tend to increase the resultant pressure, while a negative one will lead with an decrease it. This correlation explains how this mechanism leads to a stabilization of the pressure inside the cavity pocket, as shown in Figure 2.

6 Simulation setup

For the present study a 2D steady cavitating flow over an hydrofoil NACA66(MOD) is considered. The hydrofoil is described by a camber ratio of $Y_c/C = 0.020$, a NACA mean line of a = 0.8 and a thickness ratio of $t/C = 0.09$, where t is the maximum thickness, Y_c the maximum camber and C the chord length of the hydrofoil section. The hydrofoil model was considered completely smooth and with the chord length $C = 0.15$m. The main analysis is performed with a free-stream velocity of $U = 12m/s$, a cavitation fraction of $\sigma = 1$ and angle of attack $\alpha = 4°$, although simulations using $\sigma = 0.91$ and $\sigma = 0.84$ are also performed. The fluid kinematic viscosity is set to $\upsilon = 8.92 \times 10^{-7} m^2/s$ and liquid and vapor density are kept constant and equal to $\rho_l = 997$ kg/m3 and $\rho_v = 0.02308$kg/m3, respectively. A mesh of 59874 elements with a turbulence wall-resolved approach ($y^+ = 1$) is used. The experimental results described in [Shen and Dimotakis, 1989] are taken as a reference.

7 Results and conclusion

To sketch the statement described in section 5, Figure 2 shows the resultant profile of the normalized pressure coefficient, for the test case, with the cavitation module enabled and disable during the simulation. Figure 2(a) shows that along the upper face of the profile the pressure reach values below the vapor pressure making evident the formation of vapor. Figure 2(b) presents the resultant Cp when the

cavitation module is enabled, it shows that the pressure on the upper surface does not go below the vapor pressure and instead a flat region around the saturation vapor pressure value, corresponding to the cavitation pocket, is formed.

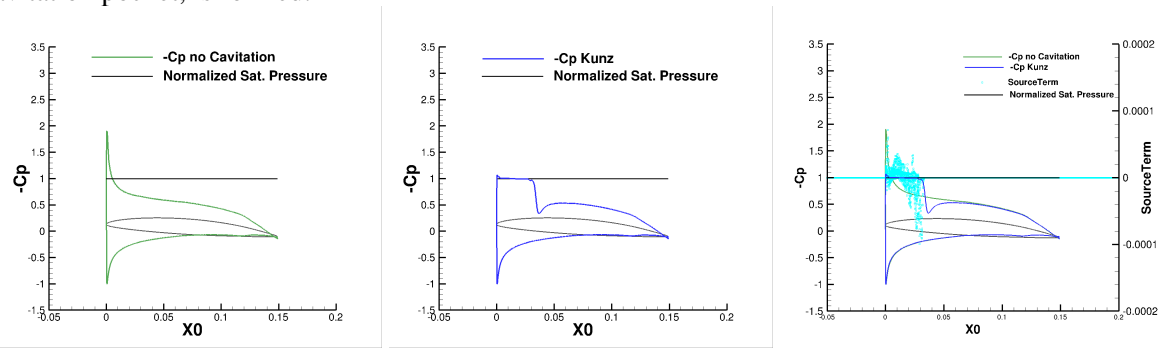

(a) Cavitation module disabled (b) Cavitation module enabled (c) Overlapping of Cp and the source term of Kunz's model

Fig. 2: Normalized pressure coefficient Cp around a hydrofoil (test case).

Figure 2(c) summarizes the process, overlaying the two previous graphs with the resultant source term of Kunz's model. It can be confirmed that in regions where pressure tends to go below the vapor pressure, the source term acts on the pressure equation in such a way that the pressure will be increased, and on the contrary the source term reduces the pressure on the region where the pressure is above the vapor pressure, keeping the pressure around the value of vapor pressure along the sheet cavitation.

Regarding the results of the mechanism proposed, Figure 3 presents the modified mean used to model the mixture density implemented, as it was described in section 4. Figure 4 presents the comparison between the original implementation of Sauer's model and the extended version proposed in this work. Using the barotropic law of Delannoy (similarly to what is done in [Frikha et al., 2008]), the liquid mass transfer $\dot{m}_l$ for a given vapor fraction α_v is plot. It is remarked that the use of the mixture density increments the magnitude of the source term for low values of the vapor fraction.

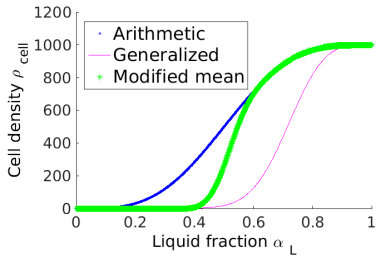

Fig. 3: Different studied means of the cell density.

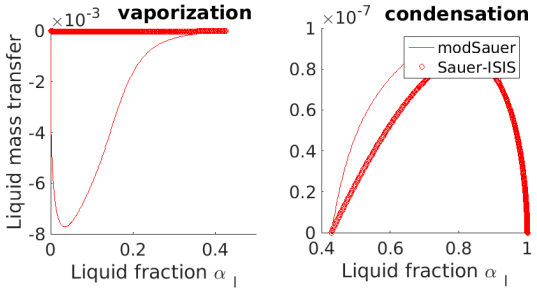

Fig. 4: Not normalized $\dot{m}_l{}^{vap}(\alpha_l)$ and $\dot{m}_l{}^{cond}(\alpha_l)$.

Furthermore, to illustrate the improvement achieved by the modification proposed, Figure 5 presents the resultant normalized pressure coefficient $-Cp$ along the foil surface of the test case, for the ISIS implemented models, and Figure 6 presents the results for the original and the extended implementation of Sauer's model. The pressure predicted by the original model of Sauer is extremely low compared with the one determined by the other models and the one depicted by the experimental results. Nonetheless, the modified version of Sauer leads with a prediction closer to the experimental results, not only reducing the peak of low pressure, but also increasing the length of the sheet cavitation.

Within this work it has been shown that given the influence on the pressure equation, the defect of Sauer's model could be related with the magnitude of the mass transfer term. Keeping this in mind, the source term was increased, for the range of low vapor fraction, using a physical concept within the simplified Rayleigh equation, which leads with the improvement of the prediction of cavitation phenomena done by this model.

Unfortunately, when studying the modified model of Sauer, it was observed a large dependency to the turbulence modeling approach. That is to say that good results are obtained when using a wall-resolved turbulence model for the boundary layer, however they are lost when a wall function is used, and moreover. This issue may be caused by the larger velocity imposed, near the foil, when a wall function is used, which rapidly convects the short vapor induced by the source term. Therefore, for Sauer's model, the process of vaporization has to deal, first, with the low magnitude of the source term, but also with the fact that this term will be quickly convected. On the contrary, this dependency is less observed for the other cavitation models. They overcome the lack of physics, imposed with the use of the wall-function approach, with a source term larger, by several orders of magnitude.

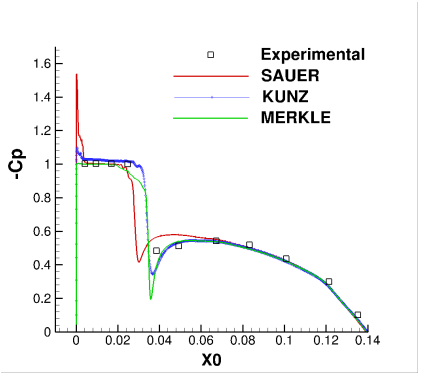

Fig. 5: $-Cp$ ISIS-CFD models

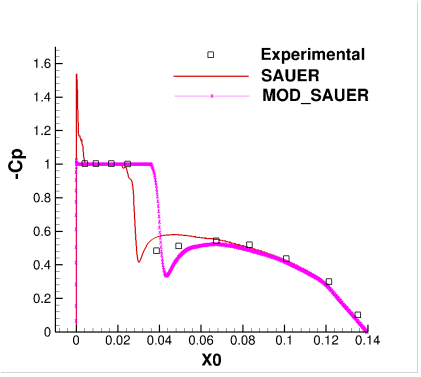

Fig. 6: $-Cp$ Original and Extended Sauer

The improvement of the model is still ongoing, nonetheless given the benefits of a model and and the improvements achieved, this work seeks to expand the modified model of Sauer to be used with a wall function approach, and the future work include to assess the model with different foils, unsteady conditions and also 3D flow condition.

References

Bauer, M. and Abdel-Maksoud, M. (2001). A 3-D Potential Based Boundary Element Method for Modelling and Simulation of Marine Propeller Flows. *German Research*.

Frikha, S., Coutier-Delgosha, O., and Astolfi, J. A. (2008). Influence of the cavitation model on the simulation of cloud cavitation on 2D foil section. *International Journal of Rotating Machinery*.

Kubota, A., Kato, H., and Yamaguchi, H. (1992). A new modelling of cavitating flows: a numerical study of unsteady cavitation on a hydrofoil section. *Journal of fluid Mechanics*, 240:59–96.

Kunz, R. F., Boger, D. A., Stinebring, D. R., Chyczewski, T. S., Lindau, J. W., Gibeling, H. J., Venkateswaran, S., and Govindan, T. (2000). A preconditioned navier–stokes method for two-phase flows with application to cavitation prediction. *Computers & Fluids*, 29(8):849–875.

Martynov, S., Mason, D., and Heikal, M. (2006). Numerical simulation of cavitation flows based on their hydrodynamic similarity. *International Journal of Engine Research*, 7(3):283–296.

Menter, F., Ferreira, J. C., Esch, T., and Konno, B. (2003). The sst turbulence model with improved wall treatment for heat transfer predictions in gas turbines. In *Proceedings of the international gas turbine congress*, pages 2–7.

Merkle, C. L., Feng, J., and Buelow, P. E. (1998). Computational modeling of the dynamics of sheet cavitation. In *3rd International symposium on cavitation, Grenoble, France*, volume 2, pages 47–54.

Sauer, J. (2000). *InstationaÌr kavitierende StroÌmungen: ein neues Modell, basierend auf front capturing (VoF) und Blasendynamik*. PhD thesis, Karlsruhe, Univ., Diss., 2000.

Schnerr, G. H. and Sauer, J. (2001). Physical and numerical modeling of unsteady cavitation dynamics. In *Fourth international conference on multiphase flow, New Orleans, USA*, volume 1.

Shen, Y. and Dimotakis, P. E. (1989). The influence of surface cavitation on hydrodynamic forces. *American Towing Tank Conference.*, (22nd).

Yakubov, S., Maquil, T., and Rung, T. (2015). Experience using pressure-based CFD methods for Euler-Euler simulations of cavitating flows. *Computers and Fluids*, 111:91–104.

Zwart, P. J., Gerber, A. G., and Belamri, T. (2004). A Two-Phase Flow Model for Predicting Cavitation Dynamics. (152).

Towards cavitation modelling accounting for transition effects

Antoine Reverberi[*,†], **Thomas Lloyd**[†], **and Guilherme Vaz**[‡]
[*]ECN, Nantes/FR; [†]MARIN Academy, Wageningen/NL; [‡]MARIN, Wageningen/NL
t.lloyd@marin.nl

1 Introduction

Cavitation is an important phenomenon which should be taken into account when designing propellers in order to minimise noise radiation, vibration and erosion. The occurence of cavitation is however highly sensitive to a number of factors which influence its inception; these include water quality, surface roughness and transition from laminar to turbulent flow. Since cavitation observations of propeller designs are typically made at model scale, it is important to understand and control for differences in the flow conditions between model and full scale (Arndt, 1981). At MARIN, work has previously been carried out to examine cavitation inception (Kuiper, 1981) and the effects of viscosity on cavitation (Van Oossanen, 1974) for marine propellers. One method for reducing the scale effect on cavitation inception is to apply roughness, thereby also ensuring a fully turbulent boundary layer which more closely resembles that seen at full scale. However, in cavitation tests where roughness is not applied, the observed cavitation patterns are highly dependent on transition to turbulence (Figure 1 shows typical model scale flow regimes). In this case, cavitation inception is driven by intense pressure fluctuations resulting from laminar separation or transition to turbulence (Arndt, 1981).

From a modelling perspective it therefore makes sense to account for transition in the prediction of cavitation. Typical two-equation RANS models do not predict transition correctly, although this behaviour can be adjusted by combining them with a transition model (Eca *et al.*, 2016). Most commonly used homogeneous mixture-based cavitation models only use a simplified inception criterion, that is $p < p_v$, where p and p_v are the local and vapour pressures, which does not account for the effects of turbulence. Figure 2 shows an example of overprediction of cavitation in a region of the blade where laminar flow may be expected (Vaz *et al.*, 2015). A parameter representative of the turbulence level can be included, such as the turbulence kinetic energy (Singhal *et al.*, 2002), yet this only serves to increase vapour production. Asnaghi (2015) modified the model of Sauer and Schnerr (2001) to account for the effect of strain rate in the cavitation inception criterion and model vapourisation rate. In this paper, we present a preliminary investigation into how application of a transition model influences the flow prediction for a cavitating marine propeller (without modifying the cavitation model), as well as identifying potential areas for further model development.

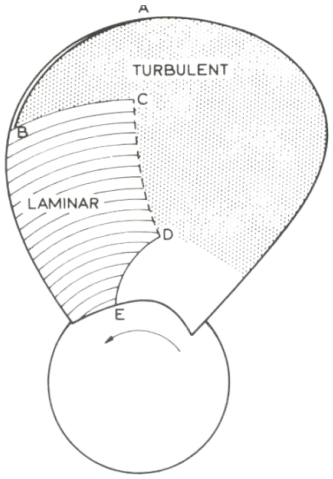

Fig. 1: Schematic representation of flow regimes on model scale propeller blade (Kuiper, 1981).

2 Computational methods

2.1 Flow solver and solution approach

We solved the the steady incompressible Reynolds-averaged Navier Stokes (RANS) equations using the computational fluid dynamics (CFD) code *ReFRESCO* (www.refresco.org), developed by MARIN in collaboration with various universities worldwide, and previously verified and validated for propulsor computations (Rijpkema *et al.*, 2015). The *absolute formulation* (AFM) was used, with additional transport equations for turbulence, transition and cavitation. In the AFM approach, the governing equations are formulated in the absolute (body-fixed) frame of reference, with variables formulated in an earth-fixed frame. Rotation is accounted for by including the grid velocity in the momentum equations and adding a source term to the right-hand side. This solution method is attractive for propellers operating in open water, since it avoids the need for computationally expensive unsteady computations, although cavitation dynamics cannot then be resolved.

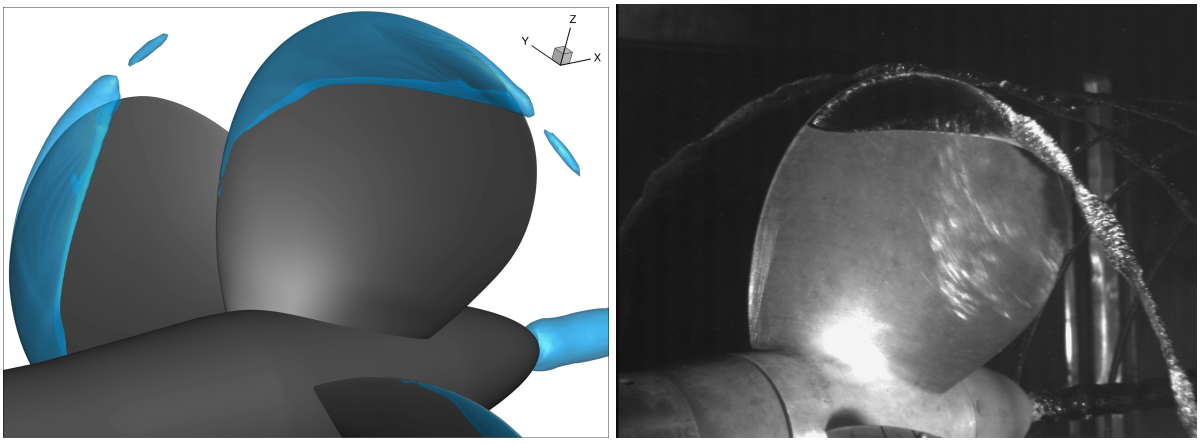

(a) MARIN computation (Vaz *et al.*, 2015)

(b) Experimental observation (Salvatore, 2007)

Fig. 2: Computational cavitation prediction and experimental observation (Vaz *et al.*, 2015).

2.2 Turbulence and transition modelling

Turbulence was modelled using the two-equation $k-\omega\ SST$ eddy-viscosity model of Menter *et al.* (2003). Transport equations for the turbulence kinetic energy (TKE) and specific dissipation ω are solved, from which the eddy viscosity ν_t is derived. Values of the turbulence intensity TI and eddy viscosity ratio ν_t/ν must be specified at the inlet. However, the $k-\omega\ SST$ model is known to predict transition too early and over a too narrow region (Eca *et al.*, 2016). Therefore, we also applied the $\gamma - Re_\theta$ transition model of Langtry and Menter (2009), also referred to as the local correlation-based transition model (LCTM), in order to modify the production and destruction terms in the transport equation for the turbulence kinetic energy. The modifications may be summarised as

$$\tilde{P}_k = \gamma_{eff} P_k; \qquad \tilde{D}_k = min\left\{max\left\{\gamma_{eff}; 0.1\right\}; 1.0\right\} D_k, \tag{1}$$

where P_k and D_k are the TKE production and destruction terms, and a tilde denotes their modified form. In Eq. (1), γ_{eff} is the effective intermittency, which is the maximum of the intermittency and the separation intermittency. For full details of the model see Langtry and Menter (2009).

2.3 Cavitation model

In order to model cavitation, we adopted a homogeneous mixture-based approach. A transport equation for the vapour volume fraction α_v is solved, where the liquid and vapour volume fractions are defined such that $\alpha_l + \alpha_v = 1$. The local values of the fluid properties then enter into the continuity and momentum equations as a linear blending of the liquid and vapour values, based on the cell value of α_v. The formulation of the source term in the transport equation for α_v is based on that of Sauer and Schnerr (2001); that is, proportional to the square root of the pressure difference $p - p_v$, where p and p_v are the local and vapour pressures respectively. Model constants consist of the number of nuclei per unit volume, n_0, and the minimum bubble radius, R_{min}.

3 Test case setup

The simulated case is designed to replicate the experimental setup reported by Salvatore (2007), for the four-bladed INSEAN E779A propeller operating in a cavitation tunnel with uniform inflow velocity. The computational setup is similar to that reported by Vaz *et al.* (2015). Computations were performed for an advance ratio of $J = V/nD = 0.71$, where J is the advance ratio, V in the inflow speed, n the rotation rate, and D the propeller diameter, equal to 0.227 m here. The Reynolds number based on the relative velocity and chord at $0.7R$ is approximately 1.6×10^6. In order to account for streamwise decay in the inlet values of the turbulence variables, values of turbulence intensity and eddy viscosity/viscosity ratio were set to 2.4% and 500 respectively, targetting a turbulence intensity of 2% at the propeller (in accordance with the experiments). This is especially important when using a transition model, which is sensitive to the upstream turbulence intensity (Eca *et al.*, 2016). The fluid properties of the liquid and vapour phases were specified as $(\rho_l, \rho_v) = (998, 0.017)\ kgm^{-3}$ and $(\mu_l, \mu_v) = (1.008 \times 10^{-3}, 1.02 \times 10^{-5})\ kgm^{-1}s^{-1}$.

For cavitating cases, the cavitation number was set to $\sigma_n = 1.763$, where $\sigma_n = 2(p_0 - p_v)/\rho_l(nD)^2$, by setting $p_0 = 0$ and modifying p_v accordingly. The other model constants were set to $n_0 = 10^8$ and $R_{min} = 3 \times 10^{-5}\ m$.

Figure 3a shows the computational domain. The cylindrical form does not correspond directly to the shape of the cavitation tunnel used in the experiments, but was sized to give an equivalent projected area ratio (of $\sim 12\%$). At the inflow boundary uniform velocity and turbulence quantities were specified, with zero gradient for pressure. The outflow boundary was split into an inner part, where an outflow condition was applied, and an outer part, where a fixed pressure of zero was specified. The tunnel wall was modelled as a slip (non-viscous) wall. Finally, the propeller blades and hub were treated as rotating no-slip walls, while for the shaft a fixed no-slip wall was used. Computations were performed using a block structured grid. Particular attention was paid to achieving a fine grid at the blade edges, as seen in Figure 3b, as well as an average y_1^+ value less than one. A total of $8.6M$ grid cells were used. This is similar to the total cell count used by MARIN in the CRS SHARCS working group (Vaz *et al.*, 2015), although the chordwise grid density at the leading edge was finer in the current work.

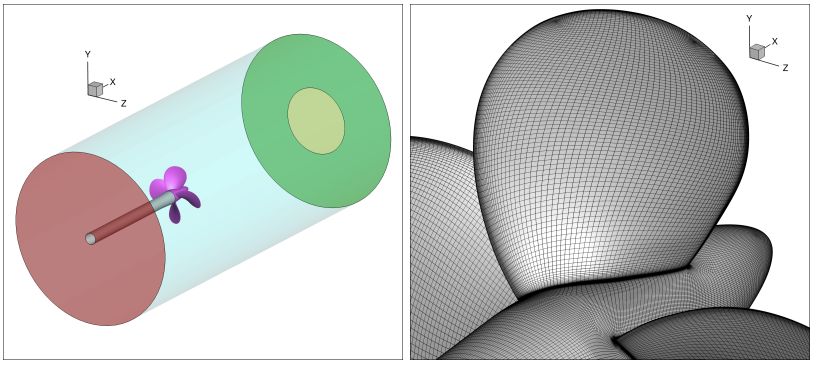

(a) domain (b) surface grid

Fig. 3: Computational domain and grid. Colours in Figure 3a denote boundary types: inflow (red); outflow (yellow); fixed pressure (green); tunnel wall (blue); rotating wall (purple); and fixed wall (grey).

4 Wetted flow results

In this paper, we focus on differences in the flow field prediction with and without the transition model. For the test case addressed here, no notable changes in the propeller performance coefficients were observed by applying the transition model. This is largely due to the relatively high blade Reynolds number; more significant differences in performance can be expected for low Reynolds numbers.

The near-wall flow is visualised in Figure 4 in terms of limiting streamlines and skin friction coefficient $C_{fn} = 2|\tau_w|/\rho_l(nD)^2$. A clear difference can be observed between the computations without and with transition model. The more radially directed lines show regions of laminar flow, which are prevalent at lower radii close to the leading edge when the transition model is applied. Laminar flow is also indicated by the lower skin friction, which extends up to the region where the noticeable discrepancy between computation and experiment was seen in the previous computations (Vaz *et al.*, 2015). By contrast the computation without transition model exhibits fully turbulent flow on most of the blade, as expected based on Rijpkema *et al.* (2015). It is also noticeable that the extent of the leading edge separation is somewhat greater when using the transition model.

Now we compare the chordwise distribution of the skin friction coefficient. This is shown in Figure 5 for $r/R = 0.3$ and 0.7. Note that no difference in the pressure distribution was observed. As expected the location of transition (indicated by grey zone) moves towards the leading edge for the higher radius, due to the higher Reynolds number and increased blade loading. Transition also occurs earlier on the suction side than the pressure side, due to the stronger pressure gradient. Another feature of the computation with transition model is the small peak in the skin friction at the leading edge of the blade for $r/R = 0.7$, as a result of the longer leading edge separation. This does not cause transition however, as the skin friction decreases further behind the separation region, before increasing due to 'natural' transition.

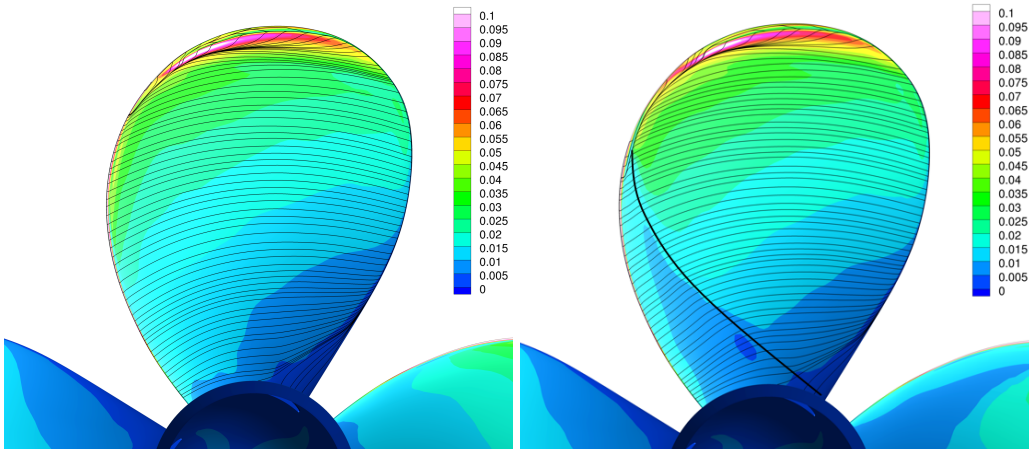

(a) without transition model (b) with transition model

Fig. 4: Suction side limiting streamlines and skin friction coefficient for computations without and with transition model. Black line on right picture illustrates transition location.

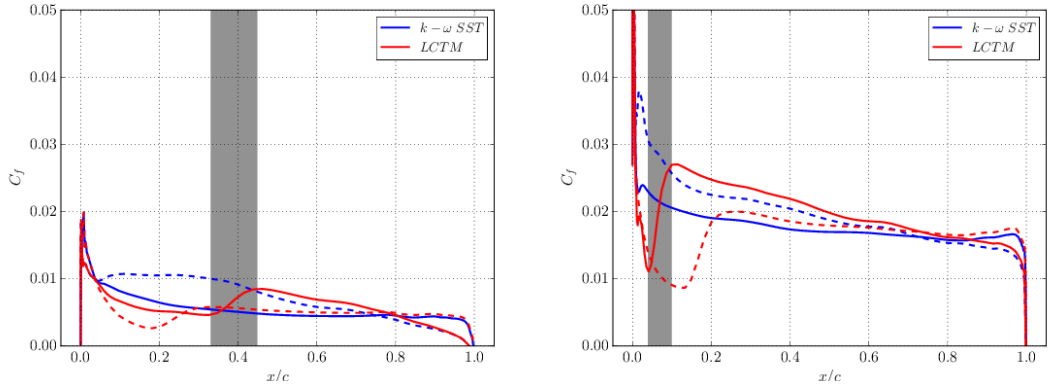

(a) pressure coefficient (b) friction coefficient

Fig. 5: Chordwise distribution of skin friction coefficient for wetted flow computations without and with transition model: $r/R = 0.3$ (left) and 0.7 (right). Suction side (solid) and pressure side (dashed). The grey bar indicates the estimated transition region on the suction for the results using transition model.

5 Cavitating flow results

Now the effect of the transition model on cavitating flow predictions is presented. Figure 6 shows the cavity extents (visualised as a translucent isosurface of $\alpha_v = 0.1$), as well as the limiting streamlines. Differences in cavitation prediction are small, with the total vapour volume predicted by the two computations lying within 2% of each other. This is mainly due to the cavitation inception criterion being based on the pressure, which does not change between the two computations. The limiting streamlines also show a larger leading edge vortex in the region where laminar flow is predicted. This does not have a significant effect on the global flow and forces however, since this feature is much weaker for cavitating flow than wetted flow.

In Figure 7, a radial slice of the vapour volume fraction is shown, for $r/R = 0.8$. At this location, differences in the cavity extent are visible, with a longer and thicker cavity predicted when using the transition model. This may be due to a lower eddy viscosity, which reduces diffusion of the cavitation, as often seen when using the $k-\omega$ SST model. This results in a higher concentration of vapour volume for the computation with transition model. This is confirmed in Figure 8, which shows the variation in the local mixture density on the blade surface equivalent to values of $\alpha_v = 0.99 - 1.00$. The transition model has the effect of increasing the concentration of vapour volume (albeit only by a few percent) over a large part of the cavity. It is also possible that the differences seen in Figure 7 could affect cavitation dynamics for unsteady flow, which should be investigated as part of future work.

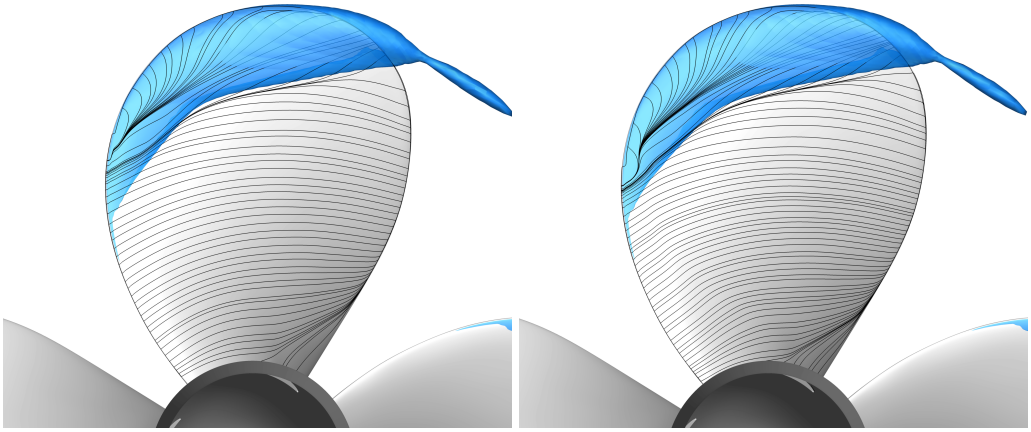

(a) without transition model (b) with transition model

Fig. 6: Cavity extent (visualised as isosurface of $\alpha_v = 0.1$) and limiting streamlines.

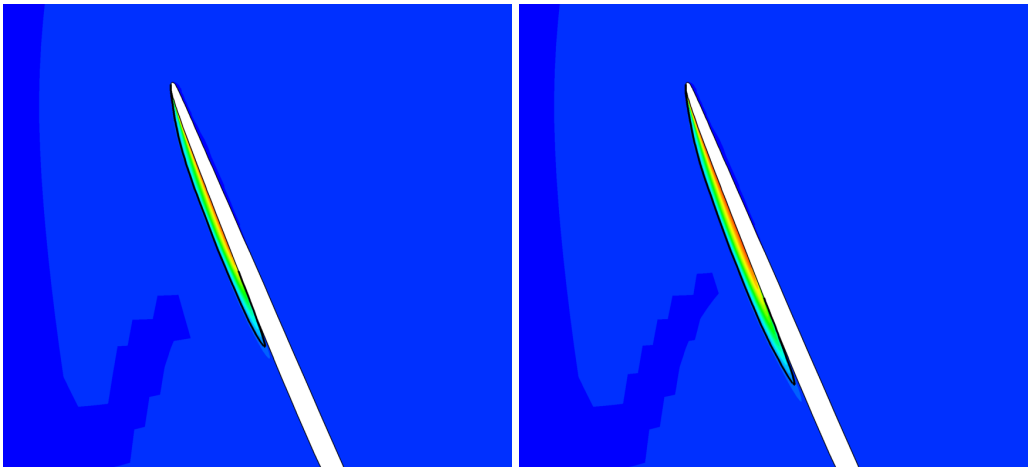

(a) without transition model (b) with transition model

Fig. 7: Slice of vapour volume fraction at $r/R = 0.8$. Blue corresponds to pure water, red to pure vapour. Black line corresponds to $\alpha_v = 0.1$.

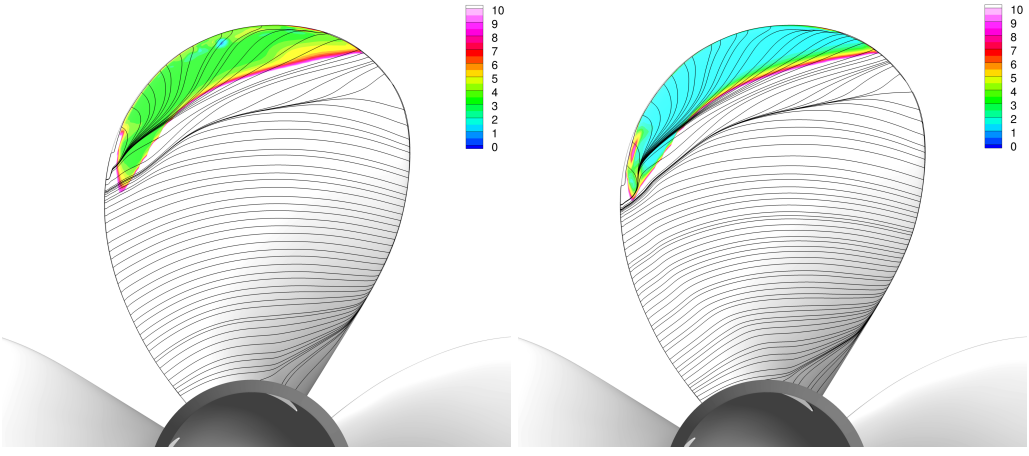

(a) without transition model (b) with transition model

Fig. 8: Surface contours of mixture density ρ_m corresponding to values of α_v between 0.99 and 1.00.

6 Summary

This work concerned a preliminary investigation into the effect of transition modelling on cavitation prediction. Results for wetted flow showed regions of laminar flow close to the blade leading edge in the location where cavitation inception is predicted. For the cavitating cases, the global cavity extent did not change significantly due to the lack of explicit interaction between the turbulence and transition models, and the cavitation inception criterion being based solely on the local pressure. Local differences were observed however, mostly related to lower mixture density and eddy viscosity.

Future work will focus on how the effects of turbulence (including transition) can be explicitly accounted for in cavitation models. Modifications should focus on using flow quantities available in the computation (physics-based), instead of the introduction of ad-hoc corrections. In addition, a more detailed investigation into the interaction between turbulence and cavitation models is required. This could include extending the use of transition models to unsteady flows.

Acknowledgements

We wish to thank Douwe Rijpkema (MARIN) for generating the grids used in this work, as well as João Baltazar (IST) for discussions on the use of transition modelling for propellers.

References

Arndt, R.E. (1981), Cavitation in fluid machinery and hydraulic structures. *Annual Review of Fluid Mechanics*, **13**(1): pp. 273–326, doi:10.1146/annurev.fl.13.010181.001421.

Asnaghi, A. (2015), *Developing computational methods for detailed assessment of cavitation on marine propellers*. Licentiate thesis, Chalmers University of Technology.

Eca, L., Lopes, R., Vaz, G., Baltazar, J. and Rijpkema, D.R. (2016), Validation exercises of mathematical models for the prediction of transitional flows. In: *Proceedings of 31st Symposium on Naval Hydrodynamics*, 11th-16th September, Berkeley.

Kuiper, G. (1981), *Cavitation inception on ship propeller models*. Ph.D. thesis, Netherlands Ship Model Basin.

Langtry, R.B. and Menter, F.R. (2009), Correlation-based transition modeling for unstructured parallelized computational fluid dynamics codes. *AIAA Journal*, **47**(12): pp. 2894–2906, doi:10.2514/1.42362.

Menter, F.R., Kuntz, M. and Langtry, R. (2003), Ten years of industrial experience with the SST turbulence model. In: K. Hanjalic, Y. Nagano and M. Tummers (eds.), *Turbulence, Heat and Mass Transfer 4*, Begell House, pp. 625–632.

Rijpkema, D.R., Baltazar, J. and Falcão de Campos, J. (2015), Viscous flow simulations of propellers in different Reynolds number regimes. In: *Proceedings of the 4th International Symposium on Marine Propulsors*, 31st May-4th June, Austin.

Salvatore, F. (2007), The INSEAN E779A propeller experimental dataset. *Tech. rep.*, INSEAN, Report No. D4.1.3.

Sauer, J. and Schnerr, G.H. (2001), Development of a new cavitation model based on bubble dynamics. *Zeitschrift für Angewandte Mathematik und Mechanik*, **81**(S3): pp. 561–562, doi:10.1002/zamm.20010811559.

Singhal, A.K., Athavale, M.M., Li, H. and Jiang, Y. (2002), Mathematical basis and validation of the full cavitation model. *Journal of Fluids Engineering*, **124**(3): pp. 617–624, doi:10.1115/1.1486223.

Van Oossanen, P. (1974), *Calculation of performance and cavitation characteristics of propellers including effects of non-uniform flow and viscosity*. Ph.D. thesis, Technical University of Delft.

Vaz, G., Hally, D., Huuva, T., Bulten, N., Muller, P., Becchi, P., Herrer, J.L.R., Whitworth, S., Mace, R. and Korsström, A. (2015), Cavitating Flow Calculations for the E779A Propeller in Open Water and Behind Conditions: Code Comparison and Solution Validation. In: *4th International Symposium on Marine Propulsors*, 31st May-4th June, Austin, pp. 330–345.

Forced movements of an immersed flexible barge studied with a viscous flow solver

Marie Robert[*,†], **Antoine Ducoin**[*], **Aurélien Drouet**[†] **and Pierre Ferrant**[*]
[*]LHEEA, Nantes/France, [†]HydrOcéan, Nantes/France
marie.robert@ec-nantes.fr

1 Introduction

The capacity of the big container ship has doubled since the beginning of the 2000's, to reach a record of 19 000 TEU (Twenty foot Equivalent Unit) in 2015. Dimensions of such container ships have also evolved, with lengths increasing from 250m to 400m.

The increase in ship dimensions shifts their structural natural frequencies towards common wave frequencies, inducing more interactions between the classic seakeeping response and the structural response. Unexpected damages occurred on recent big container ships traveling through moderate sea states. It points out failures in the design process, certainly underestimating fatigue phenomena resulting from the interaction between the global ship structure and the wave field.

The objective of the present paper is to build a new numerical model able to take into account ship hydroelasticity, viscous effects and non linearities of the flow, in order to better predict and quantify fatigue phenomena. Previous work from Malenica et al. (2003, 2008), Paik et al. (2009), Seng (2013) and Kim et al. (2013) proposed couplings between hydrodynamic codes and structure codes to address this issue. The originality of our approach lies in its efficency to take into account incident waves, viscous effects and hydrodynamic non linearities.

The validation of the diffraction part of the ship response at sea with this tool has already been published in Robert et al. (2015). The focus is here on radiation. The underlying theoretical models and their implementation will first be presented. The numerical set-up of the barge test case from Malenica et al. (2003) will then be detailed. The last part will focus on results from forced movement tests in calm water. Radiation results are compared with results from potential flow theory.

2 Numerical method

2.1 Hydrodynamic model

The viscous flow solver ICARE is used for the resolution of the fluid domain. Under the assumption of incompressible flow, the Navier-Stokes equations are solved in a fully coupled way for pressure, velocity and free surface elevation.

A RANS approach is used for turbulence modeling, with a $k-\omega$ Wilcox model. The geometry of the body is included in a O-grid representation of the fluid domain (Fig. **??**) and the equations are written using curvilinear coordinates. The solver uses 2^{nd} order finite difference schemes for space and time discretization. A bi-CGSTAB algorithm is used to solve the system at each time step.

A free surface tracking method is implemented, involving a new distribution of mesh points along the third curvilinear coordinate at each time step. A numerical damping zone is included on the outer boundary of the mesh, with cells of increasing sizes, approaching the wave length.

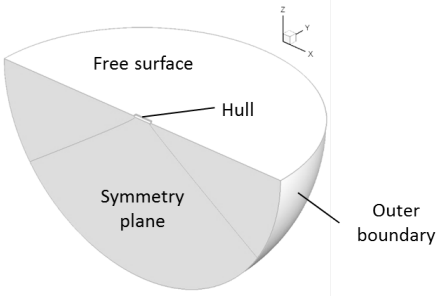

Fig. 1: Fluid domain boundaries

As shown by Fig. **??**, boundary conditions are defined on the body surface, on the free surface, on the outer boundary of the domain and the symmetry plane. A no-slip condition is imposed on the body surface, i.e. $\mathbf{u} = (u, v, w)^T = (0, 0, 0)^T$. On the outer boundary we impose a radiation condition for the perturbed wave field $p_{perturbed} = 0$ that is to say $p = p_{incident}$, p being the dynamic pressure. The symmetry plane conditions write: $v = 0$, $\partial u/\partial y = 0$ and $\partial w/\partial y = 0$. On the free surface, we impose a continuity of the pressure field, which gives the dynamic free surface boundary condition $p = \rho g z$ at $z = \eta$. The kinematic free surface boundary condition concerns velocities and free surface evolution.

2.2 Structure model

The structure model is based on the well known analytic beam model for uncoupled bending, already used as a reference for the treatment of simple hydroelastic cases in Senjanovis et al. (2007).

- **Hypothesis**
  The degrees of freedom of the structure are limited to rigid pitch, rigid heave and vertical bending. Neither transverse bending nor torsion are allowed, i.e. $\delta y = 0$. The structure is considered as a slender beam with $h << L$, where h is the height of the ship, and L its length. The structure motions are limited to small displacements so that $\delta z << L$ and $\delta x << L$. The neutral line of the structure follows the behavior of an ideal beam, that is to say displacements are only according to the vertical direction. Each slice of the structure is considered as a 2D rigid body and remains perpendicular to the neutral line. These hypothesis define the Euler-Bernouilli beam model.

- **Solution of differential equations of beam flexural vibrations**
  Fig. **??** shows the reference frame for the structure analysis. The ship structure is modeled as a beam of length $L = 2l$ with its main direction according to the X axis.

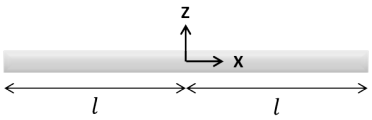

Fig. 2: Reference frame for beam model

The differential equation for beam vertical flexural vibrations (**??**) is used.

$$EI\frac{\partial^4 w}{\partial x^4} + m\frac{\partial^2 w}{\partial t^2} = q \tag{1}$$

E is the Young modulus, I is the moment of inertia of cross section, m is the distributed mass, w is the bending vertical deflection and q is the distributed external inertia load. When solving the associated homogeneous equation, variable separation is assumed for the natural vibration modes: $w(x, t) = \hat{w}(x).\sin(\omega t)$. The mode shape function $\hat{w}(x)$ is the solution of a homogeneous differential equation. The boundary conditions at free ends of the beam concern the bending moment: $M = 0$ N.m and the shear force: $S = 0$ N. The analytical solution of this problem is derived and yields symmetrical and asymmetrical mode shapes.

More details concerning the derivation of the mode shapes can be found in Senjanovic et al. (2007), which was used as a reference for the implementation of the analytic beam model.

2.3 Coupling method

The fluid-structure coupling is based on a modal description of the structure behaviour, which is coupled with a RANSE based code for the fluid. A generalized modes approach allows treating the elastic modes of bending the same way as the pitch and heave rigid modes. The key assumption for the coupling consists in considering the structural response in waves as a series of dry natural modes. The validity of this approach has already been assessed for hydroelastic BEM-FEM coupling by Malenica et al. (2003), Senjanovic et al. (2007) & Kim et al. (2013).

- **Mode shape matrix definition**
  For each mesh node Q, a mode shape matrix is defined. Taking the initial shape as a reference, it describes the displacements of point Q according to each mode, with 3 components along the cartesian directions. $h^i_{xyz}(Q)$ is the mode shape in Q for a specific mode i : $h^i_{xyz}(Q) = \left(h^i_x(Q), h^i_y(Q), h^i_z(Q)\right)$.

  Only heave, pitch and vertical bending are considered, i.e. $h^i_y(Q) = 0$. The mesh points located on the neutral axis have no displacement along X axis so that $h^i_z(Q) = \hat{w}_i(x_Q)$ and $h^i_x(Q) = 0$. For mesh points outside the neutral axis, the displacement is calculated according to the rigid slice assumption, linearized considering small slopes for the neutral line.

$$\begin{aligned} h^i_z(Q) &= \hat{w}_i(x_Q) \\ h^i_x(Q) &= -(z_Q - z_{beam}) * \frac{\partial \hat{w}_i}{\partial x}(x_Q) \end{aligned} \tag{2}$$

  With $z_Q - z_{beam}$ the vertical distance to the neutral line at rest.

- **Force projection on generalized modes**
  The total fluid forces acting on the body are obtained through integration of elementary forces $\delta\vec{F}$ on the body faces. These elementary forces are calculated by ICARE at each iteration. The fluid forces are projected on the generalized modes as described in Malenica et al. (2008), in order to obtain the modal excitation forces.

$$\vec{F}_{exc} = \begin{bmatrix} \sum_Q \delta\vec{F}(Q) \cdot \vec{h}^1_{xyz}(Q) \\ \sum_Q \delta\vec{F}(Q) \cdot \vec{h}^2_{xyz}(Q) \\ \vdots \\ \sum_Q \delta\vec{F}(Q) \cdot \vec{h}^N_{xyz}(Q) \end{bmatrix} \tag{3}$$

  Since the elementary forces are calculated on the mesh faces and the mode shape is calculated at nodes, an interpolation procedure of order 1 is implemented in order to obtain the mode shape value at the barycenter of the face.

- **Remeshing technique**
  Two types of remeshing procedures are implemented in ICARE: a vertical remeshing and a body displacement remeshing. The vertical remeshing is directly related to the surface tracking method. It takes into account changes in free surface position and gives a new distribution of mesh points according to the third curvilinear coordinate. Body displacement remeshing takes into account the movements of the body wet surface and allows new distribution of mesh points in all curvilinear directions. A weighting function is implemented to concentrate the deformations in the area close to the body and keep the outer boundary unchanged.

  The mode shape matrix depends on the position of the mesh nodes. Because of the remeshing procedure, it needs to be updated at each inner iteration.

- **Coupling algorithm**
  The coupling procedure is shown in Fig. **??**. The analytic solution for the beam model is calculated before the solver advance in time. It provides the natural frequencies of the dry modes of the structure, and the analytical form of the modes shapes.

  At each time step, the body is displaced according to the mode chosen for forced movement. An update of the mode shapes value at mesh nodes is performed with reference to the initially determined analytical solution. ICARE uses an iterative process to solve the Navier-Stokes equations.

At the end of each inner iteration, the mesh is updated in order to take into account the newly calculated value of the free surface elevation η. Thus an update of the mode shapes value at mesh nodes is needed to start each new inner iteration. For the radiation cases, 3 inner iterations are typically used.

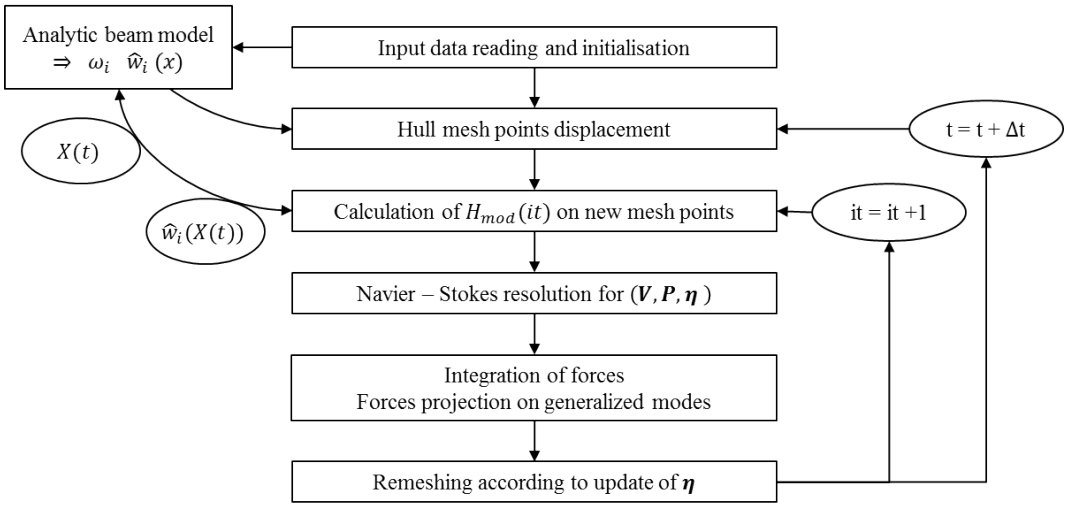

Fig. 3: Flowchart of coupling procedure

3 Numerical set-up

The segmented barge from experiments described by Malenica et al. (2003) & Remy et al. (2008) is used as a test case. Compared to usual tankers, container ships or frigates, the segmented barge is a very flexible structure. It shows visible deformation with relatively weak wave excitation. Geometrical and structural characteristics of the barge are given in Table **??**.

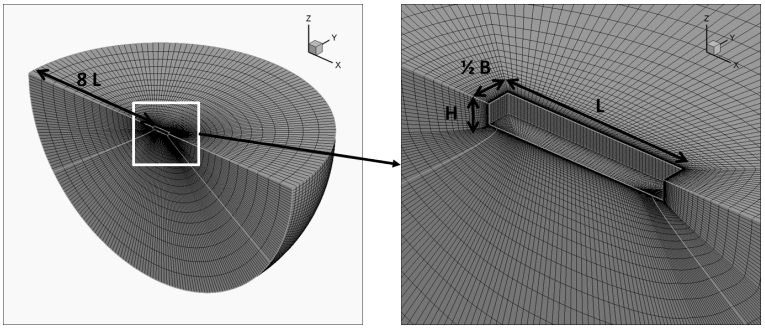

Fig. 4: O-grid mesh - 200 000 points

Table 1: Barge characteristics and physical constants

L(m)	2.445	E (GPa)	$2.10 * 10^{11}$	ρ_f (kg/m^3)	1025
H(m)	0.25	I (m^4)	$8.33 * 10^{-10}$	ν_f (m^2/s)	$9.6 * 10^{-7}$
B(m)	0.6	M (kg)	171.77	g (m/s^2)	9.81
KG(m)	0.163				

We consider cases with no forward speed. As shown in Fig. **??**, the geometry is a fully parallelepiped shape, with no specific bow. The barge is represented as a continuous body. The gaps between the pontoons are not taken into account.

The fluid domain is discretized using a half O-grid mesh. As shown in Fig. **??**, the mesh is refined close to the body surface, in order to capture the velocity gradients. An expansion factor of 1.2 is set to increase the element size towards to the outer boundary of the domain.

For the radiation tests, the motions are forced according to one elastic mode and there is no incident wave. Forcing frequencies are between 4 et 12 rad/s. Those frequencies correspond to plausible excitation from gravity waves. Movement amplitude A is 1.50% of the barge length L.

4 Results and discussion

The vertical velocity and pressure fields are analyzed together with velocity streamlines (Fig.**??**) over one period of forced movement. The vertical velocity is quadrature phased with the imposed barge displacement. The pressure inside the fluid domain is again quadrature phased with the velocity.

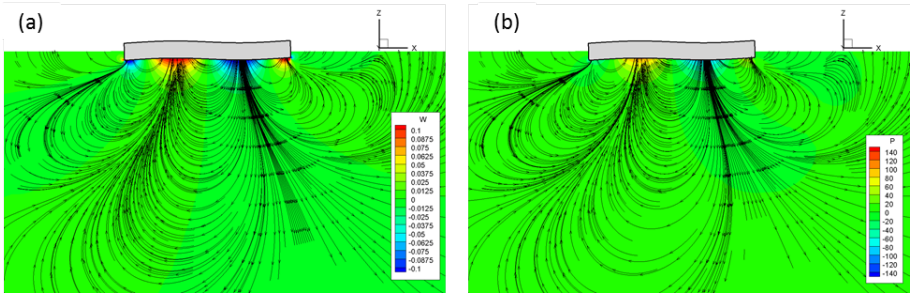

Fig. 5: Non dimensional vertical velocity (a) and pressure (b) fields for flexion mode 2

- **Added mass and damping coefficients**
  Added mass and damping coefficients are derived from the simulation results. An harmonic analysis of forces time series is performed and gives coefficients a_0, a_1 and b_1 of the following first-order decomposition: $F(t) = a_0 + a_1 \cos(\omega t) + b_1 \sin(\omega t)$.

  This decomposition is identified with the classical representation of hydrodynamic forces acting on a body in forced motion, at order 1 in displacement.

$$F - K_H X = M_A \ddot{X} + B_R \dot{X} \qquad X(t) = A \sin(\omega t) \tag{4}$$

  M_A is the added mass coefficient, B_R the radiation damping, K_H the hydrostatic stiffness.

  For the forced movement according to flexion i the harmonic analysis is issued for the difference between the total fluid force projected on flexion i mode shape and the hydrostatic force projected on flexion i mode shape. Added mass and damping coefficients for flexion i read:

$$M_A^i(\omega) = \frac{b_1^i}{A\omega^2} \qquad B_R^i(\omega) = \frac{a_1^i}{A\omega} \tag{5}$$

- **Comparison with results from potential flow theory**
  The hydrodynamic coefficients derived from the ICARE simulations of forced movement according to flexion 2 are compared with the hydrodynamic coefficients obtained for the same case with the potential flow solver HydroStar, coupled with the same analytical beam model. Results of this comparison are presented in Fig. **??**.

  For the added mass, ICARE and HydroStar show a similar trend, with ICARE estimation for A/L =1.50% above HydroStar for higher frequencies. Concerning the damping coefficient, the results are close for the lower frequencies, but the trend is different for frequencies above 8 rads, with a HydroStar coefficients decreasing towards zero for high frequencies and ICARE coefficients getting stabilized on a plateau around 70 kgs. Possible reasons for this differenciation include the presence of viscous effect not taken into account in HydroStar.

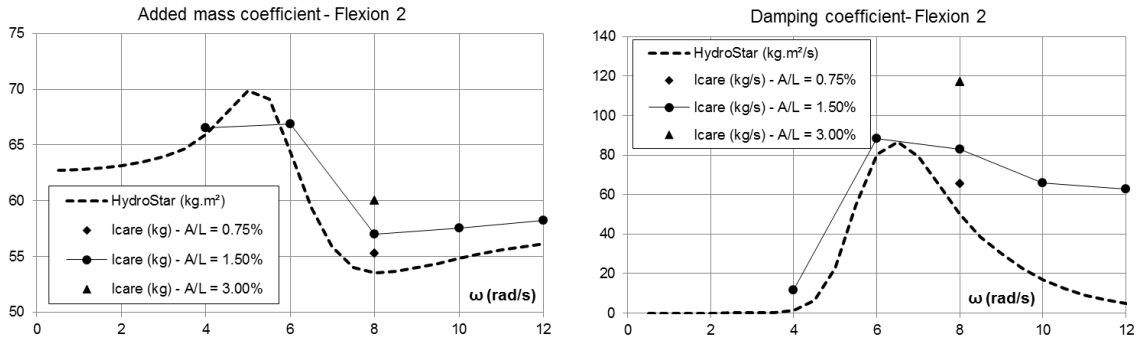

Fig. 6: Added mass and damping for flexion mode 2 of the barge

- **Variation of deformation amplitude**
  For $\omega = 8$ rad/s, the simulations have been run for three different deformation amplitudes. Results of these tests are shown on Fig. **??** with the diamond and the triangle data points. Smaller amplitudes of deformation lead to results closer to the potential solution designed for small movements, whereas higher amplitudes lead to results diverging from the potential flow solution.

5 Conclusion

Results issued from the new coupling involving the viscous flow solver show an overall agreement with results from the potential flow solver. This validates the set-up of the radiation cases in ICARE. Interesting effects are observed for increasing deformation amplitude and will require further investigation. The next step of the development will be the implementation of the equation of motion solver for the elastic degrees of freedom.

Acknowledgements

ECN, HydrOcean and Bureau Veritas would like to acknowledge the support of Jules Verne Technology and Research Institute (IRT). The reference results from HydroStar were issued by Charles Monroy and were part of BASSIN NUMERIQUE Project.

References

K.H. Kim et al. Fully coupled BEM-FEM analysis for ship hydroelasticity in waves. *Marine Structures*, Elsevier, 33:71-99, 2013.

K.J. Paik, P.M. Carrica, D. Lee and K. Maki. Strongly coupled fluidstructure interaction method for structural loads on surface ships. *Ocean Engineering*, 36(17):1346-1357, 2009.

S.Seng *Slamming and whipping analysis of ships* PhD Thesis: Technical University of Denmark, Lyngby, Denmark, 2013.

I. Senjanovic, I.Capitovic and S.Tomasevic. Coupled horizontal and torsional vibrations of a flexible barge. *Engineering Structures*, 30:93-109, 2007.

S. Malenica, B. Molin, F. Remy and I.Senjanovic Hydroelastic response of a barge to impulsive and non-impulsive wave loads. *Proceedings of 3rd International Conference on Hydroelasticity in Marine Technology*, Oxford, United Kingdom, 107-116, 2003.

S. Malenica, J.T. Tuitman, F. Bigot and F.X.Sireta Some aspects of 3D linear hydroelastic models of springing. *International Conference on Hydrodynamics*, Nantes, France, 2008

F. Remy, B. Molin and A. Ledoux. Experimental and numerical study of the wave response of a flexible barge. *Proceedings of 4th International Conference on Hydroelasticity in Marine Technology*, Wuxi, China, 255-264, 2006.

P.E. Guillerm and B.Alessandrini. Résolution du problème de radiation avec vitesse d'avance en fluide visqueux. 7^{emes} *Journées de l'Hydrodynamique*, Marseille, 1999.

Finite Mass Transfer Effects in Cavitation Modelling

Sören Schenke* **and Tom J.C. van Terwisga***†
*Delft University of Technology, Delft/The Netherlands, †Maritime Research Institute Netherlands, Wageningen/The Netherlands
s.schenke@tudelft.nl

1 Introduction

One of the key aspects classifying the various approaches in numerical simulation of cavitating flows is the equilibrium flow assumption. It states that internal processes in the flow always occur instantaneously compared to the time scale of the flow (s. Sezal (2009)). As a consequence, the density-pressure trajectory in a barotropic flow may follow a unique curve. Contrary to the equilibrium flow assumption, one may assume that the time to achieve a new state is governed by the magnitude of a finite mass transfer source term in a volume fraction transport equation (s. Asnaghi et al. (2015)). In this case, the set of possible density-pressure states is not predefined, but strongly depends on the rate at which pressure changes. Although it has been pointed out by Koukouvinis and Gavaises (2015) that the equilibrium assumption for a barotropic flow would theoretically be mimicked by the mass transfer model if the finite transfer rate tended to infinity, the model parameters triggering the finite transfer rate are generally considered as empirical (s. Frikha et al. (2008)).
In this paper, effects of the finite mass transfer rate with special focus on condensation will be studied in detail. First, a cavity collapse will be considered to demonstrate how the finite transfer source term must be modified to satisfy the equilibrium flow assumption. Second, a single bubble collapse is studied numerically and effects of the finite mass transfer rate will be discussed.

2 Finite Mass Transfer Approach and Equilibrium Flow Assumption

Following Asnaghi et al. (2015), the finite mass transfer rate is expressed as a source term in the transport equation for the liquid volume fraction γ, where u is the velocity of the mixture flow, ρ_l the liquid density and C a constant to adjust the magnitude of the source term:

$$\frac{\partial \gamma}{\partial t} + \nabla \cdot (\gamma u) = \frac{C\psi\,(p,\gamma)}{\rho_l} \tag{1}$$

The density is perceived as a mixture quantity, varying according to the volume fraction γ, such that $\rho = \gamma\rho_l + (1-\gamma)\,\rho_v$, where ρ_v denotes the vapour density. Substituting first the mixture density and then the volume fraction transport equation (1) into the mass conservation equation

$$\frac{\partial \rho}{\partial t} + \nabla \cdot (\rho u) = 0, \tag{2}$$

and further taking into account that the individual phase densities are considered as constant values, yields a local velocity divergence (s. Asnaghi et al. (2015))

$$\nabla \cdot u = S_{\text{fin}} = kC\psi\,(p,\gamma)\,, \qquad \text{where} \qquad k = \frac{1}{\rho_l} - \frac{1}{\rho_v}. \tag{3}$$

To modify the finite source term S_{fin} in a way that it satisfies the equilibrium flow assumption, the collapse of a spherical cavity is considered and C is now associated with a condensation constant C_c. The reason why condensation is addressed in particular, is the underlying assumption that the motion of a condensation front is driven by pressure gradients, similar to the motion of a bubble interface obtained from the Rayleigh-Plesset equation (s. Franc and Michel (2004)). The local condensation time in an infinitesimal small control volume dV_C as illustrated in Fig. 1 must then be in line with the accelerating condensation front to achieve an equilibrium state at any instance in time. Applying the Gauss-theorem to the control volume dV_C yields

$$dV_C \nabla \cdot u = u_e dA_e - u_w dA_w, \tag{4}$$

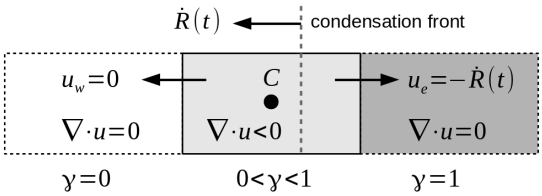

Fig. 1: Condensing control volume

where u_e and u_w denote the in- and outflow velocity of the control volume, presuming that the normal vector of the condensation front is perpendicular to the corresponding in- and outflow surface given by A_e and A_w. As the condensation front passes the control volume with a speed $\dot{R}(t)$, its density increases at a rate governed by $\dot{R}(t)$. This is reflected by the boundary conditions $u_e = -\dot{R}(t)$ and $u_w = 0$, which gives

$$dV_C \nabla \cdot u = -\dot{R}(t)\, dA_e \qquad \Rightarrow \qquad \nabla \cdot u = -\frac{\dot{R}(t)}{dx}. \tag{5}$$

To achieve an equilibrium state, the control volume must be fully condensed within the time T that it takes for the interface to pass the control volume length dx. Thus, the control volume is fully occupied by vapour at time instance $t = 0$, fully condensed at time instance $t = T$ and the relation between length dx and local condensation time T associated with the control volume is given by

$$\int_0^T \dot{R}(t)\ \mathrm{d}t = dx. \tag{6}$$

From Eq. (6) it follows that the source term must be time dependent to satisfy the equilibrium assumption. Substituting the velocity divergence by a time dependent source $S(t)$ yields $S(t) = -\dot{R}(t)/dx$. Integration and substitution of Eq. (6) gives

$$\int_0^T S(t)\ \mathrm{d}t = \frac{1}{dx}\int_0^T \dot{R}(t)\ \mathrm{d}t = -1. \tag{7}$$

Eq. (7) imposes a restriction on the time integral of the source term $S(t)$ over the local condensation time T. The time integral is now replaced by an integral over pressure by multiplying the finite source term $S_{\mathrm{fin}} = kC_{\mathrm{c}}\psi(p,\gamma)$ with the pressure time derivative $\partial p/\partial t$, such that

$$\int_0^T S(t)\ \mathrm{d}t = kC_{\mathrm{c}}\int_0^T \psi(p,\gamma)\left(\frac{\partial p}{\partial t}\right)\mathrm{d}t = kC_{\mathrm{c}}\int_{p(0)}^{p(T)} \psi(p,\gamma)\ \mathrm{d}p = -1. \tag{8}$$

The thermodynamic states corresponding to time instances $t = 0$ and $t = T$ are given by vapour pressure $p(0) = p_v$ and condensation pressure $p(T) = p_{\mathrm{c}}$, respectively. Further presuming that the interim states are given by a barotropic equation of state $\rho(p)$, the term $\psi(p,\gamma)$ can be associated with a local compressibility law for $\partial\rho/\partial p$ and we get

$$\int_{p(0)}^{p(T)} \psi(p,\gamma)\ \mathrm{d}p = \int_{p_v}^{p_c}\left(\frac{\partial\rho}{\partial p}\right)\mathrm{d}p = \int_{\rho(p_v)}^{\rho(p_{\mathrm{c}})} \mathrm{d}\rho = \rho_l - \rho_v. \tag{9}$$

Substituting Eq. (9) into Eq. (8), then solving Eq. (8) for C_{c} and substituting back into the time dependent source term $S(t) = kC_{\mathrm{c}}\psi(p,\gamma)\,\partial p/\partial t$ yields

$$\nabla \cdot u = S(t) = -\frac{\psi(p,\gamma)}{\rho_l - \rho_v}\frac{\partial p}{\partial t}. \tag{10}$$

Eq. (10) represents the modified source term that satisfies the equilibrium flow assumption. It should be noted that $\psi(p,\gamma)$ may still scale with another constant such that Eq. (9) is satisfied.
To study the effect of finite mass transfer on condensation and evaporation, the ρ-p trajectory at an

isolated point in space will be determined. To further isolate the effect of mass transfer, it is supposed that the density gradient is zero. Thus, the temporal density change at that point is only a result of velocity divergence or mass transfer, respectively. In this case, the mass conservation Eq. (2) simplifies to

$$\nabla \cdot u = -\frac{1}{\rho}\frac{\partial \rho}{\partial t}. \tag{11}$$

Following the considerations above, the equilibrium flow approach basically distinguishes from the finite mass transfer approach by the factor $\partial p/\partial t$ (s. Eq. (12)). To simplify the comparison, both the finite and the equilibrium source term is multiplied with the same condensation/evaporation constant $C_{\mathrm{c,v}} = 1$. This means for the equilibrium approach that the pressure p_c, at which full condensation is achieved, is not predefined as in Eq. (9) but a result of the magnitude of C_c.

$$-\frac{1}{\rho}\frac{\partial \rho}{\partial t} = \begin{cases} kC_{\mathrm{c,v}}\psi\left(p,\gamma\right) & \text{finite mass transfer} \\ kC_{\mathrm{c,v}}\psi\left(p,\gamma\right)\frac{\partial p}{\partial t} & \text{equilibrium flow} \end{cases} \tag{12}$$

In Eq. (12), constant $C_{\mathrm{c,v}}$ is considered as dimensionless in both cases and the dimension of $\psi\left(p,\gamma\right)$ is adjusted accordingly. Eq. (12) is solved for ρ numerically by employing a backward Euler step $\partial\rho/\partial t = \left(\rho^t - \rho^{t-1}\right)/\Delta t$. Employing the cavitation model by Merkle et al. (1998), the finite mass transfer rate is written as a superposition of a condensation and an evaporation term as follows:

$$C_{\mathrm{c,v}}\psi\left(p,\gamma\right) = \frac{1}{\rho}\left[\left(1-\gamma\right)C_c \max\left(p-p_v,0\right) + \gamma C_v \min\left(p-p_v,0\right)\right] \tag{13}$$

The volume fraction γ is updated explicitly such that $\gamma^{t-1} = \left(\rho^{t-1} - \rho_v\right)/\left(\rho_l - \rho_v\right)$. The pressure growth rate $dp/dt = \dot{p}$ is assumed as constant, such that $p^t = p^{t-1} + \dot{p}\Delta t$. Convergence with respect to the time step size was ensured by systematic variation of Δt, where $\Delta t = 10^{-4}$ s was found to be sufficiently small. For both condensation and evaporation, the starting pressure is $p_v = 2340$ Pa. The corresponding starting densities are $\rho_v = 0.02\ \mathrm{kgm^{-3}}$ and $\rho_l = 1000\ \mathrm{kgm^{-3}}$, respectively.
Fig. 2 left illustrates the impact of the pressure growth rate $\dot{p}$, which tends to stretch out the condensation/evaporation curves for increasing values in case of finite mass transfer. This is explained by the circumstance that the density growth/decay tends to lack behind when the pressure growth rate is increased for the same finite mass transfer rate. For the equilibrium flow approach, however, all the state curves merge to one single curve associated with a pressure growth/decay rate of $1.0\ \mathrm{Pas^{-1}}$ in the finite mass transfer case.

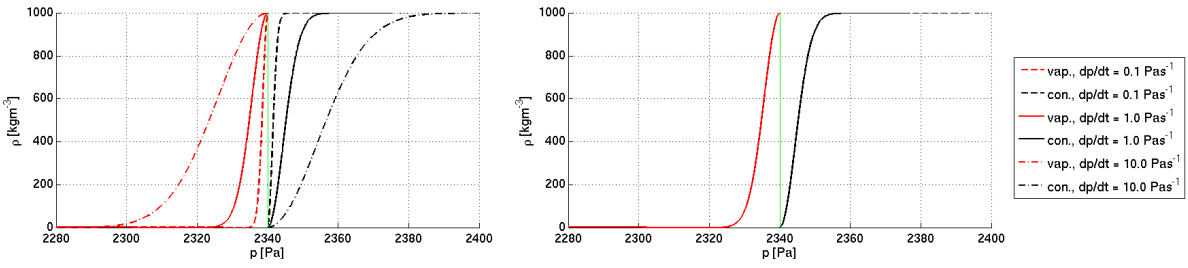

Fig. 2: ρ-p trajectories for the finite mass transfer approach (left) and the equilibrium flow assumption (right)

3 Single Bubble Collapse - Effect of Finite Mass Transfer Rate on Flow Dynamics

To further investigate the impact of the finite mass transfer rate on the flow dynamics, the collapse of a single bubble is studied numerically, using the OpenFOAM solver interPhaseChangeFOAM. The Merkle model as represented by Eq. (13) is employed and only the Euler equations are solved. Again, liquid and vapour density are assumed to be $\rho_l = 1000\ \mathrm{kgm^{-3}}$ and $\rho_v = 0.02\ \mathrm{kgm^{-3}}$. The initial bubble radius is

$R_0 = 0.4$ mm and the bubble and its vicinity is embedded in a uniform polar grid with a resolution of 50 cells per mm in radial direction and 50 cells per $\pi/2$ rad in circumferential direction. Only one cell layer of one eight of the domain is simulated, applying corresponding symmetry and wedge boundary conditions as indicated in Fig. 3. The far field boundary is located at 0.5 m from the bubble centre, where the fixed value condition $p_\infty = 10^5$ Pa and zero gradient conditions for liquid volume fraction and velocity are applied. The initial liquid volume fraction is set to 0 inside the bubble and 1 outside the bubble. The initial pressure field satisfies the Laplace equation, which gives (s. Franc and Michel (2004))

$$\frac{p(r)}{\rho} + \frac{1}{2}\frac{R^4\dot{R}^2}{r^4} - \frac{1}{r}\left(2R\dot{R}^2 + R^2\ddot{R}\right) = \frac{p_\infty}{\rho}. \tag{14}$$

In Eq. (14), r is the radial coordinate and R denotes the location of the bubble interface. Applying the initial conditions $\dot{R}(t=0) = 0$ and $p(r=R_0) = p_v$ yields $\ddot{R} = (p_v - p_\infty)/(\rho R_0)$. Further assuming vapour pressure p_v inside the bubble yields the initial pressure field:

$$p(r) = \begin{cases} p_v & \text{if} \quad r \le R_0 \\ p_\infty + \frac{R_0}{r}(p_v - p_\infty) & \text{if} \quad r > R_0 \end{cases} \tag{15}$$

As a reference, the characteristic Rayleigh collapse time τ is obtained from numerical integration of the analytical solution for the bubble interface velocity derived from the Rayleigh-Plesset equation (s. Franc and Michel (2004))

$$\frac{dR}{dt} = -\sqrt{\frac{2}{3}\frac{p_\infty - p_v}{\rho}\left(\frac{R_0^3}{R^3} - 1\right)}, \tag{16}$$

which gives $\tau = 3.6933 \cdot 10^{-5}$ s. The integration was initialised with a bubble radius of $R_0 = 0.399999$ mm and forwarded with $R^t = R^{t-1} + \dot{R}\Delta t$, where $\Delta t = 10^{-10}$ s. The dimensionless radial pressure distribution is then given by (s. Franc and Michel (2004))

$$\Pi(r,t) = \frac{p(r,t) - p_\infty}{p_\infty - p_v} = \frac{R}{3r}\left[\frac{R_0^3}{R^3} - 4\right] - \frac{R^4}{3r^4}\left[\frac{R_0^3}{R^3} - 1\right]. \tag{17}$$

The evolution of the bubble radius over time (s. Fig. 4), the pressure wave moving towards the bubble

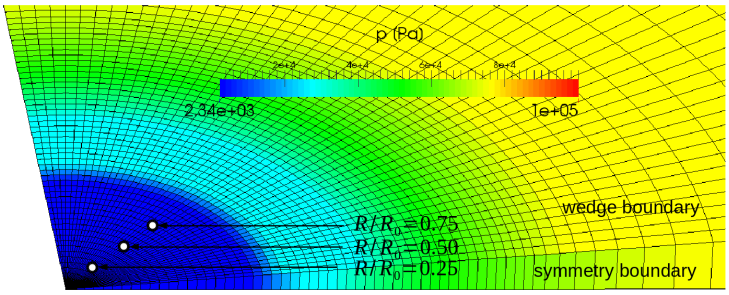

Fig. 3: Initial pressure field

centre with the bubble interface (s. Fig. 5) and the ρ-p trajectory (s. Fig. 6) at three different observation points indicated in Fig. 3 are of particular interest. The study is carried out for three different condensation rates $C_c = 10; 100; 1000$ with a time step size of $\Delta t = 5 \cdot 10^{-8}$ s. During the collapse, the initially sharp bubble interface is subjected to diffusion. The bubble radius is therefore estimated by computing the equivalent radius of a bubble that contains the same amount of vapour but which is fully occupied by vapour.

Concerning the evolution of the bubble radius in Fig. 4, a good agreement is achieved with the evolution predicted by the quasi analytical Rayleigh-Plesset equation (analytical RP). The slight overestimation is least pronounced for the medium condensation rate $C_c = 100$. For the smallest rate $C_c = 10$, however,

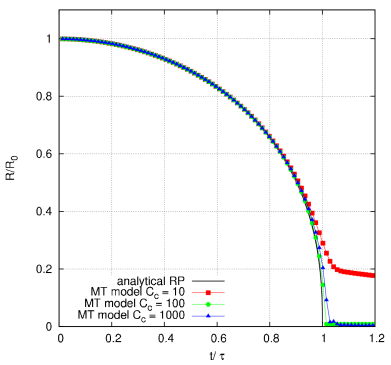

Fig. 4: Bubble radius evolution

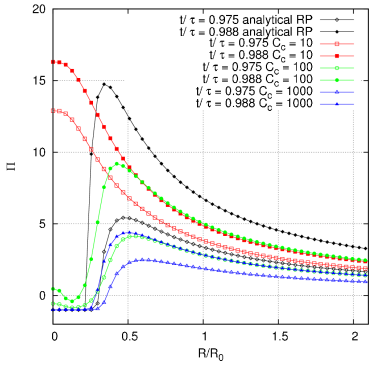

Fig. 5: Radial p-distribution

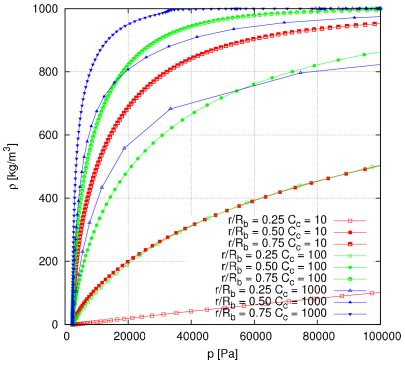

Fig. 6: ρ-p trajectories

the bubble radius evolution undergoes a sudden deceleration close to the final collapse stage. Concerning the radial pressure distribution, which is evaluated at two different time instances close to the final collapse stage, it is striking that the bubble interior pressure slightly increases above vapour pressure for the medium condensation rate $C_c = 100$, and significantly increases for the smallest condensation rate $C_c = 10$. Only the largest condensation rate $C_c = 1000$ preserves vapour pressure at the considered time instances. The steepness of the ρ-p trajectories increases with increasing condensation rate and decreases as the bubble centre is approached, where pressure changes more rapidly. This confirms the observations from Section 2. In addition, the following effects of finite mass transfer rate on the flow dynamics are identified.

Effects of finite mass transfer rate on the flow dynamics: It is recalled from Section 2 that the mass transfer rate should ideally be just large enough to prevent mass flux through the interface at any time instance. This can only be achieved by satisfying the equilibrium flow assumption, which requires a time dependent source term. Due to the neglect of time dependencies in the mass transfer term, the transfer rate is either too small or too large compared to the ideal situation and can only be correct at one instance in time. Based on that, two different mechanisms driving the flow towards the centre are identified. The major contribution results from the global pressure gradients, causing an inertia driven flow, which is observed in the analytical Rayleigh-Plesset model (s. Franc and Michel (2004)) in a similar way. In addition to that, the velocity divergence at the condensing interface is a secondary local driver. With the finite condensation rate being too small on the one hand, the inertia driven flow passes the condensing interface ($u_w > 0$ in Fig. 1). The flow then focuses to the centre quicker than the condensation front. Due to the symmetry of the flow, a stagnation point forms at the centre, explaining the pressure increase inside the bubble. With the condensation rate being too large on the other hand, the condensation time T associated with a local control volume tends to be smaller than the time that it takes for the inertia driven flow to pass the length dx of the control volume. However, the condensation front can not arbitrarily move ahead of the inertia driven flow, because the condensation rate also depends on the local pressure rise which goes along with the inertia driven flow. These two situations are further illustrated by Fig. 7 to 10.

A secondary velocity peak at the interface due to the strong velocity divergence is clearly observed in

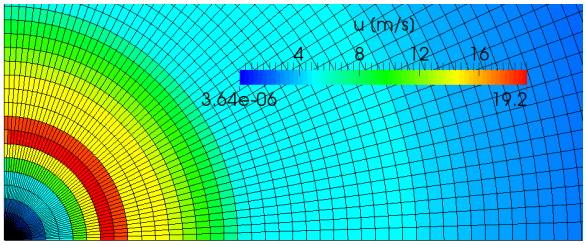

Fig. 7: Velocity magnitude for $C_c = 100$ at time instance $t/\tau = 0.8123$

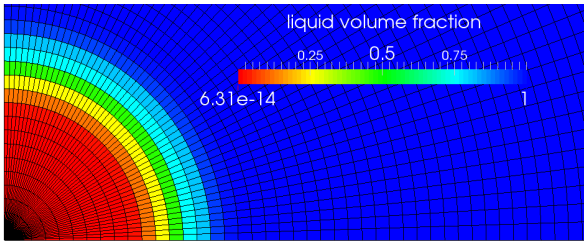

Fig. 8: Volume fraction for $C_c = 100$ at time instance $t/\tau = 0.8123$

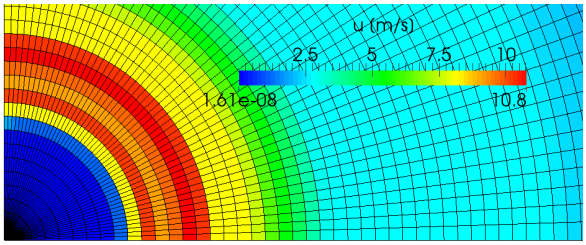

Fig. 9: Velocity magnitude for $C_c = 1000$ at time instance $t/\tau = 0.8123$

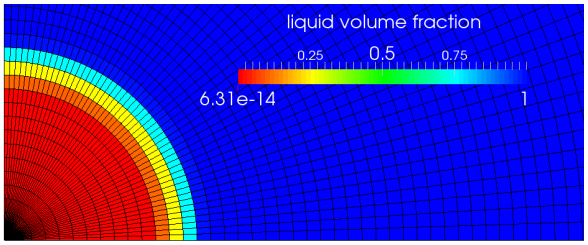

Fig. 10: Volume fraction for $C_c = 1000$ at time instance $t/\tau = 0.8123$

Fig. 9, which depicts the instantaneous velocity distribution at $t/\tau = 0.8123$ for $C_c = 1000$. Taking the instantaneous volume fraction in Fig. 10 into account, it appears that some mass flux has already passed the condensation front. However, this effect is much more pronounced in Fig. 7, which depicts the instantaneous velocity field for $C_c = 100$. The secondary velocity peak is not observed in this case and the interface itself appears to be more diffusive compared to the larger condensation rate. The misalignment of the two flow drivers when violating the equilibrium is likely one of the reasons for different predictions of the radial pressure distributions depending on the condensation rate (s. Fig. 5).

4 Conclusion

It has been demonstrated that the mass transfer approach satisfies the equilibrium flow assumption during a cavity collapse if the pressure time derivative $\partial p/\partial t$ is included in the source term of the volume fraction transport equation (s. Eq. (10)). Two different mechanisms driving the flow during the collapse have been identified. The first driver results from pressure gradients, causing an inertia driven flow and focusing it towards the cavity centre. The second driver results from the local velocity divergence at locations where the condensation source term is active, causing a local mass flux into the condensation front. The coupling of the condensation source term with the pressure time derivative establishes a dynamic equilibrium of the two drivers, such that the acceleration of the condensation front is in line with the inertia driven flow. The neglect of the pressure time derivative in the condensation source term results in a decoupling of the two mechanisms mentioned above. An equilibrium flow can still be simulated by applying very large finite mass transfer rates (s. Koukouvinis and Gavaises (2015)), thereby preventing mass flux through the condensation interface. However, the formation of a secondary velocity peak associated with the tendency of the condensation front to move ahead of the inertia driven flow, is likely to affect the pressure dynamics.

References

A. Asnaghi, A. Feymark and R.E. Bensow (2015). Numerical simulation of cavitating flows using OpenFOAM. Proceedings of NuTTS 2015, Cortona, Italy.

J.-P. Franc and J.-M. Michel (eds.) (2004). *Fundamentals Of Cavitation.* Kluwer Academic Publishers.

S. Frikha, O. Coutier-Delgosha, and J.A. Astolfi (2008). Influence of the cavitation model on the simulation of cloud cavitation on 2D foil section. *International Journal of Rotating Machinery*, vol. 2008.

P. Koukouvinis and M. Gavaises (2015). Simulation of throttle flow with two phase and single phase homogenous equilibrium model. Proceedings of CAV 2015, Lausanne, Switzerland.

C.L. Merkle, J.Z. Feng and P.E.O. Buelow (1998). Computational modeling of the dynamics of sheet cavitation. Proceedings of CAV 1998, Grenoble, France.

I.H. Sezal (2009). *Compressible Dynamics Of Cavitating 3-D Multi-Phase Flows.* Dissertation, Technische Universität München.

DES of Tip Vortex Cavitation on a Propeller

Keun Woo Shin
MAN Diesel & Turbo, Frederikshavn/Denmark
keun.shin@man.eu

1 Introduction

The formation and collapse of tip vortex cavitation on marine propellers is increasingly a subject of concern, because it is related to broadband vibration and rudder erosion. CFD has potential for predicting the tip vortex cavitation of propellers, but accurate predictions are still challenging, because it requires a sufficiently fine grid to resolve low pressure in vortex core. The helical trajectory of propeller tip vortices is altered by propeller-induced flow and hull wake so that the predefinition of a fine grid along the helical path is complicated, but additional grid refinements based on CFD solutions can be an effective approach for simulating the tip vortex cavitation.

Detached-eddy simulations (DES) are made for a cavitating flow on a propeller showing extensive tip vortex cavitation in a cavitation tunnel test. First, a cavitation simulation is made with a predefined grid refinement to evaluate the accuracy of unsteady cavitation modelling apart from the prediction of tip vortex cavitation. The first simulation result provides a basis for determining a criterion of the additional grid refinement along the tip vortex cavitation trajectory. Lastly, another cavitation simulation is made with the additional grid refinement to examine the possibility of predicting tip vortex cavitation with accuracy.

2 Test case

A 4-blade propeller on a military inspection vessel is considered for cavitation simulations. The propeller installed on the hull model has been in cavitation tunnel tests in SSPA, Sweden. The tests have been performed for three loading conditions corresponding to 60%, 90% and 100% MCR engine powers. Neither sheet cavitation nor tip vortex cavitation has been shown in the design condition of 60% MCR power, because military vessels have a stringent requirement for maximum pressure pulse on the hull surface. Restricted sheet cavitation above 0.9R and stable tip vortex cavitation have been observed for 90% and 100% MCR powers. The loading condition of 100% MCR power showing more extensive and stable tip vortex cavitation reaching the rudder is considered in cavitation simulations.

The particulars and operating condition of the ship and propeller are listed in Table 1. The model-scale speeds are from the cavitation tunnel test, which does not follow Froude's law to increase Reynolds number intentionally. The hub ratio is as high as 0.33 and the pitch is increased to $P/D_{0.7R}$=1.20 for 100% MCR power, because the propeller is on a controllable-pitch hub.

Table 1: Particulars and operating condition of ship and propeller at 100% MCR power

Scale		Model		Full	
Ship length	L_{PP}	4.31	m	61.0	m
Draught	T	0.35	m	4.95	m
Propeller diameter	D	0.23	m	3.3	m
Area ratio	A_E/A_O	0.76			
Hub ratio	D_{HUB}/D	0.33			
Pitch ratio	$P/D_{0.7R}$	1.20			
Ship speed	V_S	4.51	m/s	16.8	kn
Froude number	Fn	0.68		0.34	
Propeller speed	N	23.20	rps	185.0	rpm
Advance ratio	J	0.68			

A computational grid around the propeller and rudder is prepared by a trimmed hexahedral mesh in a cylindrical domain extending 3·D from the propeller plane to the inlet and 6·D to the outlet with a radius of 4·D. The propeller shaft is inclined by 3.5° downwards. In the computational model, the propeller shaft is aligned with the centre axis of the cylindrical domain and the rudder is rotated instead. A measurement of hull wake is applied to the propeller inflow by using non-uniform inlet flow and momentum sources instead of including the hull geometry. A cylindrical subdomain around the propeller is defined for modelling the propeller rotation with a sliding mesh. Six prism layers with 0.2 mm thickness on the surface of the propeller and rudder lead mostly to $y^+ \leq 2$. The surface grid size is 0.3-0.6 mm on the propeller and it is refined to 0.2-0.4 mm along the blade edges. A grid refinement is predefined in a cylindrical region around and downstream of the blade tip shown in Fig. 2 to resolve sheet cavitation at outer radii and the starting part of tip vortex cavitation.

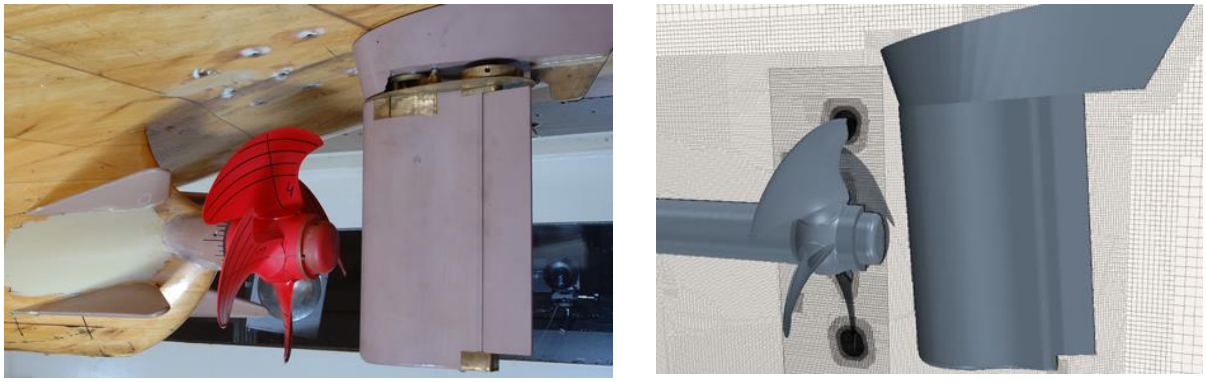

Fig. 1: Propeller model installed on the hull in the cavitation tunnel (left) and computational grid around the propeller and rudder (right)

Steady RANS computations are made for a fully-wetted flow in the open-water condition. In Fig. 3, CFD results with the predefined grid for the pitch of 100% MCR power are compared with open-water model-test results. CFD shows a good agreement with the open-water test with deviations of less than 3% in K_T, K_Q and η_O at $0.2 \leq J \leq 0.7$.

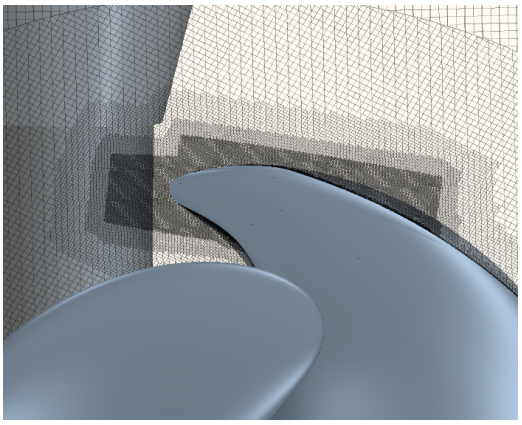

Fig. 2: Predefined grid refinement at the blade tip

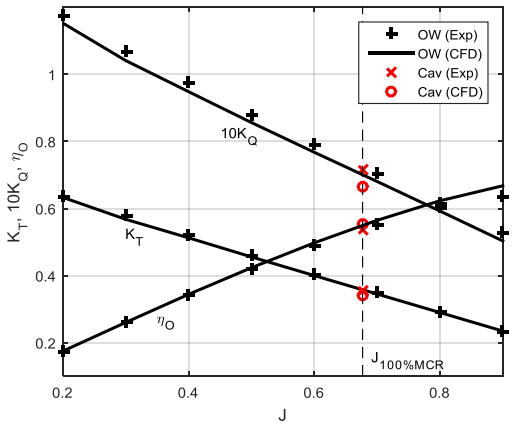

Fig. 3: Open-water curves from model test and CFD and K_T, K_Q, η_B from cavitation tunnel test and simulation

DES is made for a cavitating flow with hull wake. IDDES (improved delayed detached-eddy simulation) is adopted with k-ω SST turbulence model. The non-uniform axial wake is applied by an inlet boundary condition. The axial wake is scaled down by the ratio of the effective wake fraction w_e=0.187 to the nominal one w_n=0.247, where w_e is from the cavitation tunnel test and w_n is from the bare-hull towing-tank test. When all wake components are applied to the inlet boundary, the inflow is not preserved on the way from the inlet to the propeller plane (Shin et al. 2015). A certain distance

between the inlet and propeller plane is required to avoid numerical instability due to upstream perturbation of the propeller. Therefore, the transverse wake is separately modelled by momentum sources applied 0.6·D upstream of the propeller plane.

The hull wake modelling is tested in the same grid as used in the cavitation simulation but excluding the propeller model. The momentum source strength is adjusted iteratively by numerical tests. In Fig. 4-5, the axial and transverse wake from the wake modelling agrees well with the measurement. The unusual high wake at 8 o'clock from ice fins is also reproduced well.

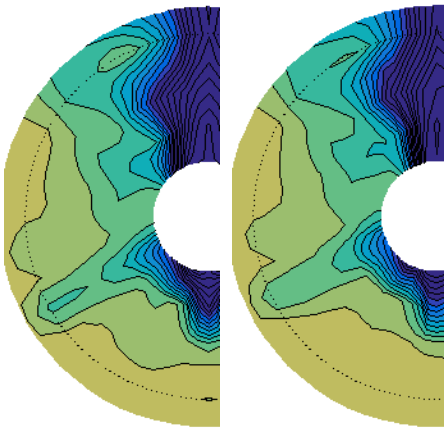

Fig. 4: Axial wake from measurement (left) and CFD modelling (right)

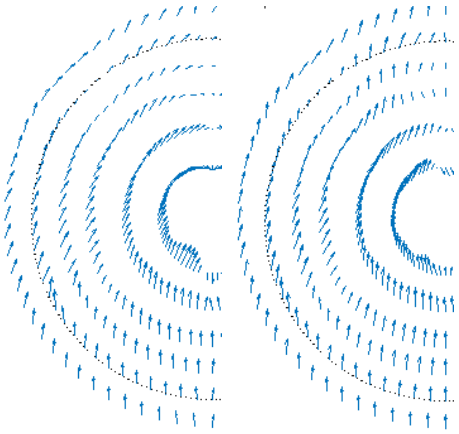

Fig. 5: Transverse wake from measurement (left) and CFD modelling (right)

All CFD simulations are made by the commercial CFD solver StarCCM+. Cavitation is modelled by the Volume-of-Fluid method and a vapor transport equation with a source term based on the Rayleigh-Plesset equation. The gravitational force is applied for taking into account hydrostatic pressure.

3 Cavitation simulation with a predefined grid refinement

An unsteady cavitation simulation is made with the predefined grid refinement. It is started with a relatively large time-step Δt corresponding to 6° propeller rotation per Δt. After Δt is gradually reduced to a value corresponding to 0.5° propeller rotation per Δt, the simulation is run for 5-6 propeller revolutions so that the averaged value of the thrust over a revolution is converged. In Fig. 3, K_T, K_Q and η_B averaged over is compared with those from the cavitation tunnel test, where η_B is the behind efficiency. Since the cavitation tunnel test has been conducted with including a hull model, K_T and K_Q are different from the open-water test values. K_T and η_O are underestimated by 4.0% and 7.3%, respectively. The larger underestimation than the open-water comparison may be related to the hull wake in the cavitation tunnel test at Vs=4.5 m/s differing from that measured in the towing-tank test at a lower Reynolds number corresponding to Vs=2.3 m/s.

The cavitation patterns of CFD are compared with the snapshots from the cavitation tunnel test in Fig. 6. Iso-surfaces of 10% vapor volume fraction are taken as the CFD cavitation interface. Sheet cavitation patterns show a good agreement at blade angles of φ=0° and 30°, where φ=0° is at the 12 o'clock. The leading-edge sheet cavitation of CFD is started from more inner radii at φ=270-330°. Tip vortex cavitation is formed and extended in similar patterns as in the experiment, but the extent is limited by that of the predefined grid refinement.

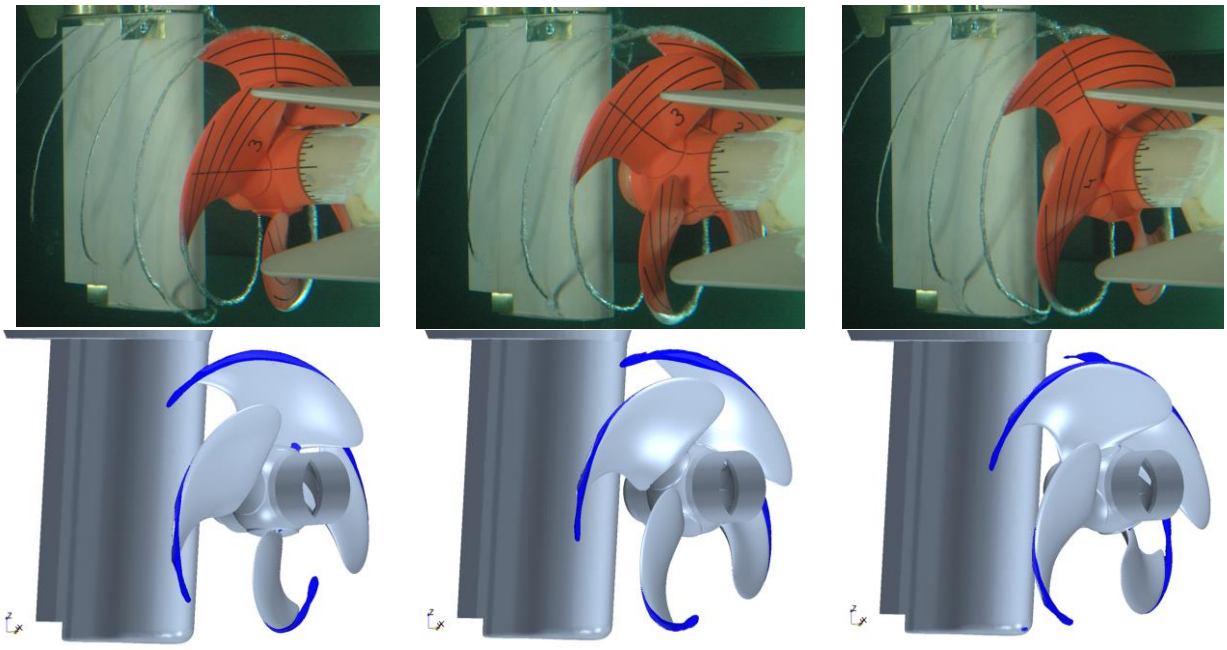

Fig. 6: Propeller cavitation from the cavitation tunnel test (top) and CFD (bottom) with a 30° blade angle interval

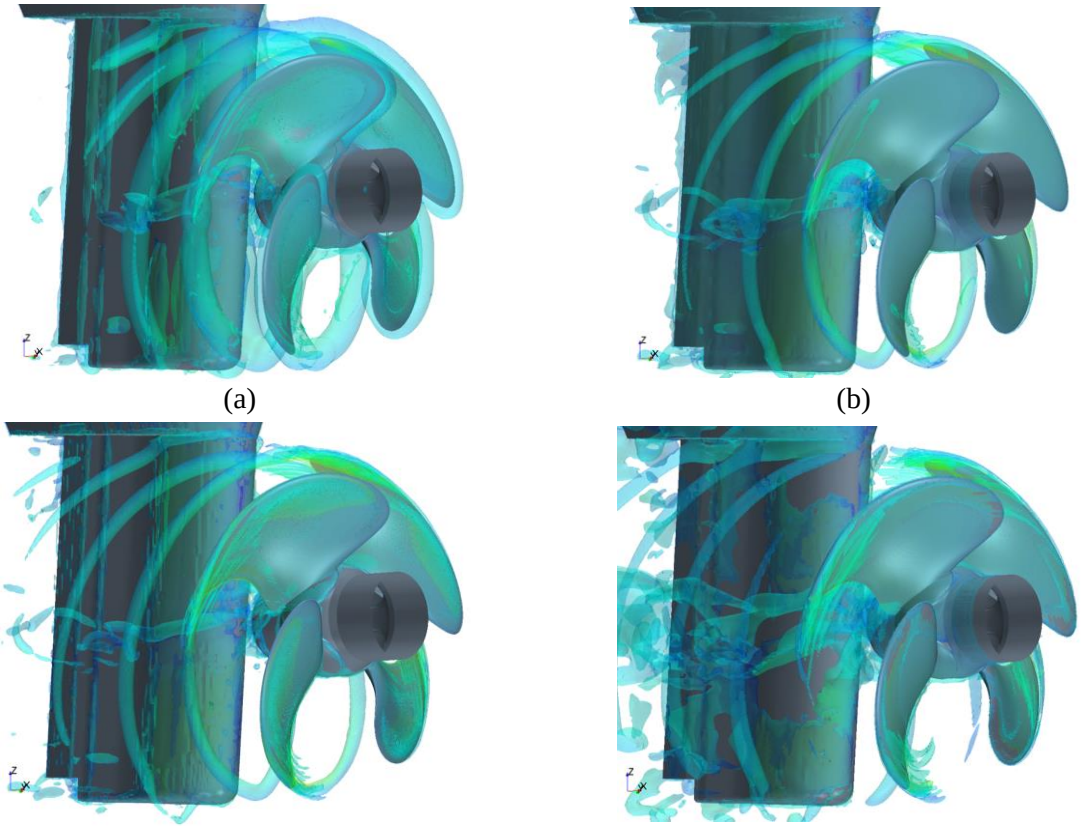

(a) (b)

(c) (d)

Fig. 7: Iso-surfaces of (a) pressure gradient=700,000, (b) vorticity magnitude=500, (c) Q-criterion=100,000 and (d) helicity magnitude=500

In Fig. 7, iso-surfaces of pressure gradient, vorticity magnitude, Q-criterion and helicity magnitude are compared to find out which variable is more suitable for defining a region of additional grid refinements along the tip vortex cavitation, where the Q-criterion is a second invariant of velocity gradient tensor and the helicity is a dot product of velocity and vorticity vectors. Iso-surface values

are specified differently for each variable to visualize the full extent of the tip vortex cavitation shown in the cavitation tunnel test. The trajectory of the tip vortex core is identified better with less other turbulent eddies and hub vortex by vorticity magnitude and Q-criterion. Q-criterion is more effective in capturing the tip vortex core with less shear-layer vortices than vorticity magnitude, so additional grid refinement for another cavitation simulation is based on the tip vortex visualized by Q-criterion.

4 Cavitation simulation with additional grid refinement

Additional refinement of volume mesh to Δx=0.2 mm is applied to a helix region manually defined along the tip vortex trajectory visualized by an iso-surface of Q-criterion=100,000, as shown in Fig. 8. The pitch and the diameter of the tip vortex trajectory before reaching the rudder are 14% shorter than the propeller pitch $P/D_{0.7R}$=1.20 at 0.7R and 1% smaller than the propeller diameter, respectively. As the tip vortex is interfered by the rudder, the pitch is reduced and the diameter is increased. Even if the core of the tip vortex cavitation deviates from the helix region core, it can remain inside the refined helix region, because the tip vortex cavitation is thinner than the tip vortex visualized by Q-criterion.

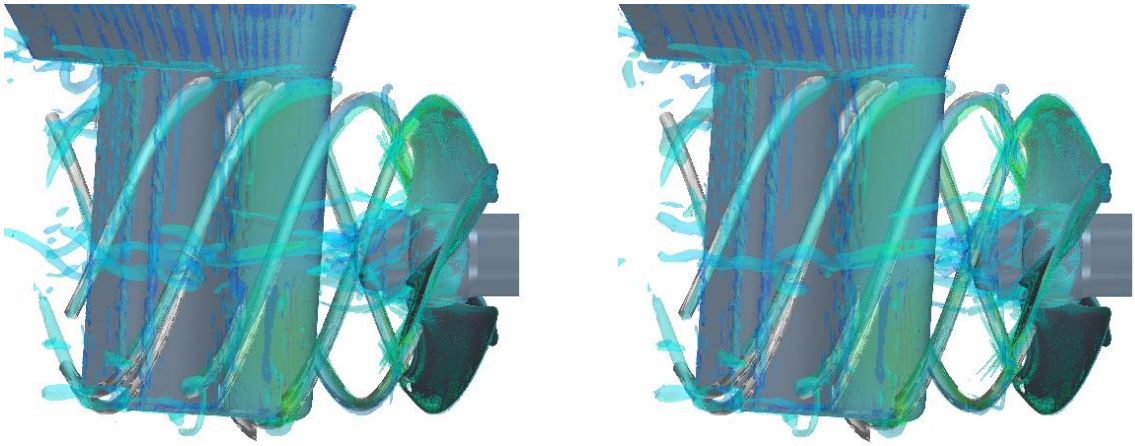

Fig. 8: Manually-defined helix region (gray) with tip vortex trajectory (greenish blue) visualized by an iso-surface of Q-criterion=100,000 before (left) and after (right) simulation with additional grid refinement

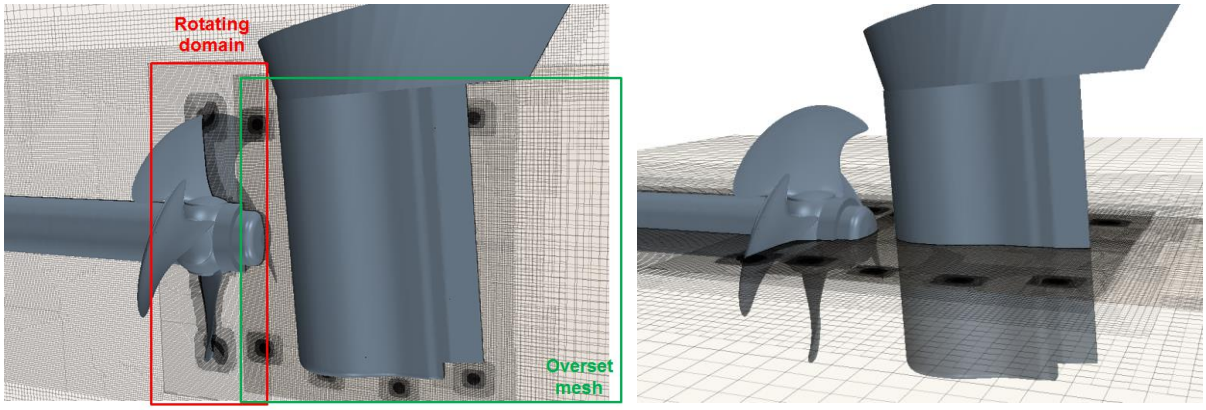

Fig. 9: Computational grid with overset mesh additional grid refinement along tip vortex trajectory

An overset mesh is defined in a cylindrical region encompassing the tip vortex trajectory outside the rotating domain. The additional grid refinement along the tip vortex is applied to the rotating domain and the overset-mesh region, which rotates around the shaft axis according to the propeller speed. Unless the rotating overset mesh is defined, the refined grid can resolve the initial tip vortex, but it will not follow the tip vortex propagation in the static region outside the rotating domain. It is also possible to extend the overset mesh over the propeller model with deleting the separate rotating region, but the rotating region around the propeller model is separately defined and the overset mesh extends

from the end of the rotating domain over the rudder, as shown in Fig. 9 (left), because sophisticated grid arrangements are necessary for mapping of complex flow solutions over the propeller blade between overset and background grids and so it can increase the computational cost additionally. Although Δx of the overset mesh is slightly larger than that in the rotating domain, the overset mesh looks finer in Fig. 9, because the overset mesh is overlapped on the background mesh.

After the previous result from the simulation with the predefined grid is mapped to the additionally refined grid, the simulation is run for 3 propeller revolutions. In Fig. 10, cavitation patterns are visualized with an interval of 30° propeller rotation. The tip vortex cavitation is more extended than that before the refinement, and the cavitation rolling around the tip vortex core is also more pronounced. But the tip vortex cavitation does not reach even the rudder and its extent is still far shorter than that in the experiment. In Fig. 8 (right), the helix region used for the grid refinement is compared with the tip vortex visualized by Q-criterion after the additional simulation. It shows that the tip vortex trajectory is not altered significantly after tip vortex is more resolved by the refinement.

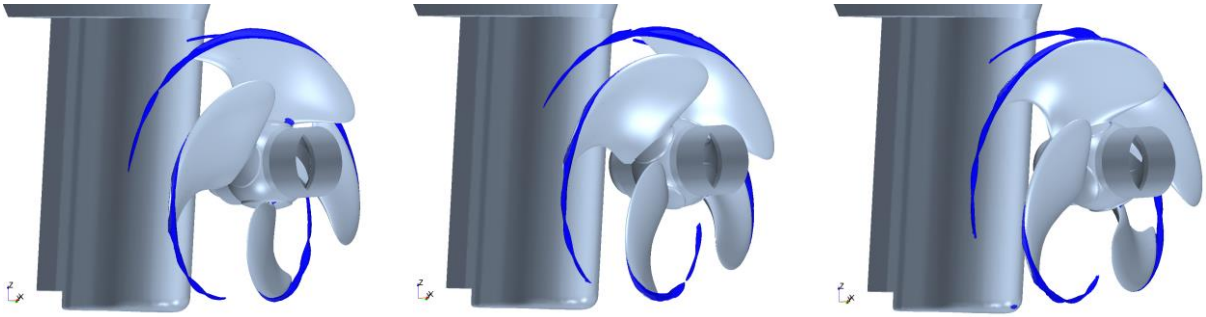

Fig. 10: CFD cavitation simulation with additional refinements along tip vortex trajectory with a 30° blade angle interval

5 Conclusion

Grid refinements along the helical trajectory of tip vortex are critical for resolving tip vortex cavitation in CFD simulations. Manual grid refinements have limitations in sufficiently resolving tip vortex, which becomes fine downstream. The underestimation of the tip vortex cavitation may be due to the grid resolution. The grid size of Δx=0.2 mm for refining the helix region may be not small enough to resolve tapering tip vortex. Tip vortex can also be weakened by numerical diffusion due to the grid size. Further investigation is necessary on grid resolution dependency. Tip vortex can also be underestimated by inherent limitations of DES. Original DES with Spalart-Allmaras turbulence model or LES can be adopted for further investigation to compare tip vortex intensity from different turbulent-flow solutions.

Repetitive adaptive mesh based on Q-criteria of CFD solutions is necessary for further improving accuracy in simulating tip vortex extents. Adaptive mesh with a variable grid size can also be more efficient in terms of computational cost than the manual grid refinement with a uniform grid size.

References

C.D. Simonsen and R. Carstens (2009). Numerical flow simulation of model ship with appendages. DCMT Report

C. Eskilsson and R.E. Bensow (2011). A mesh adaptive compressible Euler model for the simulation of cavitating flow. Proc. of MARINE 2011, Lisbon, Portugal

G. Kuiper (2001). New developments around sheet and tip vortex cavitation on ships' propellers. Proc. of CAV2001, Pasadena, CA, USA

J. Wackers, K. Ait Said, G.B. Deng, P. Queutey, M. Visonneau, I. Mizine (2010). Adaptive grid refinement applied to RANS ship flow computation. Proc. of 28th Symp. on Naval Hydrodynamics, Pasadena, CA, USA

K.W. Shin, P.B. Regener and P. Andersen (2015). Methods for cavitation prediction on tip-modified propellers in ship wake fields. Proc. of SMP'15, Austin, Texas, USA

A Study of Resistance of High-Speed Catamarans and Scale Effects on Form Factor

Sarawuth Srinakaew, **Dominic J. Taunton**, **Dominic A. Hudson**
Fluid Structure Interactions Group, University of Southampton
ss17e111@soton.ac.uk

1 Introduction

Resistance of catamaran is one of the most important aspects of Naval Architecture, Marine, Offshore and Ocean Engineering. There are various works from previous researches dealing with this challenge. Since catamarans have been introduced, resistance components have been evaluated by focusing on many aspects such as hull form, speed (Fn), hull separation to length ratio (S/L). Many methods to estimate resistance were also proposed such as direct measurement from model and full scale, theoretical mathematical model, potential flow, and computational fluid dynamics (CFD). However, resistance prediction of catamarans requires more details to overcome all resistance characteristics to achieve the most suitable design. Resistance of full scale ship is highly relied on two main extrapolation methods following Froude (1872) and Hughes (1954) and this approach is adopted by International Towing Tank Conference (ITTC).

Garofallidis (1996) and Bruzzone et al. (1997) conducted a series of experiment to investigate the scale effect on form factor; however, their results showed undesirable expectation where results are affected by turbulence due to tank interference rather than Reynolds' number. Rather than experimental study, CFD approach is also capable to investigate the scale effect on form factor. Kasahara and Masuda (1998) investigated the flow around ship using CFD at different model scales and found that form factor increase with Reynolds number for large models. ITTC Resistance Committee (1996) suggested that Reynolds number plays an important role in varying form factor. ITTC 2002 also suggested that the scale effect on form factor might be affected by friction correlation line. Tokyo Workshop was summarised by Hino (2005) that form factor of KVLCC2 was also increase with Reynolds number experiments.

Kouh et al. (2009) used CFD code to study scale effect on form factor by focusing on doubling model scales. They pointed out that the total resistance trend is to decrease relative to increasing Reynolds number when doubling model size, which showed a near linear and increasing dependence, reflected a realistic Reynolds number dependence. Raven et al. (2008) investigated scale effect of model and full-scale resistance of KVLCC2 using PARNASSOS CFD code. They focused on the scale effect by looking at the viscous and wave resistance components. Form factor is significantly high comparing with model tests, which could result in increasing ship viscous resistance. Broglia et al (2011) investigated the interference effects of the Delft 372 high-speed catamaran. CFD was used as a support tool in this investigation. The main focus of this work was to investigate the flow interference phenomena between demihulls by looking at dependence of Reynolds' number. Geosim method was used to simulate the flow at Re between 10^6 and 10^8 for two Froude numbers (0.3 and 0.45).

Following these papers, this study investigates catamaran resistance and how scale affects form factor. This paper presents the resistance prediction and scale effects on form factor of Wigley hull by focusing on doubling model scale using CFD application: STAR CCM+ with Reynolds-averaged Navier-Stokes Equations (RANS). Models are investigated at Froude number between 0.15 and 0.9. The results validated against experiment retrieved from Insel (1990).

2 Catamaran Resistance

The standard ITTC practice purpose is to break down total resistance into viscous resistance and wave resistance dependent on Reynolds' number (Re) and Froude number (Fn) respectively.

$$C_T(Fn, Re) = C_V(Re) + C_W(Fn) = (1+k)C_F(Re) + C_W(Fn) \quad (1)$$

Resistance components of catamarans are also broken down in the same way. However, the total resistance of catamaran is different from monohull due to the interference between demihulls. Normally, there are two types of interference including viscous resistance interference and wave resistance interference. To make the breakdown of catamaran resistance components more straightforward, Insel (1990) summarised the resistance components using equation (1) as:

$$\begin{aligned} C_{Tcat} &= (1+k_{cat})C_{Fcat} + C_{Wcat} \\ &= (1+\phi k)\,\sigma C_F + \tau C_W \end{aligned} \quad (2)$$

Where, σ is a frictional resistance interference, ϕ a is form resistance interference factor, and τ is a wave resistance interference factor. In this approach, ϕ is taken into account due to the effects of pressure field change around demihulls caused by flow interference. ϕ and σ can be combined together and written as $(1+\phi k)\sigma = (1+\beta k)$. It can be seen here $(1+k)$ is called form factor and β is viscous resistance interference factor.

3 Numerical Wave Tank, Grid dependence and Turbulence Models Study

3.1 Numerical Wave Tank

The numerical wave tank study focuses on how to create waves correctly. STAR CCM+ v 8.04 tutorial suggests that at least 20 cells per wave height and higher for short waves are recommended. Windén (2012) also suggested that cell per wave height is between 30 and 40. To minimize the number of conditions investigated, only cell per wave height will be investigated while cells per wavelength are kept as recommendation by STAR CCM+ tutorial. The wave used in the grid dependency study has the following specifications: λ = 4m, H = 0.04m and T = 1.60s. It can be seen from figure 1 that number of cells per wave height should be between 30 and 40.

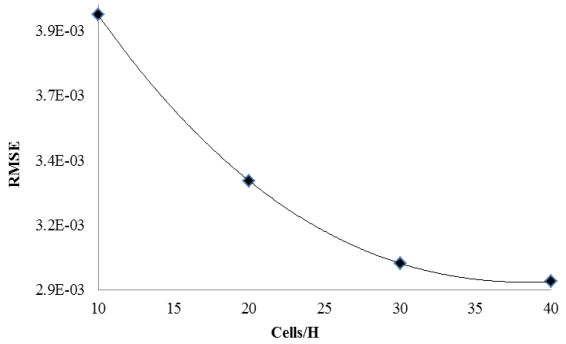

Fig. 1: Number of cells per wave height

3.2 Grid dependence and Turbulence Models Study

The domain front boundary is set to be 3L from bow and outlet is located 9L from stern. Symmetry plane is also used to avoid a very large domain and number of cells. Total grids are investigated as recommended by many researchers especially in Gothenburg workshop 2010. The most suitable number of cells should be in the millions of cells depending on hull geometry and flow characteristics.

For example, Zou and Larsson (2010) pointed out that number of cells should be between 2.97M and 4.37M cells. Wood (2011) also used low cell numbers which is about 1.8M to 2.5M cells. Windén (2003) investigated force on a fixed Wigley hull in waves and pointed out that the final mesh contained 7 million cells. Wigley hull particulars are shown in table 1. The number of cells for grid dependency study starts from 2M to 6M cells, see table 2. To minimize run time, turbulence models are also investigated simultaneously. Two turbulence models are k-ε and SST k-ω. Fig. 4 and 5 show that the optimal number of cells should be between 5M and 6M cells. Final conclusion shows that SST $k-\omega$ model provides better results than $k-\varepsilon$ model.

Table 1: Wigley hull particulars

Model	Wigley III
L, *m*	1.80
L/B	10.00
B/T	1.60
$L/\nabla^{1/3}$	7.116
C_B	0.444
WS, m^2	0.482

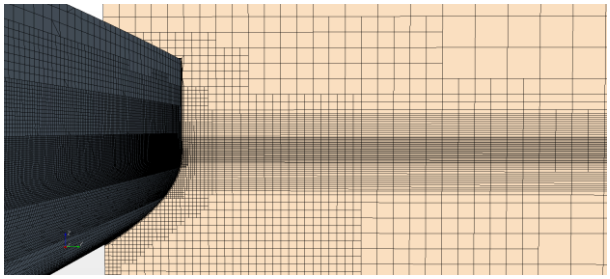

Fig. 2: Grid generation

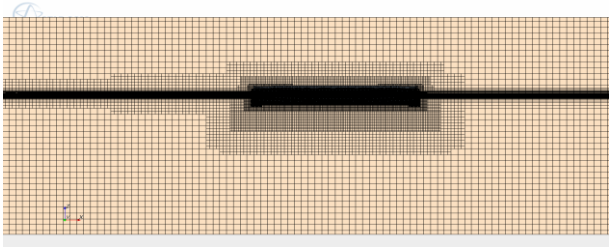

Fig. 3: Grid generation around the hull

Table 2: Grids and turbulence models

Grid	Cells (M)	CT (x 10^{-3})			
		k-ε	% Error	SST k-ω	% Error
Fn = 0.35					
Experiment		5.495			
G1	~ 2.0	5.124	-6.76	5.246	-4.53
G2	~ 3.0	5.346	-2.71	5.381	-2.07
G3	~ 4.0	5.413	-1.49	5.433	-1.12
G4	~ 5.0	5.447	-0.87	5.462	-0.60
G5	~ 6.0	5.448	-0.85	5.467	-0.51

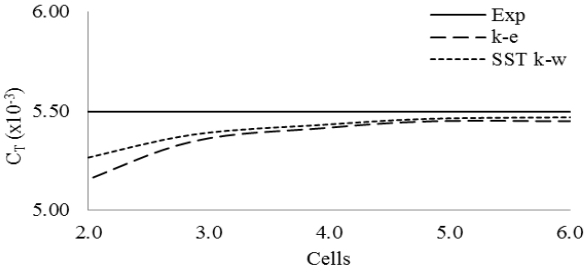

Fig. 4: Total resistance against number of cells (millions)

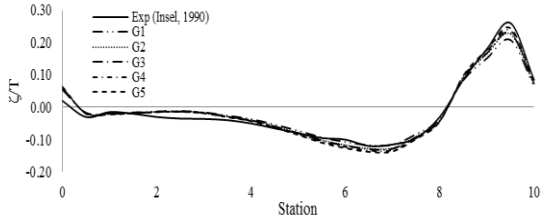

Fig. 5: Wave elevation along the hull

4 Scale effects on form factor

Three different scales of S/L=0.3 configuration are investigated here as seen in table 4. These scale ratios (λ) are selected because dimension of the hulls is not changed rapidly which will result in big tank side and mesh problem. To ensure that the larger models are scaled up correctly, wetted surface area and C_B are evaluated which can be seen in table 3. The wetted surface area and C_B differences are small and less than 1%.

Table 3: Model-scale verification

Model	λ	CFD (m^2)	$*\lambda^2$ (m^2)	%Error	$C_{B,CFD}$	%Error
Model	1	0.482	0.482	0.041	0.4452	0.227
2L	2	1.922	1.928	-0.332	0.4438	-0.045
4L	4	7.752	7.712	0.519	0.4446	0.141

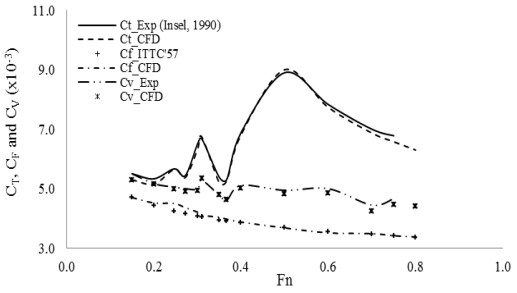

Fig. 6: C_T, C_F and C_V of catamaran S/L 0.3

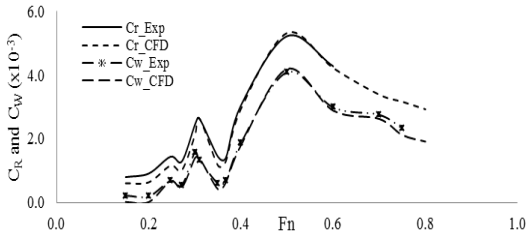

Fig. 7: C_R and C_W of catamaran S/L 0.3

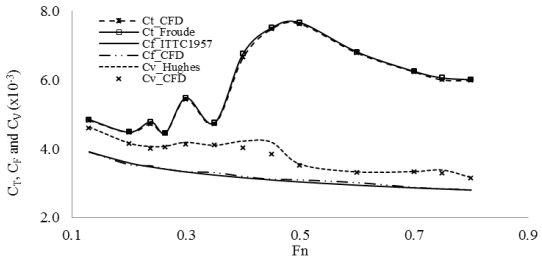

Fig. 8: C_T, C_F and of catamaran S/L 0.3 λ=2

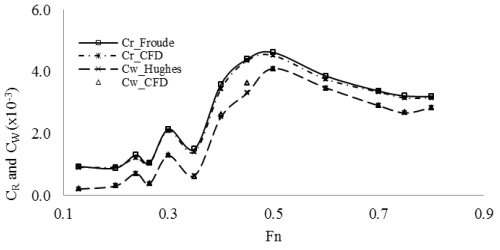

Fig. 9: C_R and C_W s of catamaran S/L 0.3 λ=2

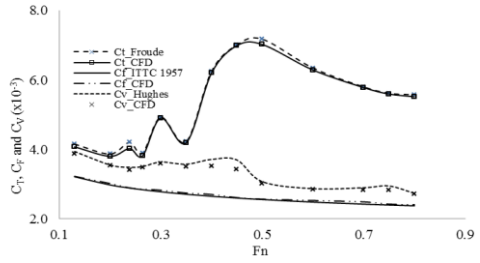

Fig. 10: C_T, C_F and of catamaran S/L 0.3 λ=4

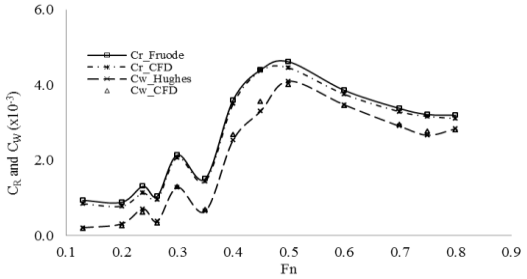

Fig. 11: C_R and C_W s of catamaran S/L 0.3 λ=4

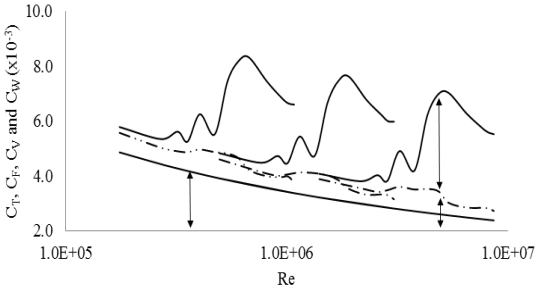

Fig. 12: Model-scale extrapolation: CFD

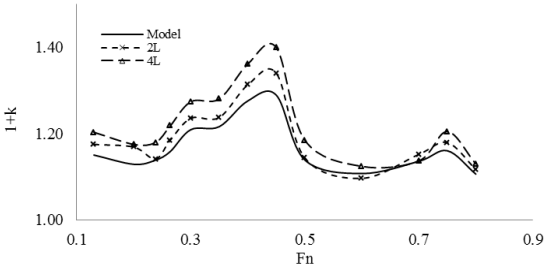

Fig. 13: Form factor at different model sclaes

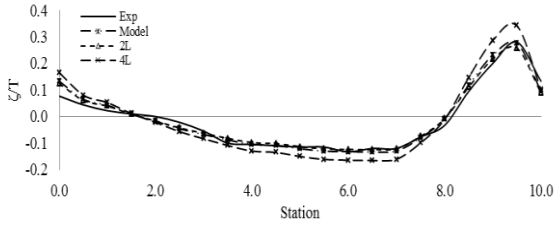

Fig. 14: Wave elevation along the hull (inboard) for different model scale at Fn 0.35

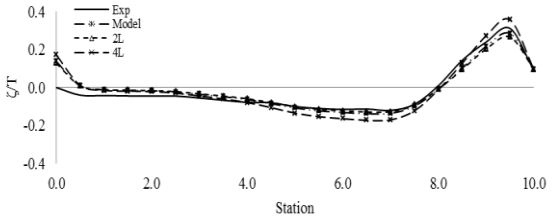

Fig. 15: Wave elevation along the hull (outboard) for different model scale at Fn 0.35

Resistance components of catamaran with S/L=0.3 are evaluated and validated against experimental data. Models are fixed with no sinkage and trim. All resistance components show a good agreement with experiments. Scale effect on form factor is also investigated for S/L 0.3 with scales $\lambda = 2$ and 4. The model scales are increased by doubling model size as seen in table 3. For the scaling up model cases, domain dimensions are also doubling in size. To validate the results, Froude and Hughes approaches are used to find the reference data for Geosim series. Double-model method is also used in this study to estimate viscous resistance. Resistance components of Geosim series show quite good agreement with Froude and Hughes approaches. Wave cut along the hull also shows a good agreement with experiment for Fn 0.35. The average form factors of model scale are 1.22 and 1.16 when applying Hughes approach and experiment respectively, and increase with Reynolds' number.

5 Conclusion

The investigation begins with numerical wave tank study with focuses on how number of cell per wave height affects the accuracy in simulating flow field around the hull. The results show that number of cell per wave height is between 30 and 40 cells. It should be noted that only cells per wave height is investigated; however, the results show a fairly good agreement with experiments, see fig.5, 14 and 15. Resistance components of catamaran with S/L=0.3 are estimated using CFD and show a good agreement with experiment. It can be concluded that CFD application with RANS equations is capable of investigating resistance of ship.

Three model scales are created by using 3D scale. In order to assess the accuracy, some hull characteristics are assessed including block coefficient and wetted surface area. To scale up the models, it should be noted that mesh techniques are different for each model size. Although size of the ship and domain increase, water particle size is not changed. It can be seen that boundary layers of bigger models are much thinner than smaller models. This means that the bigger models require more mesh refinements. Some areas also need more refinements especially the separation between demihulls. To minimize these issues, this study increases model size by doubling model size with small change.

The scale effects on form factor are investigated. The results exhibit that form factor (1+k) increases with Reynolds number (Re) when scaling up the model which agrees with the literature. Three model scales show that form factor (1+k) has a peak value at Froude numbers between 0.3 and 0.5. To ensure that these results are acceptable, wave cuts along the hull are also made. Wave cuts at Fn 0.35 exhibit an acceptable agreement with experiment; however is slightly high for the biggest model as shown in fig. 14 and 15. The differences between experimental data and CFD might be from the measurement techniques as Insel (1990) used a high-speed camera to capture the wave elevation, and the hull was marked at bow and stern at 5 mm draught. Thus, the differences between the experiment and CFD might be from this data interpretation technique.

However, a ship without transom stern is not realistic for this type of applications. Future works which are now under investigation are NPL hull with transom stern. Some areas are being investigated including interference effects, transom drag and scale effects on form factor.

Acknowledgements

Author would like to express his gratitude to all people who always give supports throughout this research especially the team from CD-adapco: the Steve Portal.

References

D. Bruzzone, P. Cassella, S. Miranda, C. Pensa, and I. Zotti, (1997). *The form factor by means of multiple geosim model tests.* Paper presented at the Proceedings of NAV.

D.A. Garofallidis, (1996). Experimental and numerical investigation of the flow around a ship model at various Froude numbers. Part II: uncertainty analysis for measurements. PhD Thesis, Department of Naval Architecture and Marine Engineering, National Technical University of Athens.

G. Hughes, (1954). Friction and form resistance in turbulence flow and a proposed formulation for use in model and ship correlation. *Trans. of the RINA,* Vol. 96, pp. 314-376.

H.C. Raven, A. Van der Ploeg, A. Starke, and L. Eça, (2008). Towards a CFD-based prediction of ship performance progress in predicting full-scale resistance and scale effects.

ITTC. (1996). Report of the Resistance Committee. *Proceedings of the 23rd International Towin Tank Conference* (Trondheim, Norway).

ITTC. (2002). Report of the Resistance Committee. *Proceedings of the 23rd International Towin Tank Conference*(Venice, Italy).

J.S. Kouh, Y.J. Chen, and S.W. Chau, (2009). Numerical study on scale effect of form factor. *Ocean Engineering, Vol.36*(5), pp. 403-413.

M. Insel, (1990). An investigation into the resistance components of high speed displacement catamarans. *PhD Thesis, University of Southampton*.

M. Kasahara, and S. Masuda, (1998). *Verification of simulation flow field around ships by using \FD code.* Paper presented at the Proceedings of the Third Osaka Colloquium Advanced CFD Applications to Ship Flow and Hull Form Design, Osaka, Japan.

R. Broglia, S. Zaghi, and A. Di Mascio, (2011). Numerical simulation of interference effects for a high-speed catamaran. *Journal of marine science and technology, Vol. 16*(3), pp. 254-269.

T. Hino, (2005). CFD workshop Tokyo 2005. National Maritime Research Institute, Japan.

W. Froude, (1872). Experiments on the surface-friction experienced by a plane moving through water. *British Association for the Advancement of Science,* 138-146.

Numerical Studies on Propellers in Open Water and behind Hulls aiming to support the Evaluation of Propulsion Tests

Heinrich Streckwall[*] and Thomas Lücke[*], Tomasz Bugalski[†] and Judyta Felicjancik[††], Tom Goedicke[‡] and Lars Greitsch[‡], Alaz Talay[§] and Mustafa Alvar[§]

[*]HSVA, Hamburg/Germany, [†]CTO, Gdansk, Poland, [††]Gdańsk Univ. of Technology, Poland
[‡]MMG, Waren, Germany, [§]MILPER Istanbul, Turkey streckwall@hsva.com

1 Introduction

A RANS based numerical analysis of propellers can contribute considerably to our understanding of propeller/hull interaction. It may also allow for a review of scaling procedures on results from experimental fluid dynamics (EFD). Using various RANS codes (Fluent, CFX, STAR-CCM+ and FreSCo+) on common test cases the authors first focused on propeller open water (POW) calculations. Next we simulated the propeller hull interaction for two in-behind cases and processed results in close comparison with the POW analysis.

2 Content

One of the treated propellers – CPP 1304 - was released as a public test case several years ago and in 2016 also served for scale effect studies in an ITTC-Benchmark call. For the CPP 1304 our viscous calculations include POW setups (treating model/full scale and hub cap variants). Also an inclined flow and an in-behind case - with a body of revolution (BoR) ahead - are treated. The other propeller - CP 469 - is working behind the research vessel 'Nawigator'. CP 469 is also analyzed in POW mode and 'in-behind' with the 'Nawigator' hull ahead.
For propellers working in-behind, the dual mesh methodology - a fixed mesh covering the hull and outer boundaries / a moving mesh capturing the propeller – represents the genuine approach within a RANS based analysis. For the POW mode a single rotating mesh including also the outer borders would be sufficient. Here, to allow for a thorough comparison of forces and moments when switching from in-behind to POW, the dual mesh methodology was also applied to simulate the POW setup. Moreover, for consistency, the moving mesh part containing the propeller blades was taken over 1:1 to serve also as sub-mesh for the propulsion mode.

3 Results for a propeller in open water and under inclined flow

It is considered that 3 effects cause deviations between POW results from EFD and CFD: a) boundary layer development, b) hub cap force with blades mounted and absent and c) resolution of the vortex wake structures.

3.1 Comparing with model tests

In the usual POW mode the hub cap is pointing upstream. A RANS analysis done under such conditions for the CPP 1304 shows a considerable reduction of the nominal cap resistance ('nominal'=cap subject to free stream / blades absent). With blades present a low-pressure field at their roots extends upstream and influences the hub cap forces. This effect may compensate the stagnation pressure contribution (see Fig. 1). If the comparison of axial forces from POW tests and POW calculations is re-considered by introducing calculated hub cap forces, the thrust curves (KT) come closer together as shown in Fig. 2. Fig. 2 also contains a comparison of HSVA's 'FreSCo+' results using the two different mesh methodologies for the rotating propeller.
The inclined flow case represents a first step into the direction of propeller/wake interaction. For the CPP 1304 related tests under an inclination of 12° were available. Fig. 3 gives the comparison of test results and 'FreSCo+'-calculations. Here the advance coefficient J involves the velocity magnitude of the incoming flow.

3.2 Changing Scales for the propeller CPP 1304

For the CPP 1304 the ITTC-Benchmark call was requesting a numerical scaling of POW data. Table 1 below gives the dimensions, rates and surface conditions which we applied to the two scales of propeller 1304. It has to be noted that the original request for the ITTC-Benchmark call was a roughness setting of 10 microns ($10*10^{-06}$ m) in full scale. In this paper an 'extreme' case is considered in addition, namely a 'slip wall' setting for the blades. Fig. 4 displays the POW performances calculated under the three above mentioned conditions.
An interesting effect was registered when we plotted the surface pressure. In Fig. 5 Model Scale pressure results and in-viscid pressure are displayed section wise. The trailing edge pressure at inner sections may show a pronounced sensitivity to the 'slip wall' setting. This effect is reduced if one moves into the direction of the tip.

			(FS)	(Mo)
Diameter	DP	[m]	3	0.25
blade roughness	kp	[m]	0.00E+00	0.00E+00
rate of revolution	n	[s-1]	4.33	15

Table 1: Dimensions, rates and surface conditions for the Model Scale and Full Scale versions of CPP 1304

4 In-behind results

The above mentioned consistent treatment of the POW setup and the propulsion mode was applied for 2 cases. The 'Nawigator', a standard single screw ship, represents Case 1 and an artificial fully wetted body with rotational symmetric shape defines Case 2. This artificial body of revolution (BoR) was driven by the CPP 1304.

4.1 Body of revolution (BoR)

Using HSVA's 'FreSCo+' for the BoR, pure resistance calculations served to confirm, that a reasonable axial wake field develops at the propeller plane. It was also intended to separate the axial wake into a contribution caused by displacement (potential flow) and an influence from viscous effects. The relevant wakes are given in Fig. 6. The distribution labeled 'viscous' in Fig. 6 is considered a typical circumferential mean axial velocity profile measured behind a single screw hull. For the mounted propeller we used the sliding interface technique to simulate rotation. The bare propeller blade forces at CPP 1304 and the reaction of the body were monitored (Fig. 7). A considerable suction force was acting on the downstream hub cap (Fig. 8).
Further studies were addressing thrust deduction. We evaluated the force difference between the pure resistance mode and the propulsion mode. This was done for the viscous flow case and the artificial in-viscid treatment of the body. The propeller (simulated 'viscous' in any case here) was kept at 15 Hz and the inflow velocity was set to 5 m/s. Combining these two settings formally to a J-value (D=0.25 m) gives formally J=1.33. The latter setting would cause a lightly loaded propeller for POW conditions. The wake effect raises thrust and torque. Note that we have no self-propulsion situation here. In the viscous case the forces on the body relate to roughly 60% of propeller thrust T. When the body is treated in-viscid they amount to roughly 13% of T. However evaluating thrust deduction values $T\text{-}R_T$, we arrive at very similar thrust deduction to thrust ratios (Fig. 9).

4.2 'Nawigator' by HSVA using HSVA's 'FreSCo+' code

The 'Nawigator'- propulsion was modeled via the double body approach with prescribed RPM. A process similar to the standard propulsion test (PT) evaluation was invoked.
The influence of the rudder's presence onto the propulsion behavior is studied especially from the propeller point of view. Even if this topic is not comparable with available model test results, it is worth to take a look into its influence. Slices on mid ship through each calculation domain are given in Fig. 10. The evaluation of the propulsion prediction is here based on a POW characteristic, performed in reverse mode, which means, with an upstream-located shaft (with slip wall condition) and with the original propeller cap pointing downstream (see Fig. 10 below). Using this constellation the evaluation is made in the most consistent manner. The above mentioned discussion about the hub's influence onto the POW results can be avoided. Of course the comparability with test results is weakened.
It turned out, that as a kind of reverse engineering, the target y+ setting on the propeller blades needed to be varied until the POW characteristic as well as the propulsion characteristic were represented reasonable. This approach is understood as an engineering work-around for this kind of design predictions to balance (besides other possible errors) the gap between the fully turbulent flow assumption in the applied RANS solution and the real flow around the blades, which can contain a high amount of laminar flow.
The y+ target of about 120 led to acceptable results for the POW condition, whereas the target y+ of about 70 was to be chosen for the propeller behind the ship model, see Table 2 for the comparison with the experiments.

	KT0	10KQ0	etaD	eta0	**etaR**	**etaB**	etaH	weff	N (Hz)	THDF
CTO EFD	0.249	0.365	0.622	0.482	**1.002**	**0.484**	1.287	0.418	10.36	0.2510
HSVA CFD	0.245	0.363	0.620	0.476	**1.015**	**0.484**	1.283	0.416	10.44	0.2510
difference (%)	**-1.6%**	**-0.5%**	**-0.3%**	**-1.2%**	**1.3%**	**0.0%**	**-0.3%**	**-0.5%**	**0.7%**	**0.0%**

Table 2: EFD-CFD comparison, Vs=11kts

The predicted η_R =1.015 is 1.3% higher than η_R from experiment. From the propeller and from the consistency point of view, the important result is the coincidence of the in behind efficiency $\eta_B = \eta_0 * \eta_R$ = T*Vs*(1-weff)/PD, which relates the increase of η_R to the decrease of η_0 and to a still inappropriate POW representation. After finding the appropriate y+ setting the influence of different boundary conditions onto the propulsion results, especially on η_R, could finally be investigated, as there are: (a) the influence of the presence of the rudder and (b) a slip-wall boundary condition on the propeller.
The first approach (a) can be investigated by experiments as well, whereas the second (b) is only possible to be achieved numerically. This academic boundary condition has the practical advantage of being relative insensible to issues like Reynolds-Number and related uncertainty of the applied grid resolution (see above). It is assumed that the results (KT and KQ) will be free of scale effects.

	KT0	10KQ0	etaD	eta0	**etaR**	etaB	etaH	N (Hz)	weff	**THDF**
w/o rudder	0.232	0.348	0.601	0.5	**0.997**	0.498	1.207	**10.548**	0.372	0.2419
with rudder	0.245	0.363	0.620	0.476	**1.015**	0.484	1.283	**10.435**	0.416	0.2510
difference (%)	**5.6%**	**4.3%**	**3.2%**	**-4.8%**	**1.8%**	**-2.8%**	**6.3%**	**-1.1%**	**11.8%**	**3.8%**

Table 3: Influence of rudder, Vs=11kts

The main influence of the rudder onto the propulsion behavior turned out to be an increased hull efficiency η_H by 6.3% and a reduced η_B by 2.8%, see Table 3. From the propeller point of view this leads via a reduction of η_0 by 4.8% to higher η_R of 1.8%. As expected, the longitudinal force acting on the propeller cap turned out to be a resistance at POW-condition (-0.8% of KT) as well as for the case w/o rudder (-0.07% of KT), but due to the presence of the rudder the force became a thrust! +1.2% of KT. A slice on mid ship through each calculation domain is given in Fig. 10 for both in behind cases as well as for the open water case, showing the total velocity fraction V/U0. The main difference due to the rudder is found to be the diffusion of the propeller slip stream radius and especially the less concentrated vortex core compared to the case w/o rudder and the POW condition. Independent of the applied wall boundary condition on the propeller (non-slip-wall/slip-wall) the influence of the rudder onto η_R is predicted to be very similar (higher η_R of 1.7%), see Table 4. So the viscous effects seem to be limited in this respect and it becomes a pressure related benefit w/o increased torque.

slip-wall	KT0	10KQ0	etaD	eta0	**etaR**	etaB	etaH	N (Hz)	weff	THDF
w/o rudder	0.237	0.323	0.690	0.555	**1.019**	0.565	1.220	10.36	0.379	0.2419
with rudder	0.253	0.341	0.702	0.521	**1.036**	0.540	1.298	10.36	0.423	0.2510
difference (%)	**6.8%**	**5.6%**	**1.7%**	**-6.1%**	**1.7%**	**-4.4%**	**6.4%**	**0.0%**	**11.6%**	**3.8%**

Table 4: Influence of rudder, Vs=11kts, slip-wall condition on propeller blades only, same N

Naturally the missing shear stress on the propeller at slip-wall condition increases KT and reduces KQ as expected, see Fig. 11. Since the propulsion case as well as the POW case is treated in the same manner, the propulsion evaluation should show more or less the same η_R, which is obviously not the case (slip-wall 1.036 Tab. 4 vs. non-slip-wall 1.015, Tab. 3). The reason can be related to a numerical inaccuracy which alters the flow characteristic at POW condition differently than at the PT condition. Besides this, it possibly shows the remaining unresolved scale effect and serves as an outlook onto η_R beyond full scale RN.

4.3 'Nawigator' by MMG

Fig. 12 shows the development of η_R comparing in behind torque with open water torque calculated at different RN. The experimental result could be reproduced with very good accuracy. When decreasing the open water RN towards the level of the in behind situation there is a clear increase in η_R. A viscous scale effect on η_R as well as a reliably recommendation of a CFD supported propulsion analysis is targeted with the results of full scale calculations at same RN in open water and in behind conditions.

4.4 'Nawigator' by MILPER using ANSYS 'Fluent'

Calculations are done viscid and in-viscid for η_R estimation. The POW analysis was set up in reverse mode. POW characteristics are shared in Fig. 13. The procedure for the open water calculations is similar to the HSVA's approach (previously mentioned). There were two main focus points for the investigation of the propeller performance including the hull, namely the validation of the propulsion point and the rudder effect. The propulsion point is determined in two operating conditions using the double body approach (see Table 5). η_R is calculated using an interpolation function on the open water efficiency calculations done beforehand. The

effect of the rudder is related to an extra high pressure field, increasing the propeller thrust while increasing the torque as well. According to the CFD analysis, if the quality of performance is expressed by η_R, the propeller performs better with the rudder since thrust increases more than torque.

	Vm (m/s)	n (rps)	T - CFD (N)	T - Test (N)	ERROR	Q - CFD (Nm)	Q - Test (Nm)	ERROR
with rudder	1.301	6.91	28.97	29.67	2.37%	0.993	0.997	0.41%
	1.789	10.36	68.89	69.58	1.00%	2.300	2.301	0.05%
w/o rud-der	1.301	6.91	26.814			0.957		

Table 5: Propeller performance in behind the Nawigator hull, Influence of rudder, Vs=11kts

5 Conclusion and Acknowledgement

In an on-going project we studied the performance of propellers in various flow environments. A combined treatment of the POW and in-behind setup allows judging the power saving quality of a wake adapted propeller. The power at POW under thrust- and RPS-identity is the reference. This is linked to the processing of performance data obtained via model tests, where the 'relative rotative efficiency' η_R is derived as quality index for wake adaption. The problem and challenge of the test evaluation process lies in the removal of any Reynolds-number dependence from η_R (POW tests are usually done at higher Reynolds-numbers than the related propulsion tests). Here CFD may support the test evaluation.

This work is linked to the INRETRO project realized as a European ERA-NET venture within the MARTEC framework. The financial support by the national funding associations is gratefully acknowledged.

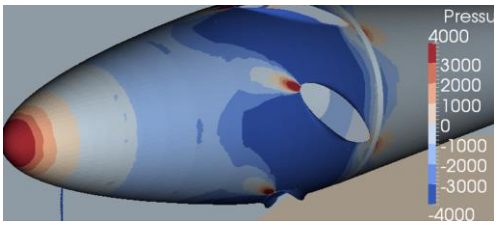

Fig. 1: Upstream cap of CPP 1304 in POW mode

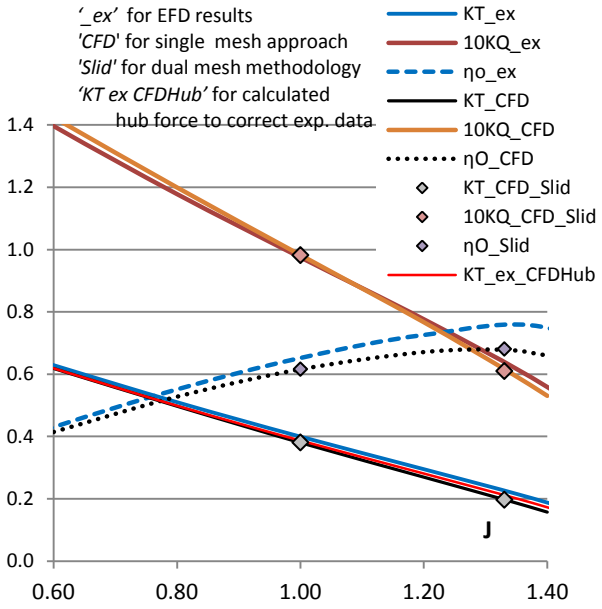

Fig. 2: CPP 1304 open water results

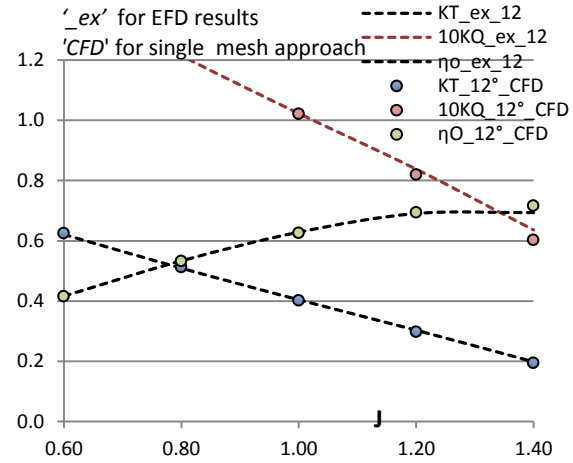

Fig. 3: CPP 1304 inclined flow results (12°)

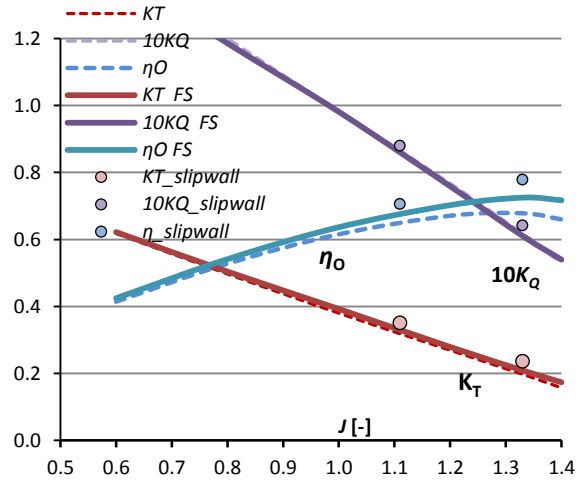

Fig. 4: POW RANS results (two scales and 'slip wall')

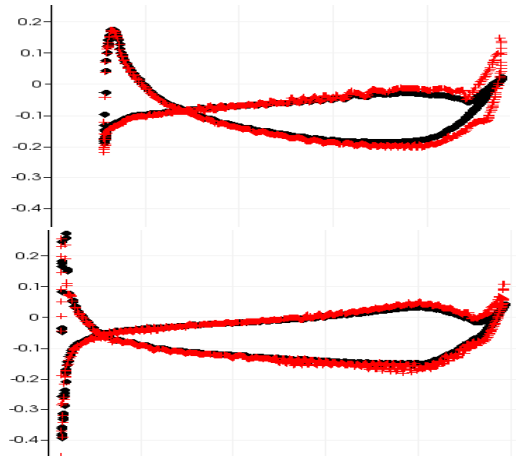

Fig. 5: CPP 1304: Surface pressure results (Cp) at two sections (upper: close to hub; lower: mid of blade) for viscid (*) and in-viscid (*) treatment of blade

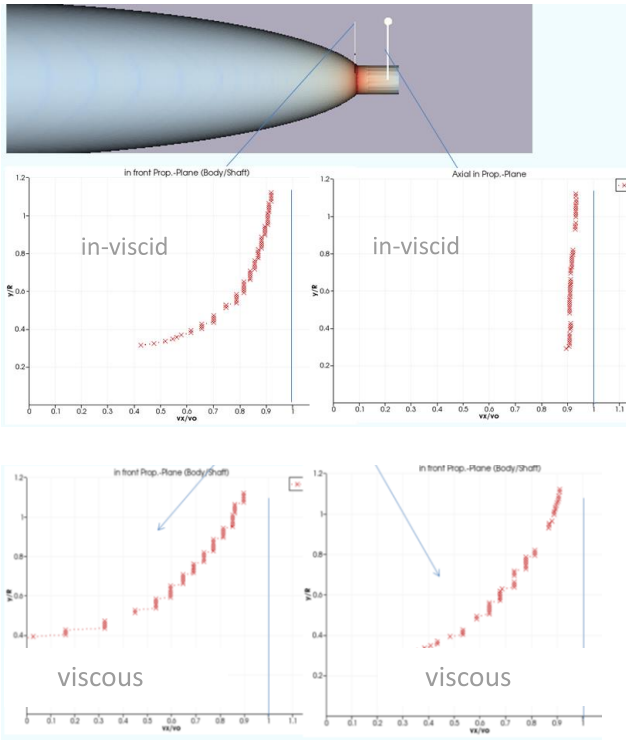

Fig. 6: Axial velocity profiles due to in-viscid and viscous BoR, ahead of (left) and at propeller (right)

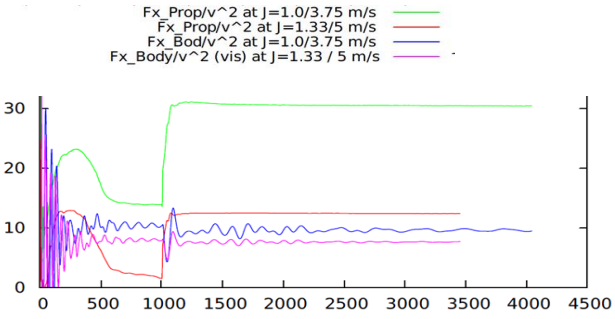

Fig. 7: History of forces on propeller 1304 and body of revolution for 2 propeller load conditions

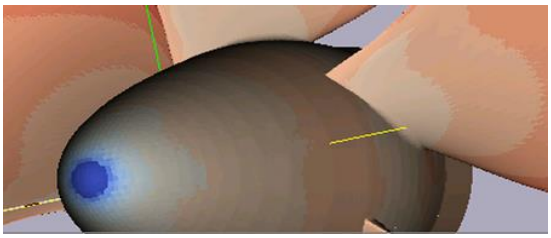

Fig. 8: Low pressure region (blue) on hub cap of propeller 1304 when working behind the BoR

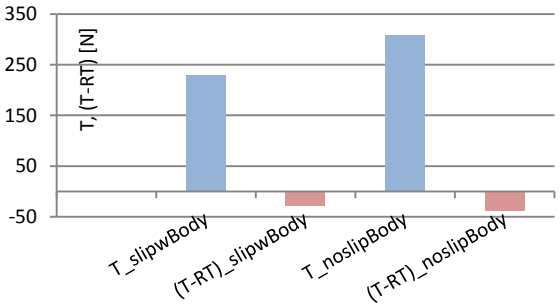

Fig. 9: Thrust and thrust deduction for propulsion of viscid and in-viscid body.

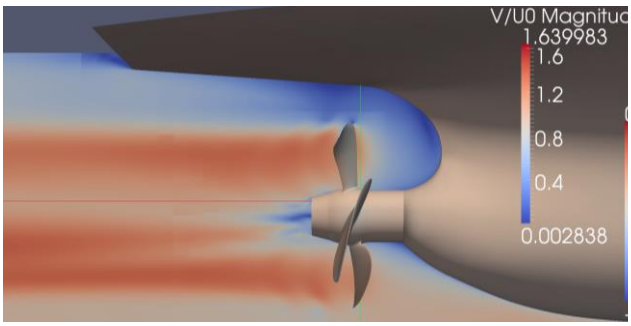

w/o rudder: weff=0.372, FxCap/FxProp=-0.07%

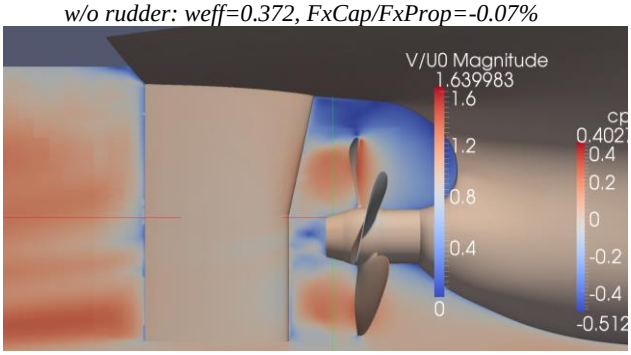

with rudder: weff=0.416 (+12%), FxCap/FxProp=+1.24%

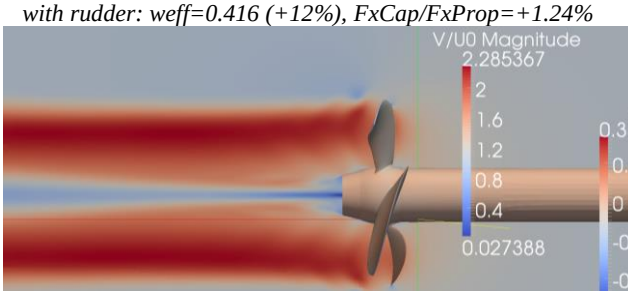

POW J=0.45, weff=0.0, FxCap/FxProp=-0.82%

Fig. 10: Velocity distribution V/U0 on mid ship of 'Nawigator' Vs=11 kts and for POW

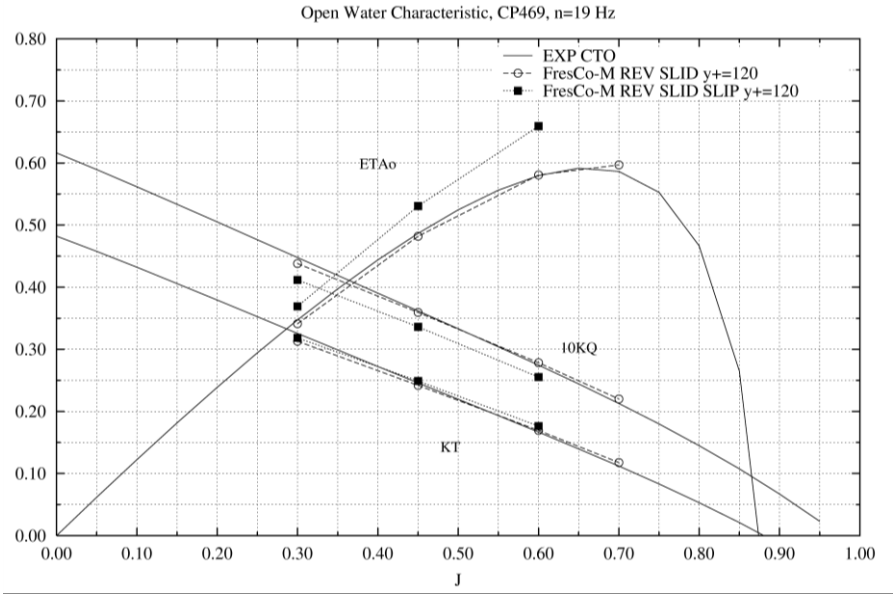

Fig. 11: POW characteristics, EFD, CFD by HSVA comparing no-slip-wall and slip-wall on blades

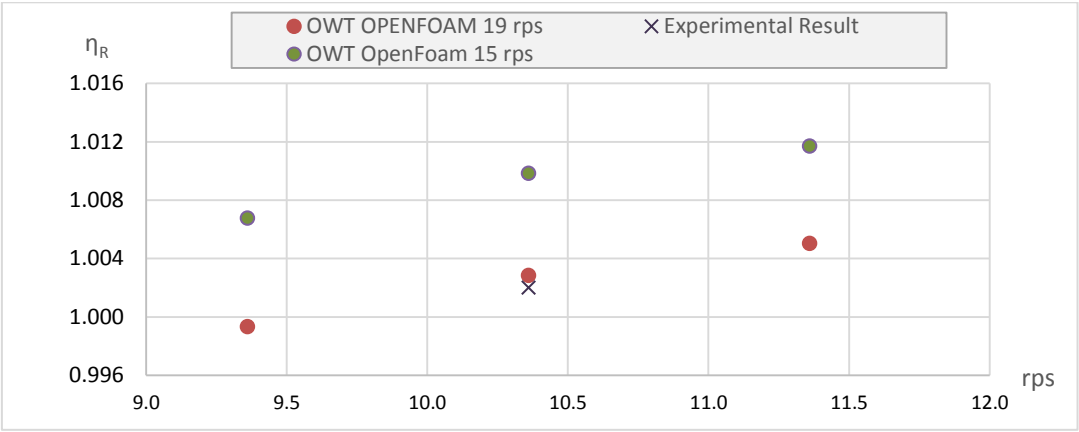

Fig. 12: Development of η_R of CP 469 according to MMG, comparing in behind torque with open water torque calculated at different Reynolds-numbers

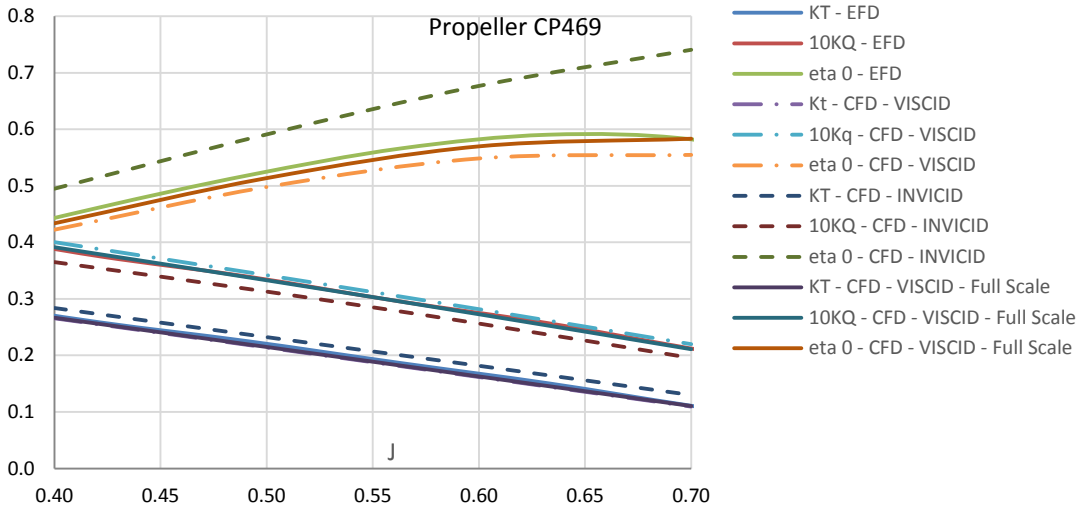

Fig. 13: POW characteristics, EFD, CFD by MILPER comparing no-slip-wall (at two scales) and slip-wall

Numerical Simulation of Fridsma Hull Using Overset Grid System

Omer Faruk Sukas[1], Ferdi Cakici[1], Metin Kemal Gokce[1]

[1]Faculty of Naval Architecture and Maritime, Yildiz Technical University, Istanbul, Turkey

1 Introduction

Hydrodynamic analysis of ships is a troublesome area especially if they are planing. For higher Froude numbers, motions like trim and sinkage are relatively greater. The hydrodynamic lift which is generated by the hull at higher Froude numbers, raises up the hull above the free surface and reduces the wave making resistance. H. Ghassemi, S. Yu-min (2008), state that planing hulls have a great advantage at high speed regions in contrast to conventional hulls . Due to motions having a direct effect on the hydrodynamic forces acting on the planing hull, they have to be estimated meticulously.

Savitsky (1964), is one of the most famous researchers that deals with planing hulls . He derived semi-empirical formulas for the motions and the resistance of the prismatic planing hulls. His formulas which are in a good accordance with the experimental results, are still in use today. After Savitsky's leading work, many other studies were done by the researchers in the field. Yousefi et al. (2013), reviewed the existing techniques for hydrodynamic analysis of planing hulls . The study covers current methods to approach planing hull problem and is considered to be useful for the new researchers in this area. In their next study, Yousefi et al. (2014), reduced the total drag by introducing two tunnels at the bottom section of a planing hull in their numerical simulations . Kohansal et al. (2010), introduced and validated an algorithm for the hydrodynamic characteristics of 3D planing hulls and the results that they estimated with this algorithm show satisfactory compliance with the experimental measurements.

In the present study, the flow around a benchmark planing hull Fridsma is simulated for an extensive Froude number range of 0.59 to 1.78 with a commercial CFD code. As in the study of Fridsma (1969) and Akkerman et.al (2012), mentioned hull has a simple hull geometry and extensive experimental data. Finite volume method is used along with the overset meshing technique to capture the large motion of the hull at higher speeds. The results obtained from the numerical simulations are compared with the results found in the work of M. Mousaviraad and F. Stern (2015) as well as Savitsky's semi-empirical approach and available experimental data.

2 Geometric Characteristics

In this paper, the hull geometry is created with the help of some analytical formulas available in [6] and the principal parameters of the hull are depicted in Table 1. A constant 20° deadrise angle with L/b=4 is selected and the position of LCG is %60 L from the bow. The model has an initial trim value due to the center of gravity lying behind the center of buoyancy. The displacement of the vessel is calculated from the displacement coefficient value given in Fridsma`s paper and it is selected as $C\Delta = 0.608$. Note that all geometric values are given for the hydrostatic case.

Table 1:Hydrostatic properties of the Fridsma hull.

Dimensions and Parameters	***Value***
L(m)	1.143
B (m)	0.286
T (m)	0.069
LCG from aft (m)	0.457
VCG from keel (m)	0.084

Wetted area (m^2)	0.3905
Deadrise angle (β)	20°
Δ (kg)	14.219
$I_{zz}=I_{yy}(kgm^2)$	0.5805
Fn (-)	0.59, 0.89, 1.19, 1.48, 1.78
Speeds (m/s)	1.97, 2.98, 3.98, 4.95, 5.96

The Fridsma model has a hard chinned prismatic form which is created based on the analytical expressions and it has a single chine line as shown in Fig. 1. These sharp and flat sections provide to generate acceptable lift on the body when the speed of the vessel increases. As it can be seen from the figure, the model has no appendages and does not include any steps.

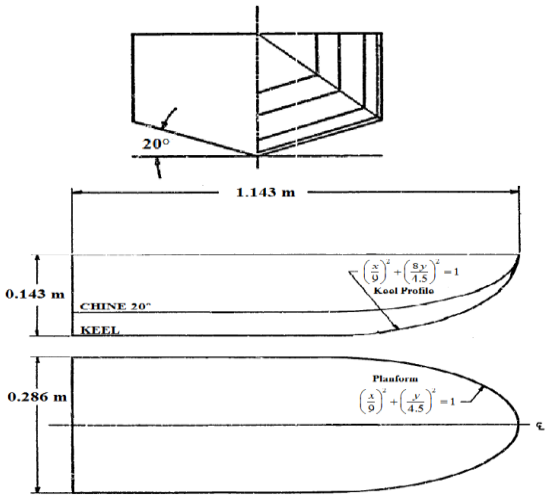

Fig. 1. Lines and analytic expressions of the Fridsma hull. [6]

3 Computational Domain and Boundary Conditions

In the present study, calculations are carried out for half of the domain due to symmetric ship hull to reduce the computational time. Domain limits are extended enough to visualize the divergent and transverse waves entirely. The computational domain is constructed according to the CFD guidelines set by the ITTC (2011b) and it extends for 3L in front of the ship, 9L behind the hull, and 4L to the side and 1.2L under the keel of the model. The air region is 0.3L above the free surface. Please refer to Fig. 2.

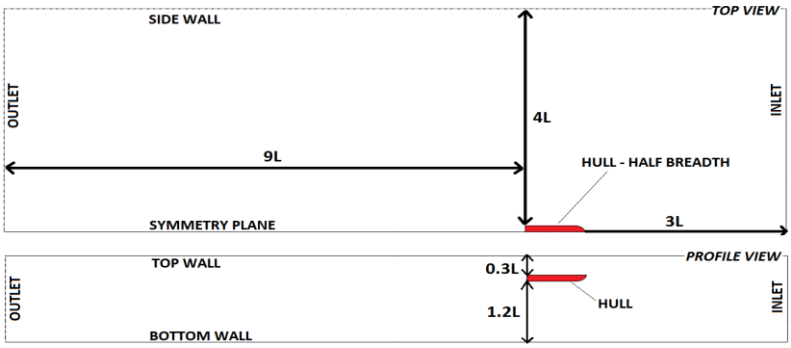

Fig. 2. Domain extents from top (above - half breadth) and profile (below) view.

Boundary conditions are applied separately for background and overset regions. All boundaries of the domain are represented in Fig. 3. Symmetry (free-slip) condition is dictated for side and symmetry boundaries while top and bottom boundaries are defined as wall (no-slip). On the inlet and outlet boundaries, velocity inlet and pressure outlet conditions are imposed, respectively. For the overset region, symmetry surface is defined as free-slip similar to the background region and overset condition is dictated for the rest. Besides that, hydrostatic pressure of flat wave and velocity of flat wave field functions are imposed to outlet and inlet boundaries since the simulations are performed by considering the calm deep water condition.

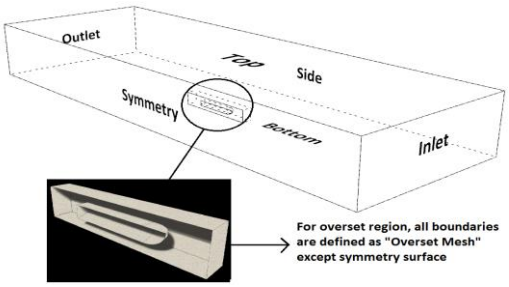

Fig. 3. Boundary conditions. The symmetry plane in the overset region is removed to allow better visualization.

4 Overset Grid Design System

From the practical point of view, in order to get accurate results from simulations, one should discretize the control volume into finite size elements corresponding to the flow characteristics around the ship hull. Motions of a body inside fluid can be represented by two different grid system; overset and deforming mesh. Deforming mesh technique has some handicaps compared to the overset grid system when simulating the body motions with large amplitude, but it can be still used in calm water simulations where the motions are quite small. Cakici et.al. (2015) presented an example study using deforming grid to solve for planing hulls is given in reference. In this study, overset mesh technique which is also known as Chimera or overlapping mesh is used to represent the large motions (especially for pitch motion) of the hull accurately. The overset mesh design system is shown below in Fig. 4 for coarse grid which has a total of 1.1 M grid elements.

Overset grid system, which is embedded in the background mesh enclosing the entire simulation domain, is used to represent the motion of the hull and there is an “overlap” zone that encompasses the overset region. The information is passed through the overlap block between overset and background regions.

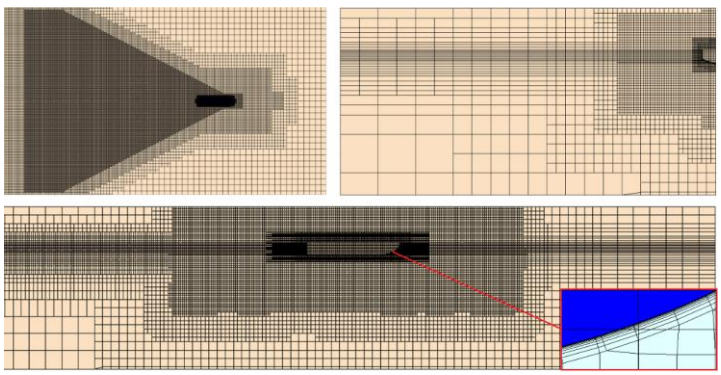

Overset grid system around the planing hull within boundary layer.

5 Results

In this section, numerical results obtained with RANSE based codes using overset grid design are compared with the experimental and the semi-empirical results in terms of total resistance, trim angle and sinkage. Our results are also compared with some other computational results from the literature. These results are discussed briefly to investigate the behavior of the hull in displacement and planing regimes. Fig. 5 depicts the non-dimensional resistance values of the Fridsma hull including our numerical results, numerical results of Mousaviraad and Stern, a semi-empirical formula and experimental data.

Results obtained with numerical methods are close to experiments in lower Froude numbers and it might be said that these results are in better accordance with experiments when compared with Savitsky's approach. This is due to Savitsky method being valid in the planing regime which is generally after Fr=0.7. On the other hand, numerical results by Mousaviraad and Stern and Savitsky's approach over-predict resistance values when compared with the present numerical study for large Fr numbers. Overall trend in Fig. 5 indicates that resistance values of the present study agree well with the experimental data for all Fr numbers.

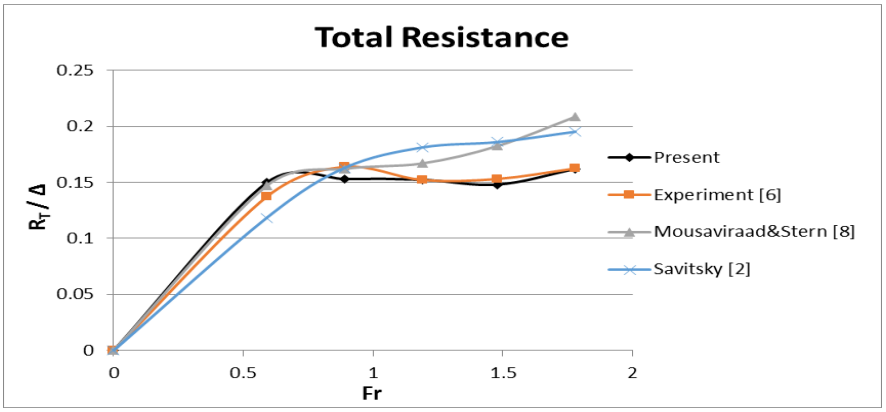

Fig. 5. Validation results of non-dimensional total resistance values for the whole range of Fr.

In order to investigate the differences of the curve characteristics in Fig. 5, values of sinkage and trim should be observed. Trim and sinkage (rise) values are given in Fig. 6 and Fig. 7, respectively. Savitsky approach under-predicts the sinkage of the vessel and this might be one of the reasons why the order of error is larger for resistance in Fig. 5.

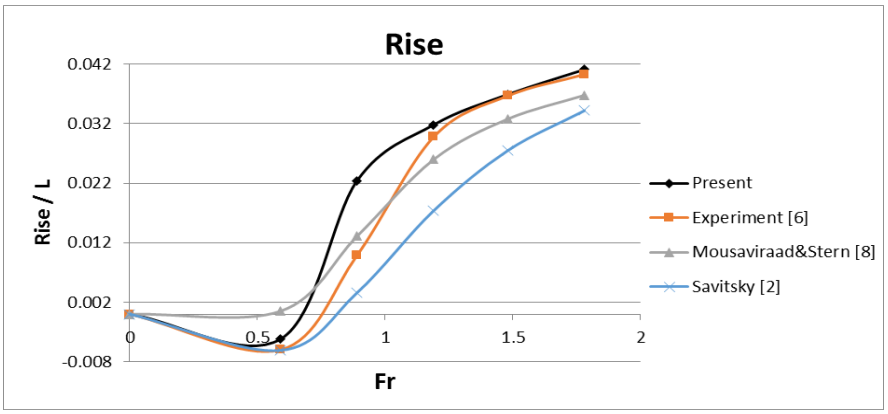

Fig. 6. Comparison of rise of the planing hull in different Fr numbers

Experimental trend shows a squat motion at Fr=0.59 which is successfully predicted by Savitsky and present study while Stern's study under-predicts the sinkage value at this displacement mode. It can be directly noted that present study grabs the experimental data at all Fr numbers although there seems to be some discrepancy at Fr=0.89 for sinkage. This also reflects to the obtained resistance value given in Fig. 5 as this seems to be the only value where there is a bias of results between CFD and experiments. Therefore it might be said that large motions of the hull at higher Fr is better simulated with the implementation of the overset grid compared to Savitsky's semi- empirical approach as can be analysed from Fig. 5 and Fig. 6. Large body motions of the hull is further investigated with trim of the planing hull. Fig. 7 shows the trim values of the planing hull for the whole range of Fr numbers and it is found that the results generated by the overset grid system are satisfactory.

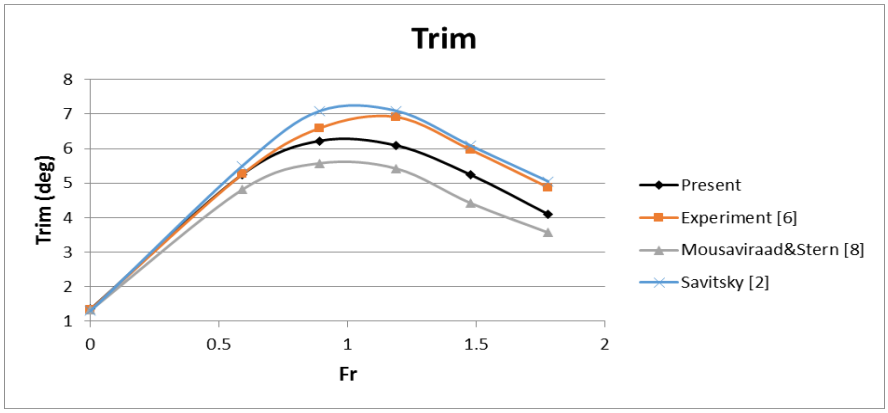

Fig. 7. Trim angles of the planing hull with respect to Fr.

Although it seems that the characteristics of the curves are same, a small discrepancy between present work and experiment is observed, especially in large Fr. On the other hand, Savitsky returns closer results with respect to numerical codes except the transition region. In this region, results from the present work and Savitsky are in good accordance. Fig. 8 shows an example wave elevation contour at the free surface at Fn=1.19.

A significant conclusion derived from Fig. 5, 6 and 7 is that the sinkage of the planing hull effects the resistance results more than the trim values of the hull in large Fr. Wetted area of the hull decreases much more when the hull rises in planing mode with respect to trim.

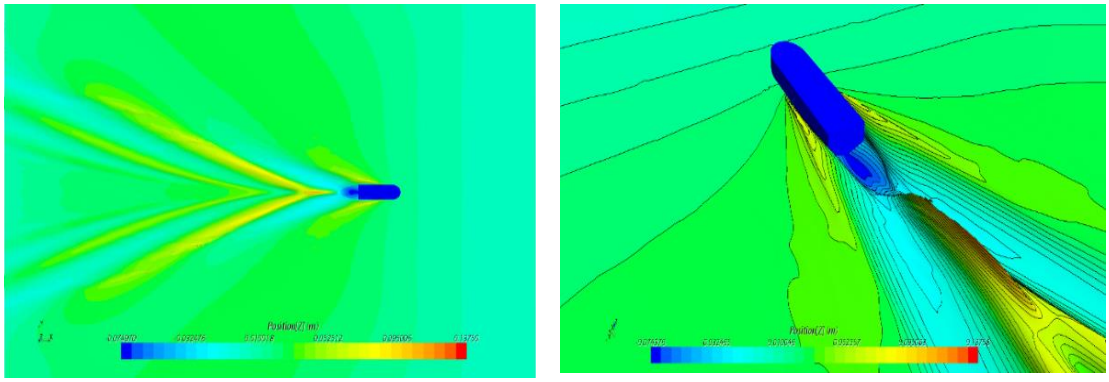

Fig. 8. Kelvin waves occurred behind the hull at Fr=1.19

6 Conclusion Remarks

Validations of CFD for the Fridsma hull which is free to heave and pitch motion in deep water were performed between Fr=0.59 and 1.78. All planing hull simulations are carried out with STAR-CCM+. Simulation results only include calm deep water condition. Numerical results obtained with RANSE based codes using overset grid design were compared with experimental and empirical results in terms of total resistance, trim angle and sinkage. Present study predicts the resistance well at planing speeds (Fr>0.9) while Savitsky's numerical approach slightly over-predicts in this range. This result shows that the overset grid design has a good capability to represent the large motions of the planing hull. Because the overset mesh system is flexible to large motions. There is no re-meshing process and the elements in the domain do not deform. In other words, the planing hull is moving together with the grid system surrounding it which makes it consistent in terms of element quality close to its boundaries. Once a high-quality grid system is settled in the fluid domain, the numerical setup will use the same elements during the analysis.

Similar trends were represented for trim results however Savitsky is closer to experiment at all speeds. At displacement regime, squatting is successfully captured in this study and also by Savitsky but Savitsky's empirical approach under-predicts the sinkage at higher Fr with respect to numerical codes.

Seakeeping validations in regular head waves for a certain range of wave frequency are planned to be added to this work. CFD validation studies for self-propulsion, course keeping and some maneuvering tests will be investigated. Further, resolving the details of the spray flow and computation of wave resistance of a planing hull will be the most important issues of the future study.

References

H. Ghassemi, S. Yu-min (2008). Determining the hydrodynamic forces on a planing hull in steady motion. Journal of Marine Science and Application, 7-147.

D. Savitsky (1964). Hydrodynamic analysis of planing hulls. Marine Technology, 1, 71-95

R. Yousefi, R. Shafaghat, M. Shakeri (2013). Hydrodynamic analysis techniques for high-speed planing hulls. Applied Ocean Research,105-113

R. Yousefi, R. Shafaghat, M. Shakeri (2014). High-speed planing hull drag reduction using tunnels. Ocean Engineering, 54-84

A.R. Kohansal, H. Ghassemi, M.Ghaisi (2010). Hydrodynamic characteristics of high speed planing hulls including trim effects, Turkish Journal of Engineering and Environmental Sciences, 34-155

G. Fridsma. (1969). A systematic study of the rough-water performance of planing boats, Davidson Laboratory Report, 1275

I. Akkerman, J. Dunaway, J. Kvandal, J. Spinks, Y. Bazilevs (2012). Toward free-surface modeling of planing vessels: simulation of the Fridsma hull using ALE-VMS. Computational Mechanics, 50(6), 719-727.

M. Mousaviraad, F. Stern. (2015). URANS studies of hydrodynamic performance and slamming loads on
High-speed planing hulls in calm water and waves for deep and shallow conditions. Applied Ocean Research, 222-240

International Towing Tank Conference (ITTC), (2011b). Practical guidelines for ship CFD applications. In: Proceedings of the 26th ITTC.

F. Cakici, O.F. Sukas, O. Usta, A.D. Alkan. (2015). A Computational Investigation of a Planing Hull in Calm Water by U-RANSE Approach. International Conference on Advances in Applied and Computational Mechanics

Tip Vortex Cavitation Inception Without a Cavitation Model

Camille Yvin and Pol Muller
DCNS RESEARCH/SIREHNA, Nantes/France
camille.yvin@sirehna.com, pol.muller@sirehna.com

1 Introduction

In the field of ship propulsion, cavitation is known as a major source of underwater radiated noise. Furthermore it can affect the propeller itself either by reducing its propulsive performances or even by causing major erosion to the blades and surrounding surfaces. For navy ships and fisheries or oceanographic research ships, this extra underwater radiated noise can considerably reduce both the stealth of the vessel and the performances of acoustic survey devices. For these types of ships, the operability of the vessel is therefore closely linked to the cavitation behaviour of its propeller(s). It is crucial that in the early design phases the designer ensures that the non cavitating operating profile of the propeller is as large as possible. In the context of the development of a numerical towing tank, DCNS Research has developed a process to model the behaviour of a propeller behind a ship, including the detection of cavitation inception. At full scale and in free sailing condition for large navy and fisheries research ships, the first region where cavitation appears when the ship speed increases is located in the tip vortex (and hub vortex) area, see G. Kuiper (1981). This paper focuses on a numerical criterion that has been developed to predict the cavitation inception speed of a propeller, or any lifting surface generating a tip vortex.

The cavitation within a vortex is due to the curl up of the viscous core which produces a low pressure area at its center. The intensity and diameter of a vortex shedding from a lifting surface are growing with the load or the circulation on the surface. As we are focusing on the inception of the cavitation phenomenon, in light to medium loaded conditions, the diameter of the viscous core which is responsible of the cavitation inception can be very small compared to the size of the propeller. This is a very local phenomenon. The numerical towing tank developed by DCNS Research is mostly focused on CFD techniques using finite volumes. The size of the mesh cells in the vicinity of the blades as used for open water or self-propulsion computations are not compatible with the large pressure and velocity gradients occurring in the tip vortex area. It is therefore necessary to refine the mesh as locally as possible to avoid tremendous increase of the number of cells and of the computation time and cost. Manual refinement can be time consuming and the cost of the effort can be larger than the reduction of the computation cost. Automatic refinement techniques are the best suited to address this topic, as demonstrated for instance by A. I. Oprea (2013).

The evaluation of the cavitation inception phenomenon is based on the analysis of the pressure field only. No cavitation model is used. This approach has three main advantages. The first one is that results are independent of the cavitation model which is often based on a simplified version of the Rayleigh-Plesset equation. The second advantage is that, for an open water case, stationary simulations can be used because only the water phase is considered (multiphase simulations require in most cases a non stationary approach). The last advantage is that, for one advance coefficient, only one simulations is needed to determine the cavitation number at the inception. On the contrary, when a cavitation model is used, several cavitation numbers have to be considered to evaluate the inception of the cavitation.

Of course, this approach raises issues concerning the definition of a cavitation appearance criterion. This criterion must be both physically relevant and adapted to numerical methods. In the same time, it is important to wonder whether current numerical methods can be used to evaluate a correct pressure field inside a tip vortex and if the answer is positive, what are the good practices to check the convergence.

In this work, ISIS-CFD which is available as a part of the FINE^{TM}/Marine computing suite is used to perform the numerical simulations, see P. Queutey (2012). Experimental conditions and data of the PPTC propeller case can be found in SVA Postdam (2011). This work was funded by DCNS.

2 Physical and numerical settings

The propeller diameter is $D = 0.25$ m (model size). The computation domain is cylindrical (open water simulations). Its diameter and length are about 10 and 15 propeller diameters respectively (5 upstream

and 10 downstream). Pressure is imposed at the downstream boundary and velocity on the other outside boundaries. The flow is considered incompressible. No-slip conditions are applied on the propeller boundaries. The turbulence model is the Explicit Algebraic Stress Model (EASM) and wall-functions are used in the vicinity of the boundary layers ($y+$ of about 70). A moving reference frame approach is used to take into account the rotation of the propeller. One advance coefficient is considered first ($J = 0.8655$) and a second advance coefficient ($J = 1.0806$) is then used to validate the approach. In all cases, the rotation rate is fixed at $N = 25$ rot.s^{-1}.

The cell sizes are given in number of successive divisions of the propeller diameter which is denoted by n. For example, 6 divisions means that the cell size is about $D/2^6$. For the reference mesh (i.e. without mesh refinement) 8 divisions are used for the blades (0.98 mm), 10 for the leading and trailing edges (0.24 mm) and 11 for the blade feet and blade tips (0.12 mm). The transition between two levels of refinement is made of at least four cells.The reference mesh is made up of 10.8 millions of cells (see Fig. 1). Of course, the thrust and torque evaluated with this reference mesh are in good agreement with the experimental data for the considered advance coefficients (differences are about 3% for K_T and 2% for K_Q).

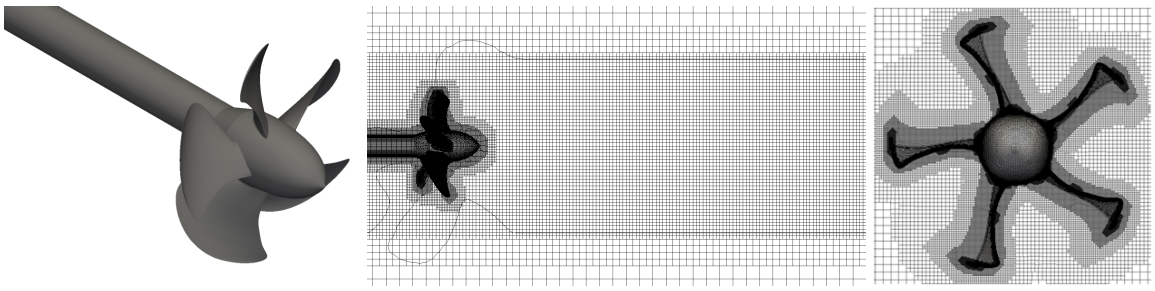

Fig. 1: Propeller geometry and reference mesh.

3 Application of an automatic mesh refinement technique on the tip vortex

The application of an automatic mesh refinement technique is not straightforward. One of the main difficulties is the definition of the refinement criterion. Here, because the goal is to capture the tip vortex, it is tempting to focus on the vorticity field. Nevertheless, the vorticity can be very large at other areas such as the boundary layer for example which can lead to unnecessary refinements. Moreover, the final objective is to accurately evaluate the pressure field so it is natural to focus on a criterion derived from the pressure. One must also know the shape of the field upon which the criterion is based. In the case of the tip vortex, the pressure field in a transversal direction looks like a Gaussian function (see Fig. 6). Mainly because it is impossible to know if the minimum of pressure is actually located in the tip vortex, a refinement criterion should not be based on the value of the pressure itself. The pressure gradient is not satisfactory either because the criterion would be null at the tip vortex center (see Fig. 2). On the contrary, the Hessian of the pressure is a quite interesting quantity because refinement would occur both at the tip vortices centres (important if the goal is to evaluate the minimum pressure value) and their bounds (important to accurately capture the volume occupied by the tip vortex).

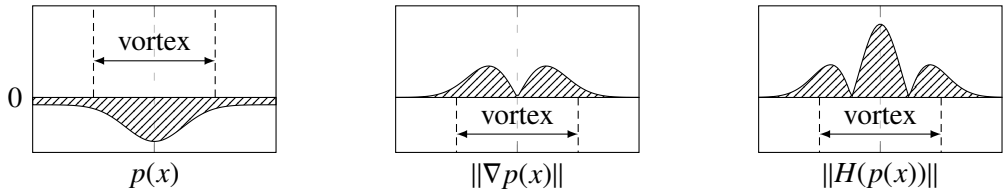

Fig. 2: Value, gradient and hessian of the pressure in a vortex as a function of a transversal direction.

The used refinement criterion is also anisotropic and depends on the local size of the cells. A cell is refined in its direction i ($i = 1, 2, 3$) if $\left|H(p)^{0.5} \cdot d_i\right| > T$ where d_i is the cell size in the i^{th} direction and

T the threshold as it is described in J. Wackers (2013). It means that the cells will have a higher chance to be refined for lower threshold values. To avoid too much refinement, a minimum cell size $n_{\min}$ is also defined. The threshold and the minimum cell size are the two parameters which are discussed in this work. As we will see, they must be jointly chosen.

Table 1: Number of cells ($J = 0.8665$).

	$n_{\min} = 12$			$T = 50$		
Reference	$T = 200$	$T = 100$	$T = 50$	$n_{\min} = 10$	$n_{\min} = 11$	$n_{\min} = 12$
10.8	11.6	17.4	34.9	16.3	23.1	34.9

For instance, if the threshold is too high, no mesh refinement occurs (see Fig. 4.a and Fig. 4.b) and the pressure inside the tip vortex is too high (see Fig. 3.b). If the minimum cell size is too high, the mesh refinement does not correctly occur at the tip vortex center (see Fig. 4.f) and the low pressures are not well evaluated (compare Fig. 3.f with Fig. 3.h). On the contrary, if the minimum cell size is too low for a given threshold, the minimum cell size is partially reached which produces heterogeneous meshes (see Fig. 6). Indeed, the highest mesh refinements are limited by the threshold value which is subject to numerical difficulties because of the Hessian operator. A heterogeneous mesh is not optimal because the precision of the results is not improved compared to the number of additional cells (see Fig. 3.h, Fig. 3.g and corresponding numbers of cells given in Tab. 1). In order to avoid this issue, it is better if the highest mesh refinements are limited by the minimum cell size instead of the threshold value. Moreover the minimum cell size is a quantity which is relatively easy to generalize, on the contrary of the threshold.

Table 2: Minimum of $Cp_N = p/(0.5\rho N^2 D^2)$ inside the tip vortex ($J = 0.8665$).

	$n_{\min} = 12$			$T = 50$		
Reference	$T = 200$	$T = 100$	$T = 50$	$n_{\min} = 10$	$n_{\min} = 11$	$n_{\min} = 12$
-9.13	-9.42	-10.42	-11.75	-10.31	-11.15	-11.75

In brief, one must first choose the minimum cell size and the threshold accordingly. The choice of the minimum cell size is a balance between accuracy and the number of additional generated cells. It seems that in this case $n_{\min} = 11$ is the best compromise. The threshold must also be lower than 100 if the low pressures have to be correctly evaluated (see Fig. 3.c and 3.d). As a consequence, for $n_{\min} = 11$, the relevant threshold value should be close to $T = 50$. With these values, the low pressures are quite well evaluated and the mesh is homogeneous (see Fig. 3.g and Fig. 4.g). The remaining question is: is it possible to determine these relevant values or a least an estimation of their order of magnitude without running systematic series of calculations? This can be done with a simplified evaluation of $\left|H(p)^{0.5} \cdot d_i\right|$ (see Fig. 5). One can see that, with no refinement (reference mesh), the maximum value is about 100 (see Fig. 5.a), so it could have been predicted that a value about $T = 200$ was not relevant and $T = 100$ was a little overestimated value. One can also check that for $n = 11$ and $T = 50$, values of the simplified evaluation are smaller than the threshold which means that it is the minimum cell size that limits the mesh refinement and not the threshold (see Fig. 5.g). For $n = 10$ and $T = 50$ (see Fig. 5.f), it is not the case which, as it was already said, it is not an optimal situation.

One can also notice that the minimum pressure is not yet converged (see the last two values in Tab. 2). This illustrates one of the reasons that prevents the definition of the mesh refinement criterion to be based directly on the pressure field because the numerical effort must be very important to get a converged value.

4 Definition and evaluation of a cavitation inception criterion

In the previous section, it was shown that the computation of the minimum pressure inside the tip vortex is a difficult task. As a consequence, the definition of the cavitation inception criterion can not be based on it. Moreover the minimal pressure is not a relevant criterion: it is not only because the pressure is lower than the vapour pressure that the cavitation starts. This is illustrated by the Rayleigh-Plesset

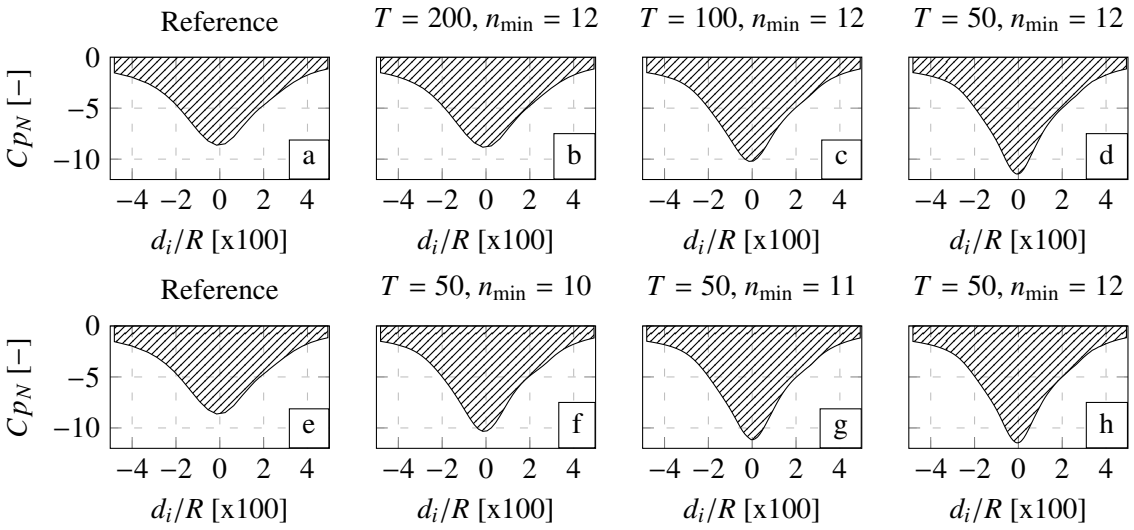

Fig. 3: Pressure inside the tip vortex along a transversal direction as a function of the distance to the center ($J = 0.8665$).

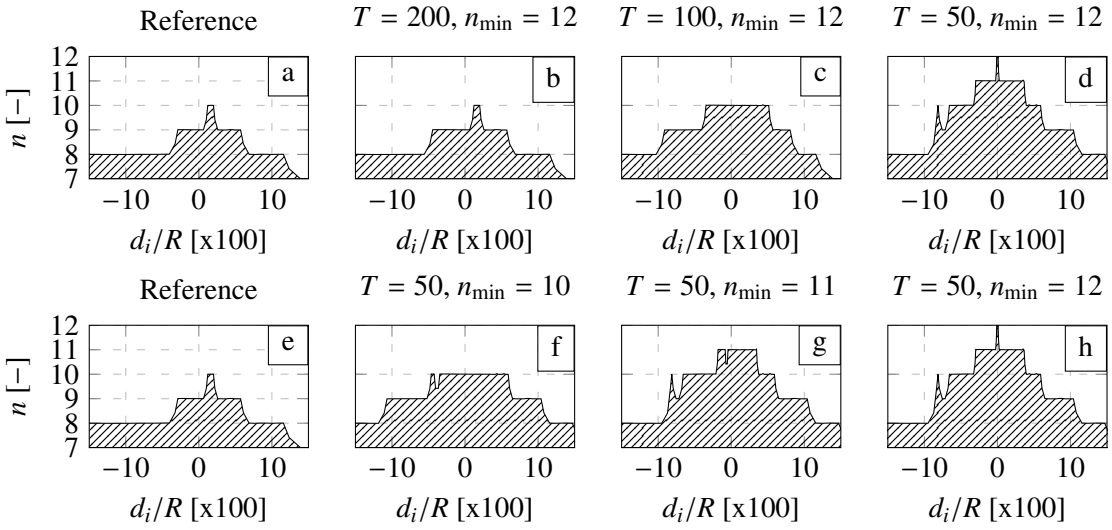

Fig. 4: Number of divisions of the cells inside the tip vortex along a transversal direction of the vortex as a function of the distance to the center ($J = 0.8665$).

equation which shows that the volume where the pressure is lower than the vapour pressure must be large enough to overcome surface tension effects on the cavitation bubble. That is the reason why the cavitation inception criterion used in this work is based on the volume occupied by the lowest pressures. It is a relevant criterion from a numerical point of view because it is easy to compute. The main difficulty is to define a relevant threshold which is not only based on physics but also on the accuracy of the detection methodology used in the experimental setup (visual, high speed video, acoustics, ...).

Because experimental results are available, we can look at the problem from another point of view: which numerical volume do we obtain for the experimental Cp_N ETVC (End Tip Vortex Cavitation, see Tab. 3)? According to the experimental report SVA Postdam (2011), differences between blade 1 and blade 3 are due to experimental uncertainties. For the first advance coefficient, the numerically evaluated volume is between 0.079 cm^3 and 0.109 cm^3 per tip vortex with the simulation g (see Fig. 7). For the second advance coefficient (the settings of the simulation g were applied), the volume is between 0.072 cm^3 and 0.095 cm^3. For this two advance coefficients, the volumes are quite close (even if the Cp_N are quite different) and the order of magnitude is consistent with what is experimentally observed.

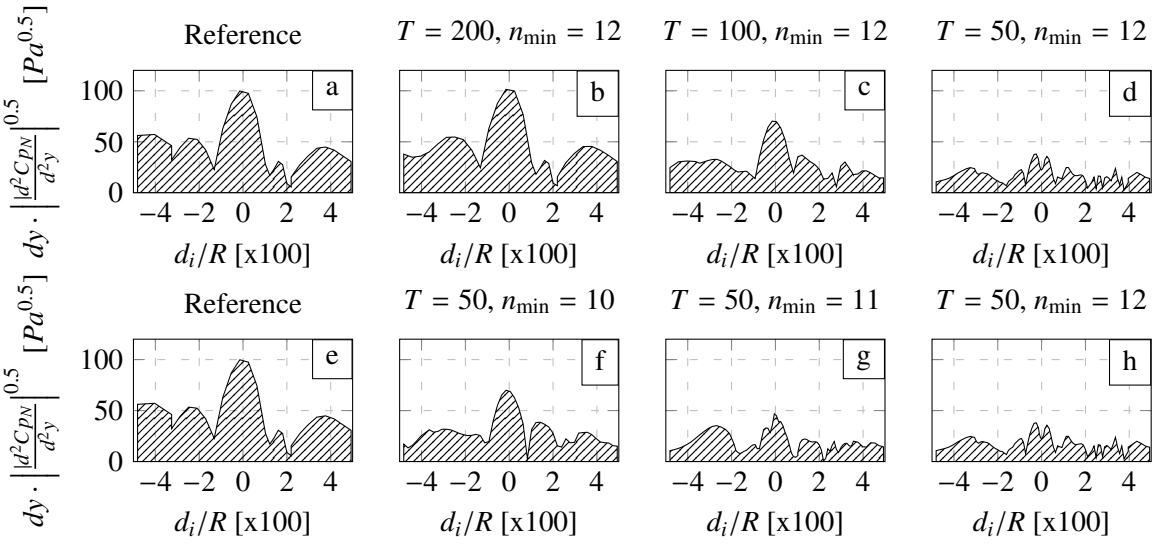

Fig. 5: Simplified evaluation of $\left|H(p)^{0.5} \cdot d_i\right|$ inside the tip vortex along a transversal direction as a function of the distance to the center ($J = 0.8665$).

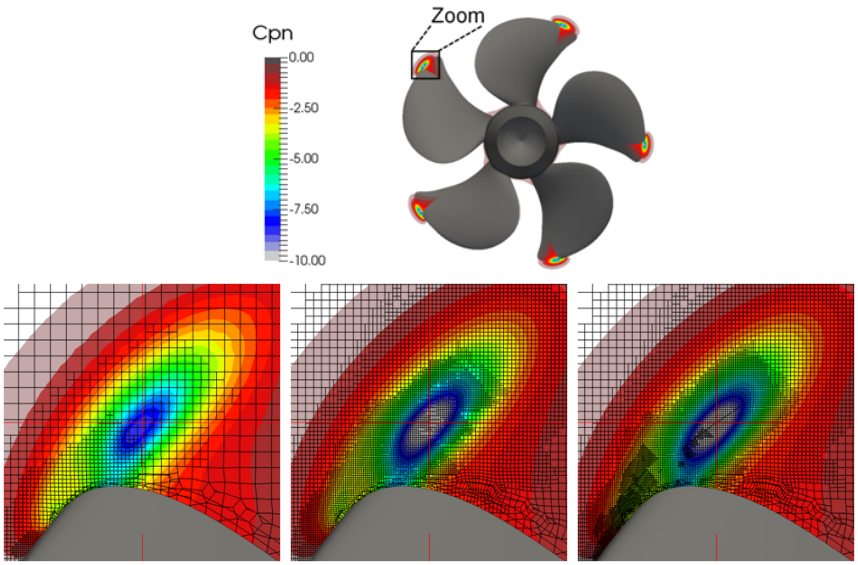

Fig. 6: Cp_n inside the tip vortex in a transversal plane centred on the minimal pressure. Reference mesh (left), $T = 50$ and $n = 11$ [g] (center) and $T = 50$ and $n = 12$ [d,h] (right).

Table 3: Experimental Cp_N ETVC.

J [-]	blade 1	blade 3	mean
0.8655	7.859	7.470	7.664
1.0806	4.961	4.661	4.811

Moreover, if the mean volumes previously evaluated are supposed to be correct values to estimate the inception of the cavitation phenomenon, it is possible to evaluate the corresponding Cp_N ETVC for all simulations. As shown in Tab. 4 for $J = 0.8665$, this criterion is not sensitive to the minimum of pressure, which it is important for the robustness of the results. It is also shown that automatic mesh refinement must be applied to obtain acceptable results. The difference between the reference meshes and the refined ones are about -18.5%. and -13.3% for $J = 0.8655$ and $J = 1.0806$ respectively (for $J = 1.0806$, Cp_N ETVC is about 4.17 with the reference mesh and 4.81 with the refined mesh).

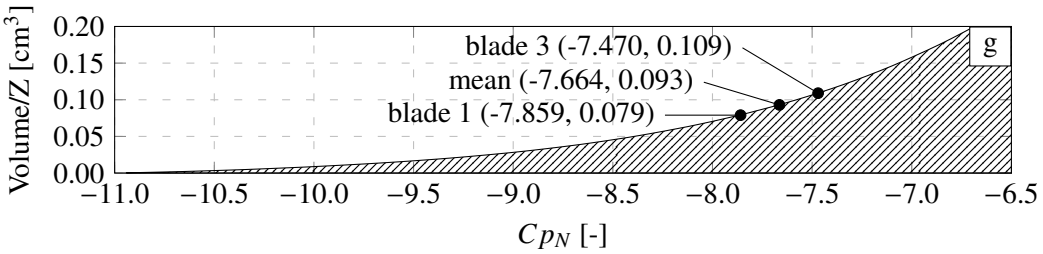

Fig. 7: Cumulated volume divided by the number of blades.

Table 4: Numerical Cp_N ETVC for V=0.093 cm^3 ($J = 0.8665$).

		$n_{\min} = 12$			$T = 50$		
Experiment	Reference	$T = 200$	$T = 100$	$T = 50$	$n_{\min} = 10$	$n_{\min} = 11$	$n_{\min} = 12$
7.66	6.24	6.46	7.41	7.52	7.53	7.66	7.52
0%	-18.5%	-15.7%	-3.3%	-1.8%	-1.7%	0%	-1.8%

To conclude, this criterion is a good candidate to numerically evaluate the inception of the tip vortex cavitation because it is easy to compute and appears to be robust. It is not very important to correctly evaluate the minimum of pressure but it is important to correctly evaluate the volume occupied by the low pressure area. An automatic mesh refinement technique is especially suitable to reach that goal.

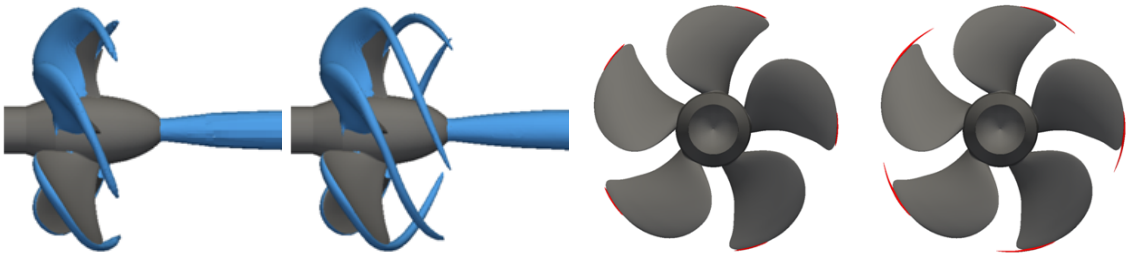

Reference $Cp_N = -1.0$ | $T = 50$, $n_{\min} = 11$ $Cp_N = -1.0$ | Reference $Cp_N = -7.66$ | $T = 50$, $n_{\min} = 11$ $Cp_N = -7.66$

Fig. 8: Several Cp_N isosurfaces.

5 Conclusion

The evaluation of the tip vortex cavitation inception with only one simulation for each advance coefficient and without any cavitation model is possible. Nevertheless, an automatic mesh refinement technique seems to be necessary and needs to be performed with special care. This allows to accurately evaluate the low pressures inside the tip vortex which are used to compute the criterion. Of course, this methodology must be applied to other cases to be further validated and to define a general threshold for the volume occupied by the low pressures. It would also be interesting to study the influence of the scale effects on the volume threshold.

References

G. Kuiper (1981). *Cavitation inception on ship propeller models*, PhD-thesis Delft University of Technology.

A. I. Oprea (2013). *Prediction of Tip Vortex Cavitation for Ship Propellers*, PhD-thesis University of Twente.

P. Queutey, G. Deng, J. Wackers, E. Guilmineau, A. Leroyer and M. Visonneau (2012). *Sliding grids and adaptive grid refinement for RANS simulation of ship-propeller interaction*, Ship Tech. Res. **59**, 44-58.

SVA Postdam (2011), *Postdam Propeller Test Case (PPTC) - Cavitation Tests with the Model Propeller VP1304 - Report 3753* (2011).

J. Wackers, G. Deng, E. Guilmineau, A. Leroyer, P. Queutey, and M. Visonneau (2013). *Combined refinement criteria for anisotropic grid refinement in free-surface flow simulation*, Comput & Fluids, **92**, 209-222.

Ship Scale Self-Propelled Added Resistance Study

Constantinos Zegos, Alejandro Caldas, Sebastiaan Zaaijer
Lloyd's Register, Southampton/UK
constantinos.zegos@lr.org

1 Introduction

A study in ship performance in sea state was carried out by the Technical Investigation Department (TID) in collaboration with the Cooperative Research Ship (CRS). The object was to assess the capabilities of Computational Fluid Dynamics (CFD) in predicting ship performance in waves. The study started with making comparisons against model scale tests in order to validate the computational set-up. Subsequently simulations of the vessel travelling through sea state were made at ship scale including the effect of the propeller. The vessel in question was a large range tanker and the experimental data was provided by the CRS.

All simulations were performed using Star-CCM+ version 9.06. The Navier-Stokes equations for multiphase incompressible flow were solved using κ-ε turbulence modelling. The near wall treatment was based on a logarithmic wall function in order to limit the sizes of the meshes, a technique that has been extensively validated in TID. Taking advantage of the symmetry of the hull and the fact that the propeller was not modelled, half the vessel was simulated except for the self-propelled case where a complete model of the hull was used.

All transport equations were solved using a second order spatial differencing scheme and the transient terms were solved using a second order up-wind differencing scheme. The motion of the ship as a result of encountering the waves was captured using the overset mesh method which used two flow domains. The first, called the overset mesh, contains the hull and its immediate vicinity and was allowed to pitch and heave with the ship. The second was the broader flow domain which remained fixed in space and through which the waves travelled.

The mesh had to capture the waves travelling through the domain as well as the waves radiated from the motion of the vessel, resulting in a relatively large vertical refinement around the free surface of the water. Cells far downstream were stretched in the longitudinal direction in order to dampen the wave propagation so as to reduce the possibility of reflections at the outlet boundary.

2 Model scale CFD

For the validation, two different scenarios were considered: the ship operating in regular and irregular sea states. The variables used for the validation were heave, pitch, drag Quadratic Transfer Function and pressure evolution in pressure sensors fitted to the ship bow.

2.1 Regular sea state

The comparison between the experimental and calculated pitch for frequencies between 0.425 and 0.9rad/s can be seen in Figure 1 which shows a close match. In order to have a measure of the accuracy of the model, the experimental results were plotted against CFD results in Figure 2. The closer the points are to a straight line of 0.5 slope that passes through the origin the better the match between CFD and experiments. The agreement between CFD and experiments was measured by means of the correlation parameter R. R=1 corresponds to a perfect correlation whereas $0<R<0.8$ the correlation is considered weak. As shown in Figure 2, a near perfect correlation is achieved for the

pitch where R=0.999. It should be noted that all results are given at ship scale in order to simplify comparison to full scale results.

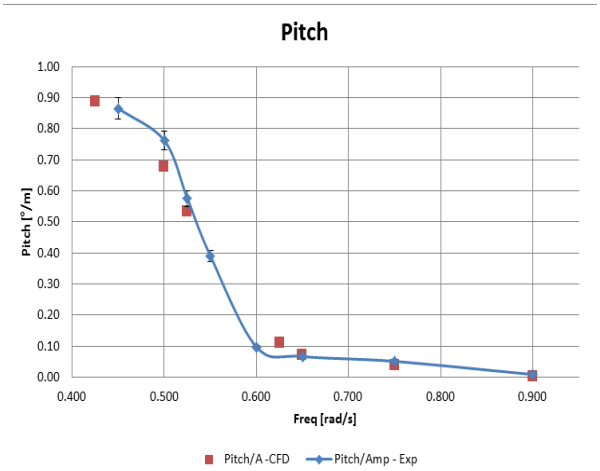

Fig.1: Pitch against frequency plot for the CFD and experimental results.

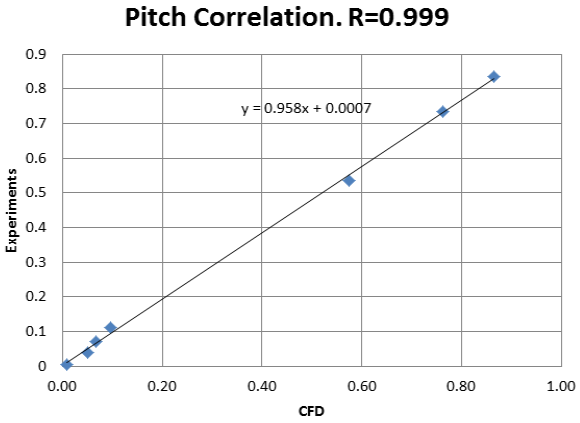

Fig. 2: Pitch against frequency correlation.

The comparison between the experimental and calculated heave can be seen in Figure 3. As for pitch, the CFD prediction and experimental values are quite close. In Figure 4, the experimental results are plotted against CFD and again show a high correlation factor of 0.993.

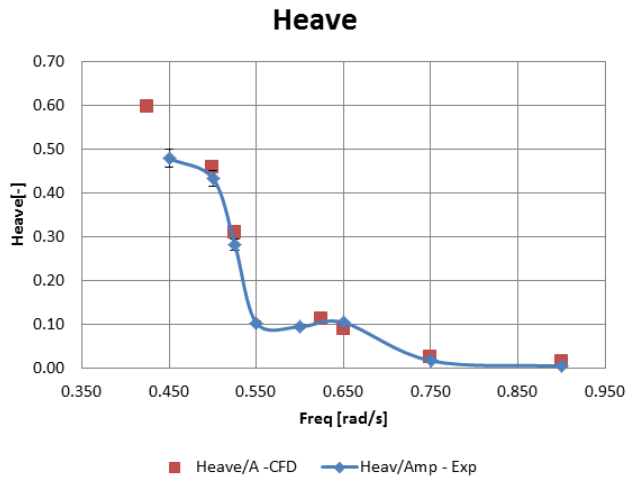

Fig. 3: Heave against frequency plot for the CFD and experimental results.

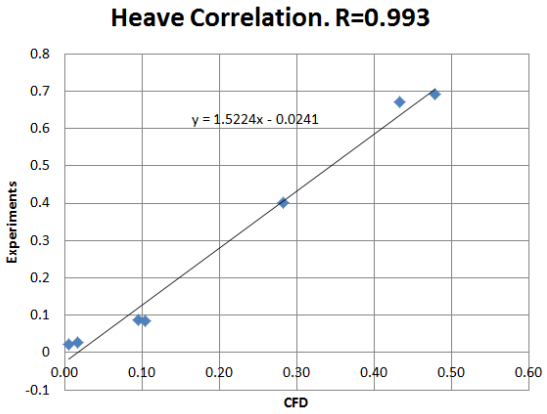

Fig. 4: Heave against frequency correlation.

A comparison between experimental and CFD added resistance results for frequencies between 0.425 and 0.9rad/s is shown in Figure 5. Overall, CFD matches the shape of the QTF from the model tests. However, for the frequencies close to resonance i.e. ~0.5rad/s the drag is over estimated, whereas for higher frequencies the tendency is to slightly underestimate the QTF, although the discrepancies are relatively small. The correlation between experiments and CFD can be seen in Figure 6; the correlation factor of 0.912 is weaker than for pitch and heave but still a strong linear correlation between experiments and CFD showing a good match in the overall QTF calculations.

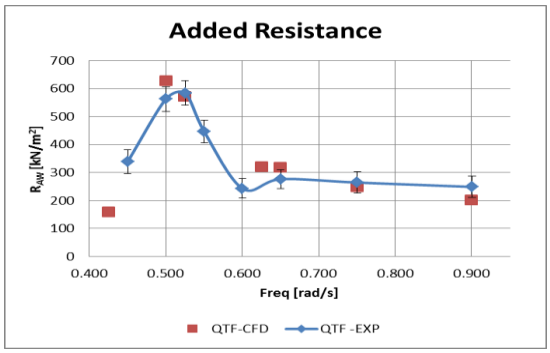

Fig. 5: Heave against frequency correlation.

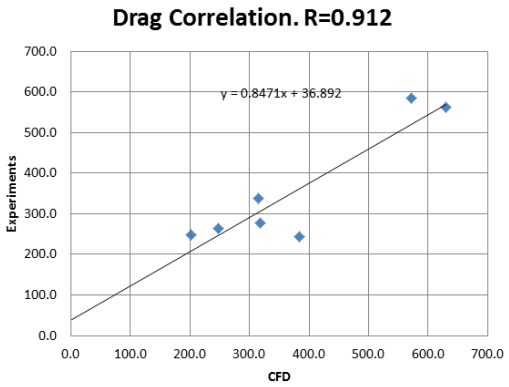

Fig. 6: Drag against frequency correlation.

Pressures on the bow section were obtained using gauges during the experiments and compared to those calculated in the CFD calculations carried out by LR. The pressure gauges were located in a range of frames near the bow of the vessel although these cannot be shown for reasons of confidentiality. Comparison between measurements and experiments can be seen in Figure 7 for the resonant frequency. The correlation between experiments and CFD is satisfactory as not only the trends but also the local values are consistently matched.

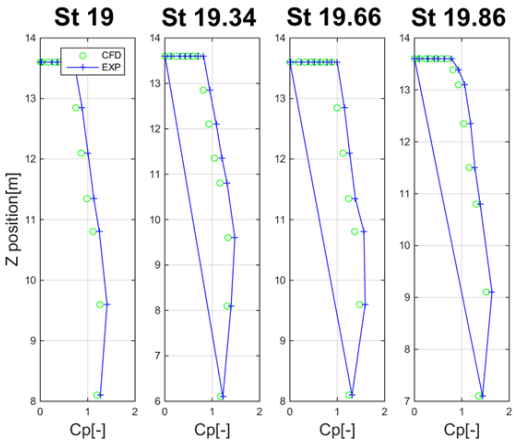

Fig. 7: Pressure amplitudes comparison (0.525rad/s 1.0m).

2.2 Irregular sea state

The irregular wave characteristics used for the towing tank tests were imposed in the CFD calculations and modelled as a Pearson-Moskowitz spectrum for sea state 5. Although the temporal evolution of measured and calculated points was not identical, the amplitudes and frequency distribution of both were in the same range as shown in Figure 8.

Table 1: Irregular sea state results at 10.0kn.

	Time (s)	HS Ship (100*wave height/L_{pp})	QTF Ship [kN/m²]
Exp	80.0	1.0444	29.2
Exp	80.0	1.1084	26.4
Exp	80.0	1.0699	29.4
CFD	80.0	1.0519	31.4
CFD	160.0	1.0372	32.0
CFD	300.0	1.0360	32.3

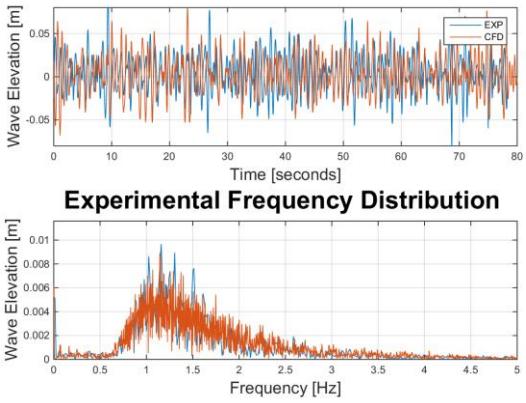

Fig. 8: Experimental and numerical wave spectra.

The agreement in terms of added resistance QTF between CFD and experiments is good as shown in Table 1.

Overall, the results of the comparison between experiments and CFD indicate the ability of CFD to predict the added resistance in regular sea states. The correlation factors of the quantities directly measured in the model scale were 0.95 (heave, pitch and pressures in the gauges). The correlation is also strong in added resistance due to irregular sea state, although with a lower correlation factor of 0.91. It was shown that the local quantities such as pressure correlate well however uncertainty is introduced to the experimental QTF through the extrapolation to full scale. Furthermore there is a strong influence from the towing force in the experimental results that also influences the comparison between experimental and computational results.

3 Full scale CFD in waves

Due to the technical difficulty in obtaining reliable data for added resistance in waves at full scale, the justification for the use of CFD is based on two earlier achievements. Firstly, the model scale validation described above and secondly, on the self-propulsion full scale validation carried out by TID and summarised in (Zegos, Ponkratov). The full scale CFD tests were carried out for the same ship used in the model scale analysis. Both regular and irregular waves were simulated and are presented below. In addition, tests were carried out under self-propulsion in regular waves in order to see what the effects of the propeller are on the added resistance.

3.1 Regular waves - Bare hull

Three frequencies (0.45, 0.525 and 0.65rad/s) were tested for the full scale bare hull. The linear response operator for pitch is shown in Figure 9, for both model scale and full scale CFD for the same wave height. They show good agreement for the higher frequencies (0.525 and 0.65rad/s), however, for the lower frequency (0.45rad/s) the pitch value predicted for full scale was ~15% higher than the predicted for model scale. Bearing in mind the difference in the order of magnitude in the Reynolds number, the discrepancies between model and full scale are attributed to viscous effects as implied by the Reynolds number. In model scale and due to the reduction on the Reynolds number, the motion damping is expected to be higher than in full scale. The higher motions appear for the lower frequencies, hence the stronger damping effects will appear for those lower frequencies.

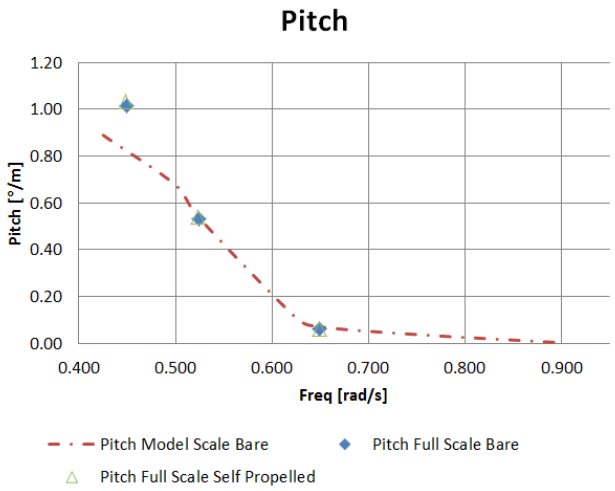

Fig. 9: Bare hull full scale pitch.

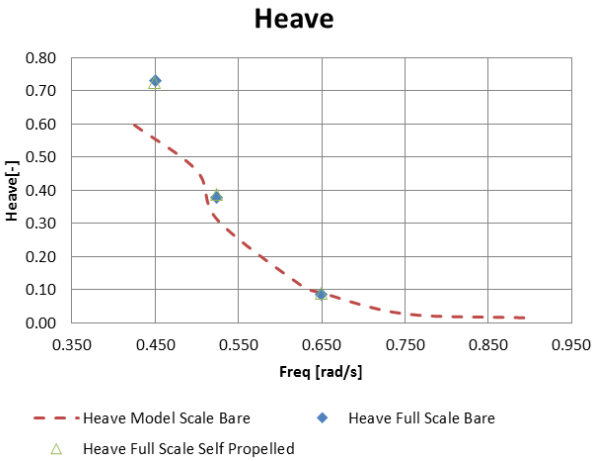

Fig. 10: Bare hull full scale heave.

The same comparison between model and full scale is shown in Figure 10 for heave. As for pitch, the agreement is very good for the higher frequencies. At the lower frequency, ship scale heave is found to be higher. The same explanation in terms of damping differences between model and full scale can be cited.

A comparison between model and full scale added resistance is shown in Figure 11. Starting from the low frequency waves it can be seen that the added resistance at ship scale matches that at model scale. It would have been expected to be lower however as was shown earlier the ship motions at ship scale were larger in magnitude for the lowest frequency which inevitably resulted in a larger than expected added resistance. For the resonance frequency and highest frequency, ship scale added resistance is lower than that at model scale although within the same order of magnitude, in line with expectations due to viscosity effects linked to the Reynolds number.

3.2 Regular waves Self-propelled

Self-propulsion full scale CFD tests were carried out for the same frequencies and wave amplitude as described in the previous section. The propeller was modelled using an actuator disc to take into account the hull – propulsion interaction thus accounting for the suction effect on the hull. The equilibrium point was reached iteratively by averaging the main force over the last ten cycles. The main disadvantage of this method is a large increase in the computational resources required as the number of cells is duplicated since it is not possible to model only half the domain with the symmetry plane down the middle of the ship. The computational time increase due to the "search" of the equilibrium point by a cyclic change of the propeller load in order to reach the equilibrium between drag and thrust.

It can be seen that the effect of the propulsion both on pitch (Figure 9) and heave (Figure 10) is relatively small and no significant differences appear. Regarding the added resistance, in Figure 11 it can be seen that the propeller increases the thrust deduction factor and hence the required power by the vessel in the sea state condition.

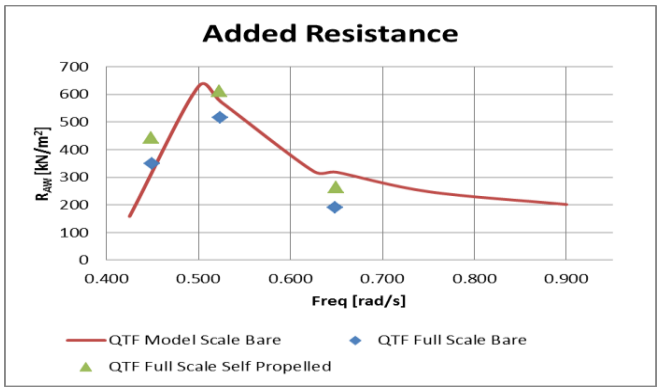

Fig. 11: Bare hull full scale added resistance.

3.3 Irregular sea states

A full scale calculation for a Pearson-Moskowitz spectrum for sea state 5 and 10 knot speed for the full scale tanker was carried out and compared to the model scale CFD presented in Section 2.2. The results for the added resistance can be seen in Table 2. These show that the added resistance in full scale follows the same tendency as for the regular waves in that the full scale predictions are slightly lower than those at model scale.

Table 2: Irregular sea state QTF for sea state 5 and 10 knot ship speed.

	QTF[kN/m²]
CFD-Model Scale Extrapolated	32.0
CFD-Full Scale	26.0

4 Conclusions and recommendations

- Computational fluid dynamics can be used effectively to predict the added resistance experienced by ships travelling in a range of sea states.
- The indications are that model tests might over-predict added resistance at ship scale.
- The suction effect of the propeller was found to be important to the accurate prediction of the added resistance
- On the computational side, attention should be paid on creating lean meshes that will not dampen the sea state wave heights excessively. Time step selection is also an area that needs to be worked on as these simulations have a tendency to take a long time.

Acknowledgements

We thank the CRS for the collaboration and kind permission to publish the model test results it provided for this study.

References

Zegos C., Ponkratov D., Ship Scale CFD Free Sink, Trim & Surge Self-Propulsion Simulation and Direct Comparison to Sea Trials, International Conference on Computer Applications in Shipbuilding 2015, Bremen, Germany, September 2015.

Progress towards CFD guidelines for zig-zag simulation in waves

Anastasia Zubova, Alvaro del Toro Llorens, Benoit Mallol, Charles Hirsch
NUMECA International, Brussels/Belgium
anastasia.zubova@numeca.be, alvaro.deltorollorens@numeca.be, benoit.mallol@numeca.be,
charles.hirsch@numeca.be

1 Introduction

SHOPERA (Energy Efficient Safe SHip OPERAtion), funded by the European Commission in the frame of FP7, was launched in October 2013, aiming at developing suitable methods and tools and systematic case studies which will enable the development of improved guidelines and their submission for consideration to IMO-MEPC in 2016. Simplified formulas, potential flow methods, motion simulators and viscous field methods, will be compared with each other and with model tests for selected cases. Among the provided cases, the Duisburg Test Case (DTC) case is selected to investigate the best meshing strategies and computations settings for zig-zag simulations in waves. The present extended abstract is the first publication from a series of papers providing experiences and guidelines using CFD techniques for complex simulations embedding seakeeping, self-propulsion and manoeuvrability at the same time.

2 Geometry and test conditions

Fig. 1: DTC ship geometry

The Duisburg Test Case (DTC) design is a post Panamax 14000 TEU container vessel. It was developed at the Institute of Ship Technology, Ocean Engineering and Transport Systems (ISMT) of the University of Duisburg-Essen and described in Sprenger et al. (2016). The main particulars of this vessel for the design loading condition (Draft T = 14.5 m) are given in Table 1 in full scale. Note that the below given wetted surface S is without the area of the appendages. On each side of the vessel, a segmented bilge keel is placed symmetrically around the midship section, consisting of five segments, each with 14.85 m length and 0.4 m profile height. The gap width between the segments is 3 m.

Table 1: DTC main dimensions

Lpp [m]	BWL [m]	T [m]	V [m3]	S [m2]	CB [-]
355.0	51.0	14.5	173467	22032	0.661

The ship's mass and inertia characteristics for the loading condition used in the seakeeping and maneuvering tests of the present paper are shown in Table 2. LCG and VCG are given on the axis, at the bottom and on the symmetry plane of the keel.

Table 2: DTC loading conditions

m [kg]	LCG [m]	VCG [m]	GM [m]	rx [m]	ry [m]	rz[m]
177804	174.059	19.851	5.1	20.3	87.3	87.4

The DTC design contains a twisted rudder with Costa bulb and a NACA 0018 base profile (see Fig. 2). The projected area of the movable part of the rudder is 95.1 m2.

Fig. 2: Rudder and propeller geometries

The coordinate system is right-handed with the X-axis positive towards the bow and the Z-axis positive upwards. The origin of the ship bound coordinate system used in the measurements is located at [Lpp/2, CentreLine, BaseLine]. Head wave is denoted by 0°, following wave by 180°, beam wave by 90° from PS. A positive rudder angle δ indicates that the rudder has been set to port side (PS). All the computations are performed with a model scale of 63.65.

3 Computation and mesh setups

3.1 Strategy of investigation

FINE™/Marine is used in the present paper. The software is a complete CFD tool chain dedicated to naval architect and marine engineers, described in more details in Hildebrandt et al. (2015). Following the idea of provide guidelines of zig-zag maneuver in waves and self-propulsion conditions, several preliminary investigations are performed and are presented in this extended abstract only.

1. Waves study for a period of 10.6s and a height of 2.0m:
    a. 2D configuration with background and ship's domain (but without the ship itself),
    b. 3D configuration with the hull with actuator disk but no rudder (no maneuver),
2. Maneuverability study for 20°/20° rudder angle (zig-zag):
    a. 3D double body configuration with the hull, rudder and actuator disk (no wave).

Due to the complexity of the investigation 2.a, the simulation is split into several steps, ensuring a simpler analysis and thorough control on the numerical parameters:

1. Resistance simulation: the ship accelerates until the cruise speed, 3 DOF (Degrees Of Freedom) are imposed: Tx, Ty and Rz(yaw), the rudder is fixed at the rudder angle δ=0°;
2. Self-propulsion simulation: the Tx DOF is solved and at the end of this simulation, the thrust balances the drag of the ship.
3. Maneuvering: the 3 DOF (Tx, Ty and Rz(yaw)) are solved and the rudder starts to rotate; specific dynamic library for the self-propulsion is applied.

3.2 Mesh characteristics

The overset technology is selected over the sliding grid method to ensure that there is no constrains on the motions of the ship. The ship is placed inside an overlapping domain freely moving over a background domain. To investigate the mesh continuity of the overlapping domains, 2D and 3D meshes have been generated for investigations 1.a and 1.b. Thus, investigation 1.a will show the pure influence of the overlapping boundary cells interpolation on the wave propagation, while 1.b includes the ship motion influence and the wave system interference with the incoming waves passing the overlapping boundary. Since the wave height and the wave length are very small, the number of cells is very important compared to more standard waves. However, for the double body simulation 2.a, the number of cells is lighter than for 1.b and does not contain a background domain. Generated numbers of cells are provided in Table 3 below.

Table 3: Number of cells per domain for all investigations

	1.a	1.b	2.a
Background	68 000	14 073 000	-
Ship	27 360	18 591 000	8 661 000
Rudder	-	1 230 000	3 549 000
Total	95 360	33 894 000	12 210 000

For 1.b, a specific mesh density area is added to get the same cell size between the background and the ship's domain boundaries in the prevision of the future maneuvers (not presented here). This principle is essential to get the best possible interpolation between the two overlapping domains. Fig. 3 shows in black solid lines the possible locations of the ship's domain during the maneuvering. Besides, this background domain is following the translations of the ship to limit its own size. The number of cells is then reduced compared to the classic idea of creating a large background domain which does not move in time, and still ensures that the ship's domain is kept within the background

domain during its motions. This idea can only work when the waves are small enough and boundary conditions from the side of the background are still far enough to avoid any extra wave creation.

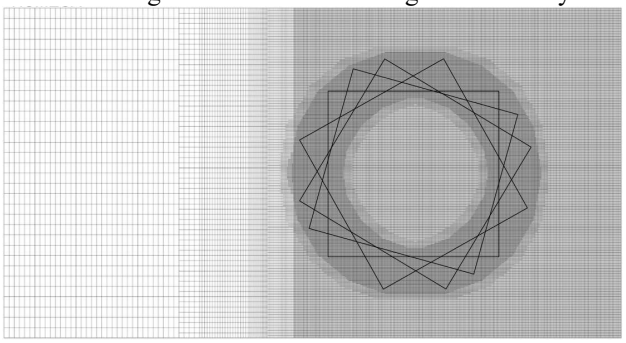

Fig. 3: Top view of the mesh density of the background with the possible locations of the ship's domain boundaries during the maneuvering

For investigation 2.a, meshes with sliding grid and overset approaches are tested for the rudder's domain. Fig. 4 shows views of the mesh of the rudder with the overset and sliding grid configurations respectively. The overset mesh has less strict cell size limitations, mainly ensuring the mesh continuity between the rudder and the ship domains. However, an additional refinement sector for the sliding grid has to be applied due to geometrical constraints, to ensure that in the area of $\delta=\pm30°$ mesh cell size at the rotating rudder and the ship domains boundaries are similar. This leads to a difference of 2.3M cells. However, the sliding grid option is still selected since it avoids numerical imperfections in the near region of the rudder.

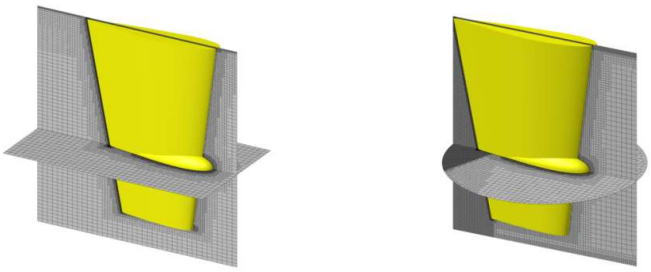

Fig. 4: Rudder domain mesh: overset and sliding grid configurations

3.3 Turbulence model

The ITTC report (2011) report indicates that both the resistance and the velocity field depend on the turbulent model, but the dependence of side force and yaw moment (the most significant for manoeuvring), is less significant since these hydrodynamic forces are dominated by pressure and less by viscosity. Wall functions and classic turbulence models can then be used to achieve a reasonable accuracy. K-ω (SST Menter) is used in the present paper but the authors will also investigate the EASM in a future publication.

3.4 Propulsion modeling

These computations are done in self-propulsion mode, with fixed rotational speed for the propeller and solved ship velocity to reach 6kn speed. However, taking the real geometry of the propeller into account during a RANS simulation is quite time consuming. Thus, body forces with an actuator disk approach, are frequently used to approximate the effect of the propeller on the flow. Different methods are known to calculate these body forces so that they yield the propeller thrust and torque: using a standard radial distribution, a coupling with a potential code as described in Deng et al. (2013) or directly using the information from the propeller open water characteristics when given or previously computed. The latest approach is used in the present paper and the principle is summarized as follows:

1. Compute the averaged inflow velocity at the actuator disc plane,

2. Giving propeller revolution rate [n], propeller advance ratio [J] is computed,
3. With the J value, the thrust coefficient [Kt] and the torque coefficient [Kq] values are read from the open water performance curve,
4. Thrust [T] and Torque [Q] are computed from the Kt, Kq coefficients and converted into the axial and tangential body force components respectively.

3.5 Dynamic libraries

The principle of dynamic libraries embedded into FINE™/Marine is to give the freedom to the user to program is own code for a variety of interactions with the flow solver: particular body motions, user-defined actuator disk model or external efforts acting on the bodies. Two of them are used here:

Motions (*kinematic_control.f90*):

- Activates the rudder motion when a wave crest reaches the amidships (wave crest probed and stored into the file *points_probe.dat*)
- Imposes the motion law of the rudder (*Rn*), which also depends on the ship heading angle (*Rz0*);
- Imposes the translations *Tx0* and *Ty0* of the background domain to be equal to the translations *Tx0* and *Ty0* of the ship domain;
- Stops the computation after a given number of rudder executes, being the total number of time steps unknown.

Propulsion (*ad_propeller_code.f90*):

- Emulates an external propeller code, which computes the axial and tangential volume forces based on an actuator disk model and the existing open water performance curves (J,K_T) and (J,K_Q).

3.6 Time step selection

The choice of the time step value is of high importance since it will drive the accuracy of the whole simulations. Also, this time step should be calculated with care to avoid useless CPU time. Five main constraints can be identified:

1. The ships advancing speed
2. The rudder rate
3. The propeller rotational speed
4. The flow particle velocity
5. The waves encounter period

Following the FINE™/Marine Documentation, Table 4 summarizes the possible time step values.

Table 4: Time step selection

	Ship advancing speed	**Rudder rate**	**Wave encounter period**	**Flow particle velocity**	***Propeller rotational speed***
Possible time step values [s]	7.2E-02	3.6E-03	5.6E-03	6.7E-03	*1.667E-4*

The time step values for the physical conditions for the rudder rate, propeller rotational speed and the flow particle velocity all ensure a Courant number below 0.3 at the interface between domains. Thus the mesh cell size should be always taken into account for the time step value selection. For the current studies the time step has been imposed based on the rudder rate. For indication (since an actuator disk approach is used in this paper), the time step due to the presence of the propeller has been computed. The computation time would be 2.15 times longer only considering the cell size and the rotational speed of the propeller.

4 Results

For investigation case 1.a., the quality of the wave propagation through the overlapping boundary is important. Two waves probes have been specified to record the wave signal before and after the overlapping domain interface; the distance between the probes is equal to one wavelength (λ_w). Plots

of the results are provided on Fig. 5 which shows an excellent superposition: the wave signal is well propagated through the boundaries.

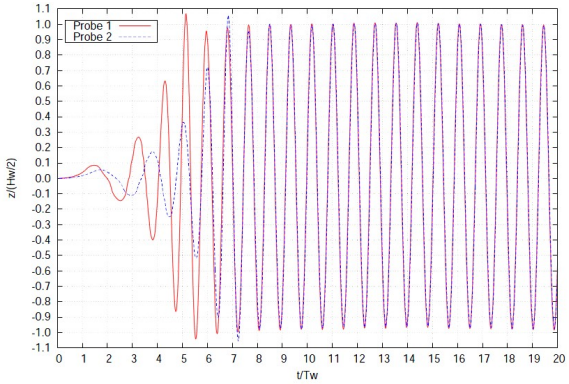

Fig. 5: Wave probes in the background domain (Probe 1) and ship's domain (Probe 2)

For the investigation 1.b., we can observe a smooth transfer of the wave system combining the wave from the wave generator and the ship motions. Representation of the wave elevation is shown on Fig.6.

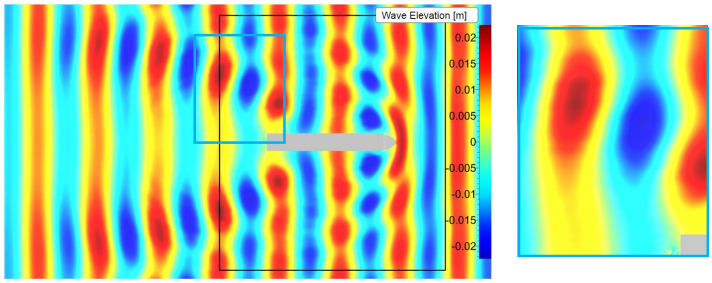

Fig. 6: Wave propagation through the overlapping boundaries (black lines) around the ship's domain (left). Blue lines show the zoom location, illustrated on the right.

Fig. 7 shows the motion response time for the ship yaw angle compared to the rudder angle for the investigation 2.a. A satisfactory delay of nearly 10 seconds is observed and is similar to BEM codes results provided by the SHOPERA workshop. Several reasons can be mentioned: no waves are considered in the double body simulation and all the degrees of freedom are not solved. Also, among the provided benchmark conditions, it was not clear if the ship speed or the rotational speed of the propeller [rpm] should be fixed. Thus, with the selected approach of the fixed rpm's for the propeller, a difference of the ship speed of approximately 16% has been observed. This should be clarified with the organizers.

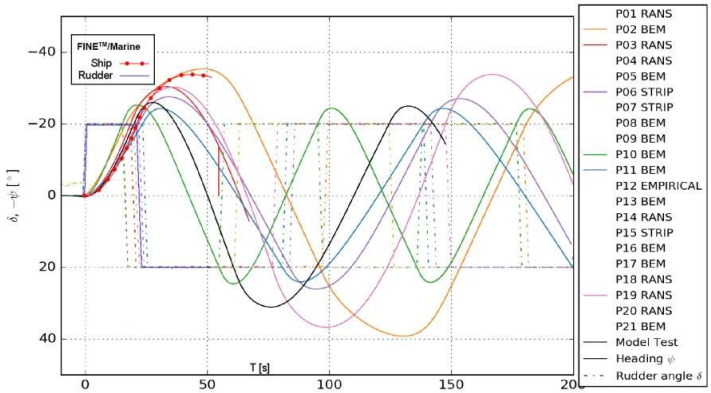

Fig. 7: Zig-zag maneuver double body configuration. comparison to the SHOPERA workshop results.

5 Conclusions

- The mesh continuity between background and overlapping domains is of the great importance. Indeed, an approximate interpolation can create numerical waves of the order of the simulated ones. It can be enforced either with a dedicated refinement sector or with the adaptive grid refinement technique.
- Due to small gradients of the values in the whole domain of simulation, low Froude number simulations require special attention to the mesh quality to avoid possible numerical errors in the order of the physical effects simulated. Increasing the number of non-linear iterations, convergence criteria and pressure solver iterations are recommended.
- Restart computation strategy supports the idea of smooth evolution of all effects to be simulated: resistance to self-propulsion to maneuvering; added resistance in waves to self-propulsion in waves to maneuvering.
- Time step selection is based on the physics and case conditions (rudder rotation, propeller, actuator disc and etc.) but the most demanding requirement should be satisfied: encountered period for waves in case of actuator disc; rotational speed of propeller for the complete simulation. The goal is to keep the Courant number below 0.3 in the vicinity of the ship to resolve all effects properly.
- Propulsion system modeling through an actuator disk model enriched with the open water performance of the real propeller seems a promising approach. This approach should now be validated comparing with the real propeller.
- Future simulations will be changed to avoid an approximate ship speed of 16%.

Acknowledgements

This work is carried out within the scope of the ongoing Project SHOPERA 2016. The authors would like to thank the organizers of the workshop for gathering all these data and making them available to the public.

References

1. F. Sprenger, V. Hissani, A. Maron, G. Delefortie, T. Van Zwijnsvoorde, A. Cure-Hochbaum, A. Lengwinat (2016). Establishment of a Validation and benchmark database for the assessment of ship operation in adverse conditions, Proceedings of the 35th International Conference on Ocean, Offshore & Arctic Engineering, OMAE2016.
2. T. Hildebrandt, M. Reyer (2016). Business and Technical Adaptivity in Marine CFD Simulations Bridging the Gap, Proceedings of COMPIT 2015, Ulrichshisen, Germany.
3. ITTC Recommended Procedures and Guidelines (2011). Guideline on Use of RANS Tools for Manoeuvring Prediction.
4. FINE™/Marine Documentation (2016). Latest guidelines on sea keeping computations.
5. M. Visonneau, P. Queutey, G. B. Deng, J. Wackers, E. Guilmineau, A. Leroyer, Benoit Mallol (2012), Computation of Free-Surface Viscous Flows around Self-propelled Ships with the Help of Sliding Grids, Proceedings of COMPIT 2012, Liege, Belgium.
6. G. Deng, P. Queutey, M. Visonneau, F. Salvatore (2013) Ship propulsion prediction with a coupled ranse-bem approach, V International Conference on Computational Methods in Marine Engineering.
7. R. Potthoff, B. el Moctar, A. Papanikolau, (2016) Presentation of Benchmark results, SHOPERA Benchmark Workshop, London.

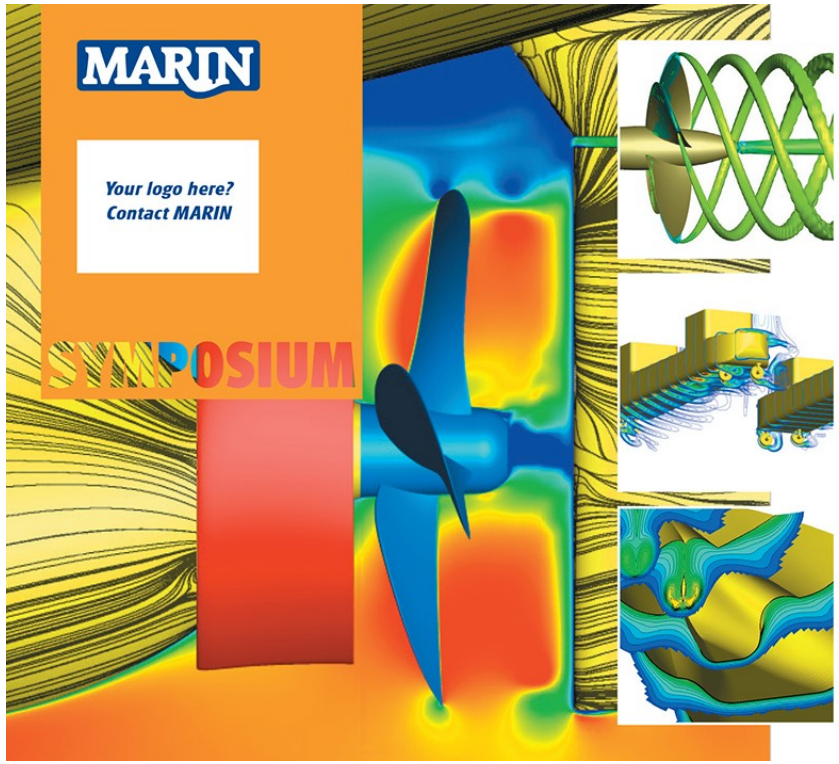

20th Numerical Towing Tank Symposium (NuTTS'17)

Wageningen, Netherlands, 1 - 3 October 2017

In 2017, MARIN is organising the 20th Numerical Towing Tank Symposium. The conference covers the numerical simulation of flows around ships and offshore structures, with a strong link to realistic applications.

The NuTTS'17 symposium provides a forum for informal discussions among experts in the field and to disseminate latest results. Younger workers and Ph.D. students are especially encouraged to participate.

Topics:

- Nonlinear flows around marine structures (LES, RANSE, Euler with or w/o free surface)
- Free-surface flows around marine structures (3D ship seakeeping, free-surface viscous flows)
- Related topics (validation experiments, numerical techniques, grid generation, etc)

Contact
Thomas Lloyd t.lloyd@marin.nl
Auke van der Ploeg a.v.d.ploeg@marin.nl

Venue
Hotel De Wageningse Berg, Wageningen
www.hoteldewageningscheberg.nl